
Shallow Cumulus Convection

Ondiepe Cumulus Convection

Roel Neggers

Proefschrift

ter verkrijging van de graad van doctor
op gezag van de rector magnificus
van Wageningen Universiteit,
Prof. dr. ir. L. Speelman,
in het openbaar te verdedigen
op woensdag 11 december 2002
des namiddags te vier uur in de aula.

1667/11/02

ISBN 90-5808-774-3

Dankwoord

Geen proefschrift komt tot stand zonder de steun en toeverlaat van heel veel mensen, dus ik zou graag de gelegenheid willen nemen om hier een woord van dank aan hen te wijden. In de eerste plaats wil ik mijn begeleider Pier Siebesma bedanken, en natuurlijk Harm Jonker. Zij hebben me omgetoverd van een net afgestudeerde student, nog onbekend in de turbulentie-leer en wolkenfysica, naar een promovendus in de grenslaagmeteorologie. In het begin komt promotieonderzoek vaak neer op het uitvoeren van duidelijk omlijdnd werk, met de bedoeling om vertrouwen te raken met de gangbare theorieën en modellen. Vaak is het al een hele opgave om überhaupt te begrijpen waar het over gaat, en goede begeleiding is in dit stadium een pre. Pier en Harm stonden altijd voor me klaar en namen alle tijd om in te gaan op al mijn vragen. Gelukkig komt er tijdens de promotie ergens een moment dat eigen ingevingen plotseling toch geen onzin blijken te zijn, en dit is meestal ook het moment dat ook je zelfvertrouwen als onderzoeker toeneemt. Er was altijd ruimte voor nieuwe ideeën, en een van de leukste dingen was het samen zoeken naar een oplossing voor een bepaald probleem voor een volgekalkt bord met allerlei afleidingen. Het onderzoek heeft geresulteerd in enkele publicaties in gereviewde wetenschappelijke tijdschriften. Het schrijven van goede artikelen is een andere kunst die ik van Pier en Harm heb geleerd. Maar misschien wel het belangrijkste vond ik de gezelligheid, er was altijd wel wat te lachen en vaak liepen gesprekken bij de koffiehoeke of de lunch zover uit dat het werk zelf bijna vergeten werd.

Mijn promotor Bert Holtslag wil ik bedanken voor zijn begeleiding in de afgelopen vier jaar, en voor al onze discussies over het onderzoek en de artikelen die ik aan het schrijven was. Hij benadrukte vaak de rode draad in het onderzoek en gaf zo richting aan het werk dat uiteindelijk resulteerde in dit proefschrift. Met Bert en Pier heb ik samen de structuur van het proefschrift opgezet, en de vele tussenversies bediscussieerd. Zonder hun visie zou het proefschrift zoals het er nu ligt niet mogelijk zijn geweest. Bedankt!

Een speciale vermelding wil ik maken voor Peter Duynkerke. Begin dit jaar overleed hij, plotseling en onverwacht voor iedereen. In de maanden daarvoor heb ik veel met Peter samengewerkt aan een bepaalde dataset met vliegtuigwaarnemingen in cumulus wolken, die hij onder zijn beheer had. Het idee om die te vergelijken met ons LES model kwam mede van hem, en de resultaten waren zoals verwacht erg veelbelovend. Deze studie vormt nu een belangrijk onderdeel van dit proefschrift. Zijn enthousiasme voor de meteorologie was aanstekelijk, en ik zal me Peter blijven herinneren als een hartelijk, open persoon en een creatieve, enthousiaste wetenschapper. Ik wil hier ook Stefaan Rodts bedanken voor onze samenwerking aan het artikel over de SCMS dataset. Peter was tevreden over het werk en de resultaten, het resulterende artikel is nu geaccepteerd voor publicatie in the Quarterly Journal of the Royal Meteorological Society.

Ik wil graag de grenslaagmeteorologie groep vermelden in dit dankwoord, bestaande uit Stephan de Roode, Margreet van Zanten, Peter Duynkerke, Harm Jonker, Pier Siebesma,

Geert Lenderink, Aad van Ulden, Han van Dop, Arjen van Dijk, Jordi Vilà, en anderen. Het was tegelijk leuk en leerzaam om werk of artikelen te bespreken en te discussieren over hun betekenis. In de eerste jaren van mijn promotieonderzoek heb ik enkele colleges gevolgd op het Instituut voor Marien en Atmosferisch onderzoek Utrecht, zoals Grenslagen door Peter Duynkerke en Turbulentielear door Han van Dop. Het is een goede start gebleken voor een toenmalig net afgestudeerd geofysicus, nog oningewijd in de geheimen van atmosferische turbulentie en convectie. Ik heb ook colleges gevolgd bij het J. M. Burgerscentrum, de onderzoeksschool voor stromingsleer van de Technische Universiteit Delft. Tevens heb ik de cursus Parameterizatie van Diabatische Processen op het ECMWF gevolgd. Tenslotte wil ik de Buys Ballot Onderzoeksschool noemen, de jaarlijkse symposia waren een goede gelegenheid om eigen werk te presenteren aan een breed publiek, en om een kijkje te nemen in gerelateerd onderzoek in Nederland dat buiten de eigen specializatie valt.

Ik heb met veel plezier op het KNMI gewerkt aan mijn promotie onderzoek. Het is me altijd opgevallen hoe breed de kennis en expertise is die op het KNMI rondloopt, er was altijd wel iemand die me kon helpen bij een probleem dat verder ging dan de grenzen van mijn eigen onderzoeksgebied. Ik wil dan ook graag mijn collega's bedanken van de afdeling Klimaat en Seismologie op het KNMI, specifiek de medewerkers in de groep Atmosferisch Onderzoek met wie ik het meest te maken had. Geert Lenderink bedank ik voor zijn hulp bij het gebruiken van het RACMO model, en voor het lezen en corrigeren van de artikelen die ik geschreven heb. Ik wil graag Rob van Dorland bedanken voor zijn hulp bij het schrijven van de paragraaf over wolken en straling in de introductie van dit proefschrift. Ik wil natuurlijk mijn kamergenoten op het KNMI bedanken voor de gezelligheid en leuke werksfeer: Harm Jonker, Joop Konings, Anne Mathieu, Marietta van Berkel, Hartwig Deneke, en de studenten die af en toe een paar maanden op onze kamer vertoefden. Ook heb ik altijd graag een balletje getrapt op dinsdag rond lunchtijd op het KNMI meetveld. Die paar extra pieken in de meetdata vallen toch wel binnen de natuurlijke variabiliteit zullen we maar zeggen..

I would like to thank the community of atmospheric scientists participating in the GEWEX Cloud System Studies (GCSS) Working Group I and the European Cloud System studies (EUROCS). At their workshops and meetings there was always room for beginning scientists to present their work and to practice the art of presenting a talk in correct English, in a tolerant but critical scientific atmosphere. I was always pleasantly surprised by the energy and motivation of the participants in presenting and discussing new theories and results, and by the creativity behind their work. But perhaps the most enjoyable were the good debates on the latest developments in football over a glass of beer somewhere in a pub nearby. In that respect, the organizers surely never failed to find a pleasant location for the meetings to take place.

Ik wil graag al mijn vrienden bedanken voor hun interesse en steun. Het moet af en toe toch vrij vermoedend zijn om al die praatjes over wolken en weer aan te horen door een overenthousiaste meteoroloog. Tenslotte wil ik natuurlijk mijn lieve familie bedanken voor al hun steun. In de eerste plaats mijn ouders, jullie hebben me altijd mijn eigen gang laten gaan, maar waren altijd geïnteresseerd in wat ik allemaal aan het doen was. Bedankt, zonder jullie was dit proefschrift niet mogelijk geweest, alleen al natuurlijk vanwege die mooie wolkenfoto van Figuur 1.3c! Mijn broer Bas wil ik bedanken voor onze vele discussies over de wetenschap, en zijn geduld met een promovendus in de proefschriftstress. De verbouwing van ons mooie huis en de vele weekendjes klussen waren een welkome afleiding op de mentale arbeid van

het schrijven van een proefschrift. Ongetwijfeld heeft het ophangen van gipsplaten en het stucen van muren even de nodige afstand opgeleverd van mijn proefschrift voor een gezonde reflectie op de wetenschappelijke vorderingen.

*One scheme to rule all clouds,
One scheme to describe them,
One scheme to average all,
And in their variance bind them.*

Inspired by J. R. R. Tolkien's *The Lord of the Rings*

Contents

1	An introduction to shallow cumulus	13
1.1	Cumulus clouds in history	13
1.2	The atmospheric boundary layer	15
1.3	The classification of cumulus clouds	17
1.4	Climatology	20
1.5	Atmospheric modeling	23
1.6	Shallow cumulus research	26
1.7	Thesis objectives and outline	28
2	Background	29
2.1	Physics and dynamics	29
2.1.1	Atmospheric thermodynamics	29
2.1.2	Governing equations	32
2.1.3	Boundary layer structure	36
2.1.4	Conditional instability	37
2.1.5	Turbulent kinetic energy (TKE)	39
2.1.6	Conditional averaging and cloud budgets	41
2.2	Observation, simulation, parameterization	46
2.2.1	Shallow cumulus field-experiments	46
2.2.2	Cloud measurements and large-eddy simulation (LES)	56
2.2.3	Developing parameterizations	60
2.3	Research topics	64
2.3.1	An evaluation of LES	64
2.3.2	Cloud population variability	64
2.3.3	The mass flux approach	67
2.3.4	Cloud mixing theories	70
2.3.5	Cloud-subcloud interactions	71
3	A validation of LES against observations by aircraft and Landsat during SCMS	75
3.1	Summary	75
3.2	Introduction	76
3.3	Instrumentation and observations in SCMS	78
3.4	Setup of the LES case	81

3.5	Conditional sampling	83
3.6	Parameterizations	84
3.7	Results	86
3.7.1	Daytime development	86
3.7.2	Thermodynamic state	87
3.7.3	Lateral mixing	89
3.7.4	Vertical transport	91
3.7.5	In-cloud turbulence	93
3.7.6	Cloud size densities	96
3.8	Discussion and Conclusions	98
Appendix 3.A	Cloud size densities	99
4	Size statistics of cumulus cloud populations in large-eddy simulations	101
4.1	Summary	101
4.2	Introduction	101
4.3	The LES model and case descriptions	103
4.4	Definitions	107
4.5	Results	109
4.5.1	Cloud size densities	109
4.5.2	Domination by intermediate sized clouds	112
4.5.3	Sensitivity to resolution	114
4.5.4	Sensitivity to domain size	117
4.5.5	Effects of vertical wind-shear	118
4.5.6	Comparison to another LES study	118
4.6	Discussion and Conclusions	121
Appendix 4.A	Elementary definitions of cloud size densities	123
5	A multi parcel model for shallow cumulus convection	125
5.1	Summary	125
5.2	Introduction	125
5.3	Conserved variable diagrams	127
5.4	The parcel model	129
5.4.1	Governing equations	129
5.4.2	Parameterizing the mixing terms using LES	131
5.4.3	Discussion of the model	135
5.5	A multi parcel approach	136
5.5.1	An ensemble of parcels	136
5.5.2	Initialization and validation with LES	136
5.6	Numerical results	137
5.6.1	Profiles	137
5.6.2	Variability	140
5.7	Conclusions and perspectives	142
Appendix 5.A	LES case descriptions	144
Appendix 5.B	Numerics	145

6	Mass flux closures in diurnal cycles of shallow cumulus	147
6.1	Summary	147
6.2	Introduction	147
6.3	Mass flux closures at cloud base	149
6.3.1	The subcloud layer equilibrium closure	149
6.3.2	CAPE adjustment	150
6.3.3	Convective subcloud velocity scales	151
6.4	Case descriptions and large-eddy simulation.	154
6.4.1	Cases	154
6.4.2	LES results	156
6.5	Single column model results	159
6.5.1	Description of the model	159
6.5.2	Results	160
6.6	Summary and conclusions	164
7	Conclusions and Outlook	167
7.1	Comprehensive summary	167
7.2	Perspectives	169
7.2.1	The current state of cumulus representations	169
7.2.2	Contributions and implications	171
7.2.3	Future developments in convective cloud modeling	173
	Bibliography	174
	Symbols and Acronyms	191
	Nederlandse Samenvatting	195
	Publications	199
	Curriculum Vitae	201

CONTENTS

Chapter 1

An introduction to shallow cumulus

Eternal Clouds! Let us appear in dew and brightness, let us arise from the roaring depths of Father Ocean and float towards the wood-crowned summits of lofty mountains. Let us dominate the remote valleys and the harvests produced by the sacred earth, and the rushing sounds of the divine rivers, and the waves of the resounding sea, while being lightened by sparkling rays from Aether's unweary eye. Come, let us shake off the rainy mists from our immortal forms and behold the earth with far-seeing eye.

Aristophanes, *The Clouds*, 419 b.C.

1.1 Cumulus clouds in history

Descriptions of clouds date back to the dawn of written history. In those times humans lived close to nature, and the weather was an important part of every-day life. They recognized the vital role of clouds in bringing rain, they constructed wind-mills for processing corn and for the irrigation of farmlands, they sailed the seas to explore new coasts, and gazed in awe at the violence of thunderstorms. Among the first texts on clouds were written by the Babylonians, who related the weather to the movements of the heavenly bodies (Fringsinger, 1977). In general, atmospheric phenomena were seen as the work of the Gods. The classic Greeks were among the first to systematically observe atmospheric phenomena, in a metaphysical attempt to understand the world around them. One of the most influential historical works on the earth sciences and meteorology from that period is Aristotle's *Meteorologica*, written around 340 b.C. On the subject of moisture and clouds in the atmosphere he observes:

The exhalation of water is vapour: air condensing into water is cloud. Mist is what is left over when a cloud condenses into water, and is therefore a rather a sign of fine weather than of rain: for mist can be called a barren cloud.

Aristotle, *Meteorologica*, Book I Section 9.

Aristotle concluded from observations and philosophy that water evaporates into vapour, which in turn can condensate into water again to form a cloud. As scientists would find out more than two thousand years later, these conclusions were not far from the truth.

Clouds appear in many forms and many sizes, and can be categorized by many different criteria. The name *cumulus* first appears in the beginning of the 19th century, and is Latin for 'heap' or 'stack'. This is due to its appearance as a piled heap of small clouds with round edges. The name is part of the cloud-classification by the Englishman Luke Howard (1772-1864) which is still used today. His work must be seen in the context of the ongoing scientific description and cataloguing of the natural world in that period. The description of clouds in particular has been an inspiration for the school of 19th century Romantic landscape painters, such as Joseph W. M. Turner, Caspar David Friedrich and John Constable (see the front cover). Cumulus clouds continuously change shape, inspiring the human imagination to recognize familiar forms. For example, Shakespeare probably had cumulus clouds in mind when he wrote this dialogue between the Prince of Denmark and Lord Polonius:

HAMLET: Do you see yonder cloud that's almost
in shape of a camel?
LORD POLONIUS: By the mass, and 'tis like a camel, indeed.
HAMLET: Methinks it is like a weasel.
LORD POLONIUS: It is backed like a weasel.
HAMLET: Or like a whale?
LORD POLONIUS: Very like a whale.
HAMLET: ... They fool me to the top of my bent.

Shakespeare, *Hamlet*, Act 3, Scene 2

Apart from illustrating that Hamlet had a lively imagination, this quotation addresses an important scientific problem in the last sentence. Although mankind soon learned ways to predict meteorological phenomena from experience based on the appearance of clouds, a realistic physical explanation for the behaviour and existence of clouds was pending until the dawn of modern science.

The 17th century with its new philosophy of scientific method as formulated by Descartes heralded the start of scientific meteorology. For the first time reliable instrumentation was developed, such as the barometer to measure atmospheric pressure as invented by Torricelli in 1643. Boyle, Pascal and Gay-Lussac formulated laws relating the temperature, pressure and volume of air, the so-called equations of state. A big leap forward was made when Newton formulated his three Laws of Motion and invented calculus. Euler applied Newton's partial differential equations to formulate equations describing fluid dynamics. In the 19th century the First Law of Thermodynamics was formulated, which enabled a basic understanding of why clouds form in the first place. When Coriolis discovered the apparent force due to the rotation of the earth, the formulation of models for the global atmospheric circulation was finally possible.

At the beginning of the 20th century weather forecasting was still of empirical nature, primarily based on maps of the atmospheric pressure at the surface. In that period, the worldwide network of meteorological observations rapidly grew more dense, using surface meteorological stations, radiosondes and buoys at sea. The availability of this data enabled the tracing of



Figure 1.1 A drawing of clouds by L. Howard.

large weather systems in space and time, and supported theoretical research. Bjerknes (1904) was among the first to recognize that three-dimensional data can be used as an initial state from which to integrate forwards in time the differential equations which govern the atmospheric flow. This basically results in a forecast of the weather. Due to the highly non-linear nature of these equations, numerical weather prediction was not practically possible until the introduction of electronic computers (Richardson, 1922; Charney et al., 1950).

The introduction of aviation led to even more sophisticated atmospheric observations at high altitudes, and enabled direct measurements inside clouds for the first time in history. It soon became apparent that clouds play an important but complex role in the earth's weather and climate, and ever since clouds have been the subject of intensive research, starting with the work of Stommel (1947). In the second half of the 20th century technological advances such as radar and satellites gave cloud meteorology new momentum. With the appearance of supercomputers in the last decades it has even become possible to numerically simulate individual clouds, which greatly extended the research possibilities.

1.2 The atmospheric boundary layer

This thesis is concerned with clouds in the lowest few kilometers of the atmosphere surrounding the earth, see Fig.1.2. This is the sphere also known as the *atmospheric* or *planetary boundary layer* (PBL), defined as the part of the atmosphere which is directly influenced by the proximity of the surface of the earth. Usually the PBL is capped by a stable layer in which the temperature strongly increases with height, called the *inversion*. Above the inversion lies the *free troposphere*, which is the domain of the strong jet-stream winds associated with the baroclinic waves which form the low- and high-pressure systems. In turn the troposphere is capped by another inversion called the tropopause, which forms the boundary between the *stratosphere* and the troposphere.

Basically the boundary layer is formed and maintained by vertical motions of air. The radiation from the sun warms the earth's surface, which subsequently warms the adjacent

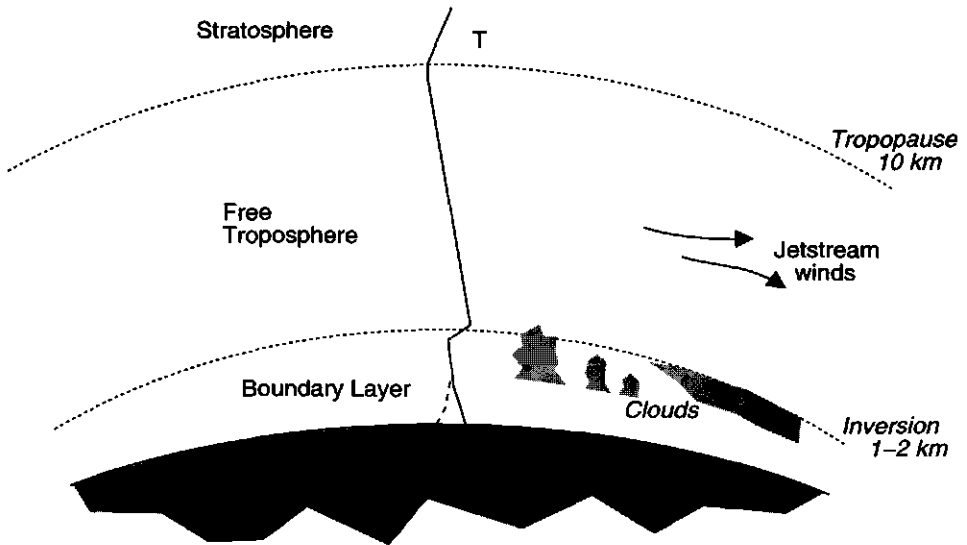


Figure 1.2 Schematic illustration of the different layers of the earth's atmosphere. The typical daytime-temperature profile (T) is plotted as a solid black line, while the dashed line shows that of the stable boundary layer at night.

atmosphere. At some places the air heats faster than at other places, partially caused by the heterogeneous thermal properties of the material forming the surface. For example, a rock lying in the sun heats faster than water does. The relatively warm air is lighter than its surroundings, and subsequently starts to rise. The vertical motions bring air from close to the ground to higher levels and vice versa, and hence determine the vertical extent of the impact of the earth's surface on the atmosphere.

The deepest convective boundary layers on earth occur in the sub-tropical desert-regions, due to the combination of intense surface heating, extremely dry air and relatively high atmospheric pressure. Their depths are known to exceed 4 kilometers. In contrast, during night-time over land the boundary layer can become very shallow, due to the radiative cooling of the earth's surface. This process cools the air closest to the surface which stabilizes the boundary layer, as cold and heavy air is then situated below warm and light air (see the dashed line in Fig.1.2). This stability suppresses upward vertical motions, and hence the impact of the earth on the atmosphere. This is the reason why commonly in relatively fair and stable weather the winds subside at the end of the day, as the air with high horizontal wind speeds at high altitudes is no longer mixed downwards towards the earth's surface.

Cumulus clouds in the boundary layer are formed by the following process. Water stored at the earth's surface evaporates into the adjacent air as a vapour. What appears to be cloud-free air often contains sub microscopic drops, but as evaporation exceeds condensation, the drops do not survive long after an initial chance clumping of molecules. As air is cooled, the evaporation rate decreases more rapidly than does the condensation rate with the result that at a certain temperature (the *dew-point*) the evaporation is less than the condensation, and a droplet can grow into a cloud drop. The release of heat associated with this phase-

change of water in clouds influences the atmospheric motions and significantly affects the characteristics of the boundary layer.

1.3 Classification of cumulus

The classification of cloud-morphology as presented in the "Essay on modifications of clouds" by Howard (1802) generally distinguishes four categories:

<i>Cumulus</i>	Piled clouds with a flat base and tops in the shape of a cauliflower
<i>Stratus</i>	Layered clouds much wider than they are thick
<i>Nimbus</i>	Precipitating cloud systems
<i>Cirrus</i>	Thin fibre-like clouds, sometimes curly

This is a general classification of cloud-types, in reality many clouds occur which show the characteristics of more than one category. This thesis is limited to cloudy processes in the planetary boundary layer, and accordingly all clouds which occur at higher altitudes are left out of consideration. Further narrowing the subject of research to *cumuliform* clouds then results in the following sub-categories of interest.

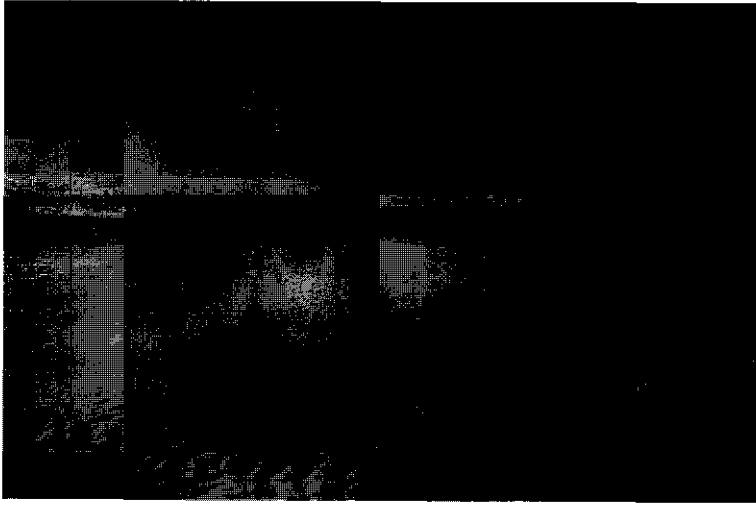
Stratocumulus.

These are layered clouds at low altitudes, typically at heights of about 1 km. They are much wider than they are deep, forming large cloudy decks often covering the sky completely, except for some occasional small openings. Despite their passive appearance the air inside these clouds is actually *turbulent*, which stands for the presence of seemingly chaotic, undirected motions occurring at many scales with varying intensities. Turbulence typically occurs in any cumuliform cloud: the cauliflower appearance is actually the result of these turbulent motions of air. When flying above a stratocumulus cloud deck their turbulent character shows in the form of a cumuliform, sometimes 'wave-like' cloud top. Stratocumulus occurs persistently in certain regions over the oceans in sub-tropical areas, immediately west of the large continents of North-America, South-America and Africa. This is due to the relatively low sea-surface temperatures in these regions, caused by cold ocean-currents

Shallow cumulus.

These are the clouds most people associate with the name 'cumulus'. They occur as a population of separated small clouds, all with a flat, relatively dark base located at the same height (at 500m–1.5km) combined with white, cauliflower shaped tops. The largest clouds may reach depths of up to 2km. The aspect ratio of a single cumulus cloud (defined as the ratio of the width to its depth) may vary, but typically the distance to the neighboring clouds is much larger than the width of the cloud. The clouds generally cover about 10 to 30% of the sky (measured as the ratio of the vertically projected area covered by clouds to the total area). The relatively large section of cloudless blue sky explains the other frequently used name of *fair-weather* cumulus. Typically the turbulence in shallow cumulus fields is more intense compared to stratocumulus, with larger vertical velocities. The more organized vertical motions in a turbulent field are referred to as *convection*. The name *shallow* is

a)



b)



Figure 1.3 a) Stratocumulus clouds over the Atlantic Ocean. b) Shallow cumulus clouds observed from the Ballon des Vosges, France.



Figure 1.3 continued: c) Deep cumulus over the Kiparissian Gulf in Greece. The dark-grey area below the clouds in the center indicates the presence of precipitation.

inspired by the relatively small depth of the clouds, and is sometimes used as a synonym for 'non-precipitating'. The diameter of the water droplets inside shallow cumulus clouds varies, from smaller than $1\mu\text{m}$ up to $40\mu\text{m}$ (Squires, 1958c; Warner, 1969a). The cloud droplets can occur in both liquid and ice phase, the former situation also being referred to as 'warm' cumulus.

Deep cumulus

Cumulus clouds which are deep enough to form precipitation. This category therefore covers a wide range of cloud formations, from single cumuli with a relatively large depth up to tropical monsoon cloud-towers with depths of sometimes 10km, reaching up to the tropopause. Large vertical velocities occur inside these clouds indicating intense turbulence, which is the reason why air-traffic tends to avoid these clouds. The cloud droplets are mostly in ice phase. The formation, fall-out and evaporation of precipitation related to deep cumulus play an important role in creating the strong vertical motions of air, which makes their dynamics different from shallow cumulus. The complex dynamics of deep cumulus sometimes causes the ice particles to grow to excessive dimensions, forming hail. The electrical charge of the ice-particles plays an important role in the formation of lightning.

1.4 Climatology

The International Satellite Cloud Climatology Project (ISCCP) was established in 1982 as part of the World Climate Research Program (WCRP) to collect weather satellite measurements and to analyze them to study the global distribution of clouds, their properties, and their diurnal, seasonal and inter-annual variations (Rossow et al., 1991). The resulting data-sets and analysis products are being used for research on the role of clouds in the earth's climate, focusing on both their effects on radiative energy exchanges and their role in the global water cycle.

Figure 1.4a shows from the ISCCP archive the global cloud amount of low (boundary layer) clouds in June, averaged over 17 years. Low clouds persistently occur over the oceans in the so-called Trade-wind regions, situated between about 40°S and 40°N. These winds blow all year round towards the equator, from the north-east in the northern hemisphere and from the south-east in the southern hemisphere. The two flows meet at the *Intertropical convergence zone (ITCZ)*, which is clearly visible on satellite images as a chain of deep cumulus systems oriented east-west, see Fig.1.5. This line of convergence forms the upwelling branch of a large tropical atmospheric circulation called the *Hadley cycle*, named after the famous British meteorologist George Hadley (1685-1768). Already in 1686 a partial explanation for the Trade-winds was given by Edmund Halley, pointing out that heated equatorial air will rise and thus cause colder air to move in from the subtropics. He could not explain though why the winds blow from the northeast in the northern hemisphere and from the southeast in the southern hemisphere. Hadley (1735) offered the explanation, arguing that the airflow towards the equator is deflected by the Earth's rotation.

A schematic vertical cross-section through this cycle is shown in Fig.1.6. The Trade-winds start in the regions in which persistently stratocumulus occurs with a frequency sometimes up to 90%, see Fig.1.4. At some point a transition takes place from stratocumulus to shallow cumulus, which then dominates the flow all the way to the ITCZ, see Fig.1.4b. At the ITCZ strong ascent occurs accompanied by deep convective clouds. At high altitudes near the tropopause the air flows away from the equator, and finally descends again at higher latitudes in the sub-tropics.

The role and impact of shallow cumulus cloud fields in this cycle is complex but significant. They distribute heat and moisture from close to the surface over the depth of the boundary layer and in that way supply the fuel for the deep convection at the ITCZ, of which the strong vertical motions are considered to be the engine of the whole Hadley circulation. Model studies have shown that the presence of cumulus convection seriously affects the distribution of precipitation and variability in the tropics (e.g. Slingo et al., 1994; Gregory, 1997). The vertical transport of moisture tends to dry the boundary layer, limiting the formation of extensive regions of stratiform clouds. The cumulus clouds also transport air of slow momentum close to the surface upwards into regions where the wind speeds are generally much larger, in that way acting as a drag on the large scale winds. Meteorological and oceanographic experimental field campaigns have been organized in the past in order to increase our understanding of the exact role of low boundary layer clouds in the Trade-wind regions. Nevertheless, due to the great effort and costs involved in organizing such field-experiments, relatively few have yet been realized. Because of this, much is still unknown about the nature of Trade-wind cumulus and its interaction with the planetary boundary layer.

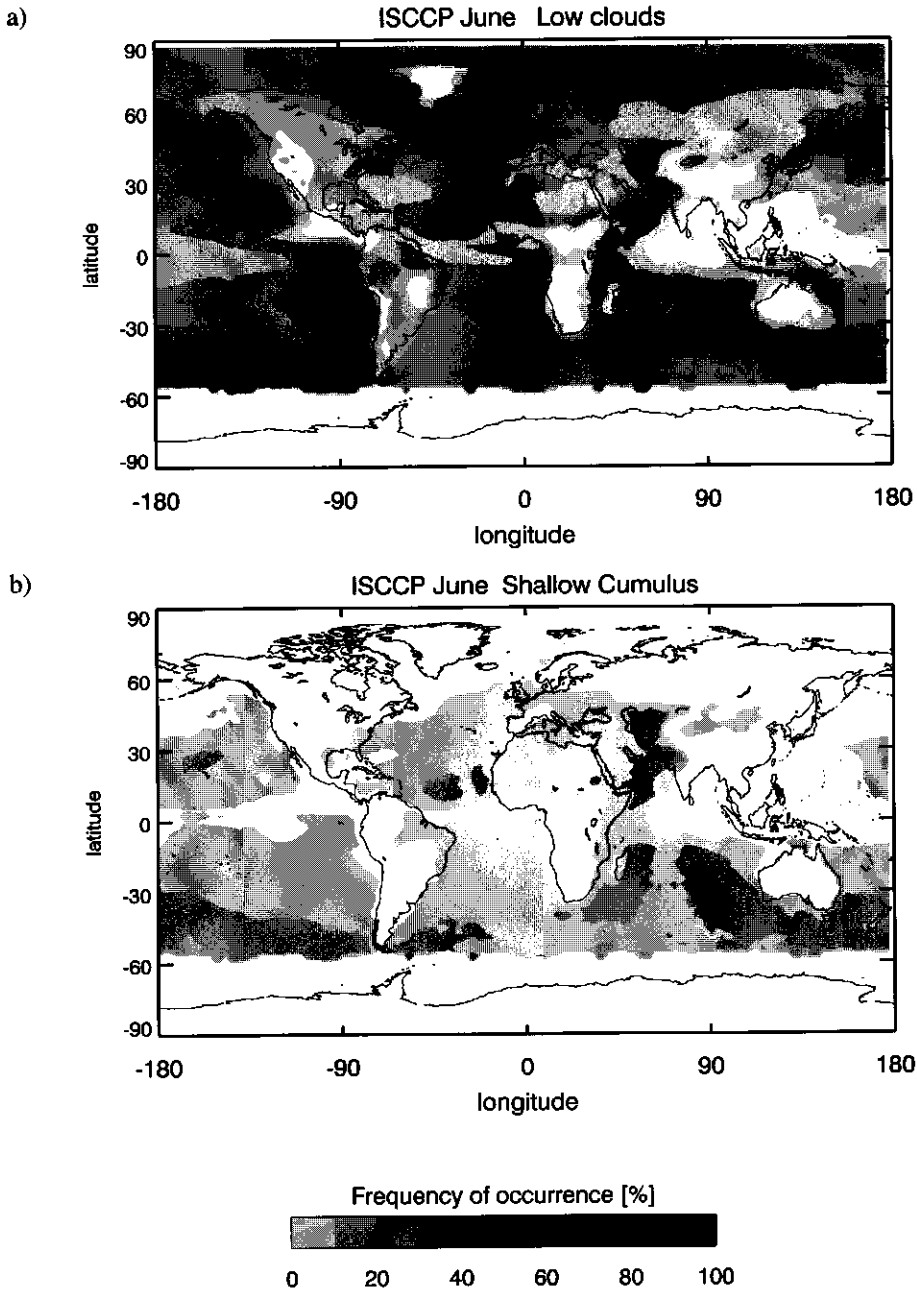


Figure 1.4 The observed cloud amount (frequency of occurrence) of low clouds, averaged over all June months from 1984 to 1999. The data is obtained from the ISCCP D2 archive. The cloud amount is calculated on grid cell areas of 280^2 km^2 . Low clouds are defined as those clouds with a cloud-top pressure larger than or equal to 680mb. Panel a) shows the cloud amount of all low clouds. Panel b) shows the cloud amount of shallow cumulus.



Figure 1.5 GOES 10 infra-red satellite image of the intra tropical convergence zone (ITCZ) above the Pacific Ocean on October 12 1998, 14:00 MESZ. In the top left lies the Hawaiian island chain. In the far right the coast-lines of the North and South American continents can be seen. The color intensity in an IR image is proportional to the cloud top height. The oceans are black. The dark-grey homogeneous area north of the ITCZ and west of North America marks low stratocumulus clouds which persistently occur in this area, with a cloud cover of almost 100%. Further to the west in the Hawaiian area the low cloud field is broken. This is the region where Trade-wind shallow cumulus most frequently occurs.

Apart from the important Trade-wind regions, other situations exist in which shallow cumulus occurs. Cumulus-topped boundary layers over land typically follow a 24-hour or *diurnal* cycle, induced by the strong variation in the surface fluxes of heat and moisture due to the solar cycle between dawn and dusk. The day starts with a cloudless sky, but one or two hours after sunrise the first small cumuli appear, which subsequently deepen in time. Just before sunset the clouds occur less frequently and finally disappear. There are several reasons why shallow cumulus convection over land is important. Firstly, as many gases and pollutants found in the higher atmosphere are produced on the continents, the convective boundary layers over land play an important role in vertically dispersing these gases. For a better understanding of the changing global climate in which exhaust gases play an important role, knowledge about these mixing processes is essential. Secondly, deep convection frequently occurs over land in equatorial regions as explained earlier. It is strongly suspected that the initiation or *triggering* of deep convective systems in these regions depends on the state of the developing planetary boundary layer. These deep convective events are associated with intense precipitation and significantly affect the large scale circulation. The exact role of shallow cumulus convection in triggering deep convection is an outstanding issue of research.

Clouds in general play an important role in the global radiative energy budget. Clouds reflect, absorb and emit radiation at a range of wave-lengths from ultra-violet (solar) to infra-red (thermal), depending on their nature. Irregular and broken clouds like cumulus have their own characteristic radiative properties (e.g. Marchuk et al., 1980; Ackerman et al., 1981; Marshak et al., 1995, 1997). The radiative properties of clouds have proven to be the cause for large uncertainties in climate predictions (Fouquart et al., 1990; Ramanathan et al., 1995). High thin cirrus clouds tend to have a warming effect: incoming shortwave solar radiation passes through these clouds but upgoing longwave radiation emitted by the earth and by lower clouds is absorbed. As a consequence thin cirrus traps solar radiative energy in the

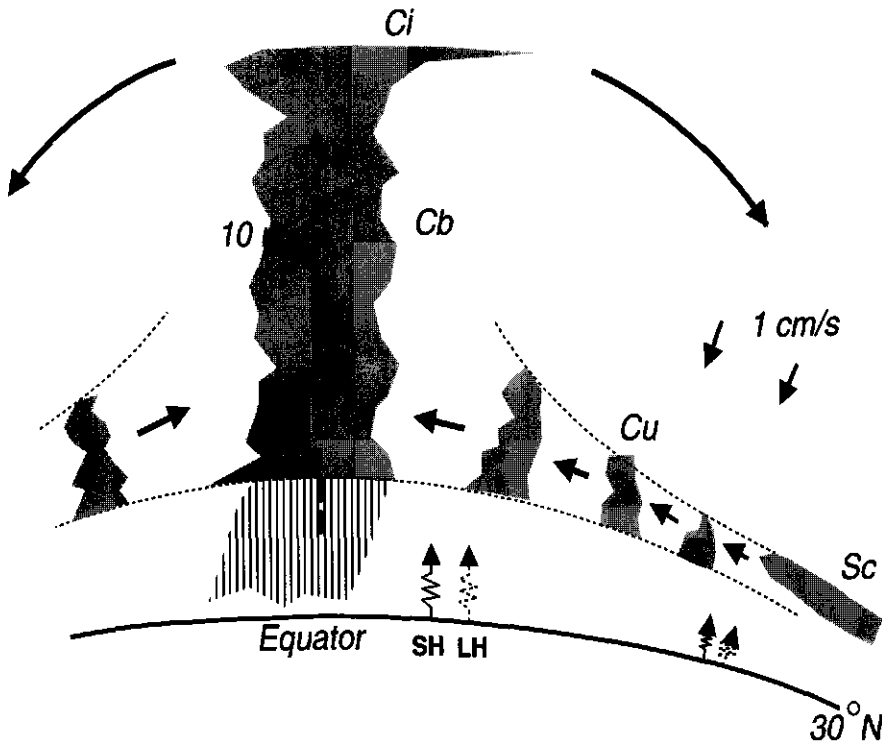


Figure 1.6 Schematic meridional cross-section of the tropical Hadley circulation. The thick arrows show the prevailing winds. *SH* and *LH* stand for the heating of the atmosphere and the evaporation of water at the earth's surface respectively. *Sc* indicates stratocumulus, *Cu* shallow cumulus, *Cb* deep cumulonimbus, and *Ci* cirrus-anvil clouds.

atmosphere. In contrast, low clouds have a net cooling effect: due to their relatively high reflectivity compared the surface of the earth, more solar radiation is reflected in their presence. The relative importance of low clouds in the global climate can be shown by budget calculations with a convection-radiation model for a vertical atmospheric column containing low clouds (e.g. Manabe and Wetherald, 1967). Although it is important to realize that eventual tendencies depend on the exact climatological situation as well as various feedback mechanisms, these studies do indicate that a 1% increase in low cloud cover can potentially result in enough extra cooling to compensate for a 25% increase of the CO_2 greenhouse gas (see e.g. Van Dorland, 1999).

1.5 Atmospheric modeling

The increasing knowledge about shallow cumulus has led to a general awareness of its important role in weather forecasting. This insight has only increased since the birth of atmo-

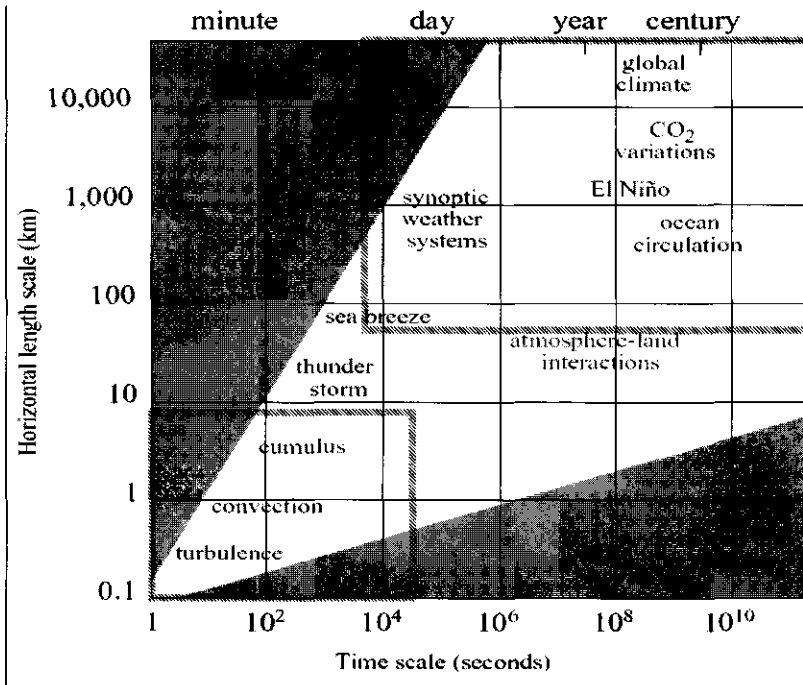


Figure 1.7 Classification of atmospheric processes based on their typical time- and length-scales. The black box in the top-right covers the range of atmospheric scales resolved by a general circulation model (GCM). The other box covers the scales resolved by large-eddy simulation (LES). From Holtslag (2002), based on Orlandi (1975).

spheric modeling and its subsequent development in the the twentieth century. Basically, an atmospheric model is a collection of governing physical conservation laws for atmospheric momentum, heat, moisture and atmospheric pressure/density in a certain three-dimensional domain. The dimensions of the modelled domain can be chosen, from very small up to very large covering the whole globe. The latter, called *general circulation models* (GCMs), have to account for all relevant atmospheric processes in the domain, ranging from small (micro) to large (macro) spatial and temporal scales.

Nowadays atmospheric models are widely used in weather forecasting and climate studies. *Numerical weather prediction* (NWP) stands for the forward integration in time of the discretized governing equations from an initialization state based on observations (e.g. see Haltiner and Williams, 1980). These numerical GCMs resolve the atmospheric processes on *synoptic* time and length scales and larger, such as jet-streams, low and high pressure systems, fronts, and planetary waves. The pioneering project in numerical weather prediction was performed by Richardson (1922) during World War I. It was a heroic attempt to manually calculate the numerical integrations. However, some flaws concerning the geostrophic balance (the balance between the pressure gradient and Coriolis forces) in his model led to huge differences between the prediction and observations. Also, it soon became clear that an enormous computing time was required for a prediction of only a few days ahead. Accord-

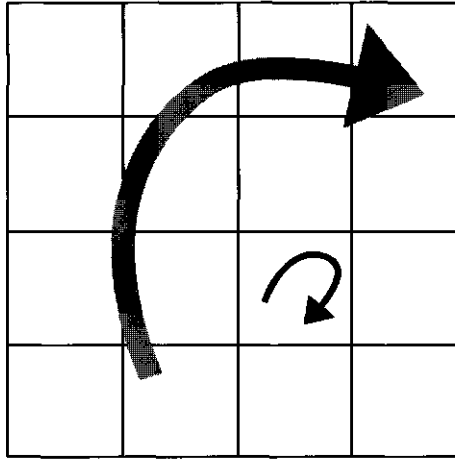


Figure 1.8 Schematic visualization of resolved motions (grey arrow) and unresolved, subgrid-scale motions (black arrow) compared to the grid of the numerical model on which the governing equations are discretized.

ingly, the conditions for the effective operational application of NWP only became favourable after the dramatic increase in calculation speed and memory capacity of computers. The first successful numerical forecasts were performed by Charney et al. (1950) at Princeton University just after World War II, using the barotropic vorticity model developed by Rossby (1938, 1939, 1940).

Present-day numerical GCMs have progressed considerably since these early days. NWP models now produce more or less realistic forecasts for the global weather for one or two weeks ahead. GCMs can also be used to model the global atmosphere on much longer timescales, and in that case are called *climate models*. Nevertheless the use of GCMs is still hampered by some significant problems. One major difficulty is the influence of small scale processes on the general circulation. Figure 1.7 shows a classification of atmospheric processes based on their typical time- and length-scale. Processes on all scales smaller than the mesh on which the governing equations are solved can not be generated by the model itself: they remain *unresolved*, see Fig.1.8. These are also known as *subgrid* processes. The typical grid-size of present-day GCMs ranges from 30 to 100km, which obviously means that cumulus clouds are unresolved. To account for the impact of such relevant small scale processes on the large scale variables in the model the technique of *parameterization* is developed: the contribution of the subgrid scales in the governing equations is formulated in terms of the resolved, grid-box average model variables. In case of shallow cumulus this means that whole populations of clouds have to be parameterized. Especially on climatological timescales, small errors in such parameterizations can accumulate to significant deviations of the resolved state from reality.

The necessity for the parameterization of subgrid processes and the lack of observational data on these small scales has inspired the formulation of models for smaller atmospheric domains. The three-dimensional fields resulting from these models can be used as a virtual laboratory for meteorological research. A range of models have been formulated in the past.

Regional models are used in weather prediction for limited areas of the globe, including detailed orography and surface-atmosphere interactions. *Meso-scale* models cover a domain of several hundreds of kilometers, covering atmospheric phenomena such as thunderstorms and sea-breezes. *Large-eddy simulation* (LES) stands for the numerical simulation of the planetary boundary layer (Lilly, 1967; Deardorff, 1970b; Sommeria, 1976). The domain of LES has dimensions of about $10 \times 10 \times 5 \text{ km}^3$, and the grid-spacing is much smaller than the dominating length-scales associated with organized cumulus convection. As a result the model partially reproduces the *micro-scale* turbulence in the planetary boundary layer, including whole populations of shallow cumulus clouds (see Fig.1.7).

1.6 Shallow cumulus research

The need for parameterizations of shallow cumulus for use in general circulation models has been an important motivation for scientific research on this meteorological phenomenon and its role in the general atmospheric circulation. Certain aspects of these boundary layer clouds make their parameterization a challenging problem. For example, boundary layer convection covers a whole range of atmospheric scales. Shallow cumulus cloud populations consist of many clouds of different sizes. In turn, the cumuli themselves are irregular and broken in structure. When focusing on such a single cloud, it may seem to the eye that its contents are

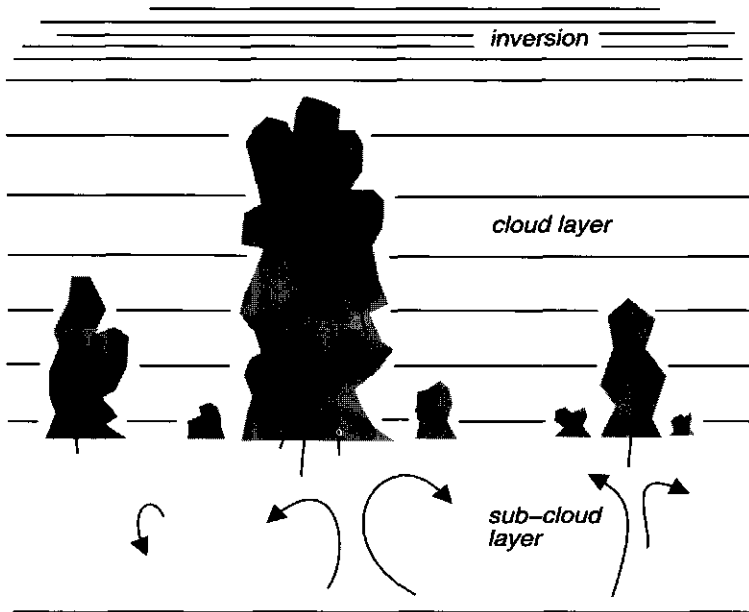


Figure 1.9 A shallow cumulus cloud population, consisting of many inhomogeneous, turbulent clouds of different sizes. The vertical spacing between the solid horizontal lines is inversely proportional to the stability of the air surrounding the clouds.

homogeneous, the cloud being a large assembly of very small liquid water droplets. However, in-cloud observations by aircraft have clearly shown that the air inside the clouds is in fact very turbulent, characterized by strong fluctuations in temperature, moisture and velocity, see Fig.1.9. To summarize, the representation of shallow cumulus in NWP requires a detailed knowledge on the complete spectrum of turbulent scales, from single eddies and clouds to the size statistics of the whole population of clouds. Together these characteristics determine the behaviour of the average properties of a shallow cumulus cloud field.

Serious observational research of shallow cumulus convection started after World War II. Several intensive experiments were organized in the oceanic Trade-wind regions to examine the local large-scale atmospheric conditions. Examples are the Barbados Oceanographic and Meteorological Experiment (BOMEX) (Holland and Rasmusson, 1973; Nitta and Esbensen, 1974) and the Atlantic Trade-wind Experiment (ATEX) (Augstein et al., 1973, 1974). These campaigns were set up around a fleet of ships, each carrying a variety of meteorological instruments. Radiosondes and wind-profilers measured the vertical profiles of temperature, moisture, pressure, wind-speed and wind-direction in the atmosphere. Other meteorological measurements were made at the surface, such as the input of heat and moisture from the earth into the atmosphere. These experiments have revealed much of the general structure of the atmospheric boundary layers in which shallow cumulus occurs.

The data-sets on the large-scale conditions have been gradually supplemented with detailed observations of the small-scale processes associated with single clouds. Laboratory experiments have been performed in which the mixing of buoyant, rising plumes in neutrally or slightly stable fluids was studied (Turner, 1962, 1973; Simpson, 1965). Aircraft have been used extensively since the 1950s to take measurements of thermodynamics and turbulence inside cumulus clouds (e.g. Squires, 1958a,b,c; Warner, 1955, 1969a,b, 1970a, 1977). Radar technology has provided remotely sensed data on the micro-physical structure of clouds, such as the size and distribution of cloud droplets (e.g. Lehrmitte, 1987; Knight and Miller, 1998; Kollias et al., 2001). Furthermore, the typical resolution of satellite imagery has become large enough to reveal the population statistics of whole cloud fields (e.g. Cahalan and Joseph, 1989; Wielicki and Welch, 1986). Finally, LES has contributed considerably to the knowledge on the physics and dynamics of boundary layer clouds. The spatial and temporal resolutions of LES are such that it simulates whole populations of cumulus clouds which are realistic enough for scientific study. The instantaneous three-dimensional fields as produced by LES are yet to be provided by experimental studies of natural cloud fields.

Research of boundary layer clouds has concentrated on their role in the vertical transport of air from near the surface to higher levels. Key questions in this problem are the nature of the mixing between cumulus clouds and their environment (Blyth, 1993; Siebesma, 1998), and the interaction between the clouds and the planetary boundary layer (e.g. Kuo, 1965; Ogura and Cho, 1974; Betts, 1976). A second important aspect of cumulus cloud fields which has received much attention is their impact on the transfer of incoming solar radiation (Fouquart et al., 1990; Ramanathan et al., 1995). This is part of the ongoing research on the impact of convective clouds on the large-scale circulation and climatology (e.g. Arakawa and Schubert, 1974; Tiedtke et al., 1988; Nordeng, 1994; Slingo et al., 1994; Gregory, 1997). Recent projects such as the Atmospheric Model Intercomparison Project (AMIP I, see Gates et al., 1999) assessed the current state of cloud representations in general circulation modeling.

1.7 Thesis objectives and outline

The general objective of this thesis is to obtain more insight in the physics and dynamics of shallow cumulus convection. The emphasis lies on evaluating the turbulent variability which characterizes shallow cumulus dynamics, in order to develop new hypotheses and parameterizations which capture the vertical transport done by the cloud population. The second main subject of this thesis is the interaction between the cloud and subcloud layer, as this process plays an important role in establishing and maintaining shallow cumulus cloud layers.

The outline of this thesis is as follows. Chapter 2 gives a comprehensive description of the background of shallow cumulus research. The basic physics and dynamics of the atmospheric boundary layer are briefly discussed. The data-sets on shallow cumulus used in this thesis are described, as well as some well-known methods of dealing with this data in developing parameterizations. Finally, the main subjects of this thesis are introduced in more detail, which are then presented in full in the next four chapters. Each one of these chapters represents a scientific paper, whether already published or still in review. Accordingly, the chapters are set-up as stand-alone entities which can be read separately. This explains some possible overlap between Chapter 2 and these chapters. Nevertheless they are arranged in a logical order, such that each chapter builds on the results and conclusions presented in the previous chapters. This provides a central line of thought running through this thesis, which eventually leads to some general conclusions and perspectives.

In Chapter 3 the performance of LES in simulating realistic shallow cumulus clouds is critically evaluated against detailed measurements of natural clouds. LES results are used extensively throughout this thesis, which demands confidence in their representativeness. Chapter 4 deals with the size statistics of cumulus cloud populations as produced by LES. The geometrical variability of these populations is assessed by calculating cloud size distributions. The variability in the thermodynamic variables and momentum is examined in Chapter 5 by using conserved variable diagrams. The interpretation of these diagrams has inspired the formulation of a conceptual model for an ensemble of rising updraft-parcels which reproduces this typical variability. In Chapter 6 several methods to describe the cloud-subcloud layer interaction are examined, each based on totally different principles. Their performance is evaluated for diurnal cycles of shallow cumulus over land. Finally, general conclusions and outlook are given in Chapter 7.

Chapter 2

Background

2.1 Physics and dynamics

In this section the basic physics of planetary boundary layers and shallow cumulus convection are presented. The aim is to introduce the reader to the various definitions and methods often used in boundary layer meteorology.

2.1.1 Atmospheric thermodynamics

In order to derive the governing equations for atmospheric flow it is necessary to introduce some basic principles of atmospheric thermodynamics first. The emphasis lies on the definition of variables often used in boundary layer meteorology. For a more complete and elaborate description of atmospheric thermodynamics see for example Iribarne and Godson (1973) or Emanuel (1994).

The equation of state

The thermodynamic state of the atmosphere is usually described by three physical variables: the pressure (p), the temperature (T) and the density (ρ). The equation of state for dry air relates the three variables,

$$p = \rho R_d T, \quad (2.1)$$

where R_d is the specific gas constant for dry air. Alternatively, the specific volume $v = \rho^{-1}$ may be used. This equation is also known as the ideal gas law. Two of these variables are independent, the third one is a state function of the other two.

Adiabatic motions

Combining the first and second principle of thermodynamics gives

$$\delta q = c_p dT - v dp, \quad (2.2)$$

where δq is the heat per unit mass added to the system and c_p is the specific heat capacity of dry air at constant pressure. In meteorology motions of dry air are often assumed to be *adiabatic* processes, in which no heat is added to or extracted from the system. This means $\delta q = 0$. Dividing by T , substituting the gas law for v , and integrating then gives

$$T p^{-\frac{R_d}{c_p}} = \text{const.}, \tag{2.3}$$

This is one form of Poisson's equations, defining an adiabatic curve in a (p, T) diagram. This equation could also be formulated in terms of the other state variables. Comparing two points (p, T) and (p_0, T_0) on this curve then gives the definition of the *potential temperature* θ ,

$$\theta \equiv \frac{T}{\Pi}, \tag{2.4}$$

where Π is the Exner-function

$$\Pi = \left(\frac{p}{p_0} \right)^{\frac{R_d}{c_p}}. \tag{2.5}$$

θ is equivalent to the temperature T_0 the gas would have were it expanded or compressed adiabatically to the reference pressure p_0 , usually set to 1000mb close to the pressure value at the earth's surface. For adiabatic motions of volumes of dry air θ is a *conserved* property (i.e. it does not change). This feature is of great use in interpreting temperature profiles of the atmosphere. It immediately shows if a volume of air has experienced any non-adiabatic process.

Moist air

A volume of atmospheric air always contains water vapour. The water in the earth's atmosphere can occur in three different phases: water vapour, liquid water and ice. In warm shallow cumulus we are mainly concerned with the vapour and liquid phase of water. The *specific humidity* q_v is defined as the ratio of the mass of water vapour m_v to the total mass m_t of a unit volume,

$$q_v \equiv \frac{m_v}{m_t}. \tag{2.6}$$

The saturation specific humidity q_s is the maximum mass of water vapour that a unit mass of air can contain, and is dependent on the thermodynamic state,

$$q_s = f(p, T). \tag{2.7}$$

see Iribarne and Godson (1973) a complete definition. The ratio of these two variables is the *relative humidity* RH ,

$$RH \equiv \frac{q_v}{q_s} \tag{2.8}$$

Condensation is accompanied by the release of latent heat, and is a non-adiabatic process.

The latent heat release in cumulus clouds is one of the most important energy-sources for cloud-dynamics.

For studying cloud processes it is important to be able to distinguish between condensation effects and other non-adiabatic processes. This has inspired the definition of variables which are conserved for moist adiabatic motions. The *total specific humidity* q_t of moist air is defined as

$$q_t = q_v + q_l, \quad (2.9)$$

where q_l is the *liquid water content*, defined as the ratio of the mass of liquid water to the total mass of the unit volume. If the air is saturated then $q_v = q_s$. Correcting the potential temperature θ for the contribution by latent heat release due to condensation of water vapour into liquid water gives the *liquid water potential temperature* θ_l (Betts, 1973), approximated by

$$\theta_l \cong \theta - \frac{L q_l}{c_p \Pi}. \quad (2.10)$$

Here L is the latent heat of the phase change between the vapour and liquid phase of water. The two conserved variables q_t and θ_l greatly facilitate the formulation of conservation laws, which will be used later to define the governing equations for moist atmospheric flow.

Stability

Density differences determine the stability of the atmosphere. The presence of moisture affects the density of a volume of air, as the specific gas constant for moist air is different from that of dry air. Correcting the ideal gas law of dry air (2.1) for the presence of moisture gives

$$p = \rho R_d T_v, \quad (2.11)$$

where T_v is the *virtual temperature*, defined as

$$T_v = T(1 + Cq_t - (1 + C)q_l). \quad (2.12)$$

T_v of moist air is equivalent to the temperature of totally dry air that has the same values of p and ρ . The constant C is defined as

$$C \equiv \frac{R_v}{R_d} - 1 \approx 0.61 \quad (2.13)$$

where $R_d = 287.0 \text{ J kg}^{-1}\text{K}^{-1}$ and $R_v = 461.5 \text{ J kg}^{-1}\text{K}^{-1}$ are the specific gas constants for dry and moist air respectively. As T_v is inversely proportional to ρ at constant pressure, it is a practical tool to immediately compare the densities of two arbitrary volumes of air at the same height. Alternatively one can use the virtual potential temperature θ_v ,

$$\theta_v = \frac{T_v}{\Pi}. \quad (2.14)$$

2.1.2 Governing equations

Now that the necessary state variables are defined, the governing equations for atmospheric flow can be formulated. This set of differential equations consists of the Navier-Stokes equations for the conservation of momentum, the conservation laws for heat, moisture and mass, and the equation of state. The prognostic variables involved are the three components of momentum $\vec{u} = (u_1, u_2, u_3) = (u, v, w)$, the liquid water potential temperature θ_l and the total specific humidity q_t . Only the equations relevant for this thesis will be given, for a complete description see Stull (1988).

First consider the Navier-Stokes equation for an incompressible Newtonian fluid. By restricting the situation to typical atmospheric boundary layer conditions, it is assumed that the density can be divided out of the terms representing storage, advection and flux of momentum. This gives

$$\frac{\partial u_i}{\partial t} + u_j \frac{\partial u_i}{\partial x_j} = X_i - \frac{1}{\rho} \frac{\partial p}{\partial x_i} + \nu \frac{\partial^2 u_i}{\partial x_j^2} \quad (2.15)$$

(Moeng, 1998). On the right hand side, X_i is the i -component of all external forcings on the system. The second term is the pressure gradient force, and the last term stands for the impact of viscous stress with ν the kinematic viscosity. Among the external forcings on the system are the gravitational force and the Coriolis force,

$$X_i = -\delta_{i3}g + \epsilon_{ij3}f_c u_j + F_i \quad (2.16)$$

where δ_{i3} is the Kronecker delta, ϵ_{ij3} is the alternating unit tensor, f_c is the Coriolis parameter and F_i stands for any remaining external forcings. Einstein's summation notation is used in the tensors.

When describing a turbulent flow, it is convenient to isolate the mean flow from turbulent perturbations. Accordingly, in numerical models any variable ϕ is split up into a grid-box average and a subgrid scale fluctuation from this average,

$$\phi = \bar{\phi} + \phi', \quad (2.17)$$

where the over-bar stands for the average over the gridbox with volume V ,

$$\bar{\phi} = \frac{1}{V} \int_V \phi \, dV. \quad (2.18)$$

Applying the Reynolds' rules of averaging to (2.15) results in the equation for the mean momentum,

$$\frac{\partial \bar{u}_i}{\partial t} + \bar{u}_j \frac{\partial \bar{u}_i}{\partial x_j} \cong X_i - \frac{1}{\bar{\rho}} \frac{\partial \bar{p}}{\partial x_i} - \frac{\partial \widetilde{u'_i u'_j}}{\partial x_j}. \quad (2.19)$$

Equation (2.19) is a general form of the Navier-Stokes equation which can be applied in any numerical model describing turbulent atmospheric boundary layer flow, such as LES as well as GCMs limited to the lowest few kilometers above the surface. The overbar denotes the gridbox-averages which are resolved by the model, the accents denote the *subgrid-scale*

(SGS) fluctuations which are not resolved. The molecular term associated with ν is omitted as it is negligible small for high-Reynolds number flow. The mean pressure gradient force is often written in terms of the geostrophic wind $\tilde{\mathbf{u}}_g$,

$$f_c \tilde{\mathbf{u}}_g = -\frac{1}{\rho} \frac{\partial \tilde{p}}{\partial y} \quad \text{and} \quad f_c \tilde{\mathbf{v}}_g = \frac{1}{\rho} \frac{\partial \tilde{p}}{\partial x} \quad (2.20)$$

The last term on the right hand side of (2.19) represents the impact of subgrid-scale fluctuations on the mean momentum, appearing in the shape of a flux divergence term. This term always acts as a sink, representing the fact that atmospheric turbulence acts to slow down the mean wind.

The hydrostatic equilibrium

Several assumptions exist for the vertical momentum equation, depending on the nature of the model. For large-scale synoptic flow as described by a GCM the mean vertical momentum budget is dominated by the vertical pressure gradient force and the gravitation force. Neglecting the other terms defines the reference state of the *hydrostatic equilibrium* (denoted by the subscript 0),

$$\frac{\partial p_0}{\partial z} = -\rho_0 g. \quad (2.21)$$

In reality many situations exist in which the hydrostatic equilibrium does not apply, caused by density fluctuations or locally large pressure gradients. Examples of non-hydrostatic situations are shallow cumulus clouds and deeper convection. However, these atmospheric processes are of subgrid scale when compared to a GCM gridbox, as the typical grid-spacing in GCMs is of the order of 50km. Therefore, the gridbox-mean variables in a GCM are often assumed to be in hydrostatic equilibrium.

In atmospheric models for a smaller domain the assumption of hydrostatic equilibrium no longer holds, as the dynamics of the non-hydrostatic motions is at least partially resolved. In those models the Boussinesq approximation is often used, stating that the density fluctuations from the reference state are neglected in all terms of (2.19) except the external buoyancy forcing. This gives for the vertical momentum component

$$\frac{\partial \tilde{w}}{\partial t} + \tilde{u}_j \frac{\partial \tilde{w}}{\partial x_j} = g \frac{\tilde{\theta}_v''}{\Theta_v^0} - \frac{1}{\rho_0} \frac{\partial \tilde{p}''}{\partial z} + F_z - \frac{\partial \tilde{u}_j' w'}{\partial x_j} \quad (2.22)$$

where the superscript '' stands for a perturbation from the reference state of hydrostatic equilibrium, and Θ_v^0 is a reference value of θ_v . Here the assumption is used that pressure perturbations are generally much smaller than temperature or density fluctuations, by which (2.11) can be used to write

$$\frac{\rho''}{\rho_0} \approx -\frac{\theta_v''}{\Theta_v^0}. \quad (2.23)$$

The class of so-called *non-hydrostatic* models includes LES, cloud resolving models (CRM) and some meso-scale models.

Remaining equations

For the conserved thermodynamic variables θ_l and q_l , the governing equations are

$$\frac{\partial \tilde{q}_l}{\partial t} + \tilde{u}_j \frac{\partial \tilde{q}_l}{\partial x_j} = F_{q_l} - \frac{\partial \widetilde{u'_j q'_l}}{\partial x_j} \quad (2.24)$$

$$\frac{\partial \tilde{\theta}_l}{\partial t} + \tilde{u}_j \frac{\partial \tilde{\theta}_l}{\partial x_j} = F_{\theta_l} - \frac{\partial \widetilde{u'_j \theta'_l}}{\partial x_j} \quad (2.25)$$

The term F_{q_l} represents all possible sources and sinks for the total moisture, excluding moist adiabatic processes like condensation and evaporation for which q_l is conserved. Examples are precipitation but also ice particle formation, as q_l is only conserved for the phase-change between liquid water and water vapour. Similarly F_{θ_l} represents heating and cooling forcings, such as results from radiative flux divergence. The set of governing equations is completed by including the mass conservation law in the Boussinesq approach,

$$\frac{\partial \tilde{u}_i}{\partial x_i} = 0, \quad (2.26)$$

and by including the equation of state for moist air, as defined by (2.11).

Subgrid-scale models

An essential characteristic of turbulent flow is that several *statistical moments* appear in (2.19) and (2.24)–(2.25). The mean is the first statistical moment of a variable, the (co)variances are the second moments, being averages of a product of two perturbations. Each prognostic equation of a certain moment contains higher order moments. To obtain a closed set of governing equations which can be solved requires formulations of the higher statistical moments in terms of the lower moments. This is the *closure problem*, and the method of ‘closing’ the SGS terms is called *parameterization*. It forms a main scientific challenge in numerical atmospheric modeling and weather prediction, as it requires knowledge of the impact of SGS motions and fluctuations on the resolved flow. The parameterization of SGS cloud-processes for GCMs is one of the main motivations for the research presented in this thesis.

The impact of subgrid scale processes on the resolved flow is represented by the flux-divergence terms in (2.19) and (2.24)–(2.25), and more indirectly by other processes such as latent heat effects and microphysics (the processes related to cloud droplet formation and evaporation). Various methods exist to parameterize $\widetilde{u'_i \phi'}$, depending on the nature of the atmospheric model. The typical grid-box in a GCM is about 30-100km wide, which means that the impact of whole shallow cumulus cloud populations has to be parameterized. In LES however, the grid-spacing is about 10-100m, and the subgrid model has to represent the impact of much smaller motions. Despite the clear difference in scale of the SGS processes in GCMs and LES, a basic approach often used in both models is to relate the turbulent flux to the local gradient of the mean variable,

$$\widetilde{u'_i \phi'} \approx -K_\phi \frac{\partial \bar{\phi}}{\partial x_i}. \quad (2.27)$$

The minus-sign implies that the flux is always directed down-gradient, meaning that the variable ϕ is mixed from high values towards low values. This acts to make the profile of $\tilde{\phi}$ well-mixed, and accordingly this parameterization represents a diffusive process. The factor of proportionality K_ϕ is the *eddy-diffusivity coefficient*, defining the efficiency of the flux in destroying the gradient. The eddy-diffusivity has the same dimensions as viscosity, and is often parameterized in terms of a mixing length-scale ℓ and a velocity difference at that scale. To this purpose the *turbulent kinetic energy* (TKE) is commonly used, which is indicated in this thesis by the symbol e ,

$$K_\phi \sim \ell \sqrt{e} \quad (2.28)$$

where e is defined as

$$e \equiv \frac{1}{2} (\sigma_u^2 + \sigma_v^2 + \sigma_w^2). \quad (2.29)$$

σ_ϕ^2 stands for the *variance* of ϕ in the grid-box volume, defined by

$$\sigma_\phi^2 \equiv \overline{\tilde{\phi}^2} \quad (2.30)$$

In a GCM parameterization ℓ and e have scales associated with the bulk of the atmospheric boundary layer. Many variations on the diffusion-scheme have been formulated for GCMs, for example those including counter-gradient transport (Holtslag and Moeng, 1991). Next to the diffusion schemes other methods exist, such as the more advective *mass flux* schemes (Ooyama, 1971; Betts, 1973; Tiedtke, 1989). These will be discussed later in this Chapter in Section 2.3.3. In LES the parameters in (2.28) are related to micro-scale turbulence (Smagorinski, 1963; Deardorff, 1980; Schmidt and Schumann, 1989; Meneveau and Katz, 2000), and will be discussed more elaborately in Section 2.2.2.

Large-scale averages

Finally a few words on the notation of the various averages in this thesis. The equations for the resolved flow discussed in this section are formulated in such a way that they are model-independent. In order to make a clear distinction between grid-box averages in LES and in a GCM, the latter are denoted by a straight over-bar $\bar{\phi}$ in the remainder of this thesis. As the volume simulated by LES is typically of the same order of magnitude as a single grid-box in a GCM, the over-bar is also used for the horizontal domain-averages in LES. Furthermore, for convenience the resolved component of the wind-vector \vec{u} in a GCM is denoted by the capitol \vec{U} .

The limited domain-sizes of the non-hydrostatic models leave the processes on larger scales unresolved. However, these phenomena can make a significant contribution to momentum, heat and moisture in the domain, for example by advection by the larger scale winds \vec{U} into the simulated volume. Accordingly, the impact of these scales has to be prescribed as a *large-scale* (LS) forcing. They will be represented by the term LS_ϕ in the governing equations for a small domain such as resolved by LES.

2.1.3 Boundary layer structure

The basic structure of a shallow cumulus topped convective boundary layer can be described by the vertical profiles of the mean potential temperature and total moisture. Figure 2.1 shows a typical example of a boundary layer in a daytime situation as is typically measured by radiosonde profiles. Immediately above the surface the temperature and moisture slightly decrease with height, in a super-adiabatic layer known as the *surface layer*. Above that layer the potential temperature and total moisture are approximately constant with height, in a layer commonly referred to as the *subcloud layer*. The next layer is the *cloud layer*, in which typically the potential temperature and total moisture have small but constant gradients with height. The cloud layer is capped by an *inversion*, characterized by very strong vertical gradients. Finally, above the inversion lies the *free troposphere*.

In order to describe the dynamics of cloudy boundary layers, it is convenient first to consider the forcings which act on the system. Firstly, the earth is warmed by the absorption of radiation from the sun. A part of this heat input is used to warm the air immediately above the surface. Another part is used for the evaporation of liquid water at ground- or sea-level. These two processes make up the sensible and latent heat fluxes at the surface (SH and LH), representing the input of heat and moisture into the atmosphere. They form a flux-boundary condition for the system. Secondly, the properties of the air in the boundary layer itself are affected by radiation. The air absorbs shortwave radiation directly causing local heating, the intensity of which depends on the presence of aerosols and water vapour. In contrast, the net emission of longwave radiation tends to cool the boundary layer air, as the temperature in

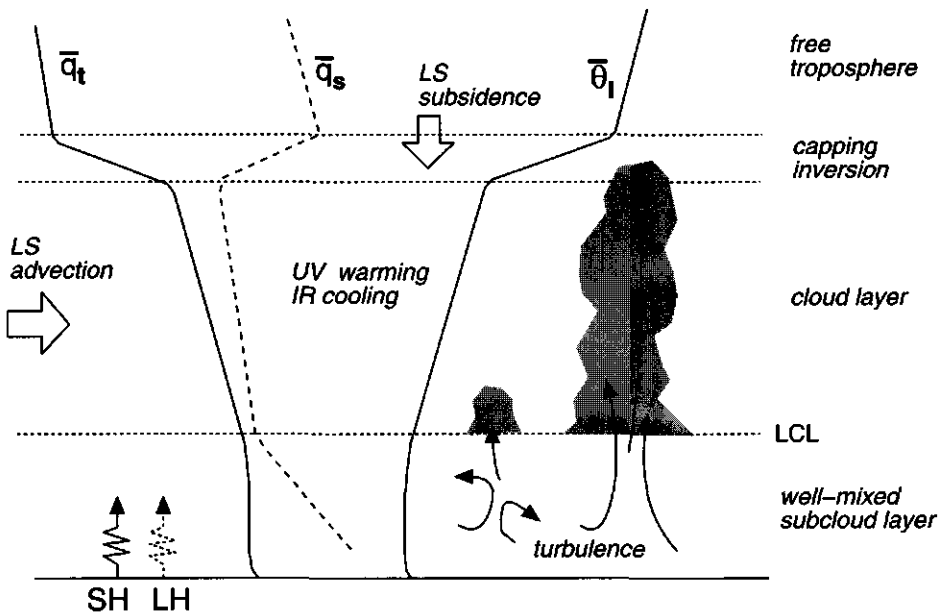


Figure 2.1 Schematic view of a shallow cumulus convective boundary layer.

the boundary layer decreases with height. These two radiative forcings are typically much smaller than the heat input by the surface fluxes, but still have to be considered for a balanced budget. Finally, advection by the large scale motions may affect the mean profiles in the boundary layer. If horizontal gradients of temperature or moisture exist, the mean winds advect air with different properties into the system. Also, large scale vertical motions of air can cause significant advective tendencies at the inversion, where the vertical gradients of temperature and moisture are large.

In short the basic dynamics of a turbulent boundary layer can be described as follows. The surface sensible and latent heat fluxes warm and moisten the air directly above the surface. This heating does not have a uniform character: the inhomogeneous thermal properties of the earth's surface cause the adjacent masses of air to warm and moisten at an unequal rate. The resulting perturbations of the thermodynamic variables cause differences in density. The resulting buoyancy force leads to vertical accelerations, and as a result turbulence develops. The density perturbations are mainly caused by the temperature differences, and accordingly the larger masses of perturbed air are referred to as *thermals*. Other names commonly used are *updrafts* or *eddies*. Rising and descending thermals act to redistribute the air in subcloud layer, transporting heat and moisture from the surface to higher levels. This makes the subcloud layer *well mixed*, as indicated by the constant profiles of the potential temperature and total specific humidity with height.

2.1.4 Conditional instability

While the potential temperature of adiabatically rising thermals is constant, their temperature decreases with height due to expansion, see (2.4). As a result the saturation specific humidity of the air also decreases with height, as shown in Fig.2.1. At some stage the thermals are cooled so much that their saturation specific humidity becomes smaller than the actual humidity content of the air, and condensation takes place. This height is the *lifting condensation level* (LCL), above which by definition the thermal becomes a cumulus cloud. The associated release of latent heat warms the thermal, and hence increases its buoyancy over the surrounding air. The local stability of the atmosphere for condensing thermals is characterized by the lapse rate of its virtual potential temperature θ_v ,

$$\Gamma = \frac{\partial \overline{\theta}_v}{\partial z} \quad (2.31)$$

It is convenient to compare Γ to the lapse-rates of parcels of air which move under specific conditions. The lapse rate of dry adiabatic motions Γ_d is zero per definition. The lapse rate of moist-adiabatic motions Γ_m is positive due to latent heat release. This defines three possible regimes of stability for the atmosphere,

$$\begin{aligned} \Gamma_m < \Gamma & \quad \text{Absolute stability} \\ \Gamma_d < \Gamma < \Gamma_m & \quad \text{Conditional instability} \\ \Gamma < \Gamma_d & \quad \text{Absolute instability} \end{aligned} \quad (2.32)$$

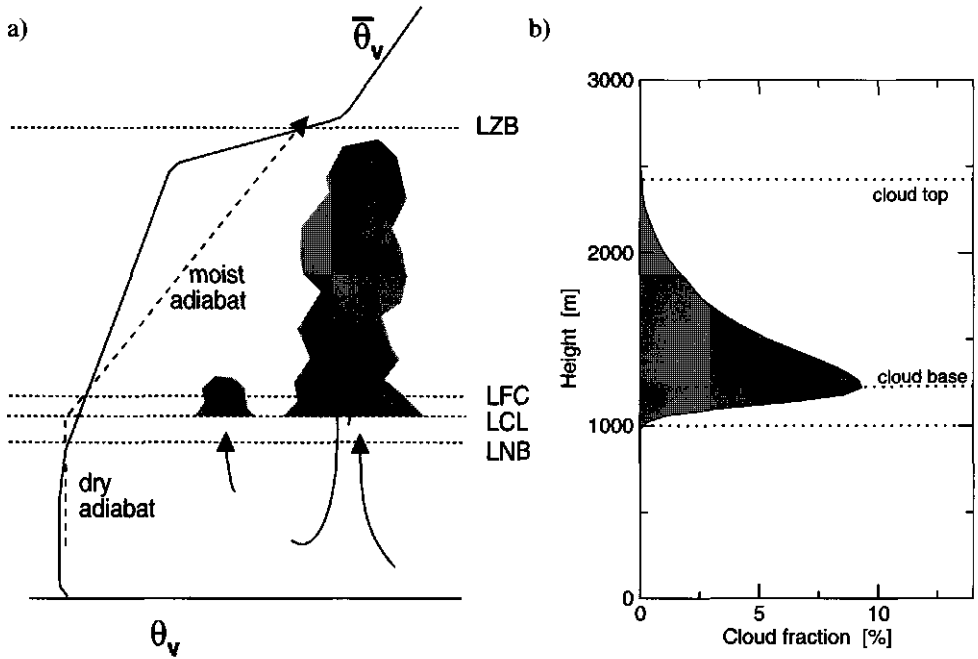


Figure 2.2 a) Schematic θ_v profile of a moist-adiabatically rising thermal in a shallow cumulus topped boundary layer (dashed line). The abbreviations are explained in the text. b) The vertical profile of the cloud fraction.

In case of absolute instability, any upward or downward movement of a parcel will make it positively buoyant. In case of absolute stability, every upward motion of the parcel will lead to negative buoyancy and its vertical motion damps out, and vice versa. In case of conditional instability, the atmosphere is stable for dry adiabatic motions but unstable for moist adiabatic motions. Observations have shown that Γ in shallow cumulus cloud layers is always conditionally unstable, as is schematically shown in Fig.2.2.

Definition (2.32) determines the *local* stability, but states nothing about the absence or presence of convection. Strong rising thermals can penetrate stable layers because of their inertia, a process also known as *overshooting*. Their presence in a stable layer is controlled by non-local properties. This is illustrated in Fig.2.2a. The thermodynamic structure of the boundary layer is such that a positively buoyant thermal which rises adiabatically in the subcloud layer first becomes negatively buoyant before it condensates at its LCL. This height is called its *level of neutral buoyancy* (LNB). When the thermal has enough inertia it reaches its LCL, after which it will follow the moist adiabat. As $\Gamma < \Gamma_m$, the thermal will become positively buoyant again at its *level of free convection* (LFC). Between LFC and its *level of zero buoyancy* (LZB) the rising thermal accelerates due to its positive buoyancy, see (2.22).

The stable layer between LNB and LFC acts as a potential barrier for rising thermals. The weak thermals are filtered out, and only the strongest will become active cumuli. This is reflected in the vertical profile of the *cloud fraction*, defined as the ratio of the horizontal

cloudy area to the total area of the domain at a certain height,

$$a^c(z) \equiv \frac{A^c(z)}{A^{tot}}. \quad (2.33)$$

This definition should not be confused with the *vertically projected* or *shaded* cloud fraction (also known as the *cloud cover*),

$$a_p^c \equiv \frac{A_p^c}{A^{tot}}. \quad (2.34)$$

where A_p^c is the vertically projected area covered by clouds. Figure 2.2b shows a typical vertical profile of the cloud fraction. The range of thermals in the subcloud layer have a different temperature and specific humidity, and as a consequence the heights of their LCL differ. This causes a sharp increase of the cloud fraction with height at the boundary between the subcloud and the cloud layer. The *cloud base* is defined as the height of the maximum cloud fraction. The weaker thermals which have become cloud at their LCL have suffered so much deceleration due to negative buoyancy between LNB and LFC that they do not rise very far into the cloud layer. Stronger, more buoyant thermals rise higher but occur less frequently. As a consequence, above cloud base the cloud fraction gradually drops with height. The mixing of air between clouds and their environment plays a complicated role in this process, as it tends to dilute the perturbations of temperature and moisture inside the cloud, which affects the buoyancy and hence the strength of the thermal.

2.1.5 Turbulent kinetic energy (TKE)

Due to the negative buoyancies near cloud base and the conditional instability in the cloud layer, the nature of the turbulence above and below cloud base is different. The intensity of turbulence is represented by the turbulent kinetic energy (TKE) defined by (2.29). Figure 2.3a shows the three components of TKE in a shallow cumulus boundary layer. Near the surface the horizontal components σ_u^2 and σ_v^2 dominate, due to the large vertical gradient in the mean wind near the surface. At those low heights a rising thermal advects air with small momentum upwards towards higher momentum and vice versa, causing large momentum perturbations and hence large values of σ_u and σ_v . If the wind-shear at cloud-base and the inversion is strong, the horizontal components of the TKE are also large at those heights. The vertical component σ_w^2 dominates in the middle of the subcloud layer, representing the relatively strong dry convective thermals. Due to the small fractional area of turbulent air in the cloud layer, the passive air dominates the slab-mean momentum variances.

In order to get more insight in the physics and dynamics of boundary layer turbulence, it is convenient to evaluate the prognostic equation for the TKE (reduced to two momentum-components for simplicity),

$$\frac{\partial e}{\partial t} = \frac{g}{\Theta_v^0} (\overline{w'\theta'_v}) - \overline{u'w'} \frac{\partial U}{\partial z} - \frac{\partial \overline{w'e}}{\partial z} - \frac{1}{\rho_0} \frac{\partial \overline{w'p'}}{\partial z} - \varepsilon. \quad (2.35)$$

The term on the left hand side represents local storage of TKE. The terms on the right hand side respectively represent the production or dissipation of TKE by buoyancy, the production

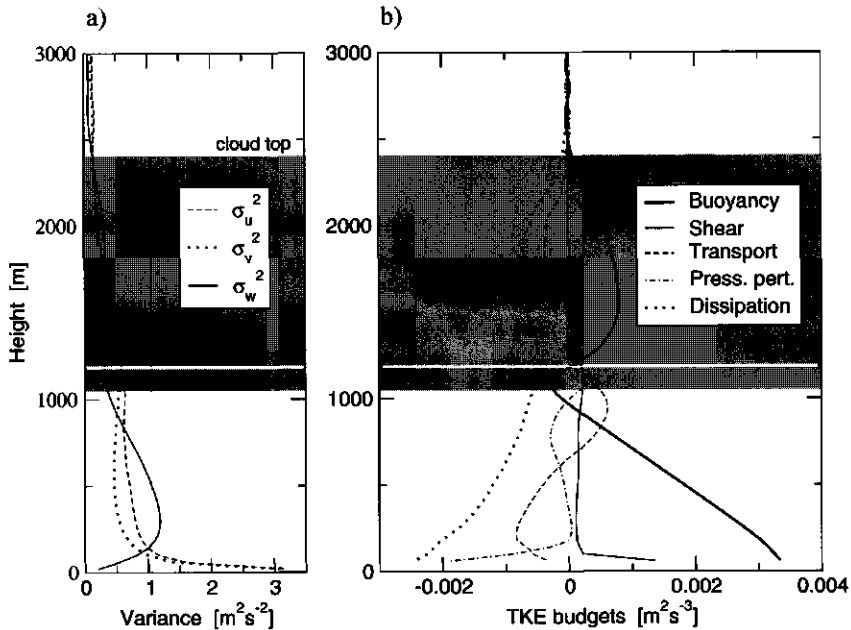


Figure 2.3 LES results on the turbulent kinetic energy (TKE) of a typical shallow cumulus topped boundary layer over land. a) The three components of the TKE in a shallow cumulus topped boundary layer. b) The various terms of the TKE equation.

of *mechanical* turbulence by mean wind shear, vertical transport (advection) of TKE by turbulent eddies, the effect of pressure correlations, and viscous dissipation. Figure 2.3 shows the vertical profiles of each separate term in a typical shallow cumulus topped boundary layer.

The buoyancy flux term is the largest producer of TKE in convective situations. It is largest near the surface, where the large sensible surface heat flux drives the dry convection in the subcloud layer. Near cloud base the buoyancy flux becomes negative, representing the overshooting of rising subcloud layer thermals into the stable layer. At this point turbulent motions are damped out by stability, by which the buoyancy flux acts as a sink term. Above cloud base the active cloudy thermals are positively buoyant again, producing TKE. The ratio of the minimum to surface buoyancy flux is approximately -0.2 , for both dry convection (e.g. Tennekes, 1973; Betts, 1976; Stull, 1976; Driedonks and Tennekes, 1984) as well as shallow cumulus convection (e.g. Siebesma et al., 2002). The other production term is the shear term, representing the generation of so-called *mechanical* turbulence which results from the difference in horizontal velocity of two adjacent layers in the atmosphere. It is always positive, due to the fact that mechanical turbulence takes its energy from the mean flow. Turbulence acts as a drag on the mean winds, slowing them down and making the presence of the earth's surface felt at higher levels.

Both the transport and pressure correlation term redistribute TKE throughout the boundary layer. The transport term advects TKE from regions where it is produced towards other

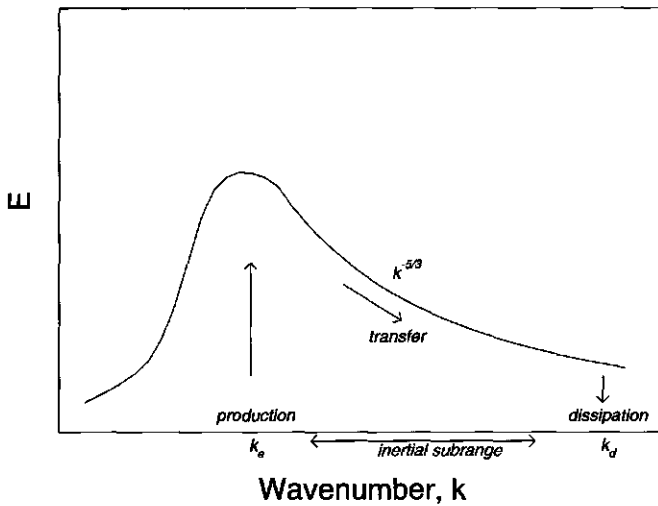


Figure 2.4 Schematic power spectrum of the turbulent kinetic energy. The turbulent energy is produced on the large convective scales k_e . The large eddies break down into smaller ones, which represents a down-scale energy-cascade in the *inertial subrange*. Finally the TKE is dissipated on the molecular scale k_d . After Hinze (1959).

regions. Typically it acts as a sink in the lower half and as a source in the top half of the sub-cloud and cloud layers. The pressure correlation term is important in the top of the two layers, and represents the impact of continuity on the thermals. As they approach a stable layer, the increasing pressure slows them down, and rising air is partially forced to move sideways due to continuity. This converts vertical kinetic energy into horizontal kinetic energy.

The final term in (2.35) is the dissipation of TKE, which balances the productive terms to a large extent. This shows that turbulence is of dissipative nature. The TKE is produced by buoyancy on large scales, which break down into smaller eddies, and so on to molecular scales at which the kinetic energy is converted into heat by viscous friction. This flow of energy from large to small scales is referred to as the *energy cascade*. One of the 'fingerprints' of micro-scale turbulence is the constant transfer rate of energy between different scales in the spectral window known as the *inertial subrange*, see Fig.2.4. In this range of scales the energy spectrum decays towards the small scales along a power law with a typical exponent $-\frac{5}{3}$, which according to the K41-theory for turbulence directly results from the assumption of a constant energy transfer rate (Kolmogorov, 1941; Obukhov, 1941). For further reading on turbulence theory see for instance Hinze (1959) or Frisch (1995).

2.1.6 Conditional sampling and cloud budgets

Detailed measurements made by aircraft have shown that in contrast to the dry environment large perturbations of vertical velocity, temperature and moisture exist inside single clouds, see Fig.2.5. These joint-perturbations are embedded in more passive saturated air, and indicate the presence of active, buoyant updrafts inside the cloud. The total vertical transport

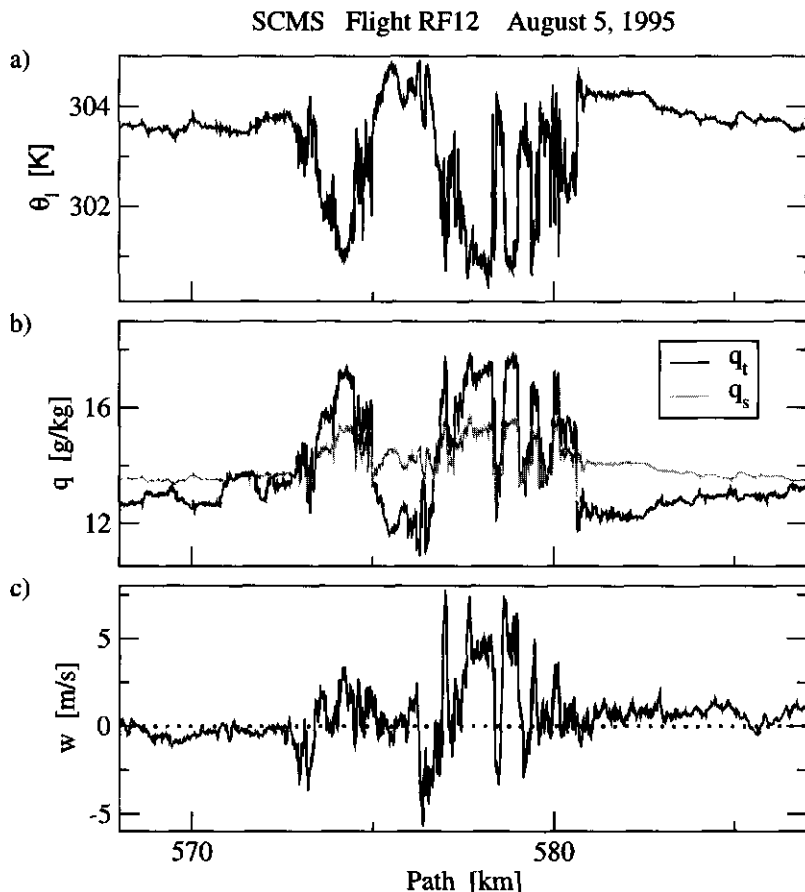


Figure 2.5 A horizontal trajectory through an active cumulus cloud by flight RF12 of the SCMS field-experiment in Florida on August 5, 1995. The three panels show a) the liquid water potential temperature θ_l , b) the total specific humidity q_t and the saturation specific humidity q_s , and c) the vertical velocity w .

by these incloud-updrafts has a more 'advective' nature than the diffusive transport by turbulence in the subcloud layer, as the updrafts are able to carry heat and moisture across the local conditional instability of the dry environment. This process is referred to as *non-local* transport, as the actual presence of the transporting up- and downdrafts is controlled by conditions at other levels.

The method of *conditional averaging* is a practical and commonly used method to separate and characterize different regimes of air. In general this method splits up a domain into two areas using a certain criterion. A range of different criteria have been used in experimental studies of dry convective boundary layers to separate convective plumes from other air.

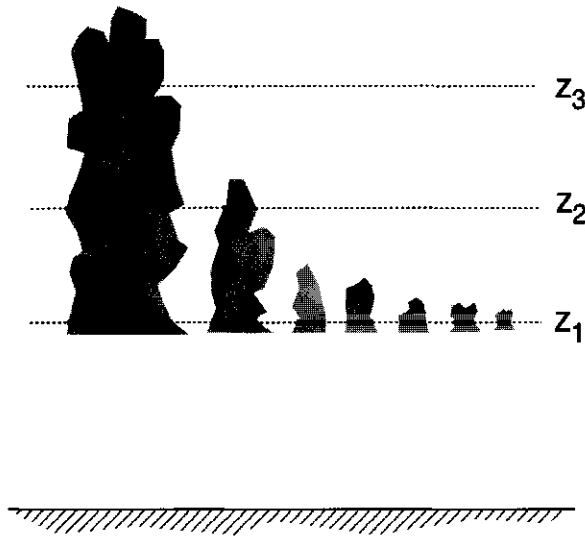


Figure 2.6 Schematic view of the method of conditionally averaging over a typical shallow cumulus cloud population. The clouds are rearranged, from the largest clouds on the left to the smallest clouds on the right, in order to visualize the changing cloud size distribution with height. The solid lines constitute the cloudy area A^c at each level. $Z_{1,2,3}$ are three heights of conditional averaging.

Scorer and Ludlam (1953) defined plumes as air having positive buoyancy, while Lenschow and Stephens (1980) used a humidity-threshold resulting in so-called "q-plumes". Greenhut and Khalsa (1982, 1987) and Taconet and Weill (1983) used a positive threshold value of the vertical velocity to define a plume. Closely related is the approach of Young (1988b,c) of defining plumes as areas with a positive vertical velocity and a minimum spatial width. Nicholls and LeMone (1980) and Penc and Albrecht (1987) used the combination of a positive vertical velocity and a positive humidity perturbation, called "wq-plumes". Schumann and Moeng (1991a,b) and Xu and Randall (2001) evaluated the budgets resulting from several of these criteria in simulated cloud fields.

In case of a cumulus cloud layer it has long been convenient to separate between cloudy air and dry environmental air (e.g. Asai and Kasahara, 1967). The average over the cloudy area at a certain height and at a certain moment is calculated using

$$\phi^c = \frac{1}{A^c} \int_A I \phi \, dA, \quad (2.36)$$

where ϕ is the variable to be averaged, A^c is the cloudy area, and A the total area of the domain. I is an indicator function, being 1 if the air is cloudy and 0 if it is non-cloudy. Comparing the cloud-averages of the conserved thermodynamic variables (2.9)-(2.10) to the moist-adiabatic profiles gives information about the presence of non-adiabatic processes, in this case the mixing between clouds and environment. However, one should realize that the cloudy area consists of many clouds of different sizes, and that the size distribution of the population changes with height. This is visualized in Fig.2.6. Larger, less diluted clouds

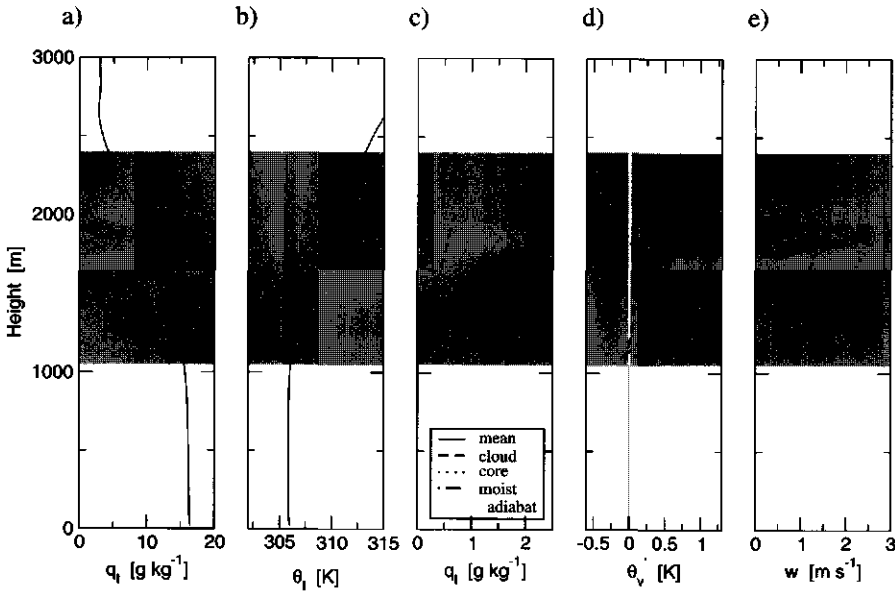


Figure 2.7 Conditionally sampled variables of a typical shallow cumulus topped boundary layer over land, as obtained from LES. The cloud-averages of a) total specific humidity q_t , b) the liquid water potential temperature θ_l , c) the liquid water content q_l , d) the excess of θ_v over the environment and e) the vertical velocity w . The conditional averages are only shown at those levels where the fraction was larger than 1%, in order to avoid unreliable statistics.

reach greater heights, and there start to dominate the cloud-average calculated with (2.36). In other words, the behaviour of ϕ^c with height is also influenced by population statistics. Applying cloud averages based on (2.36) in parameterizations is therefore effectively a *bulk* approach, in which the effect of both cloud-environment mixing and population statistics are represented.

Figure 2.7a and b show the cloud-average profiles θ_l^c and q_t^c . The rate at which the cloud-average profiles of these conserved variables change with height defines the *bulk fractional entrainment rate* ϵ^c ,

$$\frac{\partial \phi^c}{\partial z} \equiv -\epsilon^c (\phi^c - \phi^e) \quad (2.37)$$

(e.g. Betts, 1975; Anthes, 1977; Tiedtke, 1989; Raga et al., 1990). Here ϵ^c is an inverse length scale, representing the vertical mixing depth in which the excess of ϕ^c over ϕ^e has decreased by lateral mixing with a factor e^{-1} . Another method to characterize the mixing rate is based on the liquid water content of the clouds. Figure 2.7c shows that the ratio of q_l^c to the value of an undiluted parcel rising moist-adiabatically from cloud base is about 0.4, a value observed to be characteristic for cumulus clouds (e.g. Warner, 1955; Raga et al., 1990). The variety of existing models for cloud mixing will be discussed in further detail in Section 2.3 and Chapter 5.

Figure 2.7d shows that on average the clouds are only marginally buoyant, with a θ_v -excess over the environment of only a few tenths of degrees Kelvin. This is due to the existence of passive air inside the clouds caused by efficient mixing, sometimes called the *turbulent wake*, see Fig.2.5. The active moist updrafts form only a relatively small fraction of the cloud, but are responsible for most of the vertical transport. This has been the motivation to use a more stringent criterion in (2.36) in order to isolate the active updrafts in the cloud ensemble. The *cloud core* is defined as the fraction of the cloudy area which is also positively buoyant (Siebesma and Cuijpers, 1995). The profiles of the cloud core are also plotted in Fig.2.7. Generally speaking the cloud core is less diluted than the cloud, with a higher liquid water content, larger buoyancy and significantly larger vertical velocities.

Equation (2.36) can also be applied to prognostic equations, which results in *budget equations* for the fractional areas defined by the criterion. They give insight in the dominating processes in the related cloud physics and dynamics. One example is the general equation for the vertical velocity (2.22). Conditionally sampling this equation introduces terms in which the vertical derivative of the sampling-area occurs. The conditionally sampled turbulent flux by small-scale motions represents the lateral exchange of air at the interface between the two areas by small scale motions (Asai and Kasahara, 1967). In a simplified form (2.22) is used in many convection schemes in GCMs (Simpson and Wiggert, 1969; Gregory, 2001; Siebesma et al., 2002). When applied in an updraft-model it can provide an estimate for the vertical extent of the overshooting by clouds into the inversion, which is an important process in the deepening of the convective boundary layer and the exchange of air with the free troposphere.

2.2 Observation, Simulation, Parameterization

This section describes some relevant meteorological experiments during which shallow cumulus was observed and measured. Furthermore, attention is given to the numerical simulation of cumulus clouds as an alternative for these observational data-sets, which are often incomplete and not very detailed when cumulus clouds are concerned. Finally, several strategies are described for efficiently using the various data-sets in order to develop parameterizations and closure methods for use in large-scale circulation models.

2.2.1 Shallow Cumulus Field-Experiments

Relatively few intensive meteorological field-experiments have yet been realized during which aspects of shallow cumulus clouds were measured. The availability of many data-sets on a range of different cumulus-topped boundary layers would be convenient, as it enables a critical examination of the universality of physical theories and patterns thought to apply to shallow cumulus. Similarities can be sought between the different cases, resulting in relevant scales which may non-dimensionalize any formulation. The goal of parameterization is to formulate universal laws which apply to all situations and still contain only a limited number of free parameters. Therefore, ideally the experimental data on shallow cumulus should cover a broad parameter-space. In this section a number of idealized standard cases are defined, based on the data-sets obtained during several cumulus experiments at different locations and at varying conditions. Each represents a unique situation in which cumulus occurred.

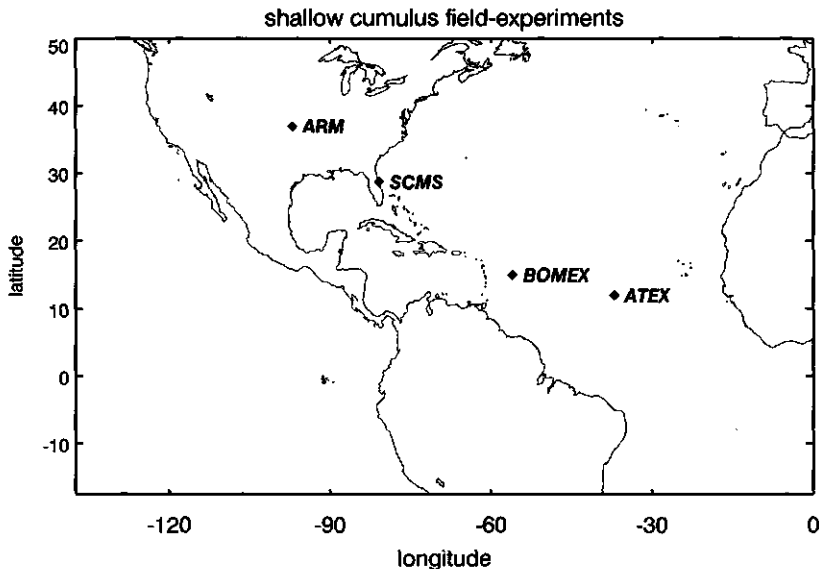


Figure 2.8 The locations of the four field-experiments. The acronyms are explained in the text.

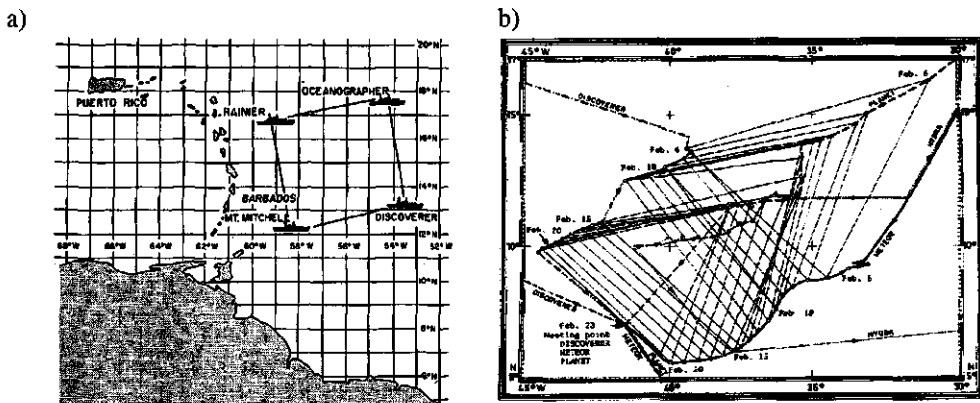


FIG. 1. BOMEX fixed-ship array during Phases 1, 2 and 3.

Figure 2.9 a) The location and configuration of the ship arrays during BOMEX (from Nitta and Esbensen, 1974) and b) during ATEX (from Augstein et al., 1973).

The shallow cumulus experiments organized in the past can roughly be separated into two groups based on their characteristics, namely *marine* and *continental* cumulus. Of both classes two experiments are described in detail, see Fig.2.8 for their locations. The experiments are briefly discussed, focusing on the characteristics of the observed cumulus-topped convective boundary layers which make them interesting for this thesis. The four resulting idealized cases based on these particular campaigns will be used throughout this thesis to study cumulus convection.

Oceanic Trade-wind experiments.

Following the southerly Trade-wind flow towards the ITCZ the sea surface temperature (SST) rises considerably. As a consequence the boundary layer gets warmer and hence can contain more moisture. Also, the surface input of heat and moisture increases significantly towards the equator. This strong supply of moisture and heat prepares the boundary layer for the initiation of the deep convection at the ITCZ near the equator. At those low latitudes the convergence of the Trade-winds from the Northern and Southern Hemisphere creates potentially unstable conditions in the troposphere overlying the boundary layer which encourage deep convection. The exact triggering of deep convection in the tropics is an outstanding issue, but the state of the boundary layer likely plays an important role. Experimental field-campaigns have been organized in the Trade-wind regions to increase the knowledge about the general structure of the boundary layers in this area. During these campaigns various budgets in the governing equations for the large-scale (Hadley) circulation were measured, with the purpose of shedding more light on the role of cumulus convection.

The Barbados Oceanographic and Meteorological Experiment (BOMEX) was organized in 1969 in the Atlantic Trade-wind region east of Barbados, near (15°N , 56°W). The field operations were divided into four observation periods of 13 to 18 days, each to support the two

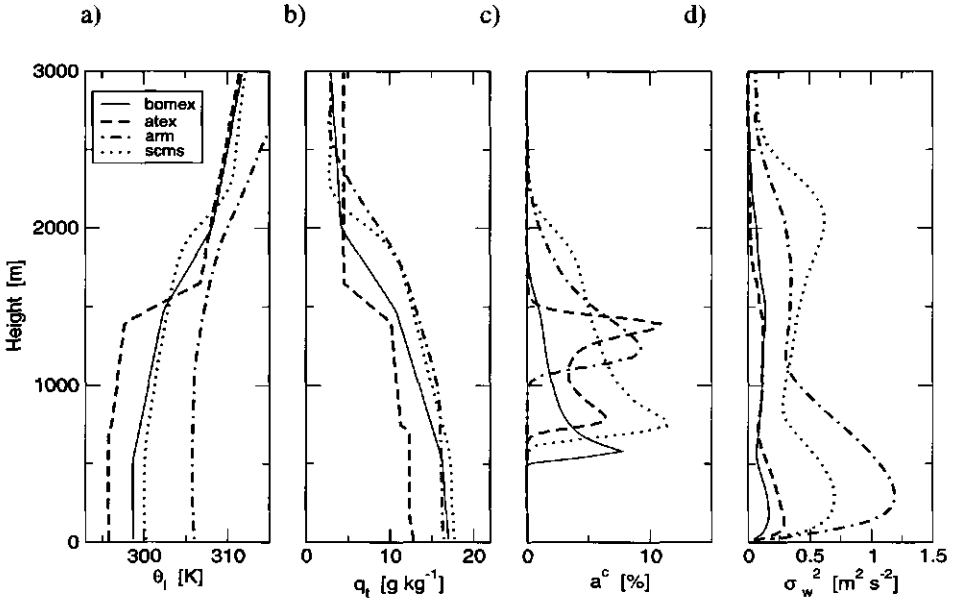


Figure 2.10 Vertical profiles calculated with LES of the four described idealized cases of BOMEX, ATEX, ARM and SCMS. a) The liquid water potential temperature θ_l , b) the total specific humidity q_t , c) the cloud fraction a^c and d) the variability of the vertical velocity σ_w^2 .

major investigations. The air-sea interaction investigation was conducted during BOMEX Period I, May 3 to May 15, Period II, May 24 to June 10, and Period III, June 19 to July 2. The investigation of tropical convective systems was conducted during Period IV, July 11 to July 28. During phase III relatively undisturbed, steady state cumulus convection was observed for a period of several days. A fleet of five ships was employed, configured as a fixed square covering roughly 500^2km^2 with one ship in the center, see Fig.2.9a. The ships measured the surface fluxes, and every 90 minutes radiosondes were released from each ship measuring the vertical profiles of the temperature, moisture and wind. The convection in the boundary layer was driven by the latent and sensible heat fluxes at the surface, being 150 W/m^2 and 8 W/m^2 respectively. A dry well-mixed layer was topped by a conditionally unstable cloud layer, which in turn was capped by a stable Trade-wind inversion (see Fig.2.10a and b). Holland and Rasmusson (1973), Nitta and Esbensen (1974) and Esbensen (1975) derived large scale budgets from the vertical profiles of the radiosondes. A detailed description of an idealized case based on this data is given by Siebesma and Cuijpers (1995), which was later used by Working Group I of the GEWEX (Global Energy and Water-cycle Experiment) Cloud Systems Studies (GCSS) in an intercomparison study of several LES codes (Siebesma et al., 2002).

The Atlantic Trade-wind Experiment (ATEX) took place in February 1969 in the north-east Trade-wind region of the Atlantic Ocean, to the south-west of the Cape-Verdian Islands at (12°N , 37°W). Compared to BOMEX this experiment is positioned more upstream in the

Case	Surface fluxes		Cloud heights		Inversion-strength	Turbulence	
	SH	LH	z_b	h^c	Γ_i	w_{sub}^*	CAPE
	[Wm ⁻²]		[km]		[K km ⁻¹]	[m s ⁻¹]	[m ² s ⁻²]
BOMEX	8	150	0.6	1	10.8	0.68	44.5
ATEX	8	144	0.75	0.8	35	0.78	15.6
ARM 19 UTC	140	500	0.9	1	7.8	1.68	45.7
SCMS 18 UTC	150	300	0.7	1.5	15	1.36	61.6

Table 2.1 Characteristics of the four described cases BOMEX, ATEX, ARM and SCMS. The characteristics of the two continental cases ARM and SCMS are those at the moment of the surface flux maxima, at 19:00 UTC and 18:00 UTC respectively. The table respectively shows the surface sensible and latent heat fluxes, the cloud base height and the cloud layer depth, the potential temperature lapse-rate in the inversion, the subcloud convective velocity scale defined by (2.42), and the convective available potential energy defined by (2.43).

Hadley cycle. An analysis of boundary layer structure during ATEX is given by Augstein et al. (1974). The ship array consisted of three ships, see Fig.2.9b. The large scale budgets derived from their measurements were evaluated by Augstein et al. (1973). In the period between February 7 and 12 the Trade-wind inversion capping the planetary boundary layer was relatively strong compared to BOMEX, see Fig.2.10a and b and Table 2.1. The structure of the cloud layer differs from BOMEX: the cloud fraction peaks at two heights, see Fig.2.10c. This is typical for a shallow cumulus cloud layer which rises into a stratocumulus-like layer. This period during ATEX represents the transition between stratocumulus and cumulus which at some stage occurs in the Hadley-cycle upstream of the ITCZ. Such a transition is characterized by a *decoupling* of the subcloud layer from the cloud layer (Bretherton and Wyant, 1997; Stevens, 2000), visible in the small temperature and moisture jump in the vertical profiles at cloud base, see Fig.2.10. Unlike the BOMEX case radiative effects at cloud top plays an important role in the large scale budgets, due to the relatively large cloud fraction of the stratocumulus layer. Firstly, long-wave radiative cooling of the cloud top is an important aspect in the stratocumulus dynamics. Secondly, the relatively high reflection of solar radiation at cloud top seriously affects the surface energy balance. An idealized case was based on the observations during ATEX by Stevens et al. (2001) for GCSS WG I.

The ships taking part in these campaigns were arranged as an array spanning a certain area in order to calculate the large-scale budgets of temperature and moisture. These can then be used to estimate the impact of convection on the large scale budgets, a method first applied by Reed and Recker (1971), Nitta (1972) and Yanai et al. (1973). Horizontally averaging the

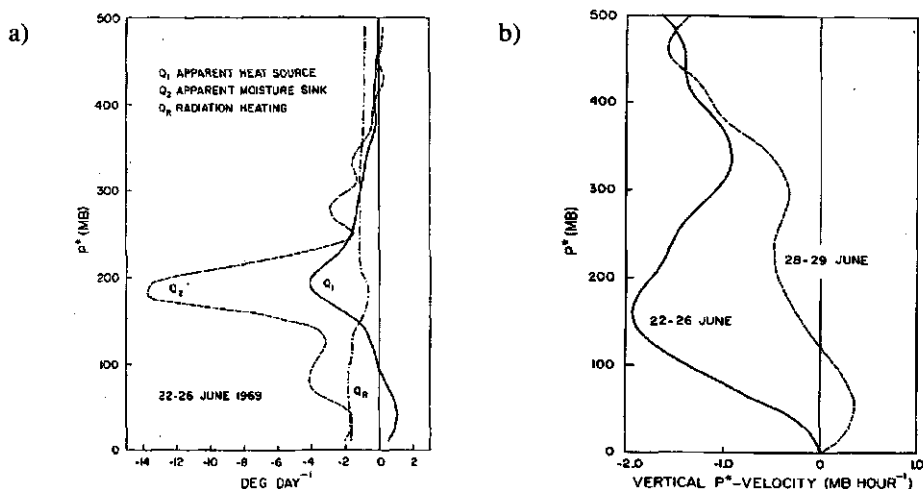


Figure 2.11 Characteristics of the undisturbed period of BOMEX derived from the large scale budgets (from Nitta and Esbensen, 1974). a) The apparent heat source Q_1 , the apparent moisture sink Q_2 and the radiative heating Q_R . b) The observed mean vertical velocity W . The vertical pressure coordinate p^* is defined as $p^* = p_s - p$ where p_s is the surface pressure. The Trade-wind inversion was located approximately just below $p^* = 200$ mb.

governing equations for moisture and heat (2.24)-(2.25) over the area gives

$$\underbrace{\frac{\partial \bar{\phi}}{\partial t} + U \frac{\partial \bar{\phi}}{\partial x} + V \frac{\partial \bar{\phi}}{\partial y} + W \frac{\partial \bar{\phi}}{\partial z}}_{LS_{\bar{\phi}}} = \underbrace{F_{\bar{\phi}} - \frac{\partial w' \phi'}{\partial z}}_{Q_{\bar{\phi}}}, \tag{2.38}$$

where $\phi \in \{\theta_l, q_l\}$. The average tendency and the advective forcing by the large scale winds $LS_{\bar{\phi}}$ on the left hand side are calculated from the measurements by the radiosondes and the ship array. In this procedure, the large scale subsidence W is obtained by applying the divergence theorem to the continuity equation (2.26),

$$\frac{\partial W}{\partial z} = - \oint_l \hat{n}_h \cdot \bar{U}_h dl, \tag{2.39}$$

where the subscript h indicates the horizontal components, and l is the contour of the area. The remaining sources and sinks are combined in term $F_{\bar{\phi}}$, which can be radiative processes for $\phi = \theta_l$ and precipitation for $\phi = q_l$. The *apparent source* $Q_{\bar{\phi}}$ for heat and moisture represents the tendency caused by cumulus convection, and is obtained as a residual from the terms on the left hand side. This method has some drawbacks, as possibly the residual is a small difference between large terms, which introduces relatively large uncertainties. Therefore, the residual Q should only be seen as a rough estimate for the tendency associated with cumulus convection. This method can be applied at multiple levels in the boundary layer.

Holland and Rasmusson (1973) showed that during BOMEX the storage tendency of moisture was very small compared to the other terms in (2.38). This is typically found in most field-experiments in the Trade-wind regions. Nitta and Esbensen (1974) expressed the Q -terms as functions of non-conserved variables,

$$\frac{Q_1}{c_p \Pi} \equiv \frac{L}{c_p \Pi} (c - e) - \frac{\partial w' \theta'}{\partial z} + F_{\theta}^R, \quad (2.40)$$

$$\frac{Q_2}{L} \equiv (c - e) + \frac{\partial w' q'_v}{\partial z}, \quad (2.41)$$

where c is the condensation rate and e the evaporation rate of cloud liquid water. F_{θ}^R is the temperature-tendency due to radiation. Q_2 is formulated as a sink term by convention (negative values stand for moistening). Siebesma and Cuijpers (1995) concluded from LES results on BOMEX that the condensation effects represented by $(c - e)$ are approximately balanced by turbulent flux divergence: generated cloud water at cloud base is immediately transported upwards to compensate the net evaporation at higher levels. This means that $Q_1 \approx c_p \Pi Q_{\bar{\theta}_i}$ and $Q_2 \approx -L Q_{\bar{q}_i}$. Figure 2.11a illustrates that the apparent sources $Q_{\bar{\theta}_i}$ are largest in the inversion. Also, the combination of large vertical temperature- and moisture-gradients with a relatively strong subsidence in the inversion (see Fig.2.11b) causes $LS_{\bar{\theta}_i}$ to be dominated by the subsidence induced by the Hadley cycle.

These results show that the large scale subsidence warms and dries the inversion, which is counteracted by the moistening and cooling effect of the overshooting and mixing cumulus clouds. A *quasi-equilibrium* exists between the slow changing large scale advection and the fast cumulus convection. The equilibrium state of the boundary layer is described by the steady-state profiles of the thermodynamic variables $\bar{\theta}_i$ and \bar{q}_i , see Fig.2.10. The concept of quasi-equilibrium is useful for parameterizations as the vertical turbulent transport by the small scales is directly linked to the large scale forcings, which as a result determines a thermodynamic state for the boundary layer. This concept is widely used in various forms in a range of existing schemes and models (e.g. Arakawa and Schubert, 1974; Fritsch and Chappell, 1980; Betts and Miller, 1986a,b; Tiedtke, 1989; Raymond, 1995; Neelin, 1997; Neelin and Zeng, 2000).

Continental cumulus experiments

In contrast to marine situations, the planetary boundary layers over land are generally not in steady state. Due to the solar or *diurnal* cycle the surface fluxes change significantly during the day, from very small values at sunrise via relatively strong maxima at noon back to small fluxes at sunset. This leads to significant temperature and humidity tendencies in the boundary layer during the day. The presence of cumulus clouds on top of these boundary layers depends on parameters such as temperature, specific humidity, the surface fluxes, and the stability of the residual layers (remnants of a convective boundary layer of the day before) and the capping inversion. The onset of clouds and the subsequent development of the cloud layer in time are critical issues in a GCM which should be represented well by a convection scheme. At dusk the clouds disappear and the convection dies out. During night-time the boundary layer stabilizes again due to the cooling of the earth's surface. How do existing

parameterizations and closures based on quasi-equilibrium marine situations cope with such a non-equilibrium state? In order to study these questions in detail two recent experiments are described during which cumulus over land was observed. In contrast to BOMEX and ATEX these experiments took place fairly recently, and state-of-the-art instrumentation was employed. This resulted in more and better measurements on the cumulus clouds themselves.

Shallow cumulus over land was observed on June 21, 1997 at the Southern Great Plains (SGP) site in Oklahoma, which is part of the Atmospheric Radiative Measurement (ARM) program, see Fig.2.13a. The SGP site consists of an array of stations equipped with instrumentation measuring a variety of meteorological variables. The area covered by this array was approximately 300^2 km². Every three hours a radiosonde was released at the central facility giving the vertical profiles of temperature and moisture. At the Central Facility many cloud properties are measured, see for example Fig.2.12. A diurnal cycle was observed in a

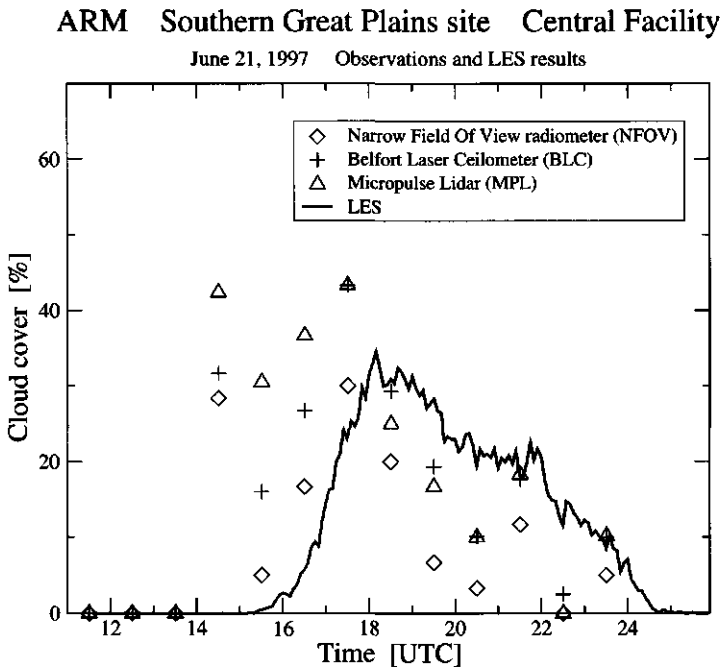


Figure 2.12 Observations on August 21, 1997 of the cloud cover at the ARM Southern Great Plains (SGP) site, Central Facility. The measurements by the various instruments as indicated in the legend were obtained from the *ARM SGP Data Archive*, which also provides extensive descriptions of these instruments. They are ceilometer-type instruments, measuring any cloud overhead each using a different method. The LES results as discussed in the text are also shown. In a short period before cloud onset in LES some high cirrus clouds were observed at the SGP site, which might explain at least some of the early observations of cloud cover.

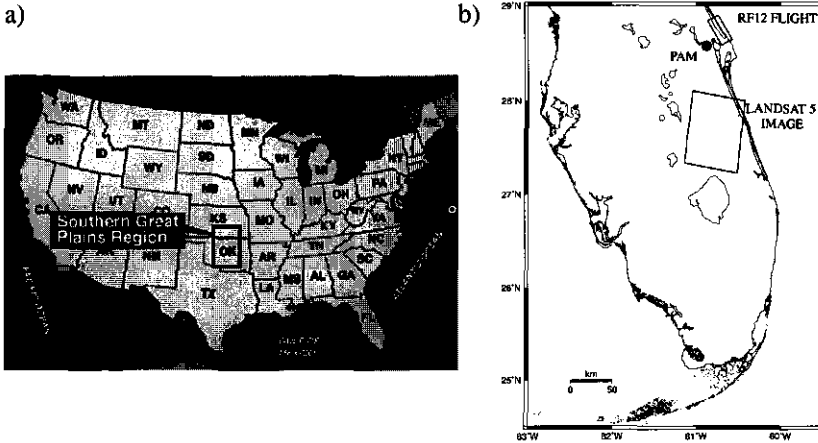


Figure 2.13 a) A map of North America, showing the location of the ARM Southern Great Plains (SGP) site. b) A map of Florida. The SCMS campaign was situated near Cocoa Beach, Cape Canaveral. The PAM ground-station is indicated by the black dot. The area of flight RF12 and the area covered by the Landsat 5 image are indicated by the rectangles.

cumulus topped convective boundary layer over land on this day. At sunrise a stable boundary layer existed. During the morning the surface fluxes increased to a maximum around noon, and as a result a dry convective boundary layer developed. A conditionally unstable cloud layer formed on top of the mixed layer which deepened in time, see Fig.2.14a. Figure 2.12 shows that the cloud cover never exceeded 50%. The large scale forcings were relatively small compared to the forcing by the surface fluxes. A case based on this data-set has been constructed for an LES intercomparison study by GCSS WG I (Brown et al., 2002). It is also used in an intercomparison study for single column models and LES as part of the European Cloud System (EUROCS) project.

The Small Cumulus Microphysics Study (SCMS) took place from July 17 until August 13, 1995 and was situated near Cocoa Beach, Florida, just north of Cape Canaveral (see Fig.2.13b). On August 5 a clear convective boundary layer over land developed in the early morning, and during the course of the day a shallow cumulus cloud layer developed. The clouds were categorized as shallow cumulus with a cloud cover of 10 – 40%. This particular 'golden day' was part of a period in which persistently a shallow cumulus topped boundary layer developed each day. One of the goals of SCMS was to examine the micro-physical and geometrical structure of cumulus clouds during their life-time. The C-130 aircraft of NCAR was employed during this campaign, measuring the turbulent and micro-physical properties inside many clouds. The resulting datasets have been reported by Knight and Miller (1998) and French et al. (1999). Two mobile meteorological stations of the PAM-type (Horst and Oncley, 1995; Militzer et al., 1995) measured the timeseries of the surface fluxes, temperature and moisture. Every three hours radiosondes were released near the PAM stations. The availability of detailed in-cloud measurements makes the SCMS case unique compared to the

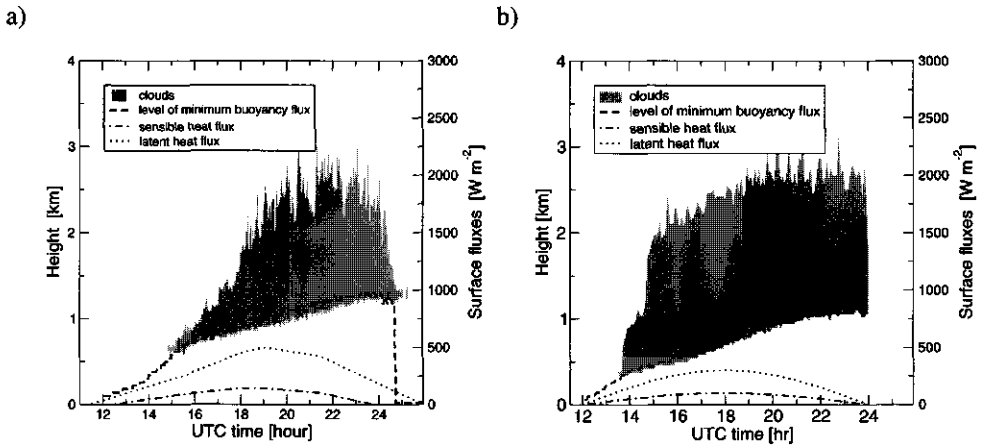


Figure 2.14 The development of the cumulus topped boundary layer in a) ARM and b) SCMS, as resolved by LES. The level of minimum buoyancy-flux is used to indicate the top of the well-mixed layer. The time-series of the surface latent and sensible heat fluxes are also plotted. Local time at the ARM site lags UTC time by 6 hours, in the SCMS area by 5 hours.

other three cases described before. On top of this, the Landsat 5 satellite made images of the cumulus cloud fields in the SCMS area during the campaign, with a high resolution of 30m. An idealized case based on this range of data is presented by Neggers et al. (2003a). A detailed analysis of the aircraft measurements and the Landsat imagery during SCMS is given by Rodts et al. (2002).

In general the SCMS case closely resembles the ARM case, but there are some subtle differences. Due to the larger surface fluxes in ARM its convection in the subcloud layer is more intense than SCMS, as is illustrated by the values of σ_w in Table 2.1. In the similarity theory for dry turbulence this parameter is scaled with the convective vertical velocity scale w_{sub}^* (Deardorff, 1970a), defined as

$$w_{sub}^* = \left(\frac{gz_b}{\Theta_v^0} \overline{w'\theta_v'^s} \right)^{\frac{1}{3}}, \quad (2.42)$$

This shows that the intensity of the subcloud turbulence is a function of the surface buoyancy flux and the boundary layer height. Figure 2.10 shows that SCMS is about five degrees cooler than ARM over the whole depth of the boundary layer while the specific humidity profiles are comparable, which is the reason for the relatively low cloud base and deep cloud layer in SCMS, see Fig.2.14. Another striking difference is the fact that the cloud layer in the ARM case deepens slowly, while in SCMS it quickly deepens to about 1.5km. This is caused by the higher instability already present at dawn in SCMS, perhaps due to the existence of a relatively unstable residual layer left over from the convective day before. A measure for the energy available for moist convection is the convective available potential energy (CAPE), defined as

$$CAPE \equiv \int_{z_s}^{LNB} \frac{g}{\Theta_v^0} (\theta_v^p - \bar{\theta}_v) dz, \quad (2.43)$$

(see Emanuel, 1994, 1997). Here the subscript p indicates a parcel rising (moist-)adiabatically from level z_s near the surface to its level of zero buoyancy (LZB) in the top of the cloud layer. The parcel represents an updraft which does not mix with its environment, and accordingly the integral (2.43) is a measure for the maximum amount of potential gravitational energy which can be converted into kinetic energy by the clouds. In contrast to w^* , the CAPE in SCMS is larger than in ARM, mainly due to the significantly larger cloud-depth. In that respect, the clouds in SCMS are closer to deep cumulus. The formation and evaporation of precipitation plays an important role in the dynamics of deep convection. Measuring the incloud micro-physics was one of the main purposes of SCMS, and all together these features would make the SCMS case a suitable test-ground for studying the transition between non-precipitating and precipitating cumulus convection.

Comparing the continental cumulus cases to the marine cumulus cases in Table 2.1, it becomes clear that the convection over land is more intense (higher σ_w values), due to the large sensible and latent surface heat fluxes. The *Bowen ratio* r_B is defined as the ratio of the sensible to the latent surface heat flux,

$$r_B \equiv \frac{SH}{LH} \quad (2.44)$$

In continental boundary layers $r_B \approx 0.3 - 0.5$, while in marine situations $r_B \approx 0.05 - 0.1$ (Holland and Rasmusson, 1973). Obviously in marine situations the latent heat flux plays a relatively important role in fuelling the convection. Concerning the CAPE in the four cases, it is remarkable that in the weakly driven marine BOMEX case the CAPE is comparable to the intensely driven continental ARM case. This shows that CAPE only represents the maximum potential energy which can *hypothetically* be converted into kinetic energy. It does not state anything about the actual occurrence of undiluted rising updrafts inside the clouds, needed to convert all CAPE. The intensity of dilution of rising updrafts is dependent on the nature of the mixing between updrafts and their environment, a process not yet fully understood. Finally, a similarity in all cases except ATEX is the value of the lapse rate of temperature and moisture in the conditionally unstable cloud layer, which is constant with height. The ATEX case is clearly different from the other cases at many points due to its transitional nature, which makes it an interesting outlier.

2.2.2 Cloud measurements and Large-Eddy Simulation (LES)

The shallow cumulus experiments have provided data-sets which give insight in the general, domain-average characteristics of large cumulus cloud fields, such as the vertical structure of temperature and moisture, the mean horizontal and vertical motions, and the budgets of temperature and moisture averaged over large areas and long periods of time. It is important to realize that these results represent the impact of the cloud field as a whole. Obviously a shallow cumulus cloud population consists of many individual clouds of different sizes, each making its own contribution to the mean properties of the whole ensemble. Accordingly, to understand why the mean properties behave as observed in the cumulus experiments it is necessary to take a closer look at these small scale processes. These arguments have inspired further research on the range of small scales associated with turbulence and cumulus clouds.

Obtaining representative three-dimensional data at high spatial and temporal resolutions from observations has proved to be difficult to realize. Surely measurements by aircraft and radar have revealed much about the dynamical and micro-physical structure of *single* clouds. An impressive number of studies is based on in-cloud measurements by aircraft. For example, Squires (1958a,b,c); Warner (1955, 1969a,b) described measurements of cloud droplet spectra. Warner (1970a, 1977) analyzed liquid water contents and vertical velocities inside clouds. More recent observational studies using aircraft-data are for instance Heymsfield et al. (1978), Paluch (1979), Raga et al. (1990), Jonas (1990) and Barnes et al. (1996).

Nevertheless, when employing aircraft it is impossible to sample all clouds in the population in a certain domain simultaneously and at several heights. The aircraft measurements are time-series along flight-tracks, which per definition consist of point-measurements in a changing cloud field with time. Many aircraft are needed to sample a realistic cloud size distribution, which presses hard on the financial feasibility of this approach. In the last decades cloud radar has shown its potential in retrieving detailed cloud properties (Lehrmitte, 1987; Knight and Miller, 1998; French et al., 1999; Kollias et al., 2001), but this technique is still in full development. It has yet to provide instantaneous three-dimensional fields of the combined thermodynamic, turbulent and geometric properties, covering a whole population of shallow cumulus clouds.

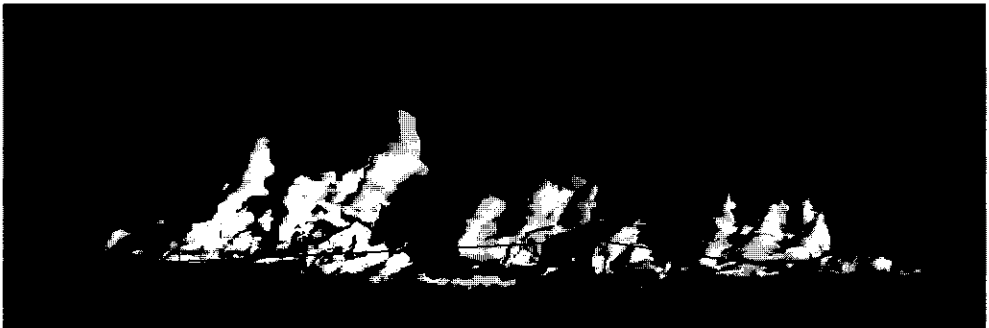


Figure 2.15 A 3D cloud field of ARM as produced by LES. The clouds are visualized by plotting iso-surfaces defined by $q_l = 0$.

A different method which emerged in the last quarter of the twentieth century and has opened new research-possibilities is the numerical simulation of micro-scale moist convection. *Large eddy simulation* (LES) is the name given to a numerical solver of the discretized governing equations for atmospheric turbulent flow including moist physics (clouds), as defined and listed in Section 2.1.2. The impact of the unresolved subgrid motions on the resolved scales is parameterized in a subgrid-scale (SGS) model. The LES concept was first applied to dry convective planetary boundary layers by Lilly (1967) and Deardorff (1970b). Sommeria (1976) first applied LES to Trade-wind shallow cumulus, and Deardorff (1980) first simulated stratocumulus. A full description of the LES model used in this thesis is given by Cuijpers and Duynkerke (1993). Figures 2.15 and 2.16 show visualizations of a simulated cumulus-topped boundary layer as produced by LES.

The most commonly used SGS model in large-eddy simulations of atmospheric boundary layers is the diffusive-type model (Smagorinski, 1963; Lilly, 1967), in which the SGS fluxes in the governing equations are expressed as the product of an eddy-viscosity and the local resolved gradients,

$$\overline{u'_i u'_j} = -K_m \left(\frac{\partial U_i}{\partial x_j} + \frac{\partial U_j}{\partial x_i} \right) \quad (2.45)$$

$$\overline{u'_j \phi'} = -K_\phi \frac{\partial \bar{\phi}}{\partial x_j} \quad (2.46)$$

The SGS eddy-viscosity K is constructed as the product of a length scale and a typical velocity difference at that scale, see (2.28). Many variations on this theme are possible and indeed have been formulated (Meneveau and Katz, 2000). The cut-off length-scale is usually assumed to be proportional to the grid-spacing $\Delta = (\Delta x \Delta y \Delta z)^{\frac{1}{3}}$ in LES. Often the typical velocity difference is related to the SGS kinetic energy e , see (2.29). This requires an additional prognostic equation for e such as (2.35). The Smagorinsky-Lilly model uses a diagnostic TKE equation, only containing the production and dissipation terms. In the model of Schumann (1975) a prognostic equation is used, including storage and transport terms which introduce memory effects in the SGS model. Making use of the fact that the cut-off length-scale in LES is situated in the inertial subrange of turbulence, Schmidt and Schumann (1989) derived the SGS eddy diffusivity by assuming a balance between production and dissipation,

$$K_m = C_e \Delta e^{\frac{1}{2}} \quad (2.47)$$

where C_e is a function of the Kolmogorov constant. The eddy-diffusivities for the conserved properties are related to K_m by the turbulence Prandtl number Pr ,

$$K_{\theta_i} = K_{q_i} = Pr^{-1} K_m. \quad (2.48)$$

where Pr is usually taken to be about $\frac{1}{3}$ (Deardorff, 1972). Often the mixing-length Δ is made a function of stability, in order to limit the activity of the SGS model in very stable conditions.

The micro-scales associated with atmospheric turbulence and boundary-layer clouds restrict the grid-spacing used in LES. In the early years of LES the three-dimensional grid only

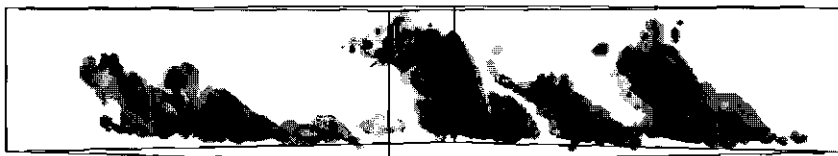


Figure 2.16 The same ARM cloud field as Fig.2.15, but now with semi-transparent iso-surfaces and seen from the side. The iso-surfaces for $w = 2\text{m/s}$ and $w = -2\text{m/s}$ are also plotted (darkgrey) to visualize the active in-cloud motions.

contained about $20 \times 20 \times 10$ points, limited by the yet small computer capacity. Due to the further development of supercomputing the resolved grid can have a much higher resolution nowadays, with typically $100 \times 100 \times 100$ points at a time-step of about 1 or 2 seconds. Observations have shown that in convective boundary layers the domain-averaged turbulent fluxes and variances are dominated by the larger eddies in the spectrum of turbulent scales. Moeng (1984), Mason (1989) and Schmidt and Schumann (1989) have shown that the present-day resolutions of 20 to 50m make LES suitable for simulating unstable, convective boundary layers, as the motions of the scales which contribute most to the total variability in momentum, heat and moisture are explicitly resolved. Critical reviews on the technique of LES were written by Mason (1994) and Moeng (1998).

The skill of LES in producing realistic turbulent fields has been studied extensively in the past (e.g. Sommeria and LeMone, 1978; Nicholls et al., 1982). In order to assess the impact of both numerics and model formulation on the resolved dynamics, the performance of several different LES models for a clear convective atmospheric boundary layer was compared by Nieuwstadt et al. (1991). They showed that the large eddies as resolved by LES are quite insensitive to the subgrid model, and that the results of the simulations are within scatter of the available observations. Since then a series of similar LES-*intercomparisons* for cloudy boundary-layers have been organized. Typically a case was set up based on as many observations as were available from the selected field-experiment. The first cases were dedicated to stratocumulus. The GCSS working group I workshop at NCAR, Boulder in 1994 as reported by (Moeng et al., 1996) was based on observations during the First ISCCP Regional Experiment (FIRE, see Betts and Boers, 1990; Duda et al., 1991). The European Cloud Resolving Modeling (EUCREM) project intercomparison (Duynkerke et al., 1999) was based on the Atlantic Stratocumulus Transition Experiment dataset (ASTEX, see Albrecht et al., 1995; Bretherton and Pincus, 1995; Bretherton et al., 1995; De Roode and Duynkerke, 1997).

The first LES intercomparison dedicated to shallow cumulus was based on the steady state marine case of BOMEX (Siebesma et al., 2002). The results showed a remarkable agreement between LES models on the mean thermodynamic state and mass flux transport. Another LES intercomparison on shallow cumulus by GCSS wg 1 was dedicated to cumulus rising into stratocumulus, as observed during ATEX (Stevens et al., 2001). One of the conclusions on this case was that the cloud-fraction of the 'stratocumulus-like' layer at the strong capping

inversion still varied considerably among the models. A recent intercomparison focused on

A different method which emerged in the last quarter of the twentieth century and has opened new research-possibilities is the numerical simulation of micro-scale moist convection. *Large eddy simulation* (LES) is the name given to a numerical solver of the discretized governing equations for atmospheric turbulent flow including moist physics (clouds), as defined and listed in Section 2.1.2. The impact of the unresolved subgrid motions on the resolved scales is parameterized in a subgrid-scale (SGS) model. The LES concept was first applied to dry convective planetary boundary layers by Lilly (1967) and Deardorff (1970b). Sommeria (1976) first applied LES to Trade-wind shallow cumulus, and Deardorff (1980) first simulated stratocumulus. A full description of the LES model used in this thesis is given by Cuijpers and Duynkerke (1993). Figures 2.15 and 2.16 show visualizations of a simulated cumulus-topped boundary layer as produced by LES.

The most commonly used SGS model in large-eddy simulations of atmospheric boundary layers is the diffusive-type model (Smagorinski, 1963; Lilly, 1967), in which the SGS fluxes in the governing equations are expressed as the product of an eddy-viscosity and the local resolved gradients,

$$\widetilde{u'_i u'_j} = -K_m \left(\frac{\partial U_i}{\partial x_j} + \frac{\partial U_j}{\partial x_i} \right) \quad (2.45)$$

$$\widetilde{u'_j \phi'} = -K_\phi \frac{\partial \bar{\phi}}{\partial x_j} \quad (2.46)$$

The SGS eddy-viscosity K is constructed as the product of a length scale and a typical velocity difference at that scale, see (2.28). Many variations on this theme are possible and indeed have been formulated (Meneveau and Katz, 2000). The cut-off length-scale is usually assumed to be proportional to the grid-spacing $\Delta = (\Delta x \Delta y \Delta z)^{\frac{1}{3}}$ in LES. Often the typical velocity difference is related to the SGS kinetic energy e , see (2.29). This requires an additional prognostic equation for e such as (2.35). The Smagorinsky-Lilly model uses a diagnostic TKE equation, only containing the production and dissipation terms. In the model of Schumann (1975) a prognostic equation is used, including storage and transport terms which introduce memory effects in the SGS model. Making use of the fact that the cut-off length-scale in LES is situated in the inertial subrange of turbulence, Schmidt and Schumann (1989) derived the SGS eddy diffusivity by assuming a balance between production and dissipation,

$$K_m = C_e \Delta e^{\frac{1}{2}} \quad (2.47)$$

where C_e is a function of the Kolmogorov constant. The eddy-diffusivities for the conserved properties are related to K_m by the turbulence Prandtl number Pr ,

$$K_{\theta_i} = K_{q_i} = Pr^{-1} K_m. \quad (2.48)$$

where Pr is usually taken to be about $\frac{1}{3}$ (Deardorff, 1972). Often the mixing-length Δ is made a function of stability, in order to limit the activity of the SGS model in very stable conditions.

The micro-scales associated with atmospheric turbulence and boundary-layer clouds restrict the grid-spacing used in LES. In the early years of LES the three-dimensional grid only



Figure 2.16 The same ARM cloud field as Fig.2.15, but now with semi-transparent iso-surfaces and seen from the side. The iso-surfaces for $w = 2\text{m/s}$ and $w = -2\text{m/s}$ are also plotted (darkgrey) to visualize the active in-cloud motions.

contained about $20 \times 20 \times 10$ points, limited by the yet small computer capacity. Due to the further development of supercomputing the resolved grid can have a much higher resolution nowadays, with typically $100 \times 100 \times 100$ points at a time-step of about 1 or 2 seconds. Observations have shown that in convective boundary layers the domain-averaged turbulent fluxes and variances are dominated by the larger eddies in the spectrum of turbulent scales. Moeng (1984), Mason (1989) and Schmidt and Schumann (1989) have shown that the present-day resolutions of 20 to 50m make LES suitable for simulating unstable, convective boundary layers, as the motions of the scales which contribute most to the total variability in momentum, heat and moisture are explicitly resolved. Critical reviews on the technique of LES were written by Mason (1994) and Moeng (1998).

The skill of LES in producing realistic turbulent fields has been studied extensively in the past (e.g. Sommeria and LeMone, 1978; Nicholls et al., 1982). In order to assess the impact of both numerics and model formulation on the resolved dynamics, the performance of several different LES models for a clear convective atmospheric boundary layer was compared by Nieuwstadt et al. (1991). They showed that the large eddies as resolved by LES are quite insensitive to the subgrid model, and that the results of the simulations are within scatter of the available observations. Since then a series of similar LES-*intercomparisons* for cloudy boundary-layers have been organized. Typically a case was set up based on as many observations as were available from the selected field-experiment. The first cases were dedicated to stratocumulus. The GCSS working group I workshop at NCAR, Boulder in 1994 as reported by (Moeng et al., 1996) was based on observations during the First ISCCP Regional Experiment (FIRE, see Betts and Boers, 1990; Duda et al., 1991). The European Cloud Resolving Modeling (EUCREM) project intercomparison (Duynkerke et al., 1999) was based on the Atlantic Stratocumulus Transition Experiment dataset (ASTEX, see Albrecht et al., 1995; Bretherton and Pincus, 1995; Bretherton et al., 1995; De Roode and Duynkerke, 1997).

The first LES intercomparison dedicated to shallow cumulus was based on the steady state marine case of BOMEX (Siebesma et al., 2002). The results showed a remarkable agreement between LES models on the mean thermodynamic state and mass flux transport. Another LES intercomparison on shallow cumulus by GCSS wg 1 was dedicated to cumulus rising into stratocumulus, as observed during ATEX (Stevens et al., 2001). One of the conclusions on this case was that the cloud-fraction of the 'stratocumulus-like' layer at the strong capping inversion still varied considerably among the models. A recent intercomparison focused on the diurnal cycle of shallow cumulus over land as observed on the SGP site of the ARM program near Oklahoma (Brown et al., 2002).

The use of LES results next to measurements in developing parameterizations significantly adds to the research possibilities. There is full control over all conditions in the simulated domain. This enables its use as a 'virtual' laboratory to study shallow cumulus: key-parameters can be altered over a certain range to study their impact on the system, while other conditions are kept constant. The availability of a range of different shallow cumulus cases for LES covering a wide parameter-space is certainly useful in this respect. The control over all conditions also means that in contrast to observations LES data can be reproduced exactly. Finally, LES offers almost unparalleled statistics, as the three-dimensional fields of the model variables are simulated at high spatial and temporal resolutions. Since the first simulations the use of LES has already led to important advances in boundary-layer parameterization (Moeng, 1998), such as quantitative descriptions of turbulence statistics, new PBL scaling laws, characteristics of plume-dispersion, and new bulk transport models for cloudy convection.

Nevertheless, one should always remain cautious when interpreting LES results, as the model is still a simplification of reality. The discretization of a continuous system involves numerical truncation errors, in particular in regions of strong gradients. For instance, Stevens et al. (1999) showed that in highly stable conditions LES results have shown moderate dependency on the resolution and the SGS model. Close to the surface the turbulent motions are of very small scales which are not resolved by the model, and hence LES is totally dependent on the SGS model in this layer (e.g. Mason and Thompson, 1992; Sullivan et al., 1994). Also, there is strong evidence that important processes like the mixing between clouds and environment occur at very small unresolved scales (De Roode and Bretherton, 2002; Stevens et al., 2002). Another problem is situated at the other end of the spectrum of resolved scales. As shown by Jonker et al. (1999a) and Neggers et al. (2002b), the limited size of the modelled domain in LES can significantly affect the geometric structure of the cloud population. It is reported that the growth of the dominating scales in the spectra of some scalars and (co)variances in the boundary layer can get limited by the domain size of the LES model (Jonker et al., 1997, 1999b). Finally, cloud micro-physics are still parameterized in LES. These results emphasize that the necessity remains to critically compare the cloud statistics as produced by LES to relevant observations in natural clouds.

2.2.3 Developing parameterizations

Comparing the typical time- and length-scales in Figure 1.7 indicates that boundary layer turbulence and cumulus convection are relatively small and fast processes compared to the slow advective forcing by the large-scale winds. Early energy spectra based on the observed windfield suggested that a clear spectral gap exists between the scales of forcing and boundary layer convection (Van der Hoven, 1957; Fiedler and Panofsky, 1970). This observation has been used as an excuse for the strict separation between the resolved and parameterized processes in GCMs, as it corroborates Reynolds' rules of averaging (Stull, 1988). However, a series of studies on kinetic energy spectra at a range of scales derived from various observational datasets have seriously questioned the existence of a true spectral gap (e.g. Vinnichenko, 1970; Nicholls and LeMone, 1980; Lilly and Petersen, 1983; Nastrom and Gage, 1983; Nucciarone and Young, 1991), see Figure 2.17.

Figure 1.7 shows that many atmospheric processes occur at intermediate scales between micro-scale cumulus convection and the macro-scale circulation, such as deep cumulus, cumulus congestus and large meso-scale convective systems like squall-lines. Furthermore, results have shown that certain dominating boundary layer scales themselves significantly grow in time (Jonker et al., 1997, 1999b). The presence of energy at intermediate scales complicates subgrid parameterization for GCMs, as it makes some phenomena partially resolved by the GCM.

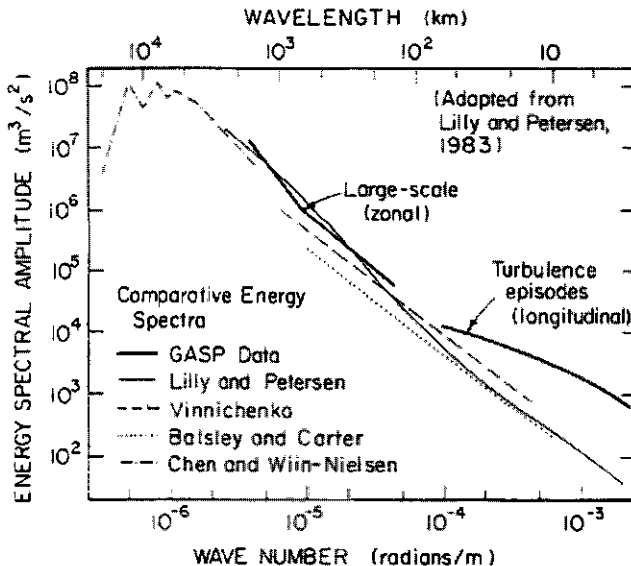


Figure 2.17 A comparison between several kinetic energy spectra derived from various observational datasets (from Nastrom and Gage, 1983). The NASA Global Atmospheric Sampling Program (GASP) is a dataset containing wind fields measured by commercial aircraft (Papathakos and Briehl, 1981). Also shown are the analyses on similar jetliner-data by Lilly and Petersen (1983), the free atmospheric data presented by Vinnichenko (1970), the surface Doppler radar data reported by Batsley and Carter (1982), and the radiosonde large-scale data of Chen and Wiin-Nielsen (1978).



Figure 2.18 Visualization of a single vertical column in the 3D mesh of a general circulation model (GCM).

The shallow cumulus clouds in this thesis are assumed to occur in relatively undisturbed conditions, without much activity on the meso-scales. The fast convective overturning by the many small cumuli quickly destroys any instability created by the slow changing forcings, establishing the quasi-equilibrium state as discussed before. This creates the image of large-scale forcing and small-scale cumuli strictly acting as dominating master and obeying slave. Nevertheless, this view is somewhat misleading. Averaged over a large domain the tendencies associated with the whole population of clouds are significant enough to counteract the forcings. Collectively the cumuli affect the large scale thermodynamic structure and circulation, which in turn affects the advective forcing. In other words, the interaction is not strictly down-scale: the presence of many slaves (the clouds) makes the master (the forcing) adjust his actions (Randall et al., 1997). The goal of parameterization is to capture this complex interaction.

A cumulus cloud is the result of many different interacting physical processes, such as vertical turbulent transport, cloud formation and dissipation, radiation, and occasionally precipitation. In order to effectively parameterize cumulus clouds in a GCM all these processes have to be modeled. Commonly they are bundled in a *single column model* (SCM), also known as a *one-dimensional (1D)* model. All modules act on a complete vertical column of gridboxes of the GCM, as cumulus convection in principle acts as a *vertical* redistributor of heat, moisture and momentum (see Fig.2.18). The SCM feeds on the gridbox-mean resolved variables and forcings, and the output is a vertical column of new values adjusted for the impact of shallow cumulus convection.

Developing 1D models requires detailed process studies. Reviews on the range of existing convective models and parameterizations and on the observations of the interaction between the large-scales and convection were presented by Cotton and Anthes (1989) and Emanuel (1994). In general all parameterizations have to meet certain generally accepted requirements as formulated by the Global Atmosphere Research Program (GARP) (World Meteorological

Organization, 1972). This report states that successful parameterization requires five steps:

- 1) Identification of the process,
- 2) Determination of the importance of the process for the large-scale flow resolved by the GCM,
- 3) Intensive case studies to get insight in the physics and dynamics involved in the process,
- 4) Formulation of quantitative rules for the location and the frequency of occurrence of the process,
- 5) The formulation of quantitative rules for the grid-box average effect of the process on mass, momentum, heat and moisture, and the verification of these rules by observations.

The chain of actions involved in the development of parameterizations as prescribed by these 'rules of engagement' is illustrated schematically in Fig.2.19. Several ways exist to approach this scheme. The **down-scaling** strategy starts with critically comparing the large scale fields as resolved by the GCM to global measurements. These can be in-situ observations during a field-experiment, measured climatological time-series by fixed meteorological surface-instruments (e.g. Mather et al., 1998; Mace et al., 1998), remotely sensed fields (e.g. Duynkerke and Teixeira, 2001), or any combination of datasets (e.g. Fiorino, 1998). These studies should bring to light typical situations in which the GCM persistently mispredicts reality. The performance of different GCMs for such problematic situations can then be evaluated in so-called *model intercomparisons*. Current intercomparison projects are the Atmospheric Model Intercomparison Project (AMIP I, see Gates et al., 1999) and the EUROCS GCM-intercomparison on the Pacific Hadley cycle (<http://www.knmi.nl/samenw/eurocs/>). The essence of the down-scaling method is that the performance of the GCM determines the issues of interest, and therefore specifies and directs the research on the subgrid scales. Another strong point of the down-scaling strategy is that the total impact of subgrid parameterizations in the GCM can be evaluated, including the interactions in the model between convective cloud representations and the large-scale circulation and climatology.

The evaluation of GCM results against observations may show what goes wrong in model predictions, but often does not reveal the cause behind these symptoms. Complex interactions and feedbacks between different processes and different scales obscure the transparency of the model. Another complication of the down-scale method is the relatively small number of field-experiments with the purpose of measuring the typical impact of SGS cloud processes on the large scales which have until now been organized. Some new field-experiments are planned in the near future, such as the Rain in Cumulus over the Ocean (RICO) experiment near Puerto Rico in the Atlantic Trade-wind region, scheduled to take place in 2004.

Fortunately, the last decades have seen a steady increase in the quantity and quality of data-sets on the *micro-scales* involved with boundary layer clouds, as discussed in the previous section. These new opportunities have caused meteorologists to specialize their primary field of research to these subgrid-scales. The new results and insights have inspired new parameterizations for processes on these scales, capturing more of the physics involved. The new parameterizations are subsequently tested along the prescribed scheme of Fig.2.19. This is an **up-scaling** approach, as it starts on the small scales and works its way up-scale. New parameterizations are first evaluated in isolated and controlled conditions such as an offline

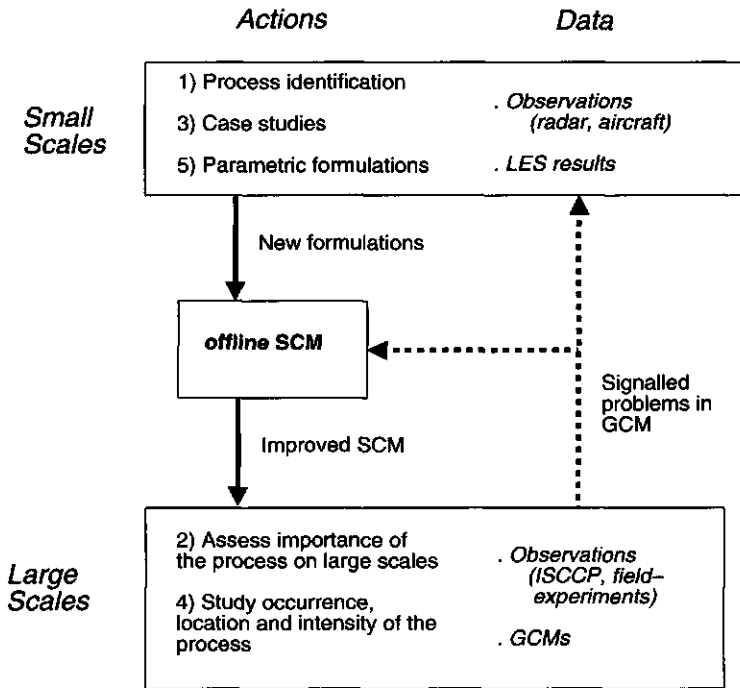


Figure 2.19 A schematic visualization of the actions and data on various scales which are involved in developing and improving parameterizations, according to the GARP scheme (see text). The dashed arrows represent the down-scaling steps, the solid arrows indicate the up-scaling actions.

SCM before being applied in GCMs, in order to fully evaluate their impact before becoming operational. These next-generation schemes are gradually replacing the first-order complexity parameterizations of the earliest GCM versions.

In practice both methods are used alongside each other. New ideas and concepts are constantly developed and formulated as parameterizations, while the NWP community continues to emphasize the critical situations which cause problems in the GCMs. The present-day SCMs are in a constant state of development and improvement, especially where shallow cumulus convection is involved.

2.3 Research topics

This section gives a brief overview of the research topics addressed in the next chapters. The existing theories and hypotheses on these issues are shortly described, and some methods of approach are introduced.

2.3.1 Validation of LES

Chapter 3 deals with the critical validation of LES results against measurements. As discussed in Section 2.2.2 LES is a model, which implies that although promising it is still only a simplified representation of reality. As a consequence, before using LES results in cumulus research, the capability of LES in reproducing the characteristics of natural cloud fields should be assessed. Although the characteristics of turbulence and dry convection as produced by LES have already been validated extensively, qualitative and quantitative comparisons of simulated cloud properties with reality are yet scarce. In the study presented here certain key-parameters often used in parameterizations of shallow cumulus are derived from both LES and an observational data-set suitable to this purpose, and are critically compared.

The Small Cumulus and Micro-physics Study (SCMS) is described in Section 2.2.1. The SCMS data-set is chosen for the LES validation because it provides a unique combination of a range of different measurements which make it suitable for this purpose. Meteorological stations were employed during the campaign measuring the surface fluxes, temperature and moisture. Radiosondes were released every 3 hours, providing the vertical thermodynamic profiles in the boundary layer. These observations describe the development of the boundary layer during the day, and hence enable the construction of an idealized case for LES. Furthermore, the C-130 aircraft of NCAR made detailed in-cloud measurements of turbulence and thermodynamics at many levels in the cloud layer. The number of sampled clouds was large enough to enable the calculation of statistically reliable cloud-averages from these measurements. Finally, high-resolution Landsat images were made of the SCMS area during the campaign, from which cloud size distributions are derived. This can answer the question if next to population-average properties LES is also capable of reproducing the typical geometrical build-up of the population itself.

2.3.2 Cloud population variability

Cumulus cloud fields consist of many clouds of different sizes, which are themselves inhomogeneous in structure (see Fig.2.5). These perturbations cover a whole range of length- and time-scales, and together make up the total *variability* of the cloud field. The parameterization of the variability of the key-variables in the shallow convective cloud field is a challenging problem. The first step is to characterize, quantify and visualize the typical variability, for which several possible methods exist.

A visualization method which gives insight in the characteristics of the higher statistical moments for shallow cumulus is the *conserved variable diagram* (Paluch, 1979). This is a scatter-plot of the values of of two variables conserved for moist adiabat ascent of all points on a horizontal slice of the domain. An example for the BOMEX case is plotted in Fig.2.20. One of the strong points of these diagrams is that the shape of the probability density func-

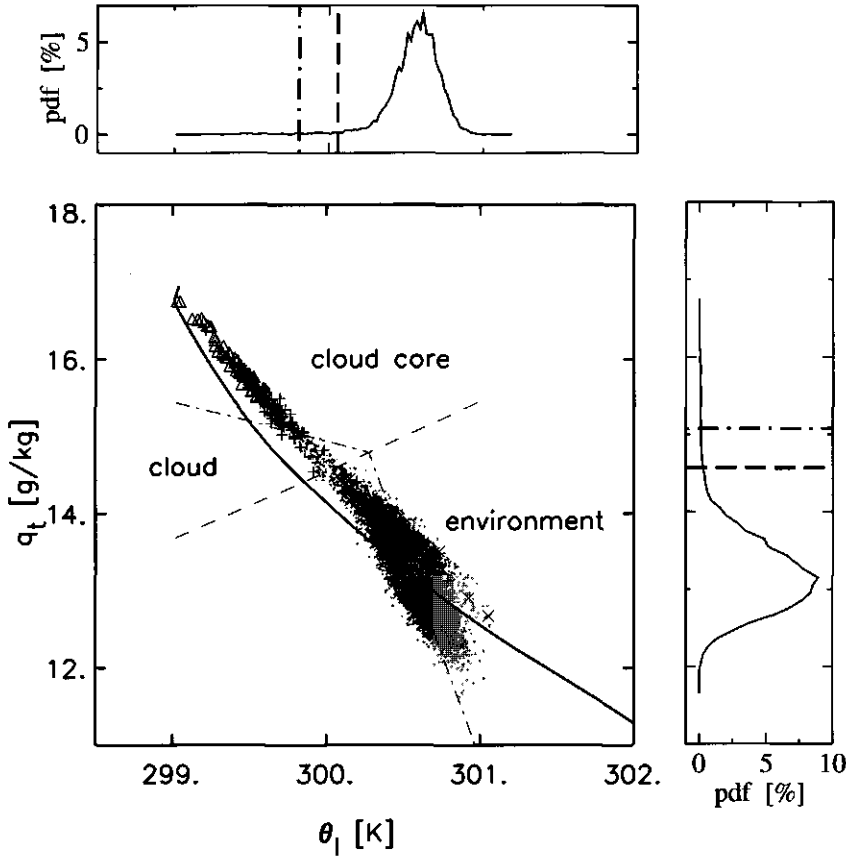


Figure 2.20 Conserved variable diagram at 1020m height of the BOMEX case. The vertical profile of the mean $\bar{\theta}_l$ and \bar{q}_t is plotted as a solid line, of which the subcloud layer values are situated in top-left corner of the plot. The dashed line is the saturation curve at this height, while the dash-dotted line is the line of neutral buoyancy relative to the mean state at this height. Points with $-1 < w < 1$ are plotted as a grey \diamond , $1 \leq w < 2$ as a $+$ and $2 \leq w$ as a \triangle , and $-2 < w \leq -1$ as a \times . The two side-panels show the probability density functions of the two variables.

tions (pdf) of the two variables can be clearly distinguished. The second statistical moment of the pdf is its width and is a measure for the variance, while the third moment represents the skewness of the pdf. The diagram immediately shows any cross-correlation between the two conserved variables. As the two variables are conserved for moist adiabatic motions, the typical shape of these "joint"-pdfs (Wyngaard and Moeng, 1992; Wang and Stevens, 2000) is the fingerprint of non-adiabatic processes, such as the dilution of cloudy updrafts by entrainment of environmental air. The plot can be sub-divided into distinct regions by plotting iso-lines representing a certain physical state: the saturation-curve separates the cloudy from the non-cloudy points, and combined with the zero-buoyancy line (Taylor and Baker, 1991) this defines the cloud-core. Finally, an extra dimension is added to the plot by indicating the

vertical velocity of the points with a color in a certain range. These diagrams then immediately show which points contribute most to the vertical turbulent transport: in the cloud-core high perturbation values of temperature and moisture are combined with high vertical velocities caused by positive buoyancy, which accounts for large fluxes. The use of the conserved variable diagrams is further discussed in Chapter 5.

A classical method to characterize the energy associated with the turbulent variability is to calculate power-spectra, see Fig.2.4. The spectrum is a decomposition of the total turbulent energy over the whole associated spectrum of scales, and its shape is characteristic for the physical processes taking place. Closely related to this spectral approach is the method of calculating *cloud size densities*, defined as the probability density function (pdf) of the number of clouds as a function of size. The cloud size density only represents a selection of the spectrum of turbulent motions, as it covers only those perturbations which have the shape of a cloud: it offers a geometrical characterization of the population variability. Several functional forms have been proposed to describe the cloud size density, see Fig.2.21b: a log-normal (Lopez, 1977), various power-laws (Cahalan and Joseph, 1989; Kuo et al., 1993; Benner and Curry, 1998), and an exponential (Plank, 1969; Wielicki and Welch, 1986). Due to the scarcity of detailed measurements of population statistics which cover a wide range of scales, it has not yet been possible to exclude any candidate for certain.

The size decompositions of other physical variables are based on the cloud size density. For example, relatively small clouds occur more frequently but cover a little area individually (see Fig.2.21a). Accordingly it is not trivial which cloud size dominates the total cloud fraction. As a consequence, knowledge on the cloud size density is useful in the parameterization of various physical processes. Firstly, the transfer of incoming solar radiation depends on

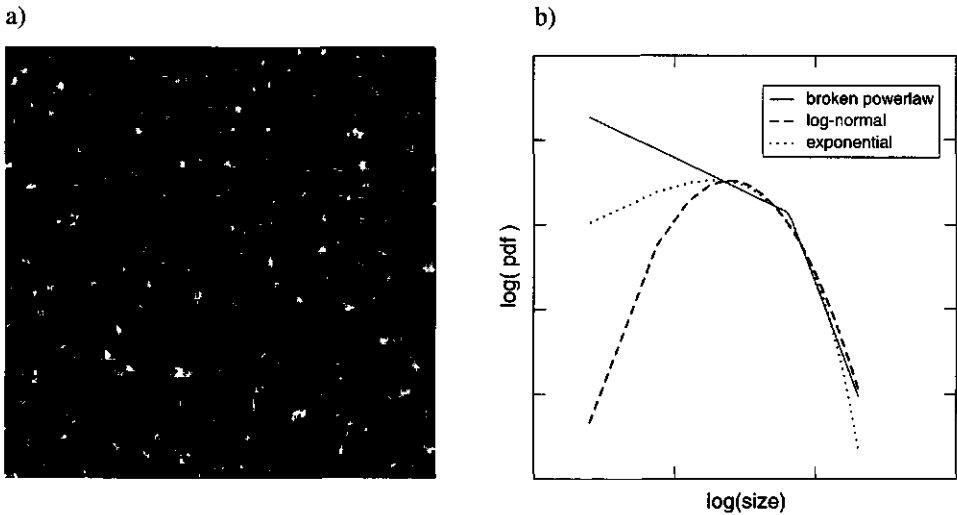


Figure 2.21 a) Top-view of a simulated cloud field of BOMEX, with an area of 25^2km^2 . b) Several formulations which have been proposed to describe the cloud size density of a shallow cumulus population.

this pdf, as large clouds reflect radiation differently than small clouds. Secondly, the vertical transport by a cloud likely depends on its size (e.g. Arakawa and Schubert, 1974). Chapter 4 deals more extensively with the issues related to the size statistics of shallow cumulus.

2.3.3 The mass flux approach

Early observational studies have shown that a large part of the cumulus domain consists of passive air. The region which dominates the vertical transport of a variable ϕ is concentrated in narrow, cloudy updrafts (e.g. Warner, 1970a, 1977). This has inspired the *mass flux* approach, based on the assumption of a simplified pdf (Ooyama, 1971; Betts, 1973; Yanai et al., 1973), see Fig.2.22. A decomposition is made in which the total domain is split up into two parts: the *cloud core* is defined as the area a^c which is positively buoyant as well as over-saturated, and the *environment* is the area $1 - a^c$ which does not meet this criterion. This results in a pdf which consists of only two possibilities, sometimes referred to as the "top-hat" approach: dealing with only two *domain-averages* implies that all remaining variability on subcloud scales is neglected (Wang and Stevens, 2000), which means that an imaginary horizontal trajectory of ϕ through this cloud resembles a top-hat profile. Typically the cloud core a^c covers a relatively small area compared to the environment, but is nevertheless associated with large perturbations in thermodynamics and vertical velocity, as is indicated by the skewness of the original pdfs, see Fig.2.20

How does the top-hat approach affect the turbulent flux-terms in the governing equations? The vertical flux of a variable ϕ at a certain level can be written as

$$\overline{w\phi} = a^c \overline{w\phi}^c + (1 - a^c) \overline{w\phi}^e. \quad (2.49)$$

The superscript c denotes the horizontal average over the cloud core, and e denotes the hor-

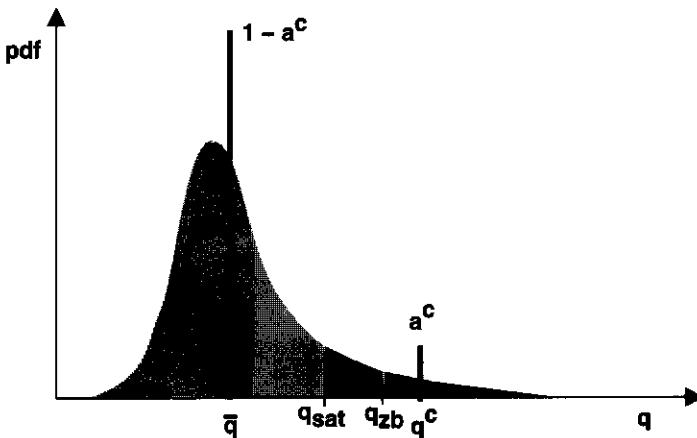


Figure 2.22 The two-peak pdf resulting from the 'top-hat' assumption. a^c is the area covered by the saturated, buoyant part of the pdf (darkest grey), and $1 - a^c$ the area covered by other air (middle grey). The height of the two peaks is identical to these areas. q_{sat} is the saturation specific humidity, and q_{zb} is the specific humidity at zero buoyancy in saturated conditions.

horizontal average over the environment. a^c is the fractional area occupied by the cloud core. Reynolds-averaging splits up a flux into an advective and a turbulent part (e.g. see Stull, 1988), which gives for (2.49)

$$\overline{w'\phi'} + \overline{w}\overline{\phi} = a^c(w^c\phi^c + \overline{w''\phi''^c}) + (1-a^c)(w^e\phi^e + \overline{w''\phi''^e}) \quad (2.50)$$

where the superscript $'$ denotes a perturbation from the horizontal domain-average and $''$ denotes a perturbation from the core- or environmental average. In the top-hat approach the $''$ terms are neglected, by which only the terms remain which represent the more organized part of the turbulent flux. Equation (2.50) can then be rewritten as an function of only top-hat averages (Ooyama, 1971; Betts, 1973; Yanai et al., 1973),

$$\overline{w'\phi'} \approx M^c(\phi^c - \phi^e) \quad (2.51)$$

where the core mass flux M^c is defined as

$$M^c \equiv a^c w^c. \quad (2.52)$$

Here we assumed $\overline{w} = 0$, based on observations in reality and on LES results that a shallow

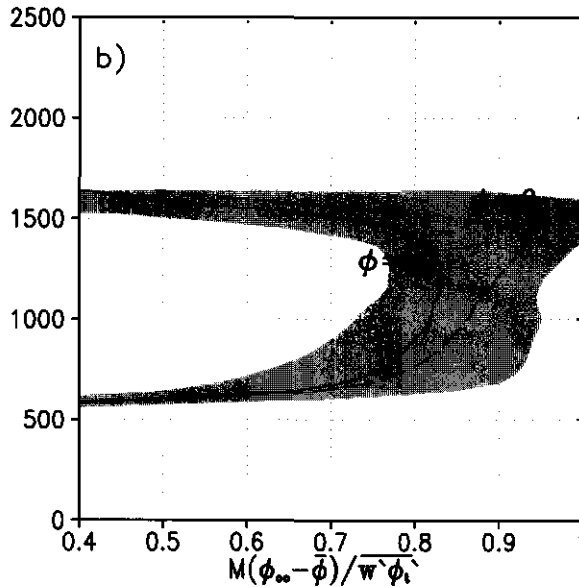


Figure 2.23 LES intercomparison results on the BOMEX case for the ratio of the mass flux approach to the resolved turbulent flux (from Siebesma et al., 2002). The solid line marks the average over all codes participating in the intercomparison for $\phi = q_f$, and the dashed line for $\phi = \theta_f$. The width of the grey band is the standard deviation over the various LES codes.

cumulus cloud field consists of many closed convective cells. Also, a^c is assumed to be much smaller than 1, which is supported by many observations. LES results have shown that (2.51) reproduces about 80% of the total turbulent flux in the cloud layer, see Fig.2.23.

The advective part $\overline{w\phi}$ is a product of averages on the scale of the GCM gridbox, which are resolved by the model. The turbulent flux by subgrid-scale motions $\overline{w'\phi'}$ is the unknown in the equation, and has to be parameterized. Equation (2.51) is the starting point of the *mass flux model* (Betts, 1973; Tiedtke, 1989). To close the scheme the profiles of M^c , ϕ^c and ϕ^e in the cloud layer have to be provided. The full version of the mass continuity equation (2.26) is conditionally averaged in order to write the change with height of the mass flux of the cloudy part in terms of lateral *entrainment* and *detrainment* rates E and D ,

$$\frac{\partial a^c}{\partial t} = -\frac{\partial M^c}{\partial z} + E - D \tag{2.53}$$

(Arakawa and Schubert, 1974). It is assumed for the moment that density ρ is constant. Here E indicates the rate of mixing of environmental mass into the cloud per time-unit, and D vice versa. E and D can be written in terms of the *fractional* entrainment and detrainment rates ϵ and δ relative to the total mass flux,

$$E \equiv \epsilon M^c \quad D \equiv \delta M^c. \tag{2.54}$$

Here ϵ and δ are inverse mixing-length scales. Assuming the cloud fraction a^c to be in steady state results in an equation for the change of mass flux with height,

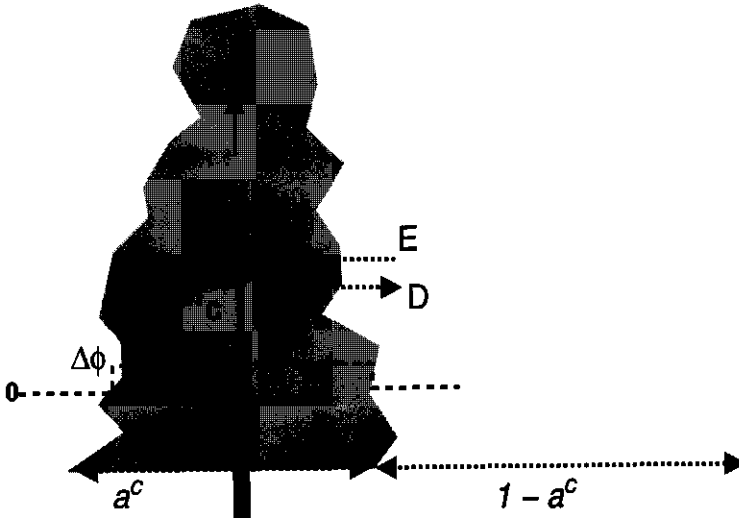


Figure 2.24 Schematic view of the mass flux model. The cloudy area a^c is visualized as one big cloud. The dashed line represents a trajectory of $\Delta\phi = (\phi - \bar{\phi})$ through the cloud, resembling the profile of a top-hat. The mass flux changes with height due to lateral entrainment and detrainment.

$$\frac{1}{M^c} \frac{\partial M^c}{\partial z} = \varepsilon - \delta. \quad (2.55)$$

Integration of this equation gives the vertical profile of the mass flux, and in combination with (2.51) this finally results in the vertical profile of the turbulent flux in the cloud layer. Integration of (2.55) still requires knowledge on the intensity of the mixing processes represented by ε and δ , as well as the mass flux at cloud base M_b^c , see Fig.2.24. These free parameters in the model are the subject of ongoing research, shortly described in the next two sections.

2.3.4 Cloud Mixing Theories

It is evident from (2.55) that mixing processes affect the mass flux in the cloud layer, and accordingly it is an important issue in cloud parameterization. However, the mixing process between clouds and environment is extremely difficult to measure in natural clouds, as it takes place at the boundaries of the clouds which continuously change shape. As a consequence, more indirect methods have to be used to quantify and characterize the mixing between clouds and their environment.

A range of conceptual models for cloud mixing have been formulated, resulting from a long period of research starting with the work of Stommel (1947). Recent reviews on the various mixing models were published by Blyth (1993) and Siebesma (1998). The first laboratory-experiments to study mixing processes between thermals and their environment were performed in the 1960s (e.g. Turner, 1962; Simpson, 1965). Positively buoyant single plumes were released in laboratory tanks in a neutral or slightly stable environment, and were colored with a certain dye to distinguish them from their surroundings. This visualized the amount of environmental air which was *entrained* by the rising plume. These studies revealed an inverse proportionality between the fractional entrainment rate and plume radius,

$$\varepsilon_r = \frac{2\alpha}{R}, \quad (2.56)$$

where α is a constant of proportionality, usually set to 0.1 which results in an entrainment rate of the order of magnitude 10^{-4}m^{-1} . This relationship found its way into many parameterizations (e.g. Squires and Turner, 1962; Simpson and Wiggert, 1969; Simpson, 1971; Arakawa and Schubert, 1974).

It is important to realize that the entrainment rate of single plumes or clouds is not equivalent to the population-average or *bulk* entrainment rate defined by (2.37) which is needed in the mass flux model. Later observational and LES studies have shown that the bulk entrainment rate is typically one order of magnitude larger, at about $\varepsilon = 2 \cdot 10^{-3} \text{m}^{-1}$ (Raga et al., 1990; Siebesma and Cuijpers, 1995). As a first-order approach the bulk entrainment rate is assumed to be constant with height in many mass flux models (Tiedtke, 1989), but recently LES results have shown that it decreases with height (Siebesma and Cuijpers, 1995). The aircraft which took in-cloud measurements during the SCMS campaign sampled many clouds for a long period of time, which enables the calculation of statistically reliable bulk entrainment rates. The results are presented in Chapter 3.

The conserved variable diagram reveals much about non-adiabatic processes such as mixing. Extracting the mechanism of mixing from these figures implies finding the source of the

entrained air present inside clouds. This has led to the concept of spanning *mixing lines* in these figures between undiluted subcloud air and the source of the entrained air. However, there is no consensus on the results of this method. Generally the opinions vary between strictly vertical mixing between cloudbase air and cloudtop air, and strictly lateral mixing between incloud air and the local environment at that height. One of the reasons for this disagreement is the fact that various different conserved variables for moist adiabatic ascent are in use. In studies of deep convection, the *equivalent* potential temperature θ_e is commonly used as a conserved variable (Emanuel, 1994),

$$\theta_e \approx \theta + \frac{L}{c_p \Pi} q_v \quad (2.57)$$

As deep cumulus clouds reach great heights where the specific humidity is very low, any vertical sounding has a distinct curve in a (θ_e, q_t) diagram. This facilitates the visualization of non-adiabatic processes. Also, great fluctuations in the specific humidity occur in deep cumuli due to the formation, fall-out and evaporation of precipitation, which may favour the use of θ_e in order to study deep cumulus dynamics and micro-physics. However, comparing (2.57) to (2.10) shows that the difference between θ_e and θ_l is a function of the total specific humidity q_t , which is also a conserved variable for moist adiabatic ascent. θ_e is therefore the sum of two variables which are conserved themselves. As a consequence, when plotted in a θ_e, q_t frame the mixing line of shallow cumulus as visible in a θ_l, q_t diagram (see Fig.2.20) is misleadingly well-correlated (e.g. Taylor and Baker, 1991), due to the correlation of q_t with itself.

The conserved variable diagram has been an inspiration for the formulation of so-called *multi-parcel* methods. These models consist of a distribution of different parcels which are to predict each point in the diagram (e.g. Telford, 1975; Raymond and Blyth, 1986; Kain and Fritsch, 1990; Hu, 1997). In Chapter 5 a new multi parcel model for shallow cumulus is presented. The mixing rate of a rising updraft-parcel is formulated as a relaxation or adjustment term,

$$\epsilon_w = \frac{1}{h_p} = \frac{1}{\tau_p w_p}, \quad (2.58)$$

where h_p is the mixing depth of the parcel, τ_p its a turn-over time-scale, and w_p its vertical velocity. LES results indicate that τ_p is constant for all updrafts, which makes the mixing rate inversely proportional to the vertical velocity. This represents a feedback between mixing and dynamics. It is shown that a distribution of rising parcels obeying this deterministic relation reproduces the typical increasing variability of the temperature, moisture and vertical velocity with height in the cloud layer. The only free parameters in the multi parcel model are the initial conditions and those of the surrounding environment, acting as a background with which the parcels interact.

2.3.5 Cloud-subcloud interactions

The closure of the mass flux at cloud base M_b^c in (2.55) provides the possibility to couple the physics and dynamics of the cloud layer with those of the subcloud layer. It is evident from

observations that these two layers strongly interact (e.g. Ogura and Cho, 1974; Esbensen, 1975; LeMone and Pennell, 1976; Betts, 1976). Without the subcloud layer the clouds can not exist, as the cloudy thermals are observed to originate close to the earth's surface (Emanuel, 1997). On the other hand, the cumulus clouds themselves are strongly accelerated by local latent heat release, which affects the connecting updrafts under the clouds due to continuity. Also, the compensating subsidence induced by the convective updrafts warms and dries the cloud layer and feeds back on the subcloud layer at cloud base. These complex interactions between cloud- and subcloud layer should be represented well in a proper closure of the mass flux at cloud base.

A range of closure-methods exists, based on different principles. In general all methods originate from two conceptual views on the cloud-subcloud interaction, see Fig.2.25. In the first view the cumulus clouds are assumed to be driven by forced convection, controlled entirely by the dry convection in the subcloud layer which is driven by the surface heat fluxes. The clouds are simply seen as overshooting thermals which condensate and quickly stop rising. In contrast, the second view favours the idea that the interaction is controlled by the moist convection in the cloud layer itself. The latent heat release in the clouds is thought to be of such intensity that the resulting vertical accelerations control the inflow of air from the subcloud layer. In this view the moist convection is rather thought of as an autonomous, self-sustaining system: the mass flux at cloud base is totally induced by the convection in the cloud layer itself.

In reality, both mechanisms probably cooperate, the one sometimes being more dominant than the other. For example, a diurnal cycle of cumulus over land normally starts with a very shallow cloud layer in which the convection is totally forced. At some stage the shallow clouds become deep enough to reach their level of free convection, see Fig.2.2a. At an even later stage the shallow convection may progress into deep convection, which can be thought of as such an intermediate situation in which both mechanisms of interaction play a role. Finally, fully developed deep convection is dominated by cloud-associated physics like CAPE-consumption and the formation and evaporation of precipitation, in such a degree

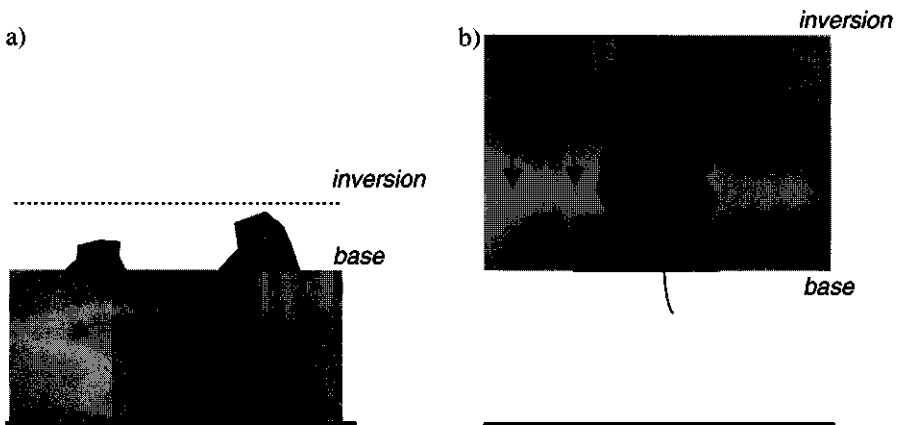


Figure 2.25 The two basic views on the cloud-subcloud interaction. a) Forced cumulus convection by the subcloud layer turbulence and b) free cumulus convection driven by latent heat release.

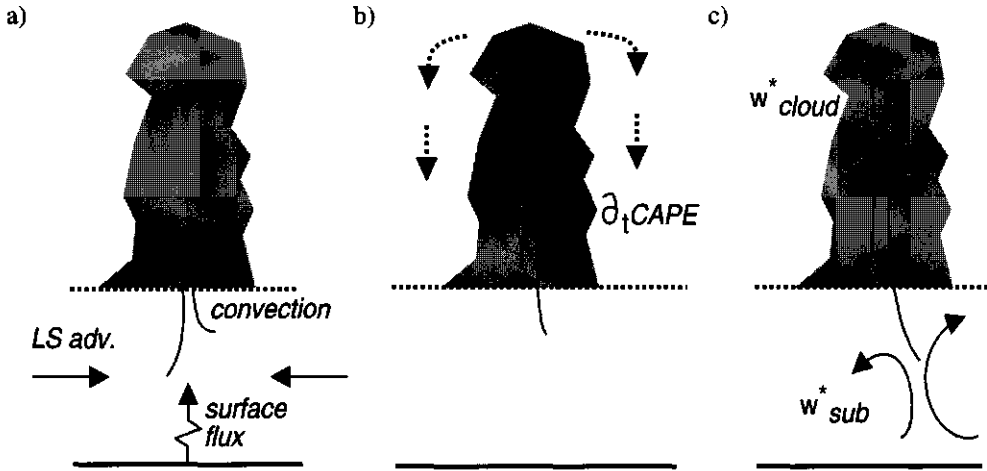


Figure 2.26 Schematic illustrations of the three mass flux closures. a) The boundary layer equilibrium closure, using subcloud moisture convergence. b) The CAPE adjustment closure. c) The closure based on vertical velocity scales.

that the dry subcloud layer plays no longer a serious part other than perhaps in the initiation or "triggering" of the deep convective event. Chapter 6 deals with the performance of three well-known mass flux closures. First the parameters on which the closures are built are sampled in LES during a diurnal cycle of shallow cumulus. This results in time-series of the mass flux at cloud base as predicted by the closures. Comparing this to the real cloud base mass flux in LES immediately shows the characteristic (mis)behaviour of the closures. With these results in hand the closures are implemented in a single column model, and their impact on the development of the boundary layer is studied.

The first mass flux closure which is studied evolved from the outcome of a series of cumulus field-experiments in the oceanic Trade-wind regions (BOMEX, ATEX). Budget studies based on such datasets (Augstein et al., 1973; Holland and Rasmusson, 1973; Ogura and Cho, 1974; Esbensen, 1975) have shown that the moisture-tendency in the subcloud layer is typically negligible. This implies that the moisture flux at cloud-base is equal to the moisture flux at the surface plus lateral advection at the sides of the domain, a situation referred to as *moisture convergence* (Kuo, 1965, 1974; Tiedtke, 1989). As the mass flux at cloud base is exclusively coupled to subcloud-layer properties, this closure belongs to the first type of closures. In contrast to marine situations the boundary layers over land are not in equilibrium: significant tendencies of temperature and moisture are typically observed during the course of the day. The question is how this closures perform in those situations.

The quasi-equilibrium assumption states that any instability created by the slow changing large-scale forcings is quickly destroyed by fast process of cumulus convection (e.g. Arakawa and Schubert, 1974; Randall et al., 1997). Adjustment schemes associate a typical relaxation timescale with this process, relaxing the system towards a certain reference state (e.g. Manabe et al., 1965; Betts and Miller, 1986a,b). For a more elaborate review of closures based on this method see for instance Emanuel (1994). The scheme developed by Fritsch and Chappell

(1980) goes a step further by assuming that all CAPE adjustment is done by the compensating subsidence induced by the cloud ensemble, as it destroys the existing instability in the cloud layer by warming and drying. This method therefore belongs to the class of closures which links the mass flux at cloud base to the properties of the cloud layer. The closure dictates the cloud base mass flux which is *required* to totally break down the CAPE present in the cloud layer by compensating subsidence in a given time-scale τ . This causes problems when the moist convection is forced or when the convection gets limited by the decreasing surface fluxes at the end of a diurnal cycle.

The third closure has a more kinematic nature, as it couples the cloud base mass flux to the *turbulent velocity scale* of the subcloud layer, w_{sub}^* . There are several ways to derive this formulation. (Grant, 2001) integrated a simplified TKE equation over the depth of the subcloud layer and used the cloud base mass flux as a velocity scale in the TKE transport term at cloud base. Secondly, as the mass flux the product of the cloud fraction and the vertical velocity it can directly be scaled with w_{sub}^* . Both approaches result in a linear dependency of the cloud base mass flux on w_{sub}^* , the only difference being that the latter form also includes the cloud fraction. The validity of linking the cloud vertical velocity at cloud base to the subcloud TKE is evaluated in Chapter 6, using LES results. An advantage of this closure is the possibility to use a combination of appropriate velocity scales, based on both cloud- and subcloud layer properties. Basically this would make the closure a superposition of both conceptual views on the interaction.

Chapter 3

A validation of LES against observations by aircraft and Landsat during SCMS

Neggers, R. A. J., P. G. Duynkerke and S. M. A. Rodts. *Accepted for publication in the Quarterly Journal of the Royal Meteorological Society pending minor revisions, August 2002.*

3.1 Summary

Large-eddy simulation (LES) results of shallow cumulus convection are directly evaluated against in-cloud aircraft-measurements, as made during the Small Cumulus Microphysics Study (SCMS). To this purpose an LES case is first constructed, based on available observations. Then the simulations are directly compared to the in-cloud measurements by using conditionally sampled fields. An advantage of the SCMS data-set is the combination of a range of different surface measurements, in-cloud measurements by an aircraft at many levels in the cloud layer, and the availability of high-resolution Landsat images.

The results show that given the correct initial and boundary conditions the LES concept is capable of realistically predicting the bulk thermodynamic properties of temperature, moisture and liquid water content of the cumulus cloud ensemble as observed in SCMS. Furthermore the vertical component of the in-cloud turbulent kinetic energy and the cloud size distribution in LES were in agreement with the observations. These results support the credibility of cloud statistics as produced by LES in general, and encourage its use as a tool for testing hypotheses and developing parameterizations of shallow cumulus cloud processes.

Several hypotheses which make use of conditionally sampled fields were tested on the SCMS data. The magnitudes and the decrease with height of the bulk entrainment rate following from the SCMS data confirm the typical values first suggested by Siebesma and Cuijpers (1995) using LES results on BOMEX. An alternative formulation of the lateral entrainment rate as a function of the liquid water content and the mean lapse rate agrees well with the original form based on the conserved variables. Applying the simplified equation for the cloud vertical velocity (Simpson and Wiggert, 1969) to the aircraft-measurements results in a reasonably closed budget.

3.2 Introduction

Trade-wind cumulus cloud fields cover up to 30% of the total area of the globe. Although the typical cloud fraction in the Trades of about 20–40% is relatively low, shallow (non-precipitating) cumulus clouds are vital in the vertical transport and distribution of thermodynamics and momentum over the depth of the boundary layer. Several impact studies on shallow cumulus convection in general circulation models have increased the awareness in the numerical weather prediction (NWP) community that it plays a key role in feeding and maintaining the tropical Hadley-circulation. Existing parameterizations in the general circulation models (GCM) still have great difficulty in representing shallow cumulus correctly, and are in need of significant improvement. In order to improve our understanding of the physical processes behind this type of convection, several measurement campaigns have been organized in the past in which the cloud fields were studied in many different ways (e.g. Brown et al., 2002; Stevens et al., 2001; Siebesma et al., 2002).

Parameterizations of shallow convection in GCMs are to represent the thermodynamic and turbulent state of whole cloud populations in a single GCM grid-box. A common approach in many single column models (SCM) is to make a decomposition between cloudy and non-cloudy air, and to predict the vertical profiles of the average properties of these two fractional areas (Asai and Kasahara, 1967; Tiedtke, 1989). This method is also known as the 'top-hat' approach. Applying such a decomposition on data is known as *conditional sampling*. It is important to realize that the vertical profiles of these top-hat averages are controlled heavily by the changing cloud population with height (as large clouds reach greater heights than small clouds). Unfortunately, the typical low cloud cover of shallow cumulus complicates the derivation of reliable cloud-ensemble averages from aircraft-measurements, simply because typically too few clouds are sampled. Raga et al. (1990) presented cloud-averages based on aircraft measurements in seventeen active cumulus clouds only.

In the last decades, large-eddy simulation (LES) has become an important new tool in boundary layer research. It can provide data which is almost impossible to measure directly in natural cloud fields. It has already been used widely to study the turbulent structure of clear and cloudy boundary layers. A series of intercomparison studies as part of Global Energy and Water-cycle Experiment (GEWEX) Cloud System Studies (GCSS) and EUROCS showed that most existing LES models agree on the basic structure of shallow cumulus cloud layers (Siebesma et al., 2002; Stevens et al., 2001; Brown et al., 2002). An important advantage of using LES in studying the conditionally sampled properties of shallow cumulus cloud fields is that it provides complete instantaneous three-dimensional fields with a reasonably high resolution. Several budget studies of conditionally sampled properties using LES have already been published (Schumann and Moeng, 1991a,b; Siebesma and Cuijpers, 1995; Wang and Stevens, 2000; De Roode and Bretherton, 2002).

However, despite these encouraging results, some important LES results on cumulus clouds still remain unsupported by observations, mainly caused by the scarcity of suitable in-cloud measurements. For example, after the many intercomparisons mentioned above, there has still not been a qualitative comparison of the in-cloud thermodynamics and turbulence as produced by LES with direct measurements inside natural shallow cumulus clouds. Another LES result yet unsupported by measurements is the typical decrease of the cloud fraction with height in simulated cumulus cloud fields. But perhaps the most important issue

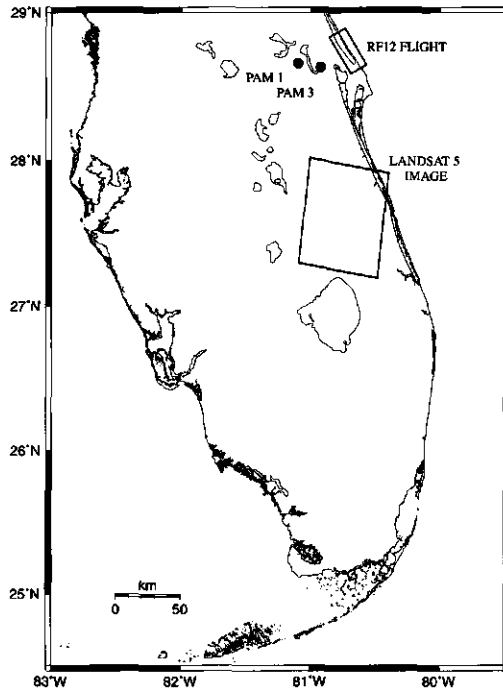


Figure 3.1 A map of Florida. The SCMS campaign was situated near Cocoa Beach, Cape Canaveral. The ground-stations PAM1 and PAM3 are indicated by the black dots. The radiosondes were released in the close vicinity of the PAM3 station. The area of flight RF12 and the area covered by the Landsat 5 image are indicated by the rectangles.

in the parameterization of cumulus convection is the interaction or mixing between shallow cumulus clouds and the dry air of their surrounding environment (Arakawa and Schubert, 1974). To describe the changing conditionally sampled profiles with height, a *bulk* mixing rate has to be used which is an average over the whole ensemble of clouds (Simpson and Wiggert, 1969; Gregory, 2001). The little observational evidence yet presented for these kind of bulk entrainment rates shows that it has to be in the order of magnitude 10^{-3} m^{-1} (Raga et al., 1990; Barnes et al., 1996).

These issues emphasize that thorough and critical evaluation of LES results against measurements inside real clouds remains necessary for a better understanding of the strong and weak points of LES. This paper describes such an attempt, using direct in-cloud aircraft-measurements of turbulence and thermodynamics during the Small Cumulus and Microphysics Study (SCMS) in Florida in 1995. In the experiment, many clouds of different size were sampled at all levels in the cloud layer. An LES case is constructed based on data from surface-instruments and radiosondes of a certain day during this campaign, on which a diurnal cycle over land was observed. It features a steadily growing clear convective boundary

layer in the morning, resulting in a well-developed cumulus cloud layer later on the day. Of both the LES and the aircraft data, conditionally sampled averages of first and second order moments of thermodynamic and turbulent properties are calculated. Based on these results, bulk entrainment rates and some other well-known parameterizations are derived and evaluated. Finally, several cloud size distributions are calculated in LES. These are compared to distributions derived from high-resolution Landsat images of the SCMS area.

The instrumentation as well as the observations of the diurnal cycle are described in Section 3.3. The LES case constructed on these data is presented in Section 3.4. The methods of conditional sampling as used for the observations and for LES are discussed in Section 3.5. Several parameterizations which will be tested in LES and the data are described in Section 3.6. The results are presented in Section 3.7. Finally a discussion and conclusions can be found in Section 3.8.

3.3 Instrumentation and observations in SCMS

The Small Cumulus Microphysics Study (SCMS) took place from July 17 until August 13, 1995 in Florida, near Cocoa Beach just north of Cape Canaveral (see Fig.3.1). On August 5th a clear convective boundary layer over land developed in the early morning. It deepened in time, and during the course of the morning a shallow cumulus cloud layer developed. The clouds were categorized as shallow non-precipitating cumulus with a cloud fraction of 10-20 %. This particular 'golden day' was part of a period in which persistently every day a shallow cumulus topped boundary layer developed. Observations of the geometrical and micro-physical structure of the cumulus clouds in this period in SCMS have been reported by Knight and Miller (1998) and French et al. (1999). The large scale conditions did not change significantly during this period, nor were they very large compared to the local forcing by the surface fluxes. These conditions make the 5th of August a suitable day on which to base an LES case. This section describes the instruments and measurements of SCMS which are relevant for the setup of the LES case and for the comparison between the model and observations.

Two portable meteorological stations of the flux-PAM type were employed in the SCMS campaign, for a detailed description see Horst and Oncley (1995) and Miltzer et al. (1995). They were situated about 50 km inland to the west of Cape Canaveral (see Fig.3.1). The near-surface fluxes of momentum and virtual temperature are measured by eddy-correlation, using a 3-component sonic anemometer. The water vapour flux is calculated from the directly-measured virtual heat flux by means of a 'virtual' Bowen ratio, measured as the ratio of the virtual heat flux to the water vapour flux. The water vapour flux can then be used to extract the sensible heat flux from the measured virtual heat flux. Figure 3.2 shows that clearly an imbalance exists in the PAM3 measurements between the incoming net-radiation plus the soil heat flux on one side and the latent plus sensible heat flux on the other. What causes this gap is unknown. Temperature and humidity are measured at a height of 2 m with a Vaisala 50Y Humitter that includes a platinum-resistance thermometer and a solid-state capacitance sensor for relative humidity. The corresponding timeseries are plotted in Fig.3.3. Near the PAM 3 station radiosondes were released at intervals of approximately 3 hours, giving the vertical profiles of the temperature, specific humidity, wind-direction and wind-speed (see

Fig.3.4). This range of measurements is used to align the LES case to reality, as will be described in section 3.4.

The C-130 operated by the National Center for Atmospheric Research (NCAR) carried instruments measuring turbulence, thermodynamics and microphysics. A detailed description of the instrumentation on this aircraft and the statistical quality of the resulting cloud-averages is given by Rodts et al. (2002). The liquid water content (q_l) of the clouds is obtained from a Particle Volume Monitor (PVM). The details of this method and its application in SCMS have been published by Gerber et al. (2001), and will therefore not be described in great detail here. Flight RF12 on August 5 started at 18:00 UTC and lasted until 21:00 UTC. Immediately after take-off, the aircraft made a vertical sounding up to 4 km, giving the vertical profiles of the temperature and specific humidity in the flight area. This was followed by a descent to lower altitudes where the clouds were located. Three consecutive hours of measurements through the whole cloud layer then followed. The area of the flight-path is shown in Fig.3.1.

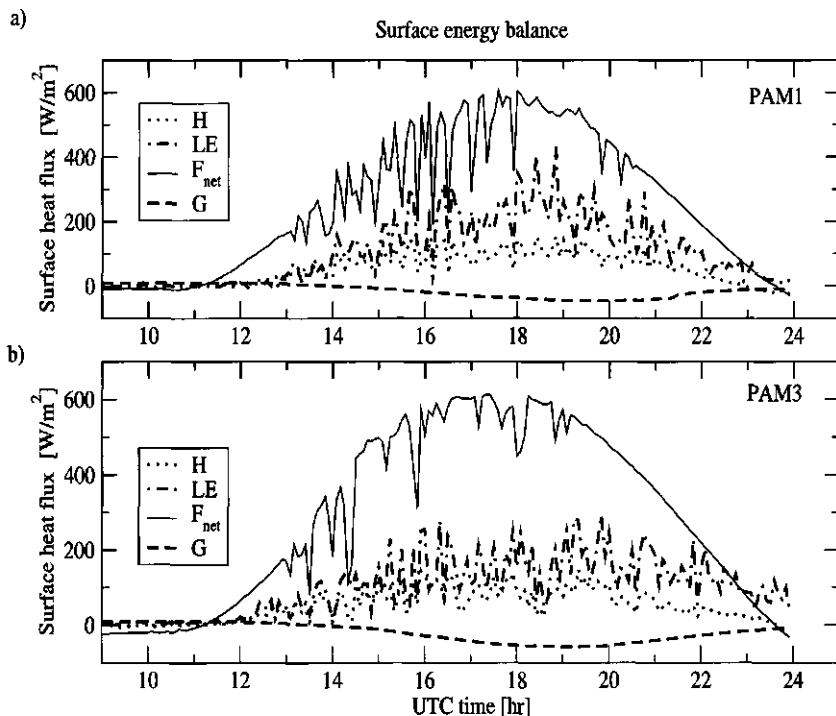


Figure 3.2 Measured time-series of the of the latent (LE) and sensible (H) surface heat fluxes at a) PAM1 and b) PAM3 on August 5, 1995. For completeness the net incoming radiation (F_{net}) and the soil heat flux (G) are also plotted.

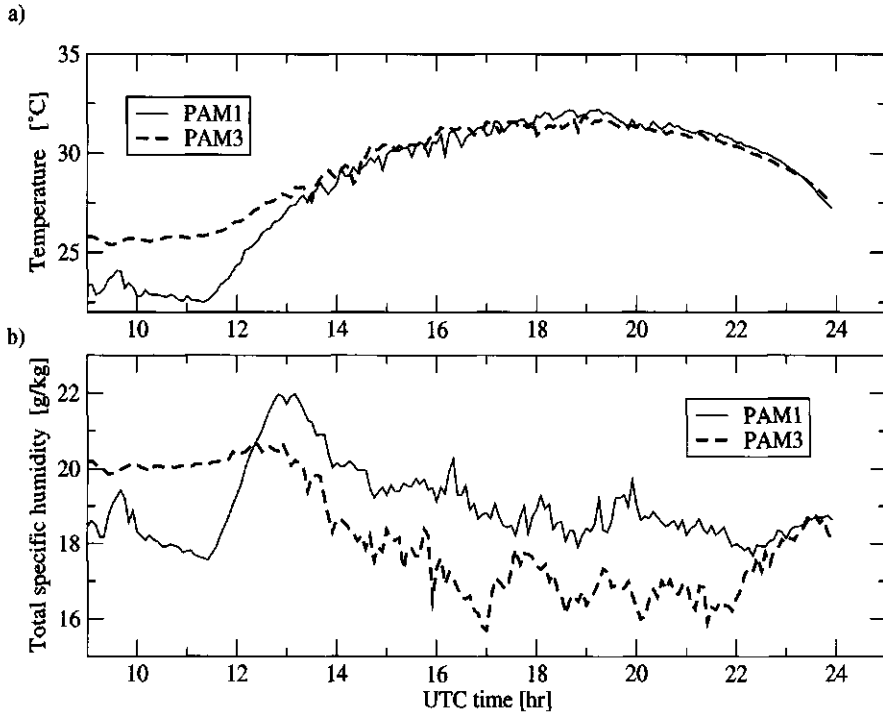


Figure 3.3 Measured time-series of a) the temperature (T) and b) the total specific humidity (q) at 2m height at PAM1 and PAM3.

These measurements are used to calculate conditionally averaged profiles in the cloud layer, as will be described in section 3.5.

On August 10, 1995 high-resolution images were taken of the cloud fields over Florida by the Landsat 5 satellite. These images can be used to calculate so-called *cloud size densities*, or the probability density function of the cloud population as a function of cloud size. Cloud size densities have been calculated in the past of many observed cloud populations, using a variety of methods (e.g. Plank, 1969; Wielicki and Welch, 1986; Cahalan and Joseph, 1989; Benner and Curry, 1998). The availability of high-resolution Landsat images of the SCMS area as well as an LES case directly based on (almost) simultaneous observations enable a direct and straightforward comparison between the simulated and observed cloud size densities (e.g. Neggers et al., 2002b). Only the images of August 10 were available to us, which is 5 days later than the day selected for simulation. Nevertheless, the large scale conditions did not change significantly during the period of 1-15 August, and the diurnal development of the shallow cumulus clouds was observed to be roughly the same every day. The method of calculation of the cloud size densities is described in Chapter 4. A more thorough analysis of

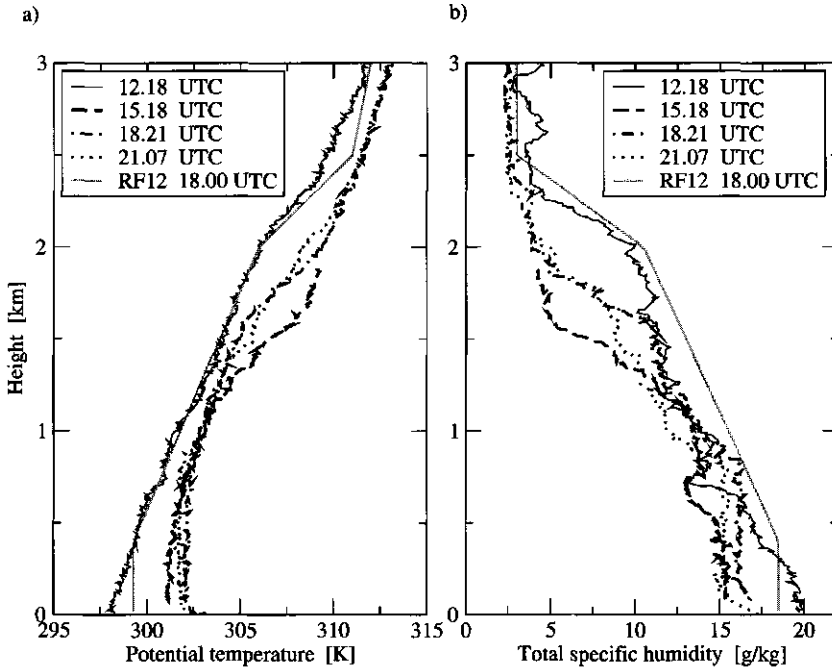


Figure 3.4 Radiosonde soundings of a) the potential temperature and b) the total specific humidity near station PAM3. The idealized profiles based on the vertical ascent of flight RF12 at 18:00 UTC are also shown for comparison.

the cloud size densities which can be obtained from this Landsat image is presented by Rodts et al. (2002). The image was taken at 14:53UTC. The size of the area captured by the image is 68.5km squared, with a horizontal grid-spacing of 30m. 8402 individual cumulus clouds were captured by the image.

3.4 Setup of the LES case

The aim is to construct a case for LES of which the development in time stays as close as possible to the range of different kind of measurements made during the day. Once that is achieved, the resulting cloud properties can be studied and compared to the available in-cloud observations in detail. Therefore, let us first consider the initial profiles of the two basic thermodynamic variables, the potential temperature (θ) and the total specific humidity (q_t). The vertical soundings by the radiosondes and the aircraft are used to this purpose. Figure 3.4 gives an overview of all radiosonde profiles. Also plotted is the idealized profiles derived from the aircraft sounding at 18:00 UTC. It is clear that the latter sounding is about 2K cooler and 2 g/kg more moist than the radiosonde sounding of the inland-station PAM 3 at the

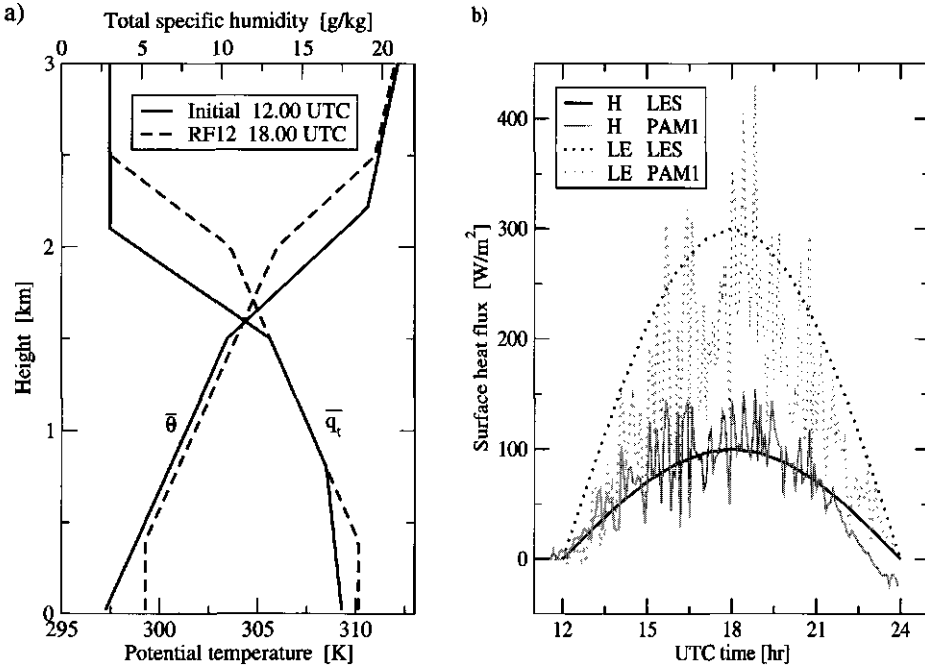


Figure 3.5 a) The initial profiles for LES at 12:00 UTC of the potential temperature θ and the total specific humidity q_t of the SCMS case. The idealized profiles based on the vertical ascent of flight RF12 at 18:00 UTC are also shown for comparison. b) The surface latent and sensible heat fluxes as measured by PAM3, as well as the corresponding values imposed on LES as a boundary condition.

corresponding time, over the whole depth of the boundary layer. This must be due to the close proximity of relatively cool and moist sea-air. The second significant difference between the aircraft- and the radiosonde profile at 18:00 UTC is that the inversion height in the flight area is about 500m higher. The final remarkable feature in the radiosonde soundings is the decrease of the inversion height between 12:18 and 15:12 UTC. In the successive radiosonde soundings, the inversion clearly rises in time.

Fortunately the lapse-rates in the conditionally unstable layer and the inversion in the two different soundings agree very well (see Fig.3.4). A problem however is the observed initially sinking inversion, because it can never be explained by a developing convective boundary layer which is driven by increasing surface heat fluxes in time. In that case the inversion height would only increase. The sinking inversion in this particular period may perhaps be caused by by some residual layer which is still present in the morning. In any case, the LES model can not be expected to resolve this sinking inversion in the early hours, and accordingly it is neglected. The initial inversion height is obtained by estimating the growth of the inversion height between 12:00 and 18:00 UTC from the radiosonde soundings and subtracting it from the inversion height in the aircraft sounding at 18:00 UTC. The resulting

initial profiles are displayed in Fig.3.5a.

Apart from the initial thermodynamic state, realistic boundary conditions have to be provided to the LES model during the numerical simulation. The measurements of the surface energy balance are used to extract the surface latent and sensible heat fluxes (see Fig.3.5b). The reason for the surface energy imbalance at PAM3 is unknown, and therefore the LES surface fluxes are based on the more balanced PAM1 data only. After several test runs we assumed a sinusoid shape for the surface fluxes, with the maximum at 18:00 UTC and corresponding values of 100 and 300 W m^{-2} for the sensible and latent heat fluxes respectively. Another boundary condition in the model is the roughness length at the surface $z_0 = 0.035\text{m}$, which is a typical value for flat land surfaces.

The radiative and large scale forcings which may act on the area have to be accounted for in the simulation. Unfortunately, a network of radiosonde measurements over the area was not available, and as a consequence no variational analysis could be applied to estimate the large scale advective temperature and moisture forcings. The offset in temperature and moisture between the soundings of the inland radiosondes and the aircraft at the coast only suggests that there was a large scale cooling and moistening tendency, probably due to the proximity of the ocean. Any measurements of the radiative forcings were neither available. This lack of observational data makes it very difficult to make a realistic estimate on the forcing tendencies. As the main interest of this paper lies in evaluating characteristic LES results used in entrainment models and budget studies, a small offset between the mean temperature or moisture profile in LES and reality is acceptable. However, it is important to realize that in order to compare the LES cloud field to the in-cloud observations, it is essential that the simulated cloud base and cloud top are located at the correct heights. Fortunately, measurements of the time-series of the surface temperature and specific humidity at the PAM stations are available, which can be used to align the development of the thermodynamic state of the boundary layer in LES during the day (see Fig.3.3). These figures clearly show that the mixed layer warms up in the morning. There is less consensus between the two PAM stations about the specific humidity.

To summarize, the LES case is designed to reproduce the heights of cloud base, cloud top and the inversion as observed by the aircraft and the radiosondes, using the large scale tendencies as a tool for calibration and the measured surface time-series as a constraint. This resulted in a net temperature forcing of -3 K/day . This tendency is set to decrease with height towards zero just above the inversion. The moisture forcing is set to zero. Finally, based on the radiosonde-data the initial mean horizontal wind in the simulation is set to $(-4,4) \text{ m/s}$ in the zonal and meridional directions. The geostrophic wind is also set to these values, as detailed information of this forcing was unavailable.

3.5 Conditional sampling

Once the LES case is constructed, a method has to be chosen to compare the LES results to the available observations. To this purpose we use the *conditional sampling* technique. In this method, horizontal averages are calculated over a certain area defined by some criterion, which can be the presence of liquid water, a positive vertical velocity, a positive buoyancy, or any combination. In other words, a decomposition is made in which the horizontal slice is

split up into two areas. Conditionally sampled fields are widely used in budget studies using LES (e.g. Schumann and Moeng, 1991a,b; Siebesma and Cuijpers, 1995; Wang and Stevens, 2000; De Roode and Bretherton, 2002) and in parameterizations of convection in GCMs (e.g. Asai and Kasahara, 1967; Tiedtke, 1989) which make use of the top-hat approximation. In LES, the conditionally sampled fields at a certain height and at a certain moment are calculated using

$$\phi^c = \frac{1}{N_D} \sum_{ij} c_{ij} \phi_{ij}, \quad (3.1)$$

where ϕ is the variable to be sampled, i and j are the horizontal coordinates, and N_D is the total number of cloudy points in the domain. $c_{ij} = 1$ if the point is cloudy and 0 if it is non-cloudy. Using flight legs to obtain conditionally sampled fields requires a different technique, because the aircraft can not measure everywhere in the domain at the same time. Therefore it is assumed that an ergodic equivalent can be used, in this case a time-average,

$$\phi^c = \frac{1}{N_T} \sum_t c_t \phi_t. \quad (3.2)$$

Here t is the time during the flight and N_T is the total number of cloudy measurements during the flight. Hereafter an over-bar will denote a domain-average, the superscript c will denote a cloud-average, and the superscript e will denote an average over the dry environment.

These two definitions essentially give the same value of ϕ^c if i) the cloud ensemble is in steady state, and ii) the aircraft flies enough straight legs through the whole domain to catch a realistic size distribution of sampled clouds. Typically, a cloud ensemble consists of many small clouds and fewer large clouds (Plank, 1969; Wielicki and Welch, 1986; Cahalan and Joseph, 1989; Benner and Curry, 1998). The contribution to ϕ^c as a function of cloud size is a balance between cloud number and individual contribution per cloud, and it is therefore important to sample a realistic distribution. Flight RF12 flew in straight legs of about 20km length, after which it turned around to stay in the same area. The length of 20 km of each straight leg is comparable to the domain-size of LES, and therefore it is reasonable to assume that the sampled cloud size distribution is of comparable quality. One of the objectives of the SCMS campaign was to study the micro-physics of the larger cumuli, and for that reason a ground-based radar guided the air-plane after each turn towards a certain large specimen. Each preferred large cloud was traced in time by the radar in order to sample it as often as possible during its lifetime. Accordingly, this may lead to a slight overestimation of the cloud fraction. For cloud-averages calculated with (3.2) a slight overestimation of the cloud fraction is not a big problem, as they are independent of the cloud fraction. In contrast, on fractional properties like the mass flux this does have a significant impact.

3.6 Parameterizations

Once the profiles of the conditionally sampled fields are known, hypotheses and parameterizations which are based on such decompositions can also be evaluated. One good example is the bulk entrainment rate (ϵ^c) of the cloud ensemble, which is normally calculated by using

the simplified lateral mixing equation

$$\varepsilon^c = -(\phi^c - \bar{\phi})^{-1} \frac{\partial \phi^c}{\partial z} \quad (3.3)$$

(Betts, 1975; Anthes, 1977; Tiedtke, 1989; Raga et al., 1990). This entrainment rate can be interpreted as the inverse of the depth in which the excess over the environment ($\phi^c - \bar{\phi}$) has decreased by a factor e^{-1} . ϕ^c can be the liquid water potential temperature θ_l^c or the total specific humidity q_l^c , which are both conserved variables for moist adiabatic ascent. Any change of ϕ^c is therefore caused by whether a diabatic process like mixing or a statistical process like a changing cloud size distribution with height. The LES results on BOMEX of Siebesma and Cuijpers (1995) gave typical values of $\varepsilon = 1.5$ to $3 \cdot 10^{-3} \text{ m}^{-1}$, decreasing with height in the cloud layer.

The process of cloud mixing has also been formulated in terms of other variables. A definition which is often used is the ratio between the measured q_l at a certain height in a cloud and the moist adiabatic value q_l^{ad} of an undiluted parcel that has risen from cloud base to that height (e.g. Warner, 1955; Raga et al., 1990). Measurements have shown that typically this ratio strongly decreases with height in a shallow cumulus cloud layer towards values around $0.3 \sim 0.4$ near cloud top, which points at significant mixing. How does definition (3.3) relate to this ratio? One possible approach is to write θ_l^c as a function of θ^c and q_l^c ,

$$q_l^c = \frac{c_p \Pi}{L} (\theta^c - \theta_l^c). \quad (3.4)$$

where c_p is the specific heat at constant pressure, L is the specific latent heat of the phase-change between water vapour and liquid water, and Π is the Exner function. At this point we introduce an assumption based on observations and LES results, which show that in shallow cumulus the cloud-average potential temperature at a certain height (θ^c) is typically almost equal to that of the environment,

$$\theta^c \approx \bar{\theta}. \quad (3.5)$$

Furthermore, the typical very small cloud cover of shallow cumulus allows for the well-known assumption $\theta_l \approx \bar{\theta}$. Substituting $\theta^c \approx \bar{\theta}_l$ in (3.4) and then using (3.3) with $\phi \equiv \theta_l$ gives

$$q_l^c = \frac{1}{\varepsilon^c} \frac{c_p \Pi}{L} \frac{\partial \theta_l^c}{\partial z}. \quad (3.6)$$

Substituting (3.4) for θ_l^c and again using (3.5) in the lapse rate finally gives

$$\varepsilon^c = \frac{1}{q_l^c} \frac{c_p \Pi}{L} \frac{\partial \bar{\theta}}{\partial z} - \frac{\partial}{\partial z} \ln(q_l^c) - \frac{\partial}{\partial z} \ln(\Pi^{-1}). \quad (3.7)$$

The advantage of assumption (3.5) is that ε^c is now only dependent on the pressure, the mean temperature lapse rate and the liquid water content. The first two properties can be obtained from data measured by a radiosonde, while a ground radar can remotely measure cloud liquid water contents. This enables the calculation of the bulk entrainment rate without direct in-cloud measurements by aircraft. The individual terms of (3.7) and the validity of assumption (3.5) will be evaluated with the aircraft data and LES results.

Knowledge of the entrainment rate is useful in other parameterizations. The clouds are responsible for the bulk of the vertical transport in the cloud layer (Siebesma and Cuijpers, 1995). Accordingly, single column models (SCM) in GCMs are often equipped with a simplified equation for the vertical velocity of the clouds,

$$\frac{1}{2} \frac{\partial}{\partial z} (w^c)^2 = -\beta \epsilon^c (w^c)^2 + \alpha B^c, \quad (3.8)$$

(Simpson and Wiggert, 1969; Siebesma et al., 2002). The term on the left hand side is the advection term, and the first term on the right is the mixing term enhanced by a factor β to account for the impact of pressure perturbations. It is assumed here that the domain-average vertical velocity \bar{w} can be neglected. B^c stands for the buoyancy of the clouds, which is reduced by a factor α to account for loss of potential (gravitational) energy to sub-plume turbulence. Simpson and Wiggert (1969) suggested $\beta = 2$ and $\alpha = \frac{2}{3}$, while the operational ECMWF model uses $\alpha = \frac{1}{3}$. Siebesma et al. (2002) applied (3.8) as a rising plume model for the BOMEX case and compared it with LES results. Here (3.8) will be applied to the RF12 data, using $\beta = 2$ and $\alpha = \frac{1}{2}$, the latter being an intermediate value between the two mentioned above.

3.7 Results

The LES model used in this study is described in detail in Cuijpers and Duynkerke (1993). The LES simulation was performed on a domain of 6.4km x 6.4km x 5km. The corresponding grid-spacing was 50m x 50m x 40m. A centered-difference integration scheme was used. In the time-integration a time-step of 1 second was used to prevent any possible numerical instability. A damping layer is implemented in the model above 3700m to prevent gravity waves from unrealistically bouncing downwards at the top. An all-or-nothing condensation scheme is used, meaning that any grid-box is entirely saturated or entirely unsaturated. Hourly averaged vertical profiles were calculated of the basic thermodynamic variables. Every 300s several cloud properties were evaluated. A period of 12 hours was simulated, covering the daytime cycle from 07:00 to 19:00 local time (which corresponds to 12:00 UTC to 00:00 UTC).

3.7.1 Daytime development

We commence with a short description of the initial development of the convective boundary layer in LES until 18:00 UTC after which in-cloud observations are available. Figure 3.6 shows the profiles of $\bar{\theta}$ and \bar{q}_r in this period. The potential temperature gradually increases with time in the mixed layer. It initially moistens, followed by a long period of drying. This is consistent with the surface measurements as shown in Fig.3.3. The temperature and moisture in the conditionally unstable layer do not change much in time, which is also apparent in the radiosonde soundings.

Figure 3.7a illustrates that the first clouds appear in LES at about 13:30 UTC. At first the cloud layer is very shallow, but within two hours it deepens to about 1500m. From 15:00 UTC the growth of the cloud top is controlled by the rise of the capping inversion. The

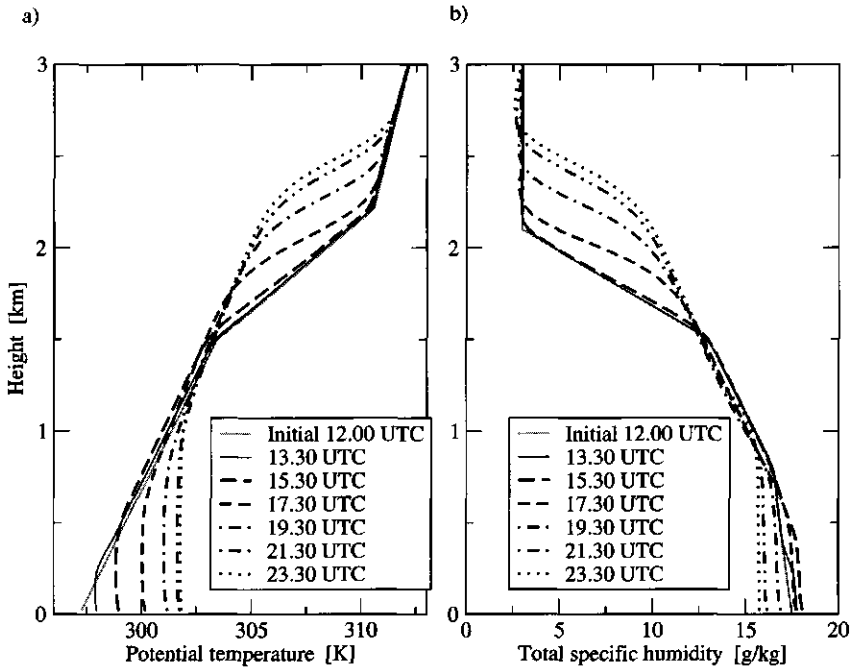


Figure 3.6 The development in time of the domain-averaged profiles of a) the potential temperature $\bar{\theta}$ and b) the total specific humidity \bar{q}_t as produced by LES.

development of the cloud fraction and the integrated liquid water path is shown in Fig.3.7b. The cloud fraction peaks with 41% at 15:00 UTC, at the same time when the clouds first reach the inversion. From then on there is a steady decrease of the cloud fraction with time. These basic results are qualitatively similar to the results of the intercomparison study between many LES models of GCSS working group 1 on a quite similar diurnal cycle, as observed over the Southern Great Plains site of the Atmospheric Radiation Measurement (ARM) program (Brown et al., 2002).

3.7.2 Thermodynamic state

From this point onwards we focus on the period between 18:00 and 21:00 UTC during which the in-cloud measurements were taken by flight RF12. In order to get reliable statistics, all measurements are averaged over this three-hour period. Figure 3.8 shows the profiles in this period of the conserved thermodynamic variables in LES and the observations. The conditionally sampled profiles are only shown at those heights where the cloud (or core) fraction was higher than 1%. Figure 3.8a illustrates that there is a remarkable agreement between LES and the observations concerning the liquid potential temperature (θ_l) in both the environment and the clouds. The same is true for the total specific humidity (q_t), although

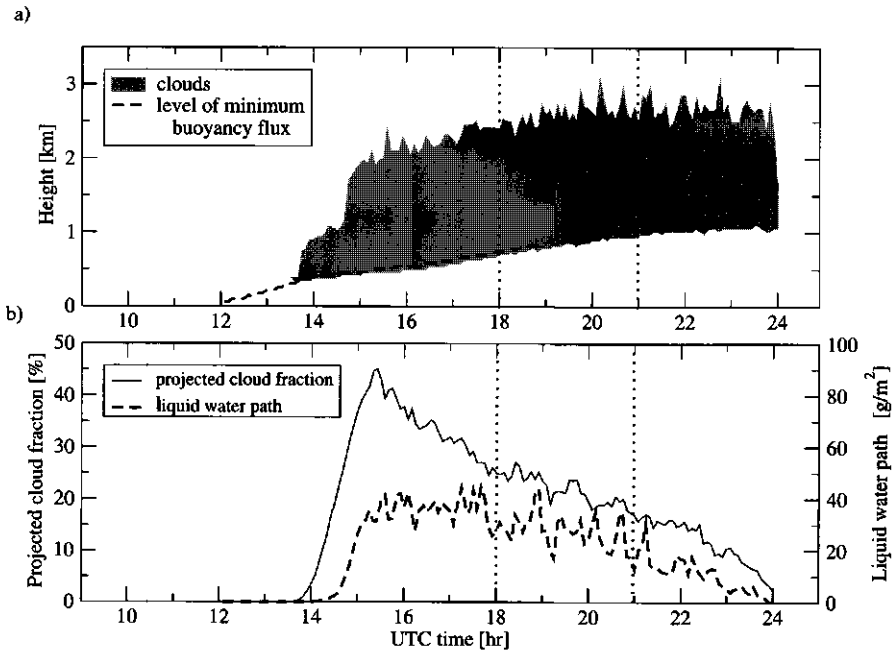


Figure 3.7 a) Structure of the simulated cloud layer. The dotted lines mark the period for which in-cloud measurements by the RF12 flight are available. b) The time-series of the projected cloud fraction (left axis) and the liquid water path (right axis) as produced by LES.

the observations show a slightly dryer layer near cloud base (see Fig.3.8b). As the exact magnitude of the conserved thermodynamic variables is highly tunable in LES, it is perhaps more interesting to look at the excess values and the vertical gradients of the conditionally sampled variables. Figures 3.9a and b show that in general the increasing excess values with height of the cloudy averages in LES are supported by the observations. Near cloud base the specific humidity excess of the clouds is somewhat under-predicted by LES. The simulated lapse rates are also in good agreement with the observations, see 3.9c and d.

The liquid water content of the clouds (q_l^c) is shown in Figure 3.10a, which illustrates that the LES profile of q_l^c lies very close to the measured values. Apparently the all-or-nothing condensation scheme in LES is capable of predicting cloud liquid water contents which increase with height in the same order of magnitude as is measured by these instruments in natural clouds. The ratio of the liquid water content to its moist adiabatic value is roughly 0.3 – 0.4 in the top of the cloud layer, and comparable to the values found by Warner (1955) and Raga et al. (1990). A current issue in the LES community is the question if the decreasing cloud fraction with height in shallow cumulus cloud layers as typically observed in LES is realistic. The profile of the cloud fraction is shown in Fig.3.10b. The six heights for which data-points exist show considerable scatter, but the cloud fraction certainly does not decrease

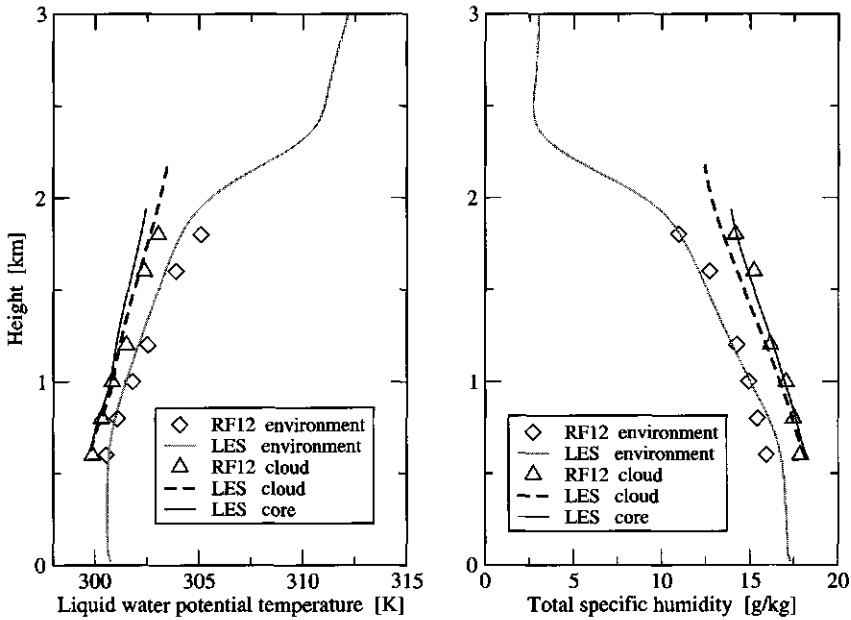


Figure 3.8 Profiles of the a) liquid water potential temperature and b) the total specific humidity. Both the mean and cloudy averages are plotted. Observations are plotted as unconnected data-points, and LES results are plotted as connected lines. The cloud core average value in LES is also plotted for comparison, defined as the average over all cloudy points which are also buoyant.

with height. However, note that the time spent inside clouds is increased by the choice to adjust the flight-path towards certain large cumuli. Accordingly the aircraft measurements give a cloud fraction which is not necessarily equal to the actual cloud fraction of the population.

3.7.3 Lateral mixing

The fact that LES produces realistic conditionally sampled fields in this case encourages the use of LES as a tool to evaluate hypotheses or parameterizations which are based on conditional averages. A good example of such a parameterization is the bulk entrainment rate ϵ^c which can be calculated from these averages using (3.3). Figure 3.11a illustrates that the order of magnitude is comparable to that found in observational and LES studies (Raga et al., 1990; Siebesma and Cuijpers, 1995). In fact, if θ_l^c is used in (3.3), the observed ϵ^c even decreases with height and lies close to the LES entrainment rate. The decrease with height of ϵ^c is mainly a result of the increase with height of the excess $(\theta_l^c - \bar{\theta}_l)$, while the lapse rate $\partial\theta_l^c/\partial z$ is fairly constant with height. In the lower half of the cloud layer, the calculation of ϵ^c using q_l^c gives much lower results for the observations compared to LES. This is caused

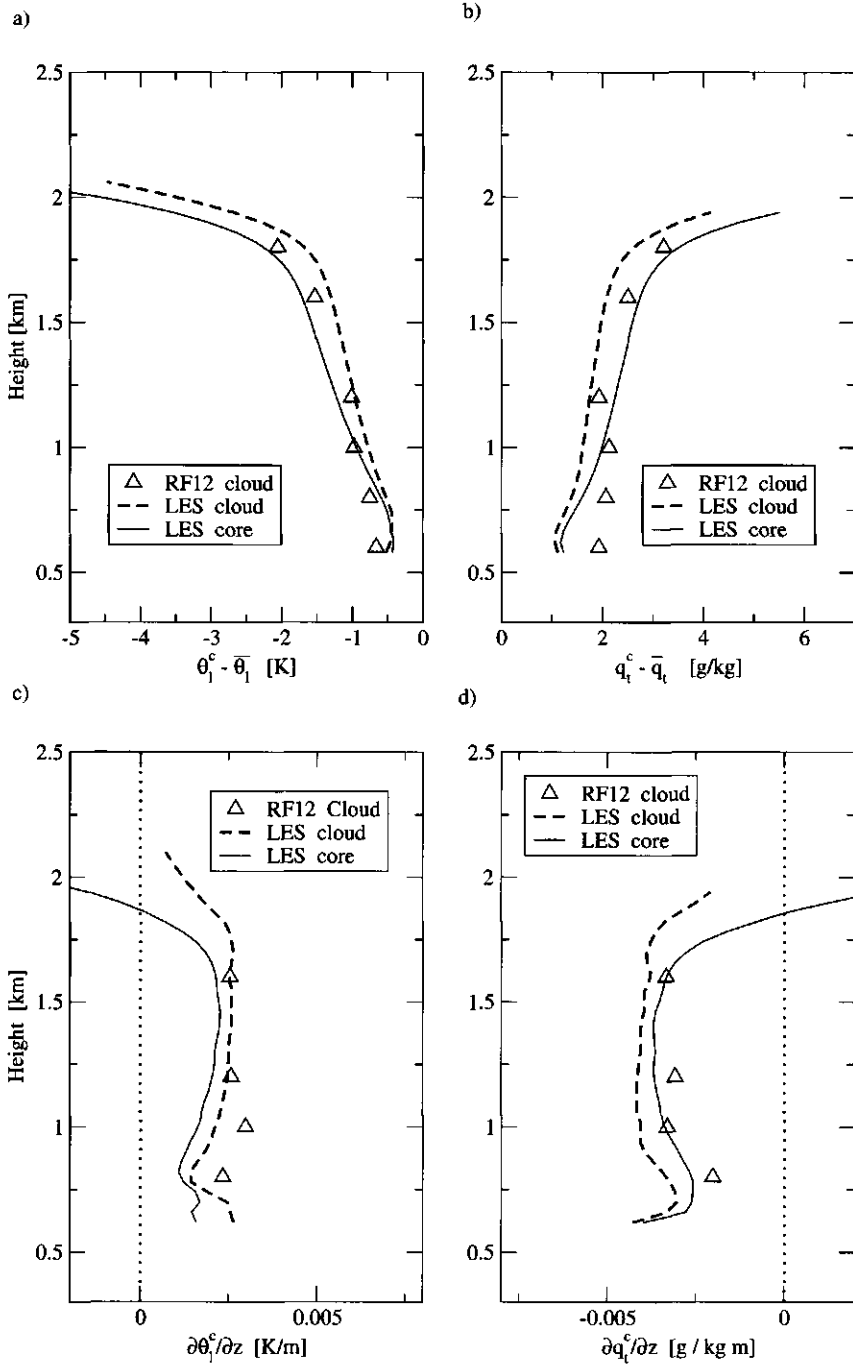


Figure 3.9 Profiles of the excess of the cloudy averages of θ_i^c and q_i^c over the dry environment (panels a and b respectively) and the gradients of the cloudy averages (panels c and d respectively).

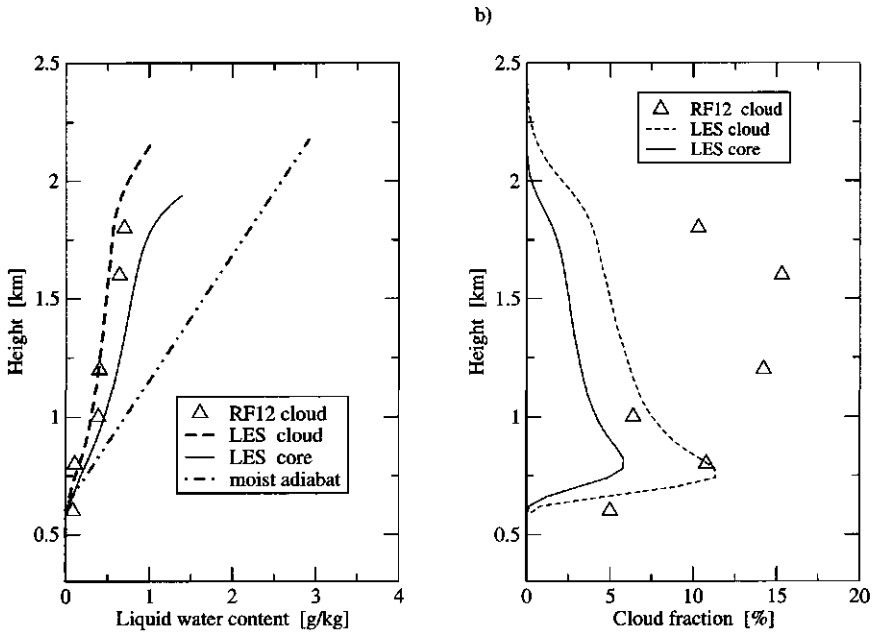


Figure 3.10 a) Profiles of the liquid water content q_l^c . Observations are plotted as unconnected data-points, and LES results are plotted as connected lines. Both the mean and cloudy averages are plotted. The cloud core average in LES is included for comparison. The dash-dotted line is the moist adiabatic profile starting at cloud base. b) The profile of the cloud fraction.

by both a smaller lapse rate near cloud base and a larger excess of the observed q_l^c .

Figure 3.10a illustrates that the measured cloud-average liquid water content is considerably smaller than the moist adiabat, pointing at significant cloud mixing. Equation (3.7) relates the bulk mixing rate ϵ^c defined in (3.3) to the liquid water content q_l^c , using assumption (3.5). Figure 3.11b shows that (3.7) corresponds well with (3.3) in both LES and the observations except at cloud base and the inversion. This is caused by assumption (3.5) (see Fig.3.12a), which applies remarkably well in the bulk of the cloud layer but no longer at its boundaries. For completeness, Fig.3.12b shows the individual terms of (3.7). It is clear that the pressure term in (3.7) can be neglected, and that the measurements support the LES budgets for the two remaining terms.

3.7.4 Vertical transport

The conditionally sampled vertical velocity w^c is plotted in Fig.3.13a. Despite the scatter in the observations we can say that the magnitude of the in-cloud vertical velocity in LES is comparable to the observations. The mass flux plotted in Fig.3.13b is the product of the cloud fraction and cloud average vertical velocity. In contrast to LES the measured mass flux

clearly increases with height. This is remarkable, as LES and the measurements agree very well on other conditionally sampled dynamical properties which are independent of the cloud fraction, like the profiles of vertical velocity and the bulk entrainment rate. It is obvious that the increasing mass flux is mainly caused by the measured increasing cloud fraction with height (see Fig.3.10b). As noted earlier, the cloud fraction as obtained from the aircraft measurements might be an overestimation of the actual cloud fraction, due to the adjustment of the flight-path towards large cumuli. As a consequence, no conclusion can be made about the decrease- or increase of the mass flux with height based on these data.

The buoyancy in the clouds is an important source for the production of TKE in the cloud layer. Figure 3.14a shows that LES is in good agreement with the observations on magnitude and shape of the vertical profile of the virtual potential temperature excess of the clouds. The clouds are only marginally buoyant, with a θ_v -excess of only a few tenths of degrees Kelvin. The negative buoyancy at cloud base and cloud top is present in both the observations and LES, indicating the statically stable layers which envelope the conditionally unstable cloud

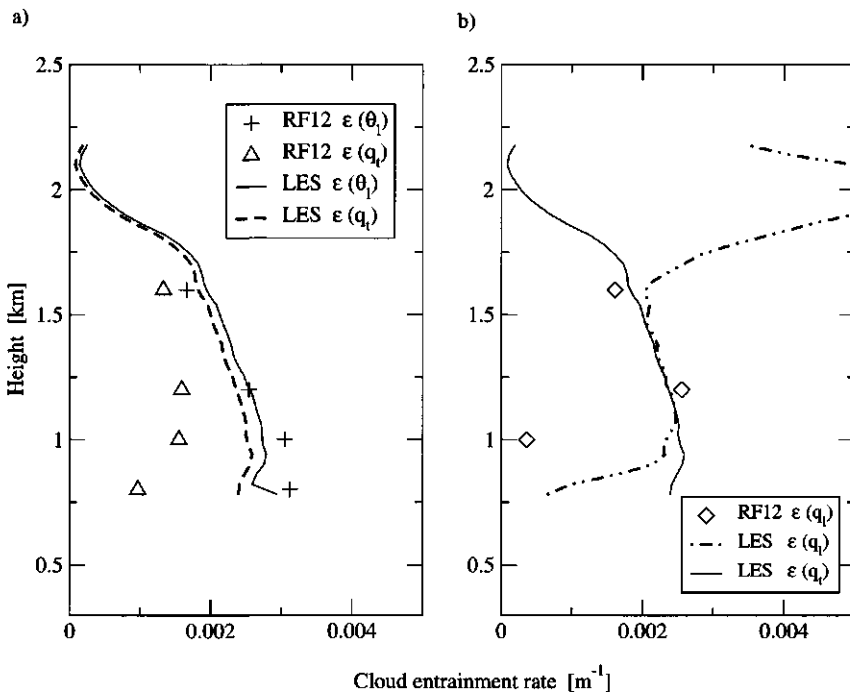


Figure 3.11 Bulk entrainment rates of the cloud field, using several different methods of calculation. These are applied to both the observations and the LES results. Panel a) shows equation (3.3) with ϵ as a function of q_t and θ_l , panel b) shows equation (3.7) based on q_t^* and $\partial\theta/\partial z$. In panel b) equation (3.3) is shown again for reference.

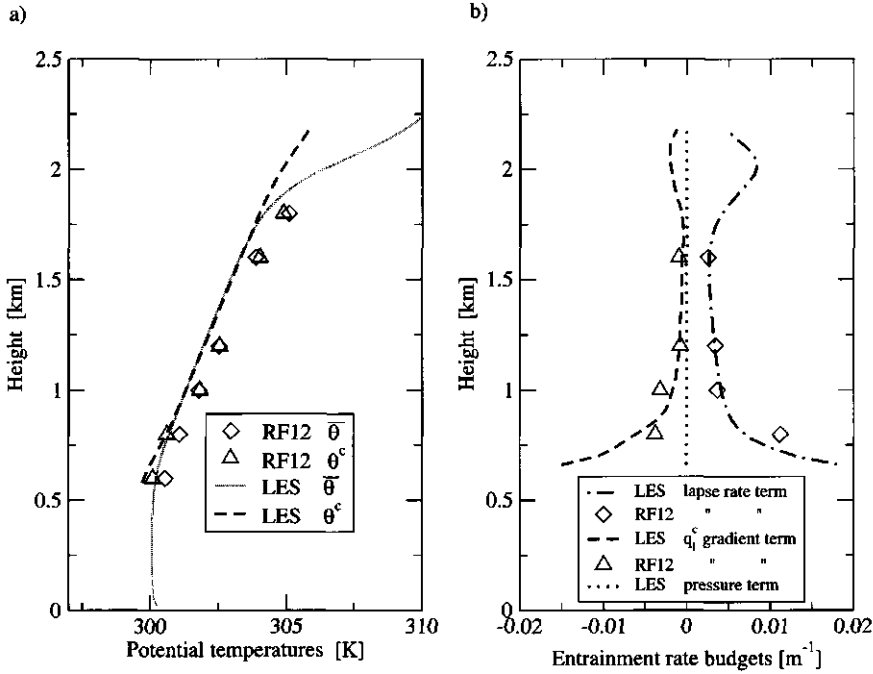


Figure 3.12 a) Profiles of the mean and cloudy averaged potential temperature. b) Budgets of equation (3.7), based on both the LES results and the RF12 data. The 'lapse rate term' corresponds to the first term on the right hand side in (3.7), the ' q_i^c gradient term' to the second term, and the 'pressure term' to the third.

layer. The LES results show that the cloud core is significantly more buoyant than the clouds and also has a much higher vertical velocity, reflecting that the production of TKE in the clouds is associated with the relatively high buoyancy of the cloud core elements.

Next some vertical velocity budgets are calculated from the RF12 data. Figure 3.14b illustrates that the cloud-average vertical acceleration is almost negligible. The simplified budget equation (3.8) reproduces this feature reasonably well in the region where the clouds are marginally buoyant. Apparently the factors α and β which are included in the equation to account for sub-plume turbulence and pressure perturbations, and of which the particular values were originally tuned for the cloud *core*, also result in a balanced budget for the *cloud*-average vertical velocity.

3.7.5 In-cloud turbulence

After evaluating the cloud average vertical velocity it is interesting to take a closer look at the turbulent kinetic energy (TKE) in the cloud layer. The vertical component of the TKE is the

vertical velocity variance σ_w^2 , defined by

$$\sigma_w^2 = \overline{w'^2} \equiv \frac{1}{N} \sum_i (w_i - \bar{w})^2, \quad (3.9)$$

where \bar{w} is the horizontally domain-averaged vertical velocity and N is the number of sampled points. Comparing the measured vertical velocity variance with that produced by LES is a critical test for the capacity of LES of resolving the organized turbulent motions in the cloud layer. Also, little observations of the in-cloud vertical velocity variance have yet been reported, while it is an important variable in parameterizations relying on TKE to define the intensity of vertical transport by turbulence in the cloud layer.

The results for the domain- and environmental average variance are shown in Fig.3.15a. The average over the whole domain (σ_w^m) in LES is much smaller than the observed value. This is probably due to the high cloud fraction resulting from the flight legs, which might be an overestimation of the actual cloud fraction as explained earlier. However, σ_w^m in LES is even somewhat smaller than the observed average over the dry environment (σ_w^e). This means that in any case the turbulent activity of the environment is slightly under-predicted in LES. The profile of σ_w^m in SCMS can be compared to flight A210 on 14 June 1992 of the

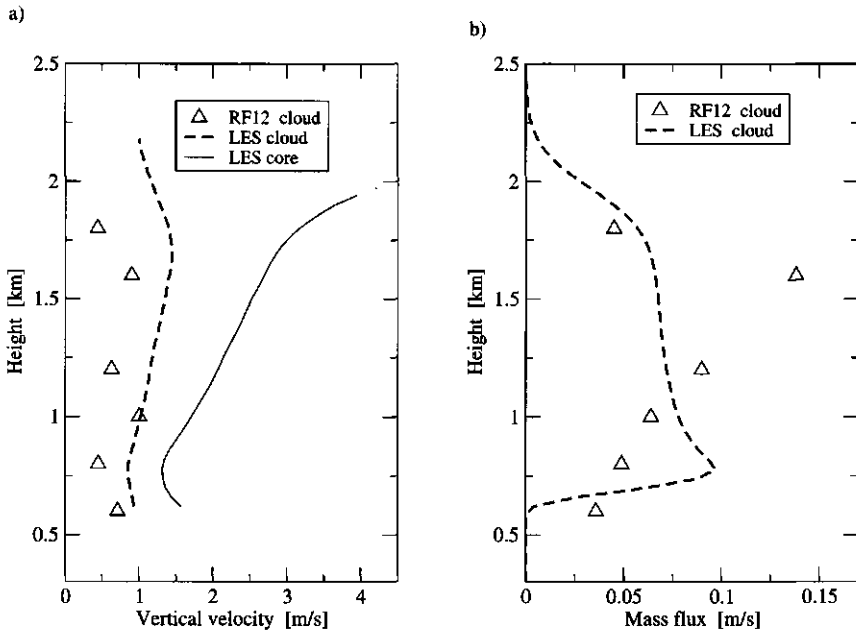


Figure 3.13 Profiles of a) the cloud-average vertical velocity and b) the vertical mass flux by the clouds. Observations are plotted as unconnected data-points, and LES results are plotted as connected lines. The cloud core average in LES is also included.

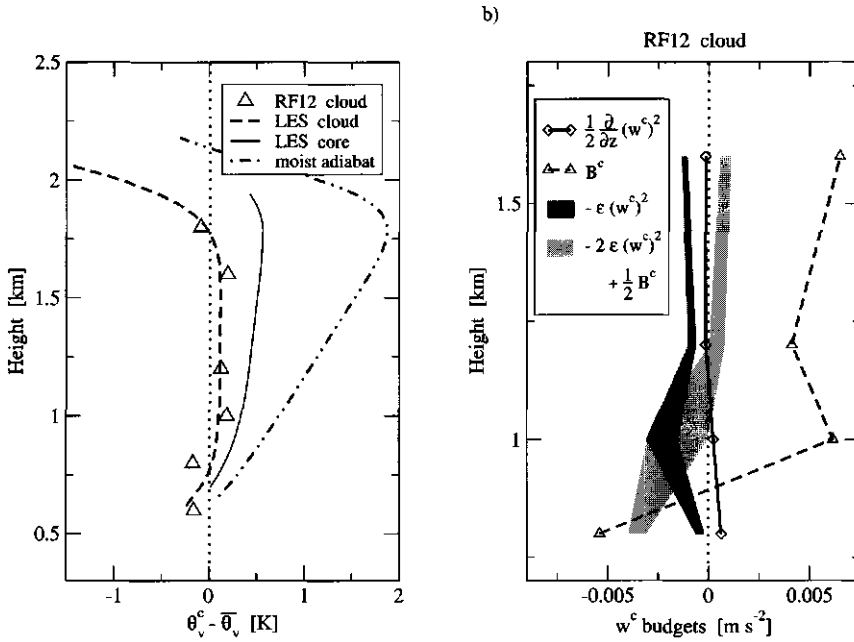


Figure 3.14 a) Profiles of the virtual potential temperature excess of the clouds. Observations are plotted as unconnected data-points, and LES results are plotted as connected lines. b) Profiles of the simplified budget equation (3.8) for the vertical velocity of the cloud, based on RF12 data. The shaded areas represent the range between the entrainment rates following from the use of θ_f^c and q_f^c in (3.3).

Atlantic Stratocumulus Transition Experiment (ASTEX, see Albrecht et al., 1995), during which cumulus clouds were sampled and σ_w^m was measured (De Roode and Duynkerke, 1997). The SCMS data are consistent with the ASTEX data in that σ_w^m slightly increases with height in the cloud layer, with a maximum near cloud top.

The cloud average variance is plotted in Fig.3.15b, illustrating that LES reproduces the observed profile of the cloud-average vertical velocity variance $(\sigma_w^c)^2$ remarkably well. The observed σ_w^c is much larger than σ_w^e , which reflects that the generation of TKE in a cumulus layer mainly takes place inside the clouds, and that the environment is fairly laminar and statically stable. Clearly the linear increase of $(\sigma_w^c)^2$ with height above cloud base in LES is supported by the aircraft data. The good agreement between σ_w^c in LES and the aircraft measurements gives confidence in the capacity of LES to realistically resolve in-cloud turbulence. This result promotes the use of LES results in parameterizations of cloud dynamics, as an alternative for the scarce and often incomplete in-cloud measurements. A recent example of a parameterization primarily based on LES results is the similarity theory for shallow cumulus as formulated by Grant and Brown (1999). They make use of the linear increase of the in-cloud vertical velocity variance with height in the cloud layer as seen in LES, a feature

now supported by the in-cloud measurements of SCMS presented here.

3.7.6 Cloud size densities

Finally the geometrical properties of the cloud population are evaluated by using cloud size densities (see Fig.3.16a). The densities are normalized by the total number of clouds N . The bin-sizes are equal to the horizontal grid-spacings of the LES and Landsat fields, being 50m and 30m respectively. The general outcome of Neggers et al. (2002b) was that the densities in LES are well described by a power-law, scaling up to a certain size (the scale-break). Accordingly, we evaluate the cloud size densities here by comparing power-law exponents and scale-break sizes. It is clear that both the densities of LES and Landsat are well described by a power-law at the relatively small cloud sizes, with an exponent of -1.70 . The area of scaling is about one decade wide, up to a scale break at about 800m which is reproduced by LES. At sizes larger than the scale-break, the densities decay rapidly with cloud size. This decay is not as strong in Landsat as in LES: significantly larger clouds occur in the Landsat

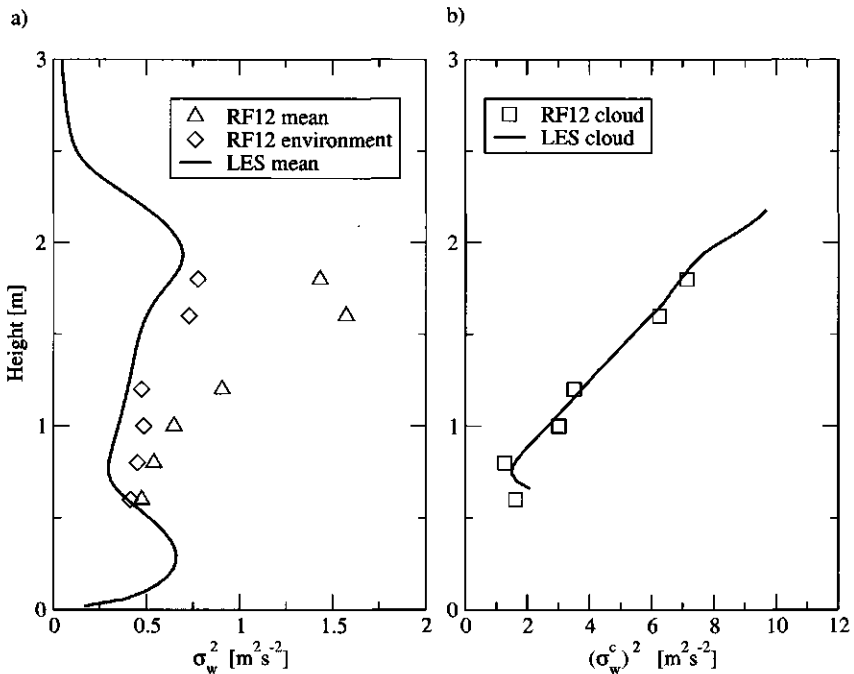


Figure 3.15 Profiles of the vertical velocity variance σ_w^2 . Panel a) shows the domain- and dry environmental averages, and panel b) shows the cloud-averages. Observations are plotted as unconnected data-points, and LES results are plotted as a solid line.

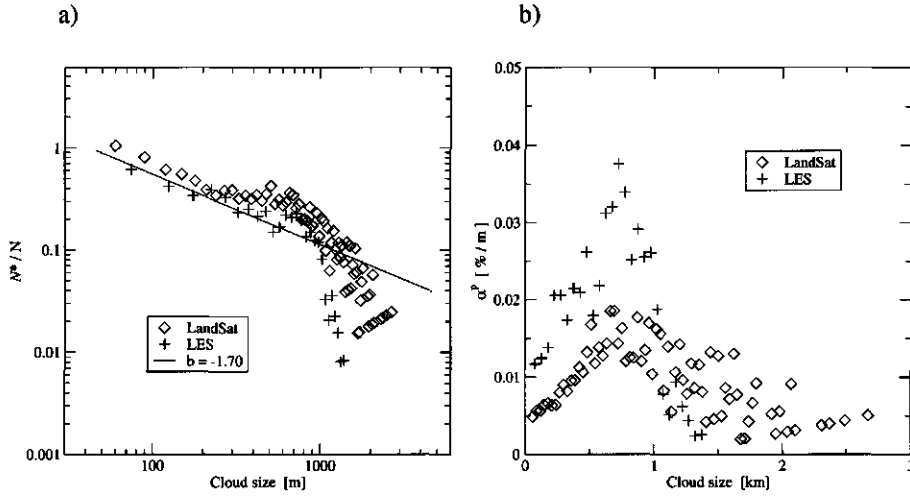


Figure 3.16 a) Log-log scale plot of the cloud size density N normalized by the total number of clouds N . The solid line represents the fit $N(l) \sim l^{-1.70}$ by Neggers et al. (2002b), which is based on LES results on a range of different cumulus cases. b) The cloud size decomposition of the vertically projected (or 'shaded') cloud fraction α_p . The area covered by the histogram is equal to the total shaded cloud fraction.

images. The limited domain size of 6.4km in LES may prevent the growth of clouds at these largest sizes.

The corresponding cloud size decomposition of the vertically projected (or 'shaded') cloud fraction is plotted in Fig.3.16b. Very clearly an intermediate dominating size exists at the same size as the scale-break in N , as was shown by Neggers et al. (2002b). The largest sizes in Landsat do not occur in the LES domain. At the sizes smaller than the scale break size, the LES clouds contribute relatively much to the shaded cloud fraction compared to Landsat. However, the total shaded cloud fraction, equal to the area covered by the histogram, does not differ that much in Landsat and LES, being 19.7% and about 20% respectively. This means that more small clouds occur in LES.

Apart from a possible physical reason, there might be other explanations for the differences between LES and Landsat. At first, the cloud fields are not exactly the same. The LES case is based on measurements on August 5, while the Landsat image is made at August 10. At second, note that the Landsat image was taken at 14:53UTC. Figure 3.7b shows that this time corresponds to the very begin of the daytime cycle of clouds in LES. To get qualitative distributions in LES, we had to sample over a three-hour period before a number of sampled clouds was reached which was comparable to the number captured by the Landsat image. In this period the cloud size distribution may change significantly. We realize that these differences may frustrate a direct comparison. However, in that view the *similarities* we found between LES and Landsat only get more meaning: the powerlaw-exponents agree remarkably well in LES and Landsat, and in both cases a scale-break is present (implying a dominating size in the cloud fraction decomposition). These results therefore emphasize the universality

of the functional form which describes the cloud size densities and decompositions in shallow cumulus cloud populations (e.g. Neggers et al., 2002b). This conclusion could be illustrated by dividing the cloud fraction decompositions by the total number of clouds N . As α^P and N are closely related by (3.12) (see Appendix 3.A), it is evident from Fig.3.16a that the size decompositions of LES and Landsat would collapse at the sizes below the scale-break.

3.8 Discussion and Conclusions

We choose to use conditionally sampled fields to evaluate the LES results against in-cloud measurements. This means that in fact we are studying the *bulk* properties of the cloud ensemble. Apart from giving good statistical averages, this also enables the analysis of some well-known parameterizations which are based on such ensemble-average properties. The SCMS data-set was chosen for this study because of the combination of a range of different surface measurements, in-cloud measurements by aircraft at many levels in the cloud layer, and the availability of high-resolution Landsat images.

The results show that LES accurately predicts the thermodynamic and turbulent state of the shallow cumulus cloud layer. More specifically, the first statistical moments of many thermodynamic variables as well as the vertical velocity variance of the cloud ensemble agree well with the aircraft observations. The evaluation of the cloud size distributions of LES against Landsat supports the results on size statistics of Neggers et al. (2002b). While Siebesma and Jonker (2000) showed that LES reproduced the typical morphology of *individual* cumulus clouds, these results show that the same is true for cumulus cloud *populations*.

Unfortunately the aircraft data can not provide reliable vertical profiles of the cloud fraction and mass flux, due to the choice to adjust the flight-path towards certain large cumuli during the flight. The question whether the cloud fraction and mass flux in shallow cumulus de- or increases with height could not be answered. To this purpose new flight campaigns would have to be organized, in which several aircraft measure the cloud fraction at different heights simultaneously. Alternatively other techniques could be used, perhaps by using ground-based or airborne radar measurements of cloud droplets at low angles.

Several hypotheses which make use of conditionally sampled fields were tested on the SCMS data. The lateral entrainment rates in LES derived from the bulk profiles compare well with those derived from the SCMS data. Their magnitudes and the decrease with height as following from the SCMS data confirm the bulk entrainment rates for shallow cumulus convection first suggested by Siebesma and Cuijpers (1995). The alternative formulation of the lateral entrainment rate as a function of the liquid water content and the mean lapse rate agrees well with the original form based on the conserved variables. Finally, the use of RF12 data in the simplified equation for the vertical velocity (Simpson and Wiggert, 1969; Gregory, 2001; Siebesma et al., 2002) results in a more or less balanced budget for the cloud-average vertical velocity.

These results give confidence in the credibility of cloud statistics as produced by LES in general. Despite all the gaps and inaccuracies in the measurements and the associated unavoidable assumptions in the setup of the case, it appears that the LES concept still predicts realistic cumulus cloud fields. This supports the intercomparison-studies by the EUROCS and GCSS working-group 1, in which specific observed cases are simulated

by many LES and SCM models in order to get more insight in the general problem of parameterizing cumulus convection. The use of LES results next to measurements in developing parameterizations significantly adds to the research possibilities. There is full control over all conditions in the simulated domain. Secondly, in contrast to observations in real cloud fields all LES data can be reproduced exactly. Finally, LES offers almost unparalleled statistics, as the three-dimensional fields of the model variables are simulated at high spatial and temporal resolutions.

Acknowledgements The data collected by means of the C-130 of NCAR during SCMS were kindly supplied by Dr. C. A. Knight. We acknowledge NCAR and its sponsor, the National Science Foundation, for the use of the observational data. Furthermore we thank Pier Siebesma for our discussions on the results and for critically reading this paper. The LES results in this study were obtained using the supercomputer facilities of the European Centre for Medium-Range Weather Forecasts (ECMWF) in Reading, UK. This study has been supported by the Netherlands Organization for Scientific Research under Grant 750.198.06.

In Memoriam During the final stages of the creation of this paper Peter Duynkerke died suddenly and unexpectedly. Our thoughts and sympathy go out to his family and friends. Peter was the inspiration behind this study. He managed and organized all the SCMS data, and contributed significantly to the LES work and the interpretation of the results. The final form of this paper had his full approval. Without him this work would not have been possible. It has been a pleasure and a great honour to have worked with Peter, and his person and his work will be missed dearly. He will be in our memories forever. Roel Neggers and Stefaan Rodts.

Appendix 3.A Cloud size densities

For a detailed description of this procedure we refer to Neggers et al. (2002b). The size of a cloud (l_n) is defined as the square-root of the vertically projected area of the cloud (A_n^p),

$$l_n = \sqrt{A_n^p}. \quad (3.10)$$

Once the linear size l_n has been defined, we can sort all the clouds by their size and build histograms. The total number of clouds N present in the domain at a certain time is defined by the integral of the corresponding cloud number density N :

$$N \equiv \int_0^\infty N(l) dl \quad (3.11)$$

where the term $N(l)$ is the number of clouds of size l in the domain. It is convenient to normalize N with the total number of clouds in the domain N .

The *projected cloud fraction* of a cloud field (a^p) is defined as the ratio between the area covered by all clouds and the total area of the domain. The cloud fraction decomposition α^p denotes the contribution to a^p as a function of cloud size l , and can be written as

$$\alpha^p(l) \equiv \frac{l^2 N(l)}{L_x L_y}. \quad (3.12)$$

This means that once N is known α^P is also known. a^P is then simply the integral of α^P over the cloud size l ,

$$a^P \equiv \int_0^{\infty} \alpha^P(l) dl. \quad (3.13)$$

Chapter 4

Size statistics of cumulus cloud populations in large-eddy simulations

Neggers, R. A. J., H. J. J. Jonker and A. P. Siebesma. *Accepted for publication in the Journal of the Atmospheric Sciences, August 2002.*

4.1 Summary

Cloud size distributions of shallow cumulus cloud populations are calculated using the Large-Eddy Simulation (LES) approach. A range of different cases is simulated, and the results are compared to observations of real cloud populations. Accordingly the same algorithm is applied as in observational studies using high-altitude photography or remote sensing.

The cloud size density of the simulated cloud populations is described well by a power-law at the smaller sizes. This scaling covers roughly one order of magnitude of cloud sizes, with a power-law exponent of -1.70 which is comparable to exponents found in observational studies (Cahalan and Joseph, 1989; Kuo et al., 1993; Benner and Curry, 1998). A sensitivity test for the resolution suggests that the scaling continues at sizes smaller than the standard grid-spacing. In contrast, on the other end the scaling region is bounded by a distinct scale-break. When the cloud size is non-dimensionalized by the scale-break size, the cloud size densities of all cases collapse. This corroborates the idea of a universal description for the whole cloud size density, with the scale-break size as the only variable. The intermediate dominating size in the cloud fraction and mass flux decompositions is directly related to the presence of the scale-break in the cloud size density. Despite their large number, the smallest clouds contribute very little to the total vertical mass transport. The intermediate size of the dominating clouds in the cloud fraction and mass flux is insensitive to the resolution of LES.

4.2 Introduction

Shallow cumulus cloud fields are inhomogeneous and broken in structure, and the individual clouds are irregular over a wide range of scales. This complicates the parameterization of the radiative and transport effects of such cloud ensembles in General Circulation Models

(GCMs) in several ways. Firstly, such cloud populations scatter incoming solar radiation in all directions. A radiation scheme that has knowledge of the geometrical structure of such a cloud field is required. Secondly, convection schemes in GCMs are used to predict the vertical transport of heat, moisture and momentum by convective cloud fields (e.g. Arakawa and Schubert, 1974; Tiedtke, 1989; Gregory, 2001). To describe the interaction between clouds and their environment, entrainment and detrainment rates are used. Many theories exist on the relation between cloud mixing and cloud size. Accordingly, more observational evidence is needed about the cloud size distribution, and about the clouds which contribute most to the cloud fraction and vertical transport.

These issues have been the motivation behind many observational studies of shallow cumulus cloud populations. Such studies have used aircraft photographic images, radar data, satellite images and other remote sensing instruments. There have been many efforts to extract a functional relation for the *cloud size density*, defined as the probability density function of the number of clouds as a function of cloud size. The goal is to find out if a universal functional form exists that contains a minimum but enough non-universal parameters to apply to all situations. However, there is no agreement on this yet. Several possible candidates are mentioned in the literature: an exponential (Plank, 1969; Wielicki and Welch, 1986), a log-normal (Lopez, 1977) and various power-laws (Cahalan and Joseph, 1989; Kuo et al., 1993; Benner and Curry, 1998). The three studies last mentioned report a scale break in the power-law, which has been related by Cahalan and Joseph (1989) to the largest individual convective cells which exist in the boundary layer. Nevertheless, Lopez (1977) pointed out that no analysis of observational results has yet been able to exclude any of these candidates for certain.

Concerning the cloud fraction, small cumulus clouds are the most numerous in the population but cover a relatively little area individually. On the other hand, large clouds individually cover a large area but seldom occur. Due to this trade-off between cloud number and cloud size, it is not known a priori what size clouds contribute most to the total cloud fraction of the population. Observational evidence was presented by Plank (1969) using photographs of cumulus cloud fields over Florida taken from aircraft, and by Wielicki and Welch (1986) using Land-Sat images. In all cases, an intermediate size between the largest and smallest size present in the population dominated the cloud fraction. The dominating size varies over the cumulus scenes studied, but is always well-defined and intermediate. Closely related to the cloud area is the vertical mass flux by a cloud, being the product of cloud area and cloud vertical velocity (Arakawa and Schubert, 1974; Tiedtke, 1989). Knowledge of the vertical velocities inside clouds is required to calculate mass flux distributions. Measurements of both the cloud diameter and the vertical velocity of individual clouds can be provided by aircraft trajectories through cumulus clouds (e.g. Warner, 1970b, 1977; Raga et al., 1990; Barnes et al., 1996) or radar measurements (e.g. Lehrmitte, 1987; Knight and Miller, 1998; French et al., 1999; Kollias et al., 2001). However, the number of clouds measured with these methods is typically much smaller than the number captured by satellite images, which complicates the calculation of reliable cloud size densities.

Due to improved supercomputer capacity over the last decades, Large Eddy Simulation (LES) has become another tool to study boundary layer clouds. The LES concept has several useful advantages which observational data can not offer. Firstly, it can be used to simulate detailed, time-dependent, full three-dimensional fields of the thermodynamic variables and

(vertical) momentum. For example, mass flux distributions as a function of cloud size can be calculated easily in LES. Secondly, it offers unparalleled statistics because the number and duration of the simulations are only limited by the ever growing supercomputer capacity. Thirdly and most importantly, all conditions of the simulated case are exactly defined and completely controlled by the user, which enables the reproduction of obtained results for similar settings. This makes LES useful for studying the impact of certain key variables which are thought to be relevant in the problem. It is therefore ideal to test hypotheses or parameterizations for GCMs. Several LES inter-comparison studies by the GEWEX Cloud Systems Studies Working-group 1 (GCSS WG1) have shown that LES is robust in reproducing the bulk vertical turbulent transport of the cloud ensemble (Siebesma et al., 2002; Stevens et al., 2001; Brown et al., 2002).

In spite of all these advantages, LES is still a numerical model, and the question remains if LES realistically resolves the individual clouds which are most important for the projected cloud fraction and mass flux. More insight into this problem can be obtained by studying the properties of simulated clouds and compare them to observations of real clouds. For example, Xu and Randall (2001) compared the updrafts and downdrafts in cumulus clouds as simulated by a cloud resolving model to aircraft observations. Siebesma and Jonker (2000) showed that the fractal dimension of *individual* cloud boundaries are in excellent agreement with observations (Lovejoy, 1982). However, to characterize whole cloud *populations*, cloud size distributions have to be used. One of the earliest attempts to do this in LES is described by Beniston and Sommeria (1981), but then the results were still hampered by a coarse resolution. The most recent study of simulated cloud size distributions using LES was published by Brown (1999b), who evaluated the sensitivity of the cloud size distributions to the numerical resolution.

This study critically compares the cloud size densities produced by LES to those of observed natural cloud fields as reported in the literature. To enable a straightforward comparison, exactly the same method is used in deriving the cloud size densities, and a comparable number of clouds is sampled. Several different shallow cumulus cases are simulated, and the results are used to study the universality of the functional form thought to be applicable to the cloud size density. To this purpose, typical relevant scales are searched in order to reduce the problem of reconstructing the cloud size density to a minimum number of parameters. Furthermore, the underlying relations between the cloud size density and the decompositions of the cloud fraction and mass flux with cloud size are used to investigate which cloud size contributes most to these properties. Finally, some sensitivity tests are performed to study the impact on these results of several numerical features and of the vertical wind-shear.

The LES model used in this study and the cumulus cases simulated are described briefly in section 4.3. The necessary definitions and the method are presented in section 4.4. The results are given in section 4.5, and are discussed in section 4.6.

4.3 The LES model and case descriptions

A detailed description of the LES model used in this study is given by Cuijpers and Duynkerke (1993), therefore only a short description will be given here. The governing equations for high Reynolds-number atmospheric flow are applied to a limited three-dimensional

domain and filtered at a certain length-scale in the inertial subrange of turbulence. The resulting discretized equations are solved using a centered difference advection scheme and time integration is performed. The sub-grid model uses a prognostic equation for the turbulent kinetic energy on sub-grid scales. The sub-grid length-scale ℓ_0 is related to the grid-spacing, $\ell_0 \sim (\Delta x \Delta y \Delta z)^{1/3}$. Close to the surface ℓ_0 is taken proportional to the height above the surface. The sub-grid length scale is also corrected for stable conditions.

Three different shallow cumulus cases are selected for simulation. Each LES case is based on the measurements and observations made during the measurement-campaign of the corresponding name. An overview of the vertical profiles of all cases is given in Fig.4.1. For the details of the simulations see Table 4.1. The first case is based on BOMEX during which steady state cumulus convection was observed for a period of several days. A detailed description can be found in Siebesma and Cuijpers (1995). The convection in the boundary layer is driven by surface fluxes, the latent and sensible heat fluxes being 150 and 8 W/m² respectively. A dry well-mixed layer is topped by a conditionally unstable cloud layer, which in turn is capped by a stable Trade-wind inversion (see Fig.4.1a). A prescribed large scale subsidence at the inversion causes drying and warming in the LES case, balancing the moistening and cooling effect of the clouds. An ensemble of 10 BOMEX runs is performed, each member initialized with a differently randomized initial temperature profile which causes the runs to be statistically independent. The first three hours of each simulation are consid-

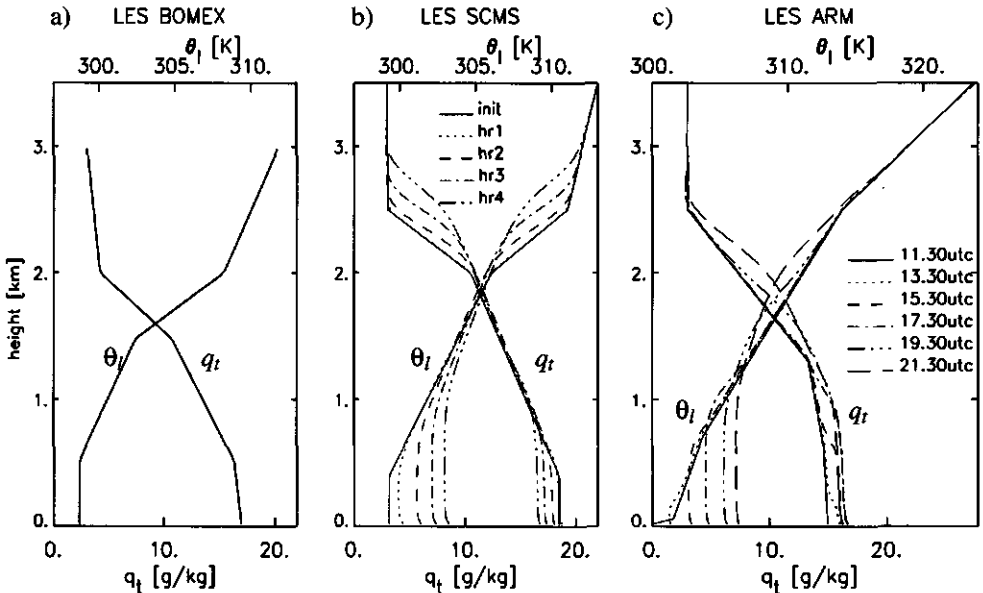


Figure 4.1 Overview of the vertical profiles of total specific humidity q_t and liquid water potential temperature θ_l of a) the BOMEX case, b) the ARM case and c) the SCMS case. The initial profiles are drawn as solid lines, subsequent hourly averages of the LES simulations have a different style as indicated by the legend.

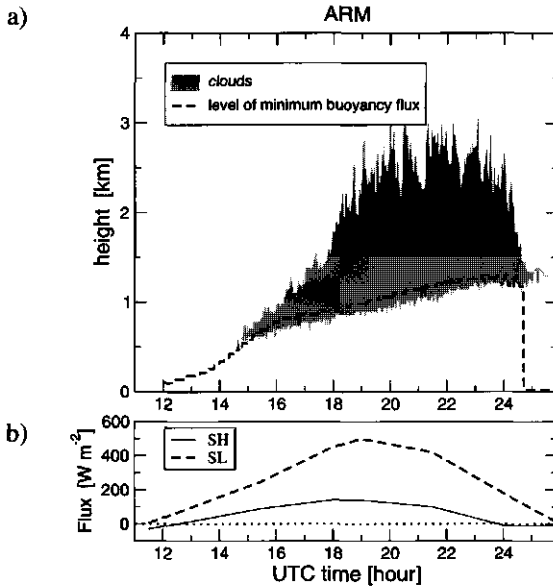


Figure 4.2 Timeseries of a) the heights of cloud top and cloud base and b) the surface fluxes during the diurnal cycle of the ARM case. The total heat flux is the sum of the latent and sensible heat fluxes. Local time is UTC minus 6 hours. The height of the level of minimum buoyancy flux z_{w0} , is also plotted in a) to indicate the depth of the dry convective boundary layer. At about 01:00 UTC the cumulus convection breaks down totally.

ered as the startup phase in which the system had to find its steady state equilibrium. This results in about $4 \cdot 10^4$ sampled clouds, which makes the statistical quality of the resulting histograms comparable to observational studies, which are typically based on 10^4 clouds.

The second case is based on observations on August 5th, 1995 of the Small Cumulus and Micro-physics Study (SCMS). This cloud measurement campaign took place near Cocoa beach, Florida. On this day, strong cumulus convection was observed over land. The initial profiles are based on flight legs made during the afternoon, during which the temperature and humidity of the cloud-free atmosphere was measured up to 4 km. The cloud layer was about 1.5 km thick and was deepening with time, see Fig.4.1b. The surface latent and sensible heat fluxes were set constant in time at 300 and 150 W/m^2 respectively. Note that the sensible heat flux is about twenty times larger than that of the BOMEX case. The geostrophic wind forcing was $(-4,4)$ m/s in the zonal and meridional direction, and fairly constant with height. The friction velocity at the surface was 0.18 m/s. The stronger surface fluxes compared to the BOMEX case cause more vigorous vertical transport by the clouds. Consequently, this case is suitable for use in a sensitivity test on the domain size used in LES. When chosen too small, the dimensions of the domain at some stage limit further growth of the maximum cloud size in the spectrum.

Finally, the third case is based on development of shallow cumulus over land such as observed on June 21st, 1997 at the Southern Great Plains (SGP) site in Oklahoma of the

case	grid spacing [m]		domain size [km]		surface fluxes [W/m ²]		number of sampled clouds
	$\Delta x, \Delta y$	Δz	L_x, L_y	L_z	SH	SL	
BOMEX							
reference	50	40	6.4	3			36.776
high resolution	25	"	"	"			25.417
low resolution	100	"	"	"	8	150	22.652
high shear 2x	50	"	"	"			18.379
no shear 0x	50	"	"	"			20.542
SCMS							
reference	50	40	6.4	5			20.268
large domain	100	"	12.8	"	150	300	16.404
small domain	25	"	3.2	"			18.118
ARM							
diurnal cycle	66.67	40	6.4	4.4	140 max. at noon	500	35.137 whole day

Table 4.1 Overview of the details of the simulations of all cases. Δ_x , Δ_y and Δ_z are the grid-spacings on the three spatial axes, and L_x , L_y and L_z are the corresponding dimensions of the simulated domain. SH and SL stand for the sensible and latent heat flux at the surface. Every 5 minutes a 3D instantaneous field was sampled for clouds. To obtain sufficient statistics, more than one run was performed, using a differently randomized initial temperature profile.

Atmospheric Radiative Measurement (ARM) program. This case has been designed for an LES inter-comparison study of GCSS (Brown et al., 2002). A diurnal cycle was observed in a cumulus topped convective boundary layer over land. Radiosonde soundings, surface flux measurements and cloud radar observations were made on this day. This case is initialized at 11:30 UTC around sunset with a stable boundary layer, see Fig.4.1c and Fig.4.2. During the morning the surface fluxes increase to a maximum at 19:00 UTC, and as a result a dry convective boundary layer develops. Above this layer a conditionally unstable cloud layer forms at about 14:30 UTC which deepens with time. It is interesting to study how the cloud population reacts to the deepening cloud layer and the changing surface fluxes in this case.

Fewer clouds could be sampled in the SCMS and ARM cases compared to BOMEX, because they are not in steady state, and the sampling period per run was therefore kept relatively short.

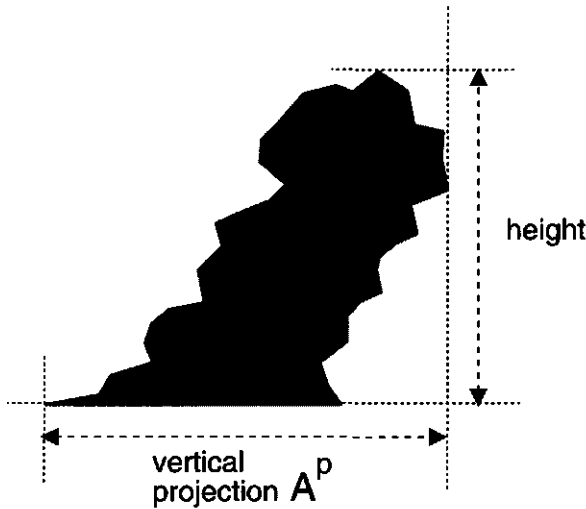


Figure 4.3 Several different measures of a single cumulus cloud, shown in a schematic vertical cross-section.

4.4 Definitions

The *cloud size distribution* of cumulus cloud populations is defined as the integral over a probability density function (pdf). This pdf, also known as a *cloud size density*, is the probability of occurrence of a cloud of a certain size. Cloud size *decompositions* can be calculated for some important properties which characterize the population, i.e. the cloud fraction and the vertical mass flux as a function of cloud size.

An algorithm has to be defined to extract cloud size densities from simulated cloud fields produced by LES. The method of deriving them will be kept as close as possible to those of previous observational studies, in order to be able to compare the LES results to data of real cloud populations. Each cloud (n) in the population is first given a unique linear size (ℓ_n). Although seemingly trivial, this is an important subject as there are many options for the definition of the ‘size’ of a cloud (see Fig.4.3). The most simple definition is to take the square root of the area of the cross-section of a cloud at a certain height. But when using two-dimensional (projected) images of real cloud fields taken from high altitudes, the vertically projected area A_n^p of a cloud n has to be used.

$$\ell_n = \sqrt{A_n^p} \quad (4.1)$$

As there have been many analyses of satellite images in the past, we want to compare the LES results to these studies and accordingly we prefer to use this definition.

Once the linear size ℓ_n has been defined, we can sort all the clouds by their size and build histograms. This algorithm is described in detail in Appendix A, only the most important definitions will be mentioned at this point. The total number of clouds N present in the domain at a certain time is defined by the integral of the corresponding cloud size density

$N(l)$:

$$N \equiv \int_0^{\infty} N(l) dl \quad (4.2)$$

where the term $N(l)$ is the number of clouds of size l in the domain. The *cloud fraction* of a cloud field is defined as the ratio between the area covered by all clouds and the total area of the domain. From vertical projections of real cumulus cloud fields as observed from high altitudes, only the *vertically projected* cloud fraction a^P can be derived, defined as the integral of the cloud fraction decomposition α^P over the cloud size l ,

$$a^P \equiv \int_0^{\infty} \alpha^P(l) dl. \quad (4.3)$$

The cloud fraction decomposition α^P denotes the contribution to a^P as a function of cloud size l , and can be written as

$$\alpha^P(l) \equiv \frac{l^2 N(l)}{L_x L_y}. \quad (4.4)$$

where L_x and L_y are the horizontal dimensions of the domain. This means that once N is known α^P is also known.

Another property often studied is the cloud fraction *at one height* $a(z)$, defined as the horizontal area covered by clouds at height z divided by the total area of the domain. This can typically be derived from data measured by aircraft flying through cumulus clouds. Evaluating $a(z)$ at different heights using cloud size densities gives information about the most important clouds for the cloud fraction as a function of height. The definition of the height-dependent cloud fraction decomposition $\alpha(l, z)$ is comparable to (4.4) and (4.3), the only difference is that N is now calculated for a number of different height ranges.

The vertical *mass flux* associated with a cloud population is usually defined as the product of the cloud fraction and the cloud-average vertical velocity w ,

$$m(z) \equiv a(z) w(z). \quad (4.5)$$

The mass flux decomposition $\mu(l, z)$ at height z is defined as

$$m(z) \equiv \int_0^{\infty} \mu(l, z) dl, \quad \mu(l, z) \equiv \alpha(l, z) w(l, z), \quad (4.6)$$

where $w(z, l)$ is the average vertical velocity of the clouds of size l at height z . In order to reach a height-independent definition of the mass flux, we introduce an average mass-flux over the depth of the cloud layer,

$$m \equiv \int_0^{\infty} \mu(l) dl, \quad \mu(l) \equiv \frac{1}{h_c} \int_{h_c} \mu(l, z) dz \quad (4.7)$$

where h_c is the depth of the cloud layer. To prevent a cloud from being represented in different bins at different levels when calculating $\mu(l)$ using (4.7), the clouds are sorted using the same size at all heights, namely its vertically projected area (see (4.1)). In this way, $\mu(l)$ is analogous to $\alpha^P(l)$.

It is likely that $\alpha^P(l)$ differs from $\alpha(l, z)$, as cloud overlap has a significant impact. Brown (1999b) calculated cloud fraction decompositions at one height in BOMEX using LES. In contrast, we will concentrate on the vertically projected fields to enable a straightforward comparison to satellite data.

4.5 Results

In order to critically compare the cloud populations produced by LES to high-resolution observations of real cloud populations, the cloud size densities need to be characterized by fitting one of the functions proposed in the literature. Subsequently the resulting parameters can be compared to the observed values.

As mentioned in the introduction, there have been many efforts to extract a functional relation for the cloud size density from observations of natural cloud populations, but there is no agreement on this yet. An early proposed functional form is the exponential (Plank, 1969; Wielicki and Welch, 1986). Lopez (1977) suggested the log-normal function. The most frequently mentioned proposition in recent years is the power-law (e.g. Cahalan and Joseph, 1989; Kuo et al., 1993; Benner and Curry, 1998). Accordingly, to the purpose of a comparison of LES results with recent observations as quantitatively as possible, we also use the power-law functional form, defined by

$$N(l) = a l^b. \quad (4.8)$$

A scale-break is defined as the cloud size at which this functional relation breaks down, or in other words the size where the exponent b suddenly changes. The match between LES and observations in terms of the parameters resulting from power-law fits on the densities is a good indication of how realistic the simulated cloud populations actually are.

All histograms presented in this section were obtained by sorting in equidistant bins on a linear l axis. However, the cloud size density N is normally plotted using log-log axes, for better visualization. The relationship between the histogram N on a linear and on a logarithmic l -axis is given by

$$N^*(\log l) = N(l) \frac{dl}{d\log l} = l \ln 10 N(l). \quad (4.9)$$

Note that if $N(l)$ is a power-law, $N^*(\log l)$ is also a power-law but with the exponent increased by 1.

4.5.1 Cloud size densities

Figure 4.4a shows the histogram of the cloud size density N^* for the simulated cases based on ARM, BOMEX and SCMS. Each case is simulated using the same domain size and approximately the same resolution. N^* is normalized by the total number of clouds (N) in the domain. What immediately catches the eye is the collapse of the three histograms for the smaller clouds. In all cases the slope of the density is approximately constant in a range of sizes of more than one order of magnitude wide. This suggests that in this region the density is well represented by a power-law function with a negative exponent. The other functional forms are less likely to apply in this region, as both log-normal (Lopez, 1977) and exponential (Wielicki and Welch, 1986) functions have non-constant derivatives and intermediate maxima in a loglog plot.

Accordingly, a linear least-squares fit is applied to the scaling range of sizes bounded by the grid-spacing on one end and a distinct scale-break on the other, see Fig.4.4a. The slope of

the density is -0.70 , somewhat larger than the value of -0.89 found by Cahalan and Joseph (1989) for remote sensed real clouds. The value of -0.70 corresponds by formula (4.9) to $b = -1.70$ in (4.8). Benner and Curry (1998) calculated power-law exponents of many tropical shallow cumulus cloud populations, and found it to be on average -1.98 for the smaller clouds, with some spread around this value. Therefore, considering both the value of the power-law exponent at the smaller sizes and the presence of a scale break, these simulated cloud populations using LES seem realistic. Figure 4.4b further emphasizes the robustness of the typical slope of the cloud size density below the scale-break in LES.

The projected cloud fraction decomposition α^p is uniquely determined by the number density N , because it is simply a product of N and the projected area l^2 , see (4.4). Dividing by the total number of clouds (N) makes the cloud fraction decompositions collapse at the smaller cloud sizes, see Fig.4.5a and b. The power-law behaviour of the densities is even more profound in this figure. The intermediate maximum in α^p is located at the position of the scale-break in N . The fact that α^p and N are so closely related and behave so uniformly in the three simulated cases, supports the idea that they can be parameterized by a universal functional form. Knowledge of the position of the scale-break and the power-law exponent enables the reproduction of the cloud size density and the projected cloud fraction decomposition, at least for the cloud sizes smaller than the scale-break. The power-law exponent seems to be rather robust over all cases, but in contrast the scale-break size differs considerably, see Table 4.2. During the ARM case, the location of the scale-break also progresses towards larger sizes with time, reaching a maximum in the afternoon. One might think that the sudden break in the scaling at the larger cloud sizes is a result of insufficient statistics, as the very large clouds seldom occur. However, a convergence test (not shown) made clear that

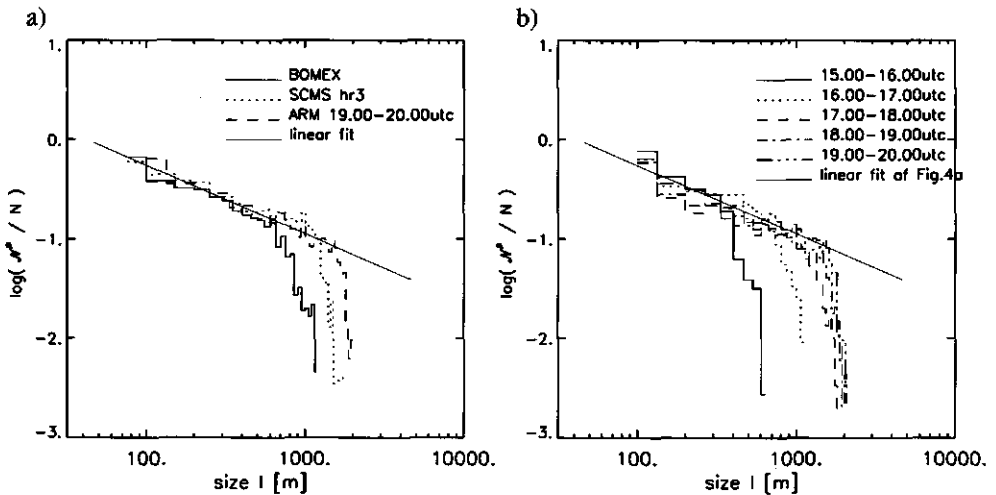


Figure 4.4 The normalized cloud size density N^*/N of a) the BOMEX, SCMS and ARM cases, and of b) subsequent stages in the diurnal cycle of the ARM case. The solid line corresponds to the linear fit $N^*/N = 1.121 - 0.70 \log l$, based on the points with cloud sizes smaller than the scale-break size.

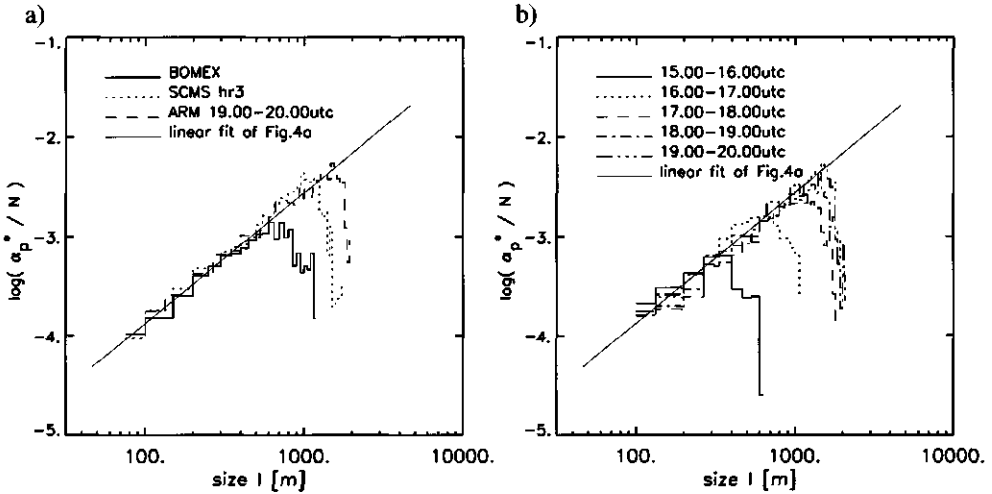


Figure 4.5 The normalized projected cloud fraction decomposition α_p^*/N of a) the BOMEX, SCMS and ARM cases, and of b) subsequent stages in the diurnal cycle of the ARM case. The linear fit corresponding to Figure 4.4a using (4.4) is also plotted as a solid line.

this is not the case: improving the statistical quality of the histogram by increasing the number of sampled clouds does not affect the position of the scale-break, nor does the histogram change at the sizes above the break.

These results suggest that the scale-break size is the only relevant length-scale in the cloud size density. Therefore we further scale the cloud size densities by non-dimensionalizing the cloud size with the scale-break size (see Fig. 4.6). The data-collapse in this figure of all cases over all sizes corroborates the idea of a universal description of the whole cloud size density, also above the scale break. In this region clearly another exponent applies, or perhaps even a

Case	Scale-break size [m]
BOMEX	700
SCMS	1050
ARM 15-16 UTC	400
ARM 16-17 UTC	700
ARM 17-18 UTC	1000
ARM 18-19 UTC	1100
ARM 19-20 UTC	1250

Table 4.2 The position of the scale-break in the cloud size densities of the BOMEX, SCMS and ARM case.

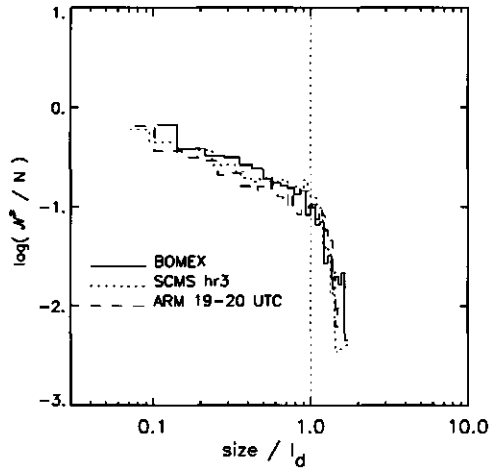


Figure 4.6 The normalized cloud size density N^*/N of the BOMEX, SCMS and ARM cases. The cloud size ℓ on the horizontal axis is divided by the scale-break size ℓ_d . The dotted line marks the scale-break.

totally different functional form. Nevertheless, Fig.4.6 illustrates that the scale-break size is the only variable. Which mechanism controls the occurrence of the scale-break size is a key question that still remains open after this study. The results on the ARM case might suggest that the depth of the (sub)cloud-layer plays a role (see also Fig.4.2). Cahalan and Joseph (1989) suggested that the scale-break size is related to the largest individual convective cells which exist in the boundary layer. Another possible mechanism was discussed by Jonker et al. (1999a). In this LES study the important role of (fluctuations in) the specific humidity field was revealed by filtering out the large scale humidity fluctuations in the sub-cloud layer. This immediately had a dramatic effect on the typical cloud size of the population.

4.5.2 Domination by intermediate sized clouds

Figure 4.7a shows the same projected cloud fraction decompositions, but now plotted non-normalized with linear axes (a common format in many presentations of observational results). The total projected cloud fraction a^p in each case is the surface covered by the histogram (see Table 4.3). Also in this figure the clouds of an intermediate size contribute most to a^p in all three cases. The fact that the dominating size is intermediate results from the existence of the scale-break in N , which is closely related to α^p , see (4.4). If N were a simple

Case	a^p [%]	m [m/s]
BOMEX	14.15	0.015
SCMS	26.72	0.060
ARM 19-20 UTC	23.27	0.043

Table 4.3 The total projected cloud cover a^p and the total mass flux m for the BOMEX, SCMS and ARM case.

power-law with exponent b without a scale-break, then

$$\alpha^p(l) \sim l^{(b+2)} \rightarrow \begin{cases} b < -2 & \text{domination by the} \\ & \text{smallest clouds} \\ b > -2 & \text{domination by the} \\ & \text{largest clouds} \end{cases} \quad (4.10)$$

Instead, in accordance with observations we do find a scale-break, with $b = -1.70$ below and $b < -2$ above the scale-break size. This implies that $\alpha^p(l)$ increases with l below the scale-break and decreases above it: hence a dominating size which is intermediate. Again this shows that the existence of the scale-break in N is essential for the presence of an intermediate dominating size in α^p . Knowledge of the position of the scale-break directly gives the dominating size in the projected cloud fraction and vice versa. This intermediate dominating size is also typically found in the projected cloud fraction decomposition of real shallow cumulus cloud fields (Plank, 1969; Wielicki and Welch, 1986). It illustrates that LES resolves a cloud population with characteristics comparable to nature. The one-gridbox-clouds in LES seem to cover somewhat too much area as would be expected from these observations, which typically show α^p to be converging to zero for the smallest clouds. This is probably caused by the numerics of the model (see next section).

In the mass-flux decomposition $\mu(l)$ as shown in Fig.4.7c the dominating size is even better defined, although shifted somewhat towards the larger sizes compared to the projected cloud fraction decomposition. This results from the fact that the mass flux is the product of the projected cloud fraction and the cloud-average vertical velocity (see Fig.4.7b). The smallest clouds in the spectrum contribute close to nothing to the vertical transport, mainly because of their very low vertical velocities.

More insight in the role of the smallest clouds may be obtained from Fig.4.8. It shows the vertical profiles of the contribution of clouds larger than a certain size to the cloud fraction $a(z)$ and the related mass flux $m(z)$. At cloud-base ($z=600\text{m}$) the clouds smaller than 200m indeed contribute the most. At greater heights the larger clouds become much more important. This reflects the presence of the numerous small clouds near cloud base which do not rise very far into the cloud layer. The smallest clouds contribute very little to the mass flux, except at cloud base where their large number somewhat compensates their low vertical velocities. The largest clouds even show a slightly increasing mass flux with height, due to their approximately constant fraction (see Fig.4.8a) and increasing vertical velocity with height.

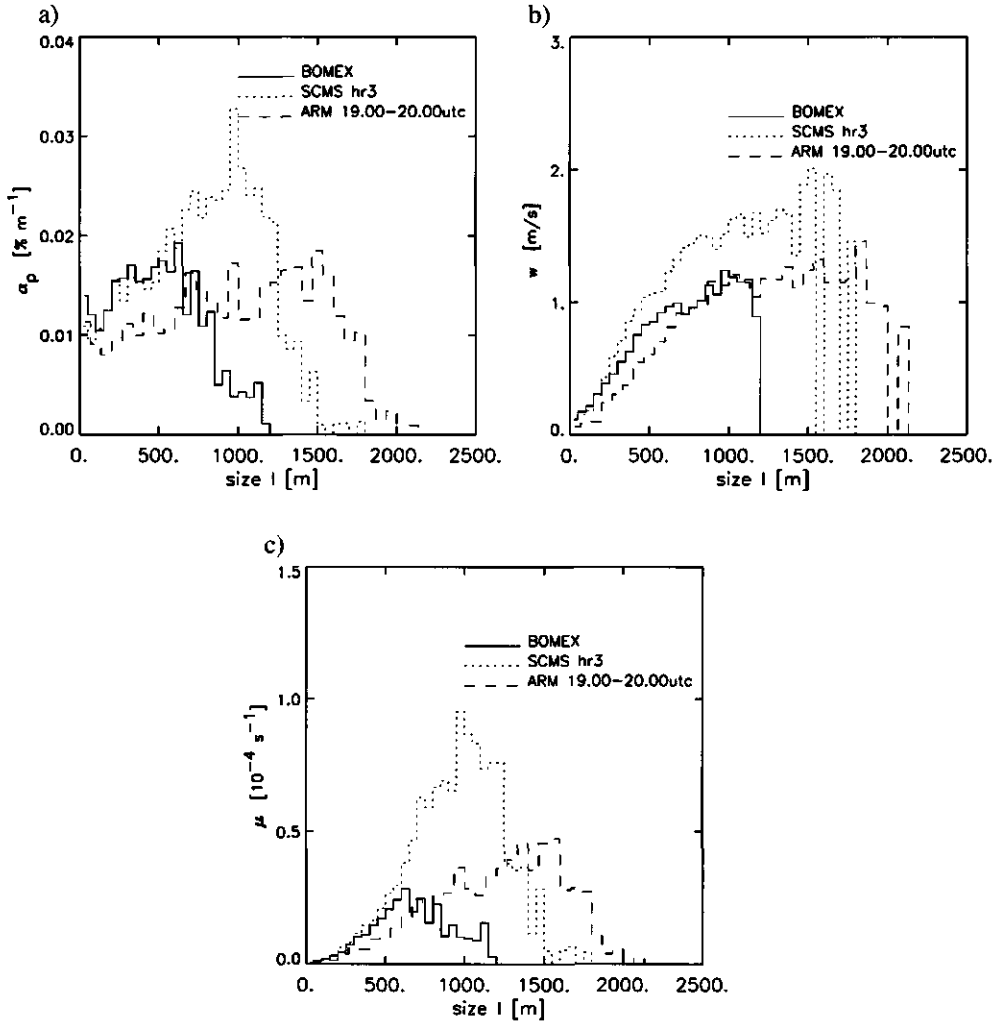


Figure 4.7 Cloud size decompositions of the BOMEX, SCMS and ARM case of a) the projected cloud fraction α^p and c) the vertical mass flux μ . Figure b) shows the cloud-average vertical velocity w as a function of cloud size.

4.5.3 Sensitivity to resolution

The results discussed previously in this section were obtained with simulations using only one particular numerical configuration. Therefore, several aspects of the numerics are altered to investigate whether the size distributions are robust with respect to changes in discretization or not. Firstly, the influence of the horizontal grid-spacing is studied by performing additional runs with horizontal grid-spacings of 25m and 100m, retaining the domain size. Fig.4.9a illustrates that the smallest clouds are always the most numerous. The scaling seems to continue at ever smaller sizes, which further supports the use of the power-law function for the

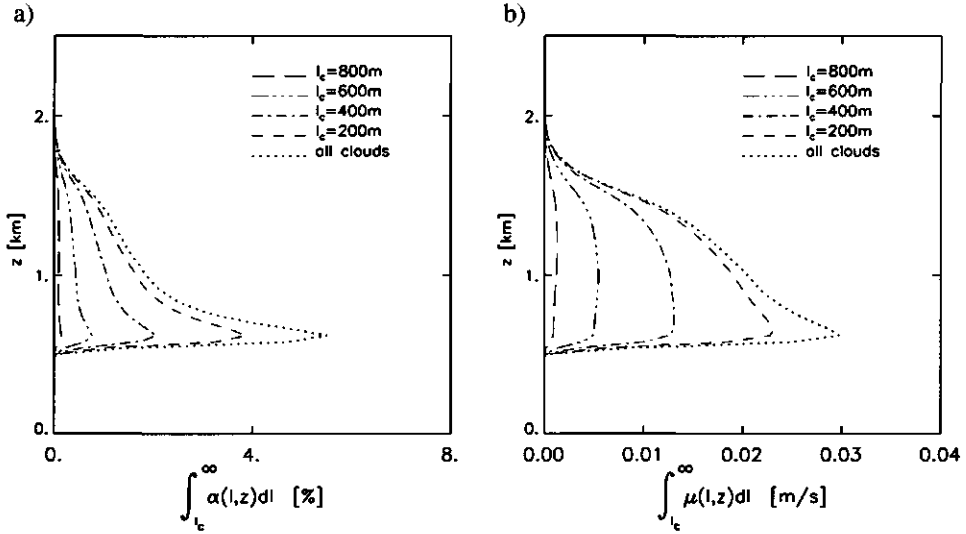


Figure 4.8 Vertical profiles of the cumulative cloud size decompositions of a) cloud fraction $\alpha(l, z)$ and b) mass flux $\mu(l, z)$. The cumulative decomposition is the sum of all bins of the sizes larger than a certain value l_c , as indicated in the legend.

Specifics of simulation	a^p [%]	a^{max} [%]	$\frac{a^p}{a^{max}}$	m [m/s]
$\Delta x = 100m$	14.48	5.85	2.48	0.0127
$\Delta x = 50m$	14.15	5.57	2.54	0.0145
$\Delta x = 25m$	16.41	6.12	2.68	0.0162
0x shear	13.04	6.58	1.98	0.0145
1x shear	14.15	5.57	2.54	0.0145
2x shear	19.38	6.36	3.04	0.0149

Table 4.4 The total projected cloud fraction a^p , the maximum cloud fraction a^{max} in the cloud layer, their ratio, and the total mass flux m for several BOMEX simulations. The first three simulations had a different horizontal resolution, the last three had a varying wind-shear.

cloud size density below the scale-break. Nevertheless, at least one extra order of magnitude of small cloud sizes is needed to get some certainty about this. This would require a grid-spacing of about 1 or 2m in LES, a resolution which is expected to be manageable in the near future.

With decreasing grid-spacing each one-gridbox cloud also contributes less to the total cloud fraction because its area is smaller. This counteracts the observed increasing number of smallest clouds. A priori it is not known which of these two processes dominates, or in other words, if the cloud fraction decomposition converges to small values for the smallest

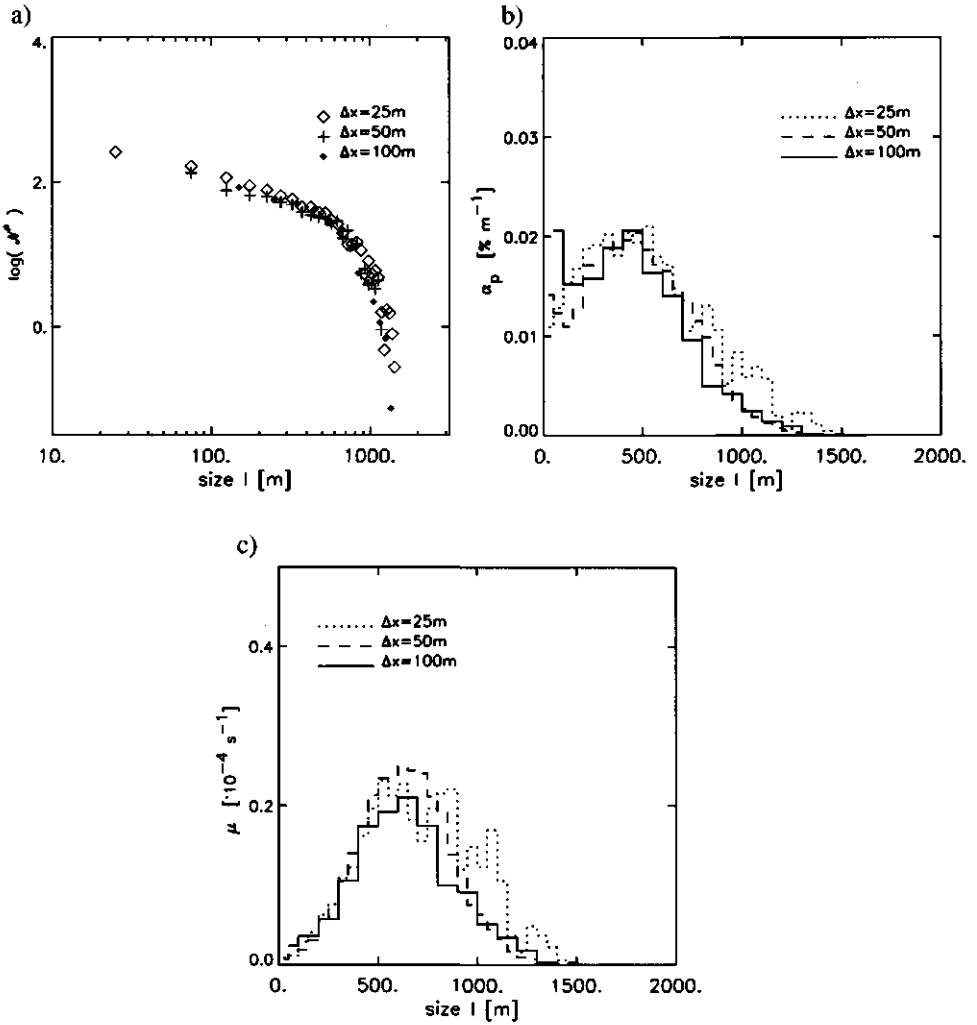


Figure 4.9 The a) cloud size densities N^* and the size decompositions of b) the projected cloud fraction α^P and c) the mass flux μ for LES runs of the BOMEX case with horizontal grid-distances of 25m, 50m and 100m.

clouds with increasing resolution. Figure 4.9b illustrates that α^P converges towards zero at the smallest cloud size with increasing resolution. As a consequence, the intermediate dominating size becomes better defined. But the most important thing is that its intermediate position as well as its amplitude are invariant in this range of grid-spacings. Even in the simulation with the very coarse grid-spacing of 100m, which is close to the dominating size in the cloud fraction and which is also used in the GCSS case of BOMEX (Siebesma et al.: *Large-eddy simulation intercomparison study of shallow cumulus convection. Submitted to J. Atmos. Sci.*), the dominating clouds have the same size. Also note that the largest cloud size

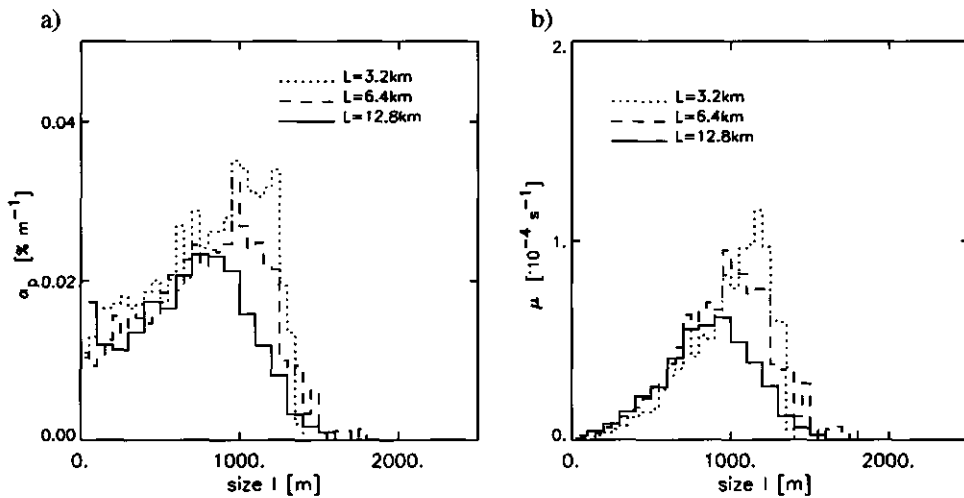


Figure 4.10 The cloud size decompositions of a) the projected cloud fraction σ^p and b) the mass flux μ for three LES runs of the SCMS case with horizontal domain-sizes of 3.2km, 6.4km and 12.8km, averaged over the 3d hour of simulation.

produced by LES is robust in this range of resolutions. In general the conclusion is that the shape of the cloud fraction decomposition is unaffected by changes of grid-spacings in this range.

Table 4.4 shows that the changes in the projected cloud fraction and in the maximum cloud fraction at any level in the cloud layer are not systematic. However, the total cloud mass flux seems to increase with improving resolution. A smaller grid-spacing makes the LES model resolve the dynamics on increasingly smaller scales, but note that the smallest clouds are not responsible for the increase in mass flux: the largest differences are caused by the clouds of sizes equal to the dominating size or larger. The histogram of $\Delta x=25\text{m}$ in Fig.4.9b and 9c clearly is not smooth and shows significant peaks at the largest sizes. Larger clouds occur less frequently, and when the period of averaging is too short this causes scatter in the cloud size density which increases with cloud size. Only a few high-resolution runs could be performed due to limited available CPU-simulation time. Furthermore, The impact of this increasing scatter with size in the cloud size density on the decompositions of the cloud fraction and mass flux is further amplified by the fact that larger clouds also cover a larger area individually. To summarize, the impact of scatter caused by bad statistics increases with cloud size. This is clearly visible in Fig.4.9b and 9c. The increase in mass flux is therefore likely a result of deteriorating statistics at the largest cloud sizes with improving resolution.

4.5.4 Sensitivity to domain size

Another numerical aspect which may affect the size densities is the dimension of the simulated domain. Three simulations are performed using the SCMS conditions, their horizontal domain sizes being 3.2km, 6.4km and 12.8km. The number of grid-boxes in the horizontal was kept constant at 128x128. This means that the resolution decreases with increasing

domain size, but from Fig.4.9 we conclude that the potential effect of the domain size on the densities probably overwhelms those of the resolution. The cloud size decompositions in Fig.4.10 illustrate that the largest clouds of the undisturbed 12.8km domain run are missing in the spectrum of the 3.2km run, which indicates that the growth of the largest cloud size with time is already limited by this very small domain size in the third hour of simulation. Also, the dominating sizes in the projected cloud fraction and mass flux decompositions have shifted to the largest cloud size. We may conclude that the individual clouds which make up the population are seriously affected if the domain size is chosen too small.

4.5.5 Effects of vertical wind-shear

Vertical shear of the horizontal wind in the cloud layer may influence the position of the dominating size in the size decompositions, as tilting of clouds increases their projected area. Several runs are performed using the BOMEX basic setup with an altered wind-shear over the boundary layer, from zero to twice the standard BOMEX initial wind profile. As may be expected, enhancing the tilting of clouds with height by intensifying the wind shear increases the projected size of a cloud and therefore broadens the cloud size density (see Fig.4.11a). As a result, the total projected cloud fraction gets larger (see Table 4.4). This is in agreement with the results of the study on the effects of shear by Brown (1999a). Note that the changes in total cloud fraction by shear are significantly larger than the impact of changes in resolution in these ranges. Brown (1999a) reported a shift of the cloud size density to smaller cloud sizes with increasing resolution. The heights of the clouds were not affected, which means that the aspect ratio of cloud width over depth is smaller, implying less cloud overlap. This would make the cloud fraction decomposition more sensitive to wind-shear. However, we can not observe such a shift to the smaller sizes with increasing resolution (see Fig.4.9a), and based on this result we do not expect that the impact of shear is dependent on the resolution.

Figure 4.11a illustrates that the position of the scale-break is quite dependent on the intensity of the wind-shear. As a consequence, the closely related intermediate dominating size in the projected cloud fraction and mass flux decompositions also changes (see Fig.4.11b and c). This increasing scale-break size is caused by the tilting of the clouds: the change of the maximum cloud size is approximately proportional to the change of the scale-break size. The existence of the scale-break itself is controlled by something else, as discussed earlier. The presence of wind-shear in the cloud layer only complicates the relation between the exact scale-break size and the process which determines its occurrence in the first place, such as perhaps the boundary layer height.

While the geometry of the individual clouds is affected by the wind-shear, the total vertical mass flux remains approximately constant in all cases (see the area under the histograms in Fig.4.11c and Table 4.4). The vertical turbulent mixing by the clouds tends to destroy the conditional instability in the cloud layer. This is not altered by a different wind-shear. The shape of the clouds itself may change by increasing the shear, but the total vertical transport associated with the cloud fields remains the same.

4.5.6 Comparison to another LES study

Brown (1999b) reported cloud size decompositions in LES which shifted to smaller sizes by

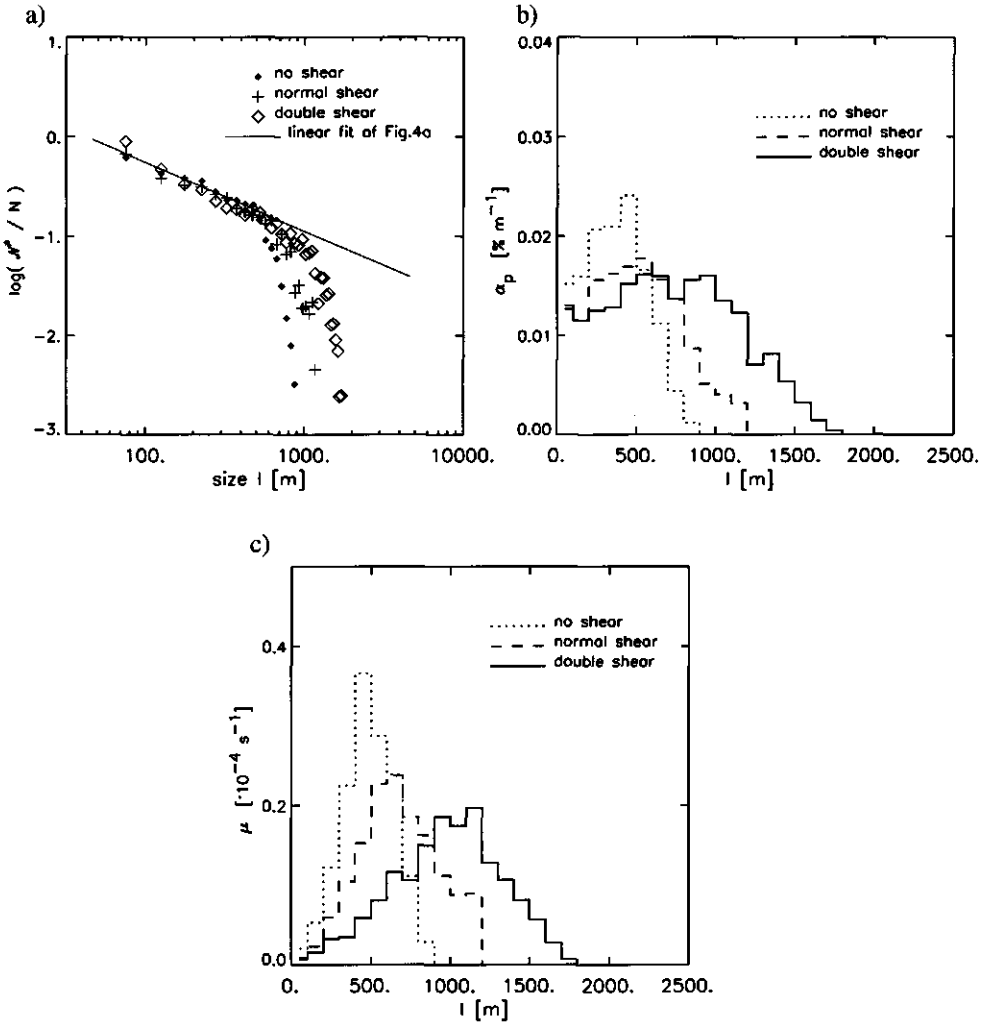


Figure 4.11 The cloud size densities and decompositions of three different LES runs of the BOMEX case, in which the initial profile of the horizontal wind is multiplied by 0, 1 and 2 at all levels, respectively. Figure a) shows the normalized cloud size densities N^*/N , and b) and c) show the size decompositions of the projected cloud fraction α^p and the mass flux μ . The linear fit of Figure 4.4a is also plotted in a) as a solid line.

increasing the horizontal resolution. This is in sharp contrast with the results presented here, in which no shifting takes place: the dominating size is robust and the largest cloud sizes are found to be insensitive to resolution. What is the explanation for these differences? Note that the methods differ at two major points. First, Brown (1999b) derived cloud fraction decompositions *at one level*, while we compute *projected* cloud fraction decompositions. Secondly, he calculated cloud sizes from the cross-sectional areas of the clouds at that particular height,

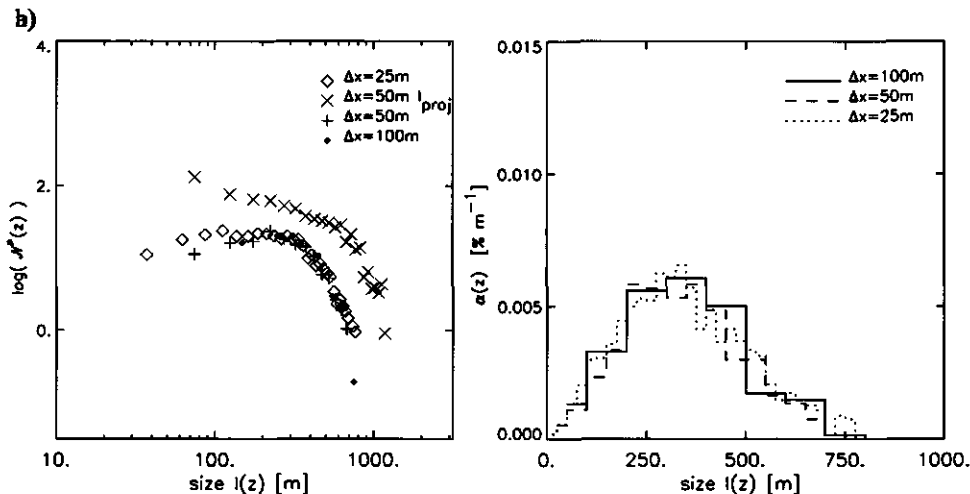


Figure 4.12 The a) cloud size density N^* and b) the cloud fraction decomposition α^p at $z = 900\text{m}$ for the BOMEX case, for three different horizontal resolutions. The cloud sizes $l(z)$ were calculated from the cross-sectional areas of the clouds at that level. The cloud size density of Fig.4.9a with $\Delta x = 50\text{m}$ is also plotted for comparison.

while in this analysis each cloud has one size, namely the square-root of its vertically projected area (see Fig.4.3). The vertical projected area of a cloud takes into account the tilting of clouds by horizontal wind shear and also the typical heterogeneity of the cumulus cloud boundary (Lovejoy, 1982; Cahalan and Joseph, 1989; Benner and Curry, 1998; Siebesma and Jonker, 2000). This method is exactly the same as used in satellite image analyses, and is chosen here to enable a straightforward comparison between the LES results and these observational results.

In order to compare our results with the results of Brown (1999b), we also applied the method he used to the cloud fields as produced by our model. One particular level in the cloud layer in BOMEX is chosen for evaluation, at $z=900\text{m}$. Figure 4.12a illustrates that the cloud size densities produced by the two different methods are very different: when using the projected cloud area, more small clouds and larger cloud sizes are obtained, and the cloud size density decays more rapidly with cloud size. Small clouds can exist at all levels in the cloud layer, while the largest projected clouds typically can be as deep as the cloud-layer itself. Therefore, when vertically projecting the cloud fractions at all heights 'onto' one projected cloud fraction, the number of smaller clouds becomes very large. This results in the typical negative power-law exponent in the cloud size density as found for projected cloud fields. Figure 4.12b shows the cloud fraction decompositions at $z=900\text{m}$, using the method of Brown (1999b). It is clear that this decomposition also does not shift to smaller sizes when the horizontal resolution of the simulations is increased: the maximum cloud size as well as the intermediate dominating size are robust in this range of resolutions.

The remarkable different behaviour of the cloud size densities in these two LES studies may be due to different statistics. Many subsequent cloud fields are needed to sample the clouds with largest sizes and time scales sufficiently. The histograms in this LES study

are always based on about 10^4 clouds or more, which is a number typically captured by high-resolution satellite images. The cloud size densities presented earlier in this paper are calculated with the same method as applied in many observational studies, and we found their power-law exponent and scale break to be realistic. This gives us confidence in the statistical quality of the histograms as presented here.

Another explanation for the different sensitivity to horizontal resolution can be the use of different types of sub-grid scale (SGS) models. The SGS model plays a significant role in the mixing processes between the clouds and their environment, and might therefore have an impact on the cloud size density. The KNMI LES model uses a prognostic sub-grid TKE equation, while a version of the Smagorinsky model is applied in the LES model of Brown (1999b). Stevens et al. (1999) reported that in smoke cloud simulations the use of a Smagorinsky type SGS model results in a much higher sensitivity of the entrainment fluxes to the effective resolution when compared to a prognostic TKE SGS model. This is due to the capacity of the latter model to compensate the SGS eddy viscosity for changes which lead to a smaller resolved entrainment flux, because the same changes simultaneously enhance the buoyant production of subgrid TKE. This feedback mechanism may also apply to the SGS- and resolved entrainment into simulated cumulus clouds, and can therefore be responsible for the observed smaller sensitivity in the KNMI LES model to horizontal resolution. These issues need to be investigated in more detail in future studies.

4.6 Discussion and Conclusions

The main conclusion of this study is that the shallow cumulus cloud populations produced by LES match natural populations at several important points. The simulated cloud size density is well described by a power-law for the smaller clouds, with an exponent of -1.70. The scaling breaks down at a certain cloud size, above which the number density quickly falls off. The sensitivity test for the horizontal resolution suggests that this scaling continues at sizes smaller than the typical grid-spacing of present-day LES, although at least one extra order of magnitude of cloud sizes is needed to actually proof this. These LES results strongly support the power-laws and scale-breaks observed by Cahalan and Joseph (1989), Kuo et al. (1993) and Benner and Curry (1998), and give no evidence for the exponential function (Wielicki and Welch, 1986) or the log-normal function (Lopez, 1977). In conclusion, the observed power law for the smaller cumulus cloud populations appears to be an important and robust geometrical fingerprint. Therefore a quantitative physical explanation for this behaviour is an outstanding scientific challenge that remains to be resolved.

The projected cloud fraction decomposition is uniquely determined by the cloud size density. The existence of the scale-break, combined with the typical power-law exponent for the smaller clouds, causes a well-defined, intermediate dominating size in both the projected cloud fraction and mass flux decompositions. This is consistent with cloud fraction decompositions of observed cloud populations. The cloud size densities show a remarkable uniformity over the three simulated cases. This feature facilitates the parameterization of these cloud size densities and decompositions. The only variable is the position of the scale-break, and with it the dominating size. Which process actually controls the scale-break size remains unclear and is not answered in this study, although we have shown that the (sub)cloud-layer height

and the intensity of wind-shear play a role. Another process which likely affects the size distribution of clouds is the nature of the dry turbulence in the sub-cloud layer, as most large clouds root in this layer. This would link the scale-break size to the cloud-subcloud layer interaction. Perhaps the two distinctly different regimes of the cloud size density above and below the scale-break represent two different processes, the one determined by the coherent structures of the sub-cloud layer turbulence and the other by the decay of the large clouds into smaller ones (the scaling region). It is evident that more thorough research is needed to give insight in this problem. LES would be a suitable numerical laboratory to conduct further research on this subject (e.g. Jonker et al., 1999a).

The intermediate position of the dominating cloud size shows that the clouds which are most important for the projected cloud fraction and vertical transport are not of resolution-scale but are significantly larger. This is fortunate, for the sub-grid model of LES plays an important role in the dynamics of the smallest clouds, while the larger clouds are resolved better by the discretized governing equations. We find here that those larger, better-resolved clouds contribute most to the total projected cloud fraction and mass flux of the population. The smallest clouds contribute close to nothing to the vertical mass transport. This feature is invariant over a range of horizontal resolutions for BOMEX. This point is important for the interpretation of the performance of LES on shallow cumulus in general. Apparently, apart from being robust in producing cloud-field-average statistics, LES is also consistent in producing realistic cloud populations. The exact definition and complete control over all conditions in LES has several important advantages: the possibility of reproducing obtained results for similar settings, and therefore the possibility to carry out systematic impact studies of key parameters in the system. On top of this LES offers almost unparalleled statistical possibilities by performing independent ensemble runs.

Acknowledgements The LES results in this study were obtained using the supercomputer facilities of the European Centre for Medium-Range Weather Forecasts (ECMWF) in Reading, UK. We acknowledge NCAR and its sponsor the National Science Foundation for the use of the SCMS data, which was provided to us by Peter Duynkerke¹. Furthermore we thank two anonymous reviewers for their critical but constructive remarks, and Dave Donovan at the KNMI for carefully prereading and correcting the manuscript. This study has been supported by the Netherlands Organization for Scientific Research under Grant 750.198.06.

¹Deceased January 18, 2002

Appendix 4.A Elementary definitions of cloud size densities

An instantaneous 3d cloud field is denoted by $c(i, j, k, t) \in \{0, 1\}$, (0: non-cloudy, 1: cloudy grid box, where cloudy is defined as the grid-box being saturated). The indices i, j, k are the 3d coordinates of the grid-box, and t marks the time. An off-line algorithm determines the number of individual clouds at time t , denoted by $N(t)$. The algorithm creates N fields $c_n(i, j, k, t) \in \{0, 1\}$, $n = 1, \dots, N$, which indicate whether or not a grid box belongs to cloud number n . We will omit indication of time hereafter.

The volume of cloud n is

$$V_n = \Delta x \Delta y \Delta z \sum_{ijk} c_n(i, j, k) \quad (4.11)$$

The area of cloud n at height $z_k = (k - 1/2)\Delta z$ is

$$A_n(z_k) = \Delta x \Delta y \sum_{ij} c_n(i, j, k) \quad (4.12)$$

The height averaged area is given by

$$A_n^a = \frac{1}{h_n} \sum_{k=k_{n,base}}^{k_{n,top}} A_n(z_k) \Delta z \quad (4.13)$$

where h_n is the height of cloud n

$$h_n = \Delta z [k_{n,top} - k_{n,base} + 1] \quad (4.14)$$

The mass-flux of cloud n at height z_k is (with $\rho = 1$)

$$M_n(z_k) = \Delta x \Delta y \sum_{ij} c_n(i, j, k) w(i, j, k) \quad (4.15)$$

It is useful to define the ‘vertically projected’ fields:

$$c_n^p(i, j) = H \left[\sum_k c_n(i, j, k) \right] \quad (4.16)$$

where H denotes the Heaviside function. The vertically projected area of cloud n is then

$$A_n^p = \Delta x \Delta y \sum_{ij} c_n^p(i, j) \quad (4.17)$$

Each cloud n in the population is given a unique size ℓ_n , as defined in the text. Then, we define the following set:

$$I(\ell) \equiv \{1 \leq n \leq N \mid \ell_n < \ell\} \quad (4.18)$$

i.e. $I(\ell)$ represents the set of clouds which have linear size smaller than a given size ℓ . The number of clouds smaller than ℓ is

$$N(\ell) = |I(\ell)| \quad (4.19)$$

Obviously

$$\lim_{l \rightarrow \infty} N(l) = N \quad \lim_{l \rightarrow \infty} I(l) = \{1, \dots, N\} \quad (4.20)$$

The 'projected' area of clouds smaller than ℓ is

$$A^P(l) = \sum_{n \in I(l)} A_n^P \quad (4.21)$$

with A_n^P defined by (4.17). The mass-flux at z_k transported by clouds smaller than ℓ is

$$M(l, z_k) = \sum_{n \in I(l)} M_n(z_k) \quad (4.22)$$

with $M_n(z_k)$ defined by (4.15).

Rather than $M(l, z)$ and $A^P(l)$ we are generally more interested in the fractional quantities, such as projected cloud fraction etc.

$$m(l, z) \equiv \frac{M(l, z)}{L_x L_y} \quad a^P(l) \equiv \frac{A^P(l)}{L_x L_y} \quad (4.23)$$

where L_x and L_y and refer to the horizontal domain sizes.

The following equations follow directly from the definitions. The total number of clouds, the total projected cloud fraction, and the total fractional mass-flux is

$$\begin{aligned} m(z_k) &= (L_x L_y)^{-1} \sum_n M_n(z_k) \\ &= \lim_{l \rightarrow \infty} m(l, z_k) \end{aligned} \quad (4.24)$$

$$\begin{aligned} a^P &= (L_x L_y)^{-1} \sum_n A_n^P \\ &= \lim_{l \rightarrow \infty} a^P(l) \end{aligned} \quad (4.25)$$

$$N = \lim_{l \rightarrow \infty} N(l) \quad (4.26)$$

Particularly interesting are the corresponding densities

$$\begin{aligned} N(l) &\equiv \frac{d}{dl} N(l), & \alpha^P(l) &\equiv \frac{d}{dl} a^P(l), \\ \mu(l, z_k) &\equiv \frac{d}{dl} m(l, z_k), \end{aligned} \quad (4.27)$$

which permits us to write

$$\begin{aligned} N &= \int_0^\infty N(l) dl, & a^P &= \int_0^\infty \alpha^P(l) dl, \\ m(z_k) &= \int_0^\infty \mu(l, z_k) dl. \end{aligned} \quad (4.28)$$

Chapter 5

A multi parcel model for shallow cumulus convection

Neggers, R. A. J., A. P. Siebesma and H. J. J. Jonker, 2002. *Journal of the Atmospheric Sciences*, vol. 59, p. 1655-1668

5.1 Summary

A new parameterization for cumulus convection is formulated, which consists of an ensemble of small, rising parcels. Large Eddy Simulation (LES) results are used to parameterize the lateral mixing of such a parcel: for the mixing process a relaxation time-scale is defined and its value is determined by investigating individual LES clouds. The time-scale is found to be nearly independent of cloud depth, which implies that the entrainment rate is inversely proportional to the vertical velocity. As a consequence a dynamical feedback mechanism is established: the parcel dynamics influence the mixing rate, which, together with the environmental properties, feeds back on the parcel properties and therefore on the parcel dynamics.

The multi parcel model is tested with LES fields. The characteristics of the buoyant part of the clouds are reproduced: the decreasing fractional cover and increasing liquid water content with height, the vertical dynamics and mass-flux, the conserved properties and the marginally buoyant state. The model also produces the variability typical for shallow cumulus.

5.2 Introduction

Turbulent mixing between a cumulus cloud ensemble and its environment has been recognized as a key issue for understanding the dynamics of cumulus convection already since the work of Stommel (1947). However, the coexistence of a wide range of models, each emphasizing different aspects of the mixing mechanism, indicates that there is still no consensus on the principal mixing mechanism for turbulence in cumulus clouds (for a review see Blyth, 1993; Siebesma, 1998). The early cloud models, developed in the sixties (Squires and Turner, 1962; Simpson, 1965; Simpson and Wiggert, 1969; Simpson, 1971), essentially consisted of a rising parcel that is diluted by environmental air through lateral mixing. But a fundamental problem was pointed out already by Warner (1970b). Comparison of a lateral entraining

cloud model with cloud measurements showed that it was impossible to simulate both the liquid water content and cloud top height for individual cumulus clouds. A second problem is the observation of strong random fluctuations of liquid water, temperature and vertical velocity in the cloud with no systematic variations from cloud edges towards the middle (Warner, 1977; Jonas, 1990). This is difficult to explain with a simple lateral entraining cloud model alone.

Not only the dynamics of individual clouds, but also the modeling of a whole cumulus cloud ensemble has always received great interest because of the use in parameterizations of cumulus convection in General Circulation Models (GCM). Recently, results from Large Eddy Simulations (LES) of non-precipitating shallow cumulus convection have been reported (Siebesma and Holtslag, 1996) that suggest that vertical transport of heat and moisture by a shallow cumulus ensemble can be described by a simple lateral entraining bulk model, *provided* that the appropriate value for the lateral mixing rate is used. Several authors (Nordeng, 1994; Grant and Brown, 1999) have formulated new parameterizations in order to estimate the mixing rate for the whole cloud ensemble. However, the typical variability of temperature, moisture and vertical velocity as observed in cumulus cloud ensembles can never be properly understood on the basis of a single pragmatic bulk model. This variability is an essential variable in statistical cloud schemes for GCMs (e.g. Cuijpers and Bechtold, 1995) which are based on the idea presented by Sommeria and Deardorff (1977).

These problems have led to the formulation of a class of models that we will refer to as *stochastic mixing models*. The essence of these models is that a cloud or cloud-ensemble is represented by an ensemble of air-parcels, each having a different mixing fraction with environmental air. The major problem in stochastic modeling is how to define the distribution of these mixing rates in the ensemble. A lack of suitable observations of mixing in cumulus clouds that could be used as a critical test, has caused a divergence in the formulation of these stochastic mixing models (Emanuel, 1991; Raymond and Blyth, 1986; Kain and Fritsch, 1990; Hu, 1997).

This study is an attempt to use LES results instead to formulate an expression for the lateral mixing rate of a small updraught-parcel as a function of its own properties and of those of the environment it interacts with. Then, as a test of this new parcel-model, a distribution of buoyant cloud parcels is released from cloud base in an attempt to reproduce the typical variability observed in cumulus convection. The parcel ensemble will be initialized on and evaluated against 3D LES fields. In previous multi parcel methods, observational cloud data were used for validation purposes.

More specifically, the model should be able to reproduce some well established properties of the dynamics of a shallow cumulus ensemble such as produced by LES: 1) the monotonically decreasing cloud cover with height, 2) the temperature, specific humidity and vertical velocity profiles, 3) the bulk value of the lateral mixing rate of the cloud ensemble, and 4) the variances and covariances of temperature, specific humidity and vertical velocity of the cloud ensemble. In section 5.3 the motivation for this study is further discussed using a conserved variable diagram. In section 5.4 the single parcel model will be described and discussed, and the method of validation will be presented in section 5.5. Results of the multi parcel test are compared with LES results in sections 5.6. Finally conclusions and perspectives will be given in section 5.7.

5.3 Conserved variable diagrams

The direct motivation for this study is given by a conserved variable diagram, also called a Paluch-diagram (Paluch, 1979). In these diagrams, the liquid potential temperature θ_l is plotted against the total specific humidity q_t . These thermodynamic variables are conserved for phase-changes in shallow non-precipitating cumulus; they can only change by mixing with air of different q_t and θ_l . Therefore these diagrams characterize the mixing processes in a shallow cumulus cloud ensemble. Figure 5.1 is an example of such a diagram for the 1260m-level of a cloud ensemble produced by LES of the Barbados Oceanographic and Meteorological Experiment (BOMEX). The vertical profile of the horizontal mean values is also plotted. The top left end of this profile represents the relatively moist and cool sub cloud layer, and the warm and dry inversion is positioned in the lower right corner. The conditionally unstable cloud layer stretches in between. The diamonds represent the values of the grid-points at the 1260m level. The saturation curve and zero buoyancy line of this height are also plotted, dividing the figure into four sectors. All points above the saturation line represent the clouds, and the so-called 'cloud core' is defined as the group of points in the saturated, buoyant sector.

What immediately catches the eye is the 'tail' formed by the cloudy points, and the diffusive 'blob' around the environmental averages. It demonstrates that the distributions of the conserved variables of the cloud ensemble are highly correlated. This is the strong fingerprint of the mixing processes in the cumulus ensemble. Note that both the highest vertical velocities and the largest excess values of θ_l and q_t are found in the cloud core. This illustrates that the cloud core is responsible for most of the vertical transport of the conserved variables in a cumulus cloud field, as was shown by Siebesma and Cuijpers (1995). The various intercomparison-studies of the GEWEX Cloud System Studies (GCSS) working-group 1 on shallow cumulus (Siebesma et al., 2002; Stevens et al., 2001; Brown et al., 2002) illustrate that there is consensus about this in the LES community.

The precise nature of the responsible mixing mechanism has been the subject of many studies in the past. Early analyses of sail-plane measurements inside developing cumuli congestus (Paluch, 1979), gave similar results as the one presented in Fig.5.1: the cloud data are scattered fairly well on a straight between cloud base and a point (the so-called source of entrainment) well above the level of observation. These results were interpreted as empirical evidence for vertical mixing of undiluted air from cloud base with environmental air near cloud top through penetrative downdrafts. Since Paluch (1979), numerous studies have been reported that used the same analysis to infer the source of entrainment, with rather ambiguous conclusions. Some studies claimed that the source of entrained air originated near the cloud top (Lamontagne and Telford, 1983; Austin et al., 1985; Jensen et al., 1985; Pontikis et al., 1987), but also entrainment sources were reported near the observation level (Raymond and Wilkening, 1982; Boatman and Auer, 1983; Blyth et al., 1988). In most cases the source level was less than 1 km from the level of observation.

A more refined view was put forward by Blyth et al. (1988) that favours a picture of the top of a cloud that consists of a undiluted rising core with a toroidal circulation. This advancing cloud top is inducing mechanically forced downdrafts of the environmental air that is mixed with the core slightly below the advancing top. The resulting mixed parcels have a reduced buoyancy and are left behind in a trailing wake. With this mechanism the mixed air at each

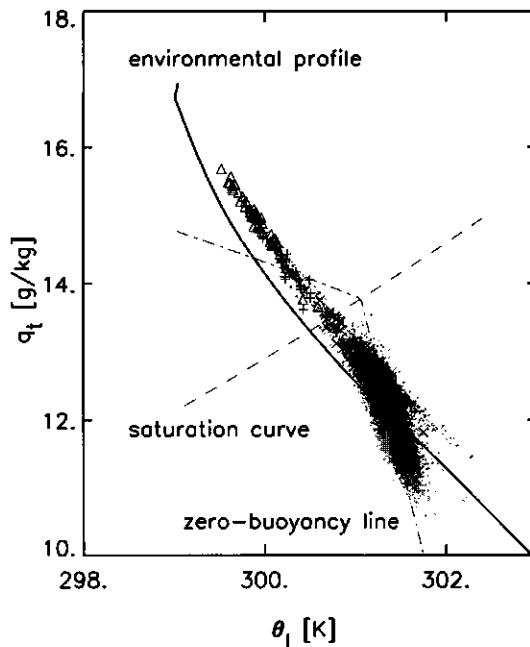


Figure 5.1 A conserved variable diagram for the BOMEX case of θ_1 and q_t as produced by LES. The vertical profile of the mean $\bar{\theta}_1$ and \bar{q}_t is plotted as a solid line, of which the subcloud layer values are situated in top-left corner of the plot. The dashed line is the saturation curve at this height, while the dash-dotted line is the line of neutral buoyancy relative to the mean state at this height. Points with $-1 < w < 1$ are plotted as a grey \diamond , $1 \leq w < 2$ as a $+$ and $2 \leq w$ as a Δ , and $-2 < w \leq -1$ as a \times .

level consists of two-point mixture of cloud base air (the undiluted core) and environmental air slightly above the level of observation, in agreement with the observed mixing line. The weak point of this proposed mechanism is that only undiluted cloud air from the cloud base mixes with the environmental air. Indeed it is true that undiluted air has been found at all levels within cumulus clouds (Heymsfield et al., 1978; Jensen et al., 1985) but this air represents only a small fraction of the cloud. It is then difficult to understand how only this small undiluted core region participates in all mixing events with the environment. Also Fig.5.1 does not support such a mechanism since most of cloudy updraft points are diluted.

Although the interpretation of straight lines as a two-point mixing process is tempting due to its simplicity, one should be cautious with it. In a recent study by Lin and Arakawa (1997), an analysis on the output of a 2-D cloud-resolving model has been applied. If the data points in a cloud are plotted in a conserved variable diagram they are distributed on a quasi-straight line that intersects the sounding close to the level of observation. At first sight one might interpret this as a two-point mixing of cloud base air with environmental air near the observation level. However, by calculating the backward trajectories it was shown that the

cloud air originated from *multiple* levels, all *below* the level of observation. These findings coincide with a mechanism put forward by Taylor and Baker (1991) in which, following Blyth et al. (1988), an active cumulus cloud can still be viewed as a rising thermal with a *lateral entraining ascending cloud top*. However, the condition that only undiluted air rises and mixes with the environment is relaxed. Instead, the rising thermal exists of different mixtures, ranging from the most buoyant undiluted parcels to nearly zero buoyant mixtures. Only when a mixture becomes negatively buoyant it will decelerate, stay behind and eventually detrain by evaporation.

This mechanism is supported by kinematic observations. Aircraft observations of Trade-wind cumulus bands off the coast of Hawaii were analyzed by Raga et al. (1990). For active clouds below the inversion they found that vertical velocities were almost exclusively positive. Only above the inversion equally strong downdrafts were observed. Similar results were found by Jonas (1990) who studied small maritime cumulus clouds over the North sea. Traverses through active cumuli showed organized updrafts in the clouds with only a thin shell of downdrafts of around 2 m/s outside the clouds. The values of θ_l and q_l in the downdrafts were not too different from the far field values at the observation heights. This led to the conclusion that the descent around the cloud edges is due to mechanical forcing rather than penetrative downdrafts driven by evaporative cooling. These results are supported by numerical simulations of Klaassen and Clark (1985).

Such an *intermittent entraining thermal* does not suffer from the Warner paradox (Warner, 1970b) since the cloud top is determined by the undiluted parcels while other parcels dilute the cloud by lateral entrainment. It is qualitatively in agreement with the observed kinematics.

The existing conceptual mixing models are of very diverse nature, ranging from lateral mixing models (Arakawa and Schubert, 1974; Tiedtke, 1989; Kain and Fritsch, 1990; Hu, 1997) to episodic / cloud-top mixing models (Emanuel, 1991; Raymond and Blyth, 1986). One particularly interesting class for modeling intermittently entraining thermals is formed by the *stochastic* models (Raymond and Blyth, 1986; Kain and Fritsch, 1990; Emanuel, 1991; Hu, 1997). The main concept of models of this type is the use of a whole distribution of small elements (parcels) with slightly differing properties. With such a distribution it is possible to reproduce the intermittency.

Our aim in this paper is to set up a simple multi parcel model of such an intermittent entraining thermal as described above, and to test whether it can reproduce the variability of the joint-distributions of temperature, moisture and vertical velocity such as displayed in Fig.5.1. The buoyant part of the cloud ensemble is modelled by releasing an ensemble of parcels. This requires knowledge of the mixing rate between such a parcel and its environment. In the next section we will present an attempt to find an expression for the mixing rate of an individual, small updraught parcel inside a cloud.

5.4 The parcel model

5.4.1 Governing equations

Consider a parcel as a small constant volume of air with a *fixed* horizontal area A_p and *fixed* infinitesimal thickness dz , see Fig.5.2. Air is allowed to flow across its boundaries. The

thermodynamic state of this parcel is described by the liquid water potential temperature θ_l , the total water specific humidity q_t and the vertical velocity w . All other variables of interest such as the potential temperature θ , the virtual potential temperature θ_v , liquid water content q_l and specific humidity q_v can all be derived from the moist conserved variables θ_l and q_t .

The dynamics of any field $\phi \in (\theta_l, q_t, w)$ can be written as

$$\frac{\partial \phi}{\partial t} + \nabla_h \cdot \vec{u}_h \phi + \frac{\partial w \phi}{\partial z} = F_\phi \tag{5.1}$$

where \vec{u}_h is horizontal velocity, ∇_h is the horizontal divergence operator, and F_ϕ contains all the sources and sinks of the field ϕ . The average value of any property of the parcel is defined as

$$\overline{(\cdot)}^p = (\cdot)_p \equiv \frac{1}{A_p} \int \int_{A_p} (\cdot) dx dy \tag{5.2}$$

and its boundary value as

$$\overline{(\cdot)}^b = (\cdot)_b \equiv \frac{1}{L_b} \oint_{L_b} (\cdot) dl \tag{5.3}$$

where L_b denotes the length of the perimeter of the parcel. Averaging (5.1) over the area A_p which is taken constant with height and time, using Gauss theorem and assuming steady state gives

$$\frac{1}{l} \overline{u \phi}^b + \frac{\partial w \phi^p}{\partial z} = F_{\phi,p} \tag{5.4}$$

where l^{-1} is the ratio L_b/A_p , and u_b is the lateral velocity component at the boundary of the parcel which is positive if the velocity is pointed outward. With $\phi = 1$ and no forcing, (5.1)

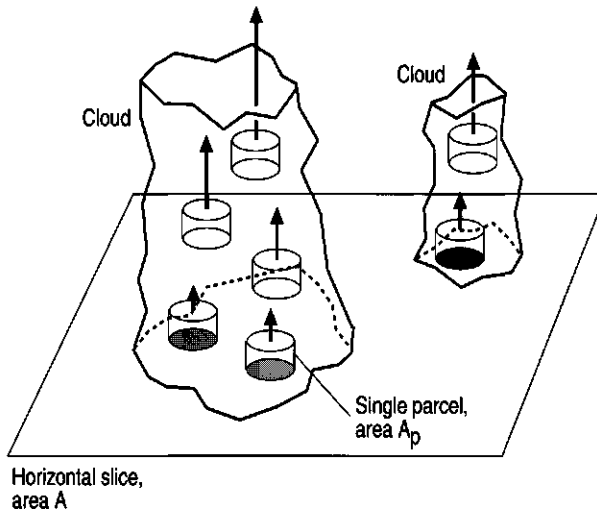


Figure 5.2 A multi parcel view on shallow cumulus clouds. A cloud is considered as a group of rising parcels, visualized as cylinders with a shaded horizontal surface A_p .

becomes the continuity equation and (5.4) reduces to

$$\frac{1}{l}u_b + \frac{\partial w_p}{\partial z} = 0. \tag{5.5}$$

Applying Reynolds averaging to the fluxes

$$\overline{w\phi^p} = \overline{w'\phi'^p} + w_p\phi_p \tag{5.6}$$

$$\overline{u\phi^b} = \overline{u'\phi'^b} + u_b\phi_b \tag{5.7}$$

and substituting (5.5)-(5.7) into (5.4) gives

$$\begin{aligned} & (\phi_p - \phi_b) \frac{\partial w_p}{\partial z} + \frac{1}{l} \overline{u'\phi'^b} \\ & \quad I \qquad \quad II \\ & + w_p \frac{\partial \phi_p}{\partial z} + \frac{\partial \overline{w'\phi'^p}}{\partial z} = F_{\phi,p}. \tag{5.8} \\ & \quad III \quad IV \quad V \end{aligned}$$

This budget-equation forms the starting point of the model.

The left hand side of (5.8) consists of four terms. Term I stands for lateral inflow through the parcel's boundary due to its vertical acceleration. Term II represents the lateral turbulent mixing across the boundary. Term III is the vertical advection of parcel-mean properties, and finally term IV represents the vertical turbulent mixing within the parcel. In both terms I and II the subscript *b* emerges, representing an average over the parcel's lateral boundary. In order to obtain a closed set of equations from (5.8) in terms of parcel-averaged variables only, these boundary fields and boundary fluxes need to be parameterized. This requires detailed knowledge of the interaction (mixing) between the parcel and its environment.

5.4.2 Parameterizing the mixing terms using LES

Finding the mixing-rate between cumulus clouds and the air surrounding them is one of the major issues in parameterizing cumulus convection, and various parameterizations have been formulated (Nordeng, 1994; Siebesma, 1998; Grant and Brown, 1999; Gregory, 2001). Direct cloud-measurements of lateral mixing in clouds are difficult to realize and therefore very scarce. On cloud entrainment there is essentially only the results of Raga et al. (1990) who estimated the order of magnitude of the entrainment rate. In the last decades Large Eddy Simulation (LES) models have become an alternative tool to study cumulus convection (Sommeria, 1976; Beniston and Sommeria, 1981; Cuijpers and Duynkerke, 1993). To evaluate the mixing terms in this parcel-model, LES results on shallow cumulus are used, such as observed during the Barbados Oceanographic and Meteorological Experiment (BOMEX) and the Small Cumulus Micro-physics Study (SCMS). For details of the LES runs see Appendix 5.A. Equation (5.8) will be treated term by term to determine which are dominating and which can be neglected.

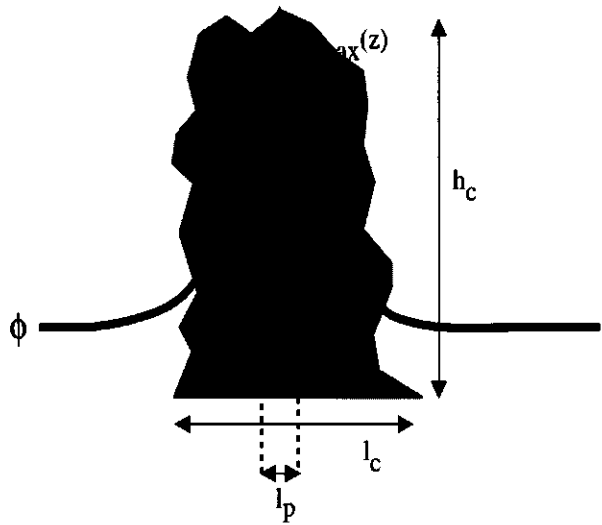


Figure 5.3 Schematic vertical cross-section through a cumulus cloud, illustrating the concept of a small parcel of a size l_p much smaller than the horizontal size l_c of the typical so called 'top-hat' anomaly in ϕ (temperature or moisture) associated with the cloud over the passive environment. To scale the turn-over time of a parcel, the ratio is calculated of cloud depth h_c and the vertical velocity of the strongest updraft in the cloud $w_{max}(z)$ (thick arrows) averaged along its path.

Firstly, the turbulent flux term IV in (5.8) is considered. Since we are dealing with small, rising parcels we can safely make the well-known 'top-hat' approximation for the vertical flux in (5.6), so that term IV can be neglected.

Secondly, term I and II have to be treated. The parcel is to describe an in-cloud volume of air much smaller than the typical dimensions of shallow cumulus clouds. To parameterize the mixing process in terms of parcel-mean and environmental properties, the characteristics of the air that this small in-cloud parcel entrains should be specified. To this purpose LES cannot yet be used, because the typical present-day horizontal resolution of LES is too low to adequately resolve the small fluctuations inside individual cumulus clouds. This also makes it difficult to determine which of the two terms I and II is dominating in the mixing process.

To solve these problems, a more indirect method is applied, without exactly specifying the properties of the air that a parcel entrains. Observational data of the conserved thermodynamic variables inside clouds obtained from horizontal aircraft-trajectories (see for example Warner (1977) and Jonas (1990)) do show a well defined 'top-hat' anomaly from the environment with many perturbations around it, as visualized Fig.5.3. These perturbations represent the turbulent mixing of air throughout the cloud. Although representing different processes, the mixing terms I and II both involve a combination of a velocity scale, a $\Delta\phi$ scale, and a length scale. We therefore parameterize both terms with a single expression, in the form of a relaxation term,

$$\left[(\phi_p - \phi_b) \frac{\partial w_p}{\partial z} + \frac{1}{l} \overline{u' \phi''} \right] \simeq -\frac{1}{\tau_p} (\phi_p - \bar{\phi}). \tag{5.9}$$

This dilution-timescale τ_p is assumed to be proportional to the eddy-turnover time (Siebesma, 1998), which is the ratio of a vertical length scale and a velocity scale.

Ideally we would like to determine these scales using cloud-observations, but as mentioned before, LES results on shallow cumulus are used instead which are resolved well. For that reason we define some particular scales of whole cloud which are also applicable to a small in-cloud parcel. For the length-scale we take the depth of the cumulus cloud h_c in which the updraught-parcel resides, see Fig.5.3. This is a measure of the vertical distance that such a parcel could rise. For the velocity scale we take the cloud averaged maximum vertical velocity $w_{max,c}$, corrected for its cloud base velocity:

$$w_{max,c} = \frac{1}{h_c} \int_{z_{0,c}}^{z_{0,c}+h_c} \max_{x,y} [(w(x,y,z) - w(x,y,z_{0,c}))] dz \quad (5.10)$$

We average the vertical velocity along the path of the strongest updraught in the three-dimensional w -field of the cloud. Therefore, the ratio of cloud depth h_c and this average maximum velocity $w_{max,c}$ gives an estimate of the time the strongest updraught needs in order to rise from cloud base to cloud top, given the sampled velocity field of the cloud. Accordingly, the turn-over time-scale τ_c of the strongest updraught in the cloud is defined as

$$\tau_c \equiv \frac{h_c}{w_{max,c}}. \quad (5.11)$$

Cumulus clouds root in the subcloud layer as thermals, and consequently they already have a vertical velocity at cloud base. The turn-over time of the thermal at that point is the height above the surface divided by its vertical velocity in the subcloud layer. Accordingly τ_c is non-zero at cloud base. In the calculation of the τ_c of LES clouds we used the height of the cloud h_c as the length scale, which can be interpreted as the vertical extent of the whole thermal (cloud + subcloud part) corrected with cloud base height. Therefore, to meet the boundary condition of a non-zero τ_c at cloud base, the vertical velocity should also be corrected with its cloud base value, as is formulated in (5.10).

Many individual cumulus clouds are sampled in LES for their $w_{max,c}$ and h_c . To this purpose the instantaneous 3D liquid water field and vertical velocity field of each cloud at a certain moment are sampled. By using instantaneous fields we have no information on the stage of life of the clouds at the moment of sampling: they can still rise further or stop rising and dissipate. Nevertheless, by sampling enough independent, instantaneous clouds of all possible sizes and life-stages, we get an effective relation between the depth of a cloud and the average vertical velocity of its strongest in-cloud updraught. After sampling many clouds this converged in a well-defined relation, see Fig.5.4. It demonstrates that despite a small increase with cloud-depth, τ_c is approximately constant for all clouds in both the BOMEX and the SCMS case. This has some important implications for the mixing rate of a parcel with its environment, as will be discussed later.

The turn-over time τ_c in Fig.5.4 is about 300s, and is much smaller than the typical lifetime of real cumulus clouds, which is observed to be of the order 10^3 s. The reason for this is that clouds are continuously fed with air from the dry subcloud layer for some time, as the cloud is just the visible part of a thermal which is rooted in the subcloud layer and which can exist for some time. That determines the real life-time of a cumulus cloud, and is therefore

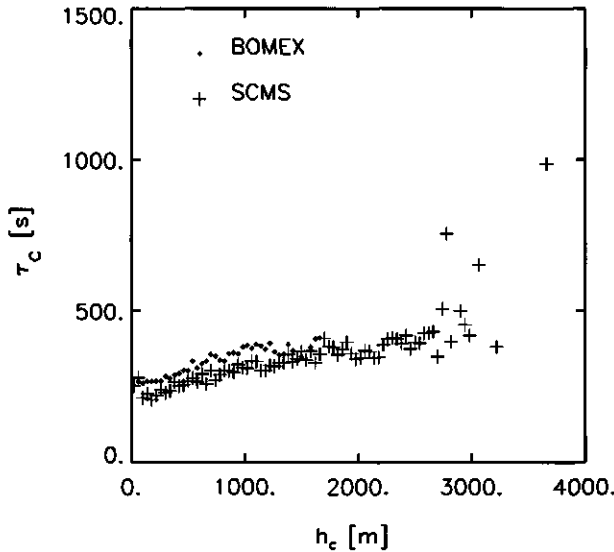


Figure 5.4 A histogram of the average turn-over time-scale τ_c per cloud depth h_c as defined in (5.11). BOMEX is marked by diamonds, and SCMS by crosses. This figure is based on approximately 60,000 independent clouds per case, simulated with LES. The vertical resolution used in these simulations was 40m. Note that the number of clouds per bin typically decreases with cloud depth in a shallow cumulus ensemble, causing a lower quality of the statistics for the larger values of h_c .

not equivalent to the turn-over time of a single updraught-parcel as defined here. The dilution time-scale τ_p is taken proportional to the turn-over time-scale τ_c , using a dimensionless constant of calibration η . Substituting (5.9) into (5.8) and neglecting terms IV and V gives for $\phi \in \{\theta_l, q_l\}$

$$\frac{\partial \phi_p}{\partial z} = -\frac{\eta}{\tau_c w_p} (\phi_p - \bar{\phi}). \tag{5.12}$$

The same mechanisms of mixing are assumed for w_p . This is not a conserved property, and forcings have to be considered. We assume that the forcing in the vertical velocity budget of a rising parcel is dominated by the buoyancy term. The vertical velocity equation then consists of three terms, an advection term, a buoyancy forcing term and a dilution term. Furthermore with $\bar{w} = 0$ we get

$$\frac{\partial w_p}{\partial z} = -\frac{\eta}{\tau_c} + \frac{B_p}{w_p}. \tag{5.13}$$

in which B_p is the buoyancy forcing,

$$B_p = \frac{g}{\theta_0} (\theta_v^p - \bar{\theta}_v). \tag{5.14}$$

Since the virtual potential temperature θ_v is a function of q_l and θ_l via the liquid water content q_l , (5.12) and (5.13) are coupled. Equations (5.12)-(5.14) together form the parcel model,

which predicts the change of θ_t , q_t and w of a parcel with height.

5.4.3 Discussion of the model

In many cloud and plume models the mixing (or entrainment) process is described as

$$\frac{\partial \phi_p}{\partial z} = -\varepsilon(\phi_p - \bar{\phi}) \quad (5.15)$$

(Betts, 1975; Anthes, 1977; Tiedtke, 1989; Raga et al., 1990). Equation (5.15) is a simple balance between vertical advection and lateral mixing. The fractional entrainment rate ε is the intensity of mixing and has the dimension m^{-1} , and could be interpreted as the inverse of the vertical mixing-depth in which the excess of the rising element is diluted with an equal mass of environmental air. As a first order approach it is often taken constant, but comparing (5.15) to (5.12), instead of a constant ε we propose

$$\varepsilon = \frac{\eta}{\tau_c} \frac{1}{w_p} \sim \frac{1}{w_p}. \quad (5.16)$$

Assuming a constant ε means that the turn-over time-scale τ_c is inversely proportional to the vertical velocity scale of the eddy. In other words, the constant mixing depth would be reached in less time by faster parcels, but the intensity of mixing per vertical meter would be constant. However, the definition of τ_c in (5.11) used in this model appeared to be approximately constant in LES, see Fig.5.4. This means that ε is not constant but is lower for higher vertical velocities, implying a larger mixing depth. This relation should be interpreted as follows: the parcel rising faster through a layer with thickness Δz is spending less time in it, and has less time to interact with the surrounding air.

The w_p^{-1} relation in (5.16) represents a feedback between the mixing rate and the vertical velocity of the rising parcel. When buoyant parcels gain vertical velocity, their entrainment rate is decreased. It therefore can accelerate further, again decreasing its entrainment, and so on. This mechanism tends to make fast parcels entrain less than slow parcels, and therefore can be responsible for creating the large variability observed in Fig.5.1. A constant entrainment rate would imply an essentially different mixing-behaviour without any feedback with the dynamics. The nature of this feedback-mechanism will be discussed in more detail in the numerical results.

Similarly we can rewrite the vertical velocity equation (5.13) in a more familiar format, by substituting the new formulation (5.16) for the entrainment rate ε :

$$\frac{1}{2} \frac{\partial w_p^2}{\partial z} = -\varepsilon w_p^2 + B_p, \quad (5.17)$$

(Simpson and Wiggert, 1969; Gregory, 2001). It demonstrates how buoyancy is transferred into kinetic energy.

5.5 A multi parcel approach

5.5.1 An ensemble of parcels

Most operational convection schemes in GCMs are bulk models in the sense that they use a single fractional entrainment rate ϵ , representative for a *whole* cloud-ensemble. In contrast to those bulk-parameterizations, this model is valid for just one small rising volume of air. By releasing a whole distribution of those parcels with slightly differing initial thermodynamic states, it is attempted here to reproduce the profiles and variability of θ_l , q_l and w of a shallow cumulus cloud-ensemble. The objective is to reproduce the cloudy 'tail' in the conserved variable diagram in Fig.5.1.

In the previous section it is attempted to find an expression for the mixing rate of a single parcel by using LES results to close the model, which resulted in the dynamical feedback in the mixing rate. All parcels in the ensemble have to obey the same budget equations (5.12)-(5.14). Consequently, each parcel will have a unique entrainment rate only dependent on its own vertical velocity, which in turn is dependent on buoyancy as a function of its conserved variables. Therefore, the variability in the parcel-ensemble is only caused by the slightly differing initial conditions, having a big impact higher up in the cloud-layer.

There are similarities between this multi parcel model and the scheme of Arakawa and Schubert (1974), in the fact that every element (or sub-ensemble) in a cumulus cloud-field has its own typical mixing rate. However there are also some major differences. In the Arakawa-Schubert scheme, a sub-ensemble represents all clouds of a certain radius. The mixing rate of a sub-ensemble is inversely proportional to its typical radius but constant with height. In contrast, this parcel-model is formulated for just one small volume of air with constant area much smaller than a cloud, with a dynamical feedback in the mixing rate, which is therefore *not* constant with height.

5.5.2 Initialization and validation with LES

It is interesting to apply the multi parcel model to a convective boundary layer which is buoyancy-driven from below by surface fluxes. In order to study the behaviour of the model, it is validated with LES model results of shallow cumulus based on data from BOMEX and SCMS. As stated before, a whole ensemble of slightly different parcels is to be released, so initial distributions of the modelled variables θ_l , q_l and w are needed for initialization. Because it is known from LES that so-called 'cloud-core' elements (elements which are both over-saturated and buoyant) are responsible for most of the vertical turbulent transport, it is interesting to compare the model with those elements. Therefore the validation of the model is limited to the cloud-layer only, and the parcel ensemble is initialized at the level of maximum fractional core-cover (LMC) which is always located close to cloud-base in a shallow cumulus regime. The initial distributions at LMC are obtained from instantaneous fields of an LES simulation. The same number of parcels were initialized as there were LES grid-boxes in the cloud-core at LMC. The fractional core-cover a_c (the ratio between cloud-core area and total area) can also be calculated for the modelled ensemble at every level in the cloud-layer, it being equal to the number of remaining parcels divided by the total number of grid-points in the horizontal LES slice. In the BOMEX case, about 3% of all 128^2 LES

grid-points at LMC belonged to the cloud core. For SCMS this was about 4%.

For all parcels in the initial ensemble, the properties q_t , θ_t and w are integrated upwards from LMC using (5.12)-(5.14). The integration stops when a parcel stops rising. For $\bar{\phi}$ in (5.12) we use the horizontally averaged profiles of LES. An explicit finite-difference scheme is used for the vertical integration. An all-or-nothing condensation scheme is used to calculate the liquid water content $q_{l,p}$ needed in (5.14). For further numerical details of the scheme, see Appendix 5.B. At each height, properties of the modelled parcels which are still buoyant and over-saturated are compared to the cloud-core of a horizontal LES slice.

The value of τ_c in (5.16) might be case-dependent, depending on stability and other properties of the environment in which the clouds rise. But most importantly, τ_c is approximately constant for all clouds in each case. This results in a totally new conceptual model, for a feedback with the dynamics is now introduced in the entrainment rate. Our main goal is to create a model which captures this important feedback, and therefore there is no sense in pinpointing an exact value for the turn-over time at this point. For τ_c we take 300s. The proportionality-constant η is considered as a calibration factor here to obtain the optimum results. The value $\eta = 0.9$ is used for BOMEX, and $\eta = 1.2$ for SCMS. The results are presented in the next section.

5.6 Numerical results

5.6.1 Profiles

Every parcel reaches a height where the mixing (sink) term becomes larger than the buoyancy (source) term in (5.13), so that the right-hand side becomes negative and the parcel starts to decelerate. Eventually it falls out of the core (by definition) when it reaches zero buoyancy. Many parcels of initially different properties are released from cloud base, and as the elevation above cloud base increases, only the initially stronger parcels remain buoyant and oversaturated, causing the decreasing fractional core cover a_c with height (the subscript c stands for core), see Fig.5.5a and 5.6a. The functional relation of the mixing rate with the vertical dynamics makes the number of modelled core-parcels decrease reasonably with height for BOMEX, but somewhat too fast for SCMS in the lower half of the cloud-layer.

Fig.5.5a also shows the approximately linearly increasing w_c with height. The product $a_c w_c$ is the core-massflux M_c , which looks quite promising in the sense that it is in the same order of magnitude as LES, and that it decreases with height, see Fig.5.5b. This is not trivial because M_c is a product of two profiles, one increasing and one decreasing with height, making it sensitive to small changes. The fact that M_c decreases in the right order for BOMEX indicates that the modelled ensemble contains the changing dynamical properties of the LES core. For SCMS, the combination of a too low a_c and a too high w_c results in a local minimum in the mass flux in the middle of the cloud layer (see Fig. 5.6b), which was not observed in LES

The core-average entrainment rate ϵ_c of the parcel ensemble is calculated with

$$\epsilon_{c,parcels} = \frac{1}{N} \sum_{i=1}^N \epsilon_i, \quad (5.18)$$

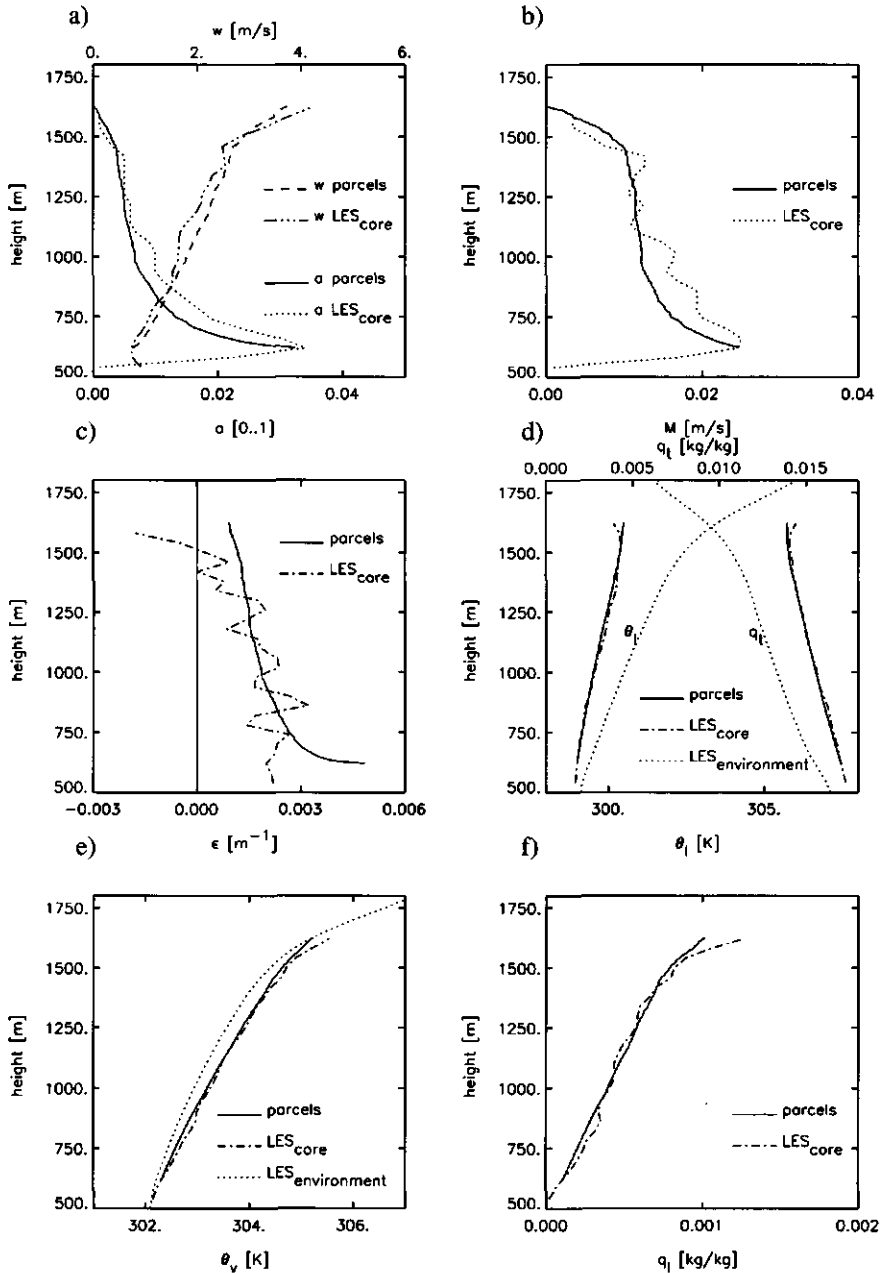


Figure 5.5 Dynamical properties of the core of the parcel-ensemble and LES for the BOMEX case. a) The fractional cover a and vertical velocity w . b) The mass-flux M . c) The fractional entrainment rate ϵ . d) The conserved variables θ_t and q_t . e) Virtual potential temperature θ_v . f) Liquid water content q_l . The label *core* denotes the average over the cloud core, and the label *environment* stands for the horizontally averaged environmental profile of LES. *LES* stands for the LES results, and *parcels* for the results of the modelled parcel ensemble.

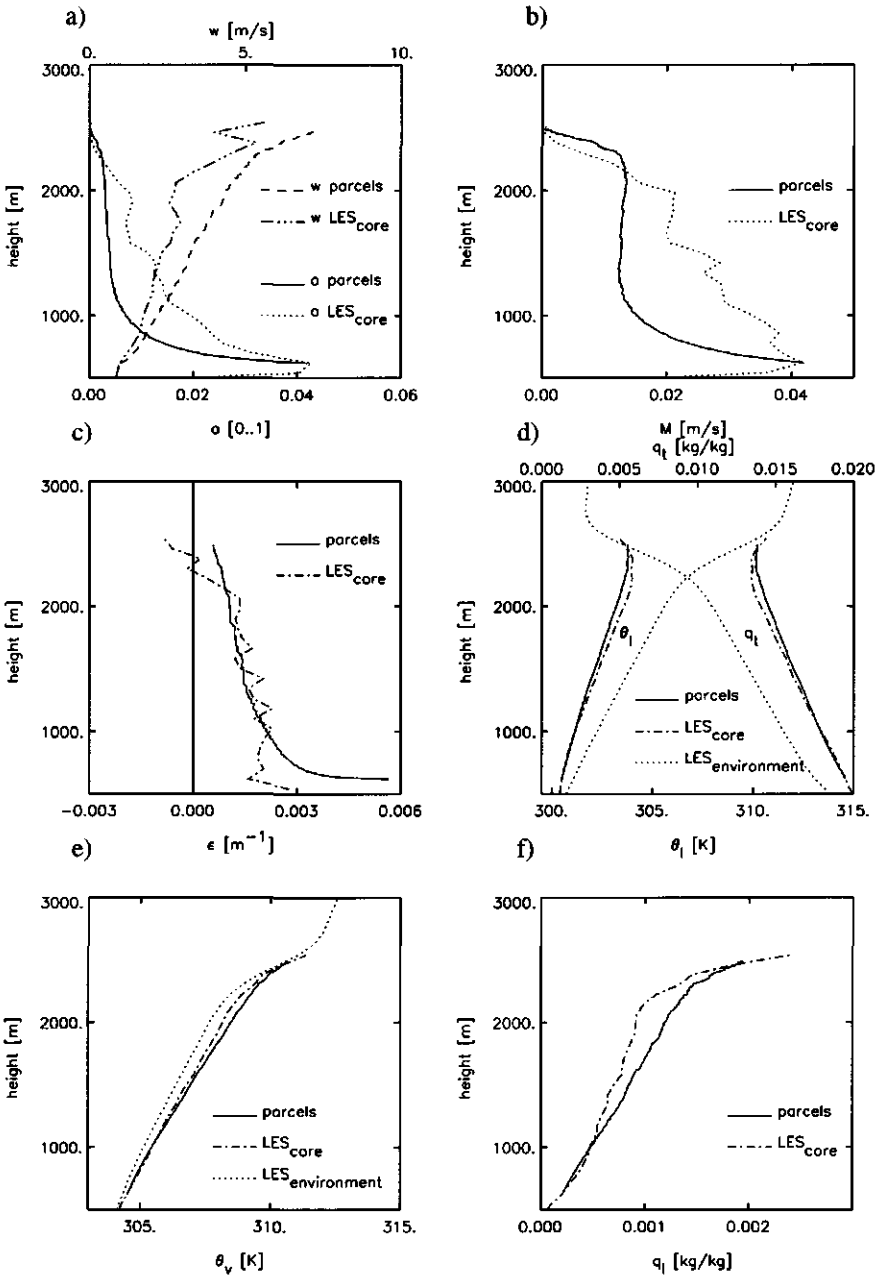


Figure 5.6 Same as Fig.5.5, but now for the SCMS case.

where ϵ_i is the entrainment rate of an individual parcel, and N is the number of buoyant, over-saturated parcels at that height. Note that every average of the parcel-ensemble is calculated with this method. In contrast, ϵ_c in LES is calculated indirectly, with help of (5.15):

$$\epsilon_{c,LES} = \frac{-\frac{\partial \phi_c}{\partial z}}{(\phi_c - \bar{\phi})} \quad (5.19)$$

(see Betts, 1975; Anthes, 1977; Tiedtke, 1989; Raga et al., 1990). This definition does not necessarily yield a positive value. Despite the different method of calculation, $\epsilon_{c,parcels}$ matches $\epsilon_{c,LES}$ in the bulk of the cloud-layer, see Fig.5.5c and 5.6c. Apparently the dynamical feedback in the entrainment-rate of the individual parcels works good enough to create a distribution of entrainment rates of which the average is close to $\epsilon_{c,LES}$. In previous stochastic models, these distributions of mixing rates were often imposed (Raymond and Blyth, 1986; Kain and Fritsch, 1990; Emanuel, 1991; Hu, 1997), while here it changes with height dependent on the changing dynamics. The parameterizations of Grant and Brown (1999) and Nordeng (1994) do introduce feedbacks in the entrainment rate, but they describe a whole cloud-ensemble at once, and are not stochastic.

Only close to cloud-base and the inversion the entrainment-profiles of LES and the parcel-ensemble differ, which is just a result of the different method of calculation. In the Trade-wind inversion the vertical derivatives of the LES core-average θ_l and q_l suddenly change sign, see Fig.5.5d and 5.6d, implying a negative ϵ_c when calculated with (5.19). This feature in the q_l and θ_l profiles is reproduced by the parcel-ensemble, and there represents a statistical result of the sudden removal of weaker parcels from the ensemble by the stability of the inversion. By this the core-averages become dominated by the few remaining parcels which stayed more or less undiluted during their ascent from cloud-base.

The parcel-ensemble can maintain the marginally buoyant state of the cloud-core until the inversion for BOMEX, see Fig.5.5e. Comparing figure 5.5a to figure 5.5f, we see that the LES liquid water content and the core-top height are both reproduced. Figure 5.6e demonstrates that in the SCMS case the modelled core is too buoyant. Also, the excess of the core-average conserved variables is too large (Fig.5.6d), and too much liquid water is predicted (Fig.5.6f). Too many weak parcels drop out of the ensemble too soon in the ascent from cloud base, and only a few undiluted ones remain which are responsible for the overestimated core-average vertical velocity, buoyancy and liquid water, and also the minimum in the mass flux in the middle of the cloud-layer which is unrealistic.

5.6.2 Variability

Figure 5.7 shows a conserved variable diagram of the parcel ensemble for the BOMEX case. It can be directly compared to Fig.5.1. The multi parcel model predicts enough parcels in the cloud-core at this height (see Fig.5.5a), they are located at the same location as the tail formed by the LES core-gridpoints, and the parcel ensemble also shows the high correlation between q_l and θ_l as observed in LES. This result illustrates that the variability of the cloud ensemble can be understood by the stochastic application of this parcel model. The model is able to predict the thermodynamic variables of the strongest updraughts in the typical cloud-core 'tail' of a conserved variable diagram of an LES cumulus cloud field.

In the model, the dynamical feedback in the entrainment rate is responsible for this. The vertical velocity feedback causes faster parcels to entrain less than slower parcels. So the q_t and θ_t of the former do not change much, while the latter are diluted heavily towards the environmental values, and the distributions of q_t and θ_t of the cloud-core get wider with height, see Fig.5.8. In this model, the passive environment $\bar{\phi}$ is the only entrainment-source for a parcel (see (5.12)), causing the modelled cloud-tail to be narrower than LES. In reality (and LES) there are many more possible sources, like passive cloud air, downdraught air (Jonas, 1990) and air from neighbouring cloud-points.

This increase of the width of the cloud-core distributions with height in the modelled parcel-ensemble is determined by the intensity of the dynamical feedback in the mixing rate. This process is demonstrated in Fig.5.8. Two different simulations are shown, one with a constant entrainment rate ε for all parcels and one with a constant turnover time-scale τ_c . In case of a constant τ_c , the width of the LES cloud-core distributions increases with height from LMC, where it is still very small. The increase with height is somewhat too slow, but the shapes of the profiles are at least similar to LES. In contrast, the variance even decreases with height when a constant ε is used, independent of its value. In that case the parcels stay together without scattering much. Therefore, the dynamical feedback is responsible for the increasing variability of the cloud-core with height.

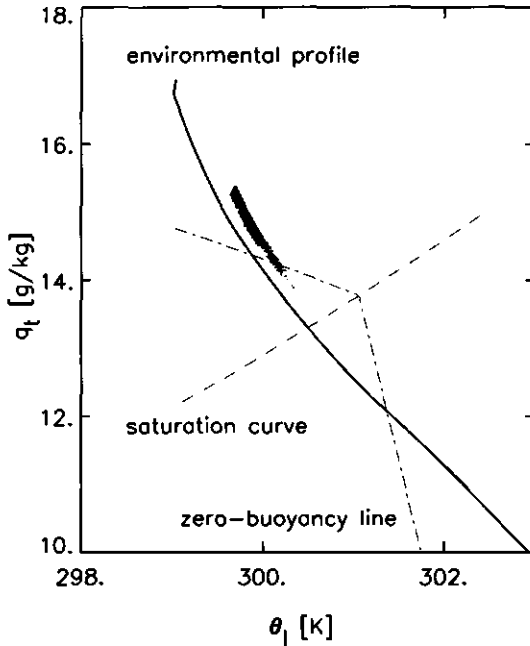


Figure 5.7 The same conserved variable diagram as in Fig.5.1, but now for the parcel ensemble.

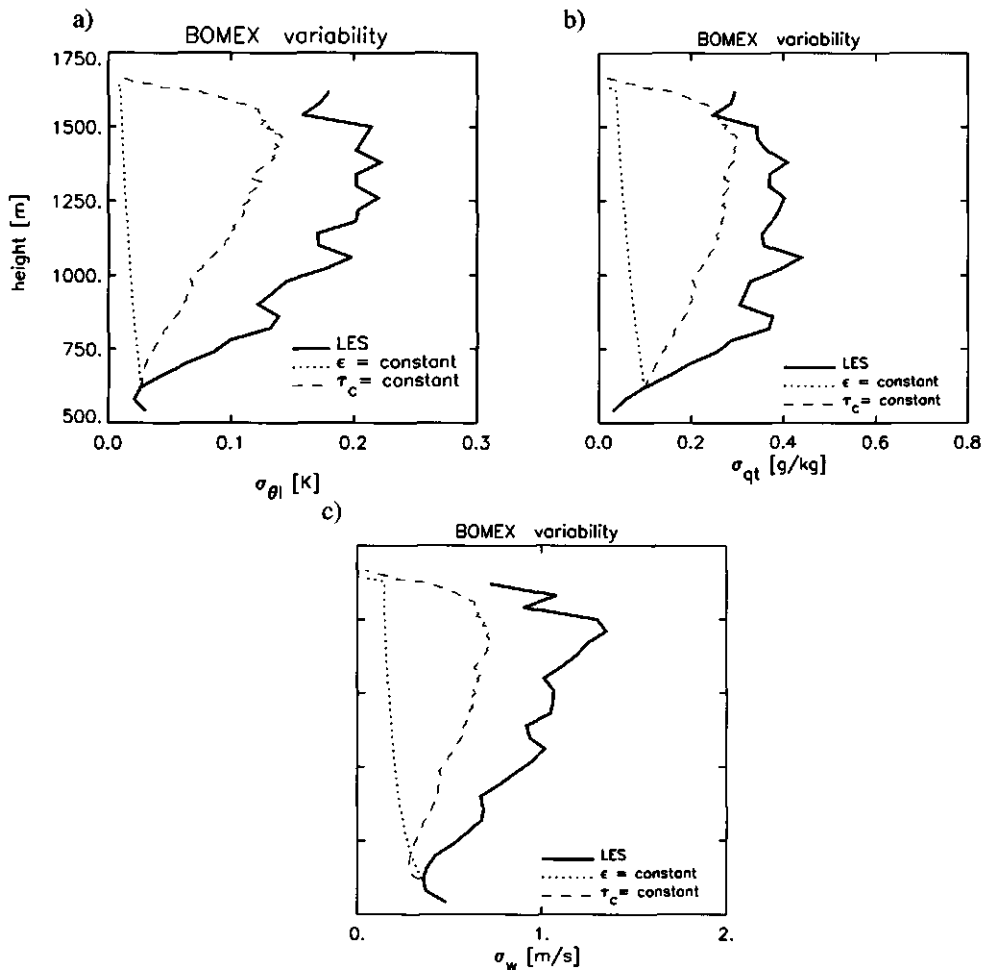


Figure 5.8 The standard deviation of a) θ_t , b) q_t and c) w of the core-ensemble around the core-average for BOMEX. The spikiness in the LES profile is caused by the fact that an instantaneous 3D field is used for the validation.

5.7 Conclusions and perspectives

In this study, an expression for the lateral entrainment rate of a small updraught-parcel is presented. The mixing terms in the parcel budget equations are written in a relaxation form, using a typical time-scale which appears to be nearly independent of cloud depth in LES. This interesting result introduces a coupling between the entrainment rate and the dynamics of the parcel, in that faster parcels have a lower intensity of mixing. This makes the mixing process sensitive to the changing properties of the parcel as it rises.

These budget equations for a single parcel are applied to a whole ensemble of small

updraft parcels. Every parcel is modelled individually, and thus it has its own unique entrainment rate, completely determined by its vertical velocity. Therefore, the problem of finding the distribution of entrainment rates in the parcel ensemble is reduced to finding the initial distributions of the model variables at the level of initialization. In this evaluation, the parcel model is validated against LES results. Both the decreasing fractional cover and the increasing liquid water content with height of the LES cloud-core were reproduced, as well as the vertical dynamics and mass-flux, the core-average conserved variables and the marginally buoyant state. The fractional entrainment rate of the parcel-ensemble is always of the order of $10^{-3}m^{-1}$, a value found by Siebesma and Cuijpers (1995) and Grant and Brown (1999) based on LES results.

The parcel model predicts the thermodynamic variables of the strongest updrafts in the cloud-core tail of a conserved variable diagram. The high correlation and the increasing variability with height of the characteristic cloudy 'tail' found in LES conserved variable diagrams were also reproduced by the ensemble of parcels. It demonstrates that the typical variability of the cloud ensemble can be understood by the multi parcel model presented here. With knowledge of the variability, the total distributions of the conserved thermodynamic variables at one level in the cloud layer can be reconstructed. These can be used in statistical cloud schemes in GCMs to parameterize total cloud cover (Sommeria and Deardorff, 1977; Cuijpers and Bechtold, 1995).

What exactly causes the shortcomings in the SCMS case is yet unclear. Because the entrainment rate is dependent on the vertical velocity of the parcel, the model becomes sensitive for the vertical momentum equation. Here a very simple budget equation (5.13) is used. But in contrast to the thermodynamic variables, vertical momentum in clouds does not show a clear top-hat average over the passive environment (Fig.5.3). This is due to the high incloud-variability of vertical momentum and the occurrence of downdrafts inside the cloud. The LES results on the SCMS case indeed show vigorous convection featuring strong saturated downdrafts. At second, other forcings like pressure perturbations and molecular dissipation that can act as a sink for the vertical momentum in clouds, are not included in the model for simplicity. Thus the relaxation-term represents all dilution processes in the w_p -budget. We expect that a more sophisticated vertical momentum equation will improve the SCMS results.

In this experiment the model is validated on an LES cloud-layer only, and the parcel-ensemble is initialized at LMC, in order to keep the validation-procedure as simple and clear as possible. But the rising thermals represented by the cloud-core originate in the dry sub-cloud layer. Whenever a large dry thermal is strong enough to reach saturation and get positive buoyancy, it becomes an active cumulus cloud. If we assume that the functional relation for the entrainment rate, as found here for the cloud layer, is the same in the dry sub cloud-layer, then we can extend the model downwards to the level where these large thermals originate, that is the surface layer (Businger and Oncley, 1990; Wyngaard and Moeng, 1992). By this the cloud-layer gets linked to the subcloud layer, and the parcel-ensemble then represents the upward transport in the whole boundary layer by all thermals starting at the top of the surface layer. The problem of finding the initial distributions is then moved from LMC to this level. In this experiment we used distributions obtained from an LES simulation. To become completely independent of LES, joint-Gaussian distributions at this level can be constructed (Wyngaard and Moeng, 1992) using surface layer similarity theory (Holtslag and

Moeng, 1991). Such a rising parcel ensemble is interesting for use in convection schemes in GCMs because it can give the heights of the cloud base and top, and the fields of the strongest updraughts. This information is needed to close mass-flux convection-schemes (Siebesma, 1996; Tiedtke, 1989). Work in this direction is still in progress.

The approximately constant turn-over time-scale resulting from LES is essential for the character of the parcel model, because it directly leads to the dynamical feedback in the entrainment rate. LES is still a model, and observational data can and should be used as well to determine the behaviour of this turn-over time-scale for real clouds. The depth and maximum velocity of individual clouds should be known for this. At second, a qualitative validation of the parcel model in the form of a stochastic test with observational data requires in-cloud measurements of high-resolution: it is necessary to have measurements of the vertical profiles of the environmental moisture and temperature, the heights of cloud base and top, and the distributions at enough levels in the cloud layer of temperature, moisture and vertical velocity. The combination of these observations is scarce, especially the observational data of the (initial) distributions form a problem. This is the reason to use LES fields instead for this study, but we are pursuing to find suitable observations to test the model with. The SCMS case has some potential because in-cloud measurements of turbulence by aircraft are available for this case, in combination with rawinsonde profiles and Landsat satellite-images.

The lateral inflow term I and the turbulent mixing term II in the budget equations for a small in-cloud parcel were parameterized together in one relaxation formula, because no detailed information is available to determine which of the two terms dominates in this situation. Nevertheless it is interesting to study the nature of these two terms, especially for parcels of larger dimensions which may represent cloud-average fields. Historically, the boundary average ϕ_b in term I was often parameterized using an upstream method (Asai and Kasahara, 1967; Tiedtke, 1989): replacing ϕ_b by $\bar{\phi}$ in case of inflow (acceleration) gives the formula for the entrainment-rate of a whole cloud ensemble as formulated by Nordeng (1994), which is currently being tested in the ECMWF model. Bulk-models of this kind can be used to simulate the behaviour of cloud-average fields, and their potential use lies in the application in convection schemes.

Acknowledgements. We thank Aad van Ulden, Geert Lenderink and Bert Holtslag for many discussions on this subject. Peter Duynkerke kindly provided the SCMS data used in this study. The LES results in this study were obtained using the supercomputer facilities of the European Centre for Medium-Range Weather Forecasts (ECMWF) in Reading, UK. We thank three anonymous reviewers for their comments which significantly improved this paper. This study has been supported by the Netherlands Organization for Scientific Research under Grant 750.198.06.

Appendix 5.A LES case description

To close the model, many LES clouds were sampled for their depth and maximum vertical velocity, see Fig.5.4. A detailed description of the LES model used here can be found in Cuijpers and Duynkerke (1993). The BOMEX simulations consisted of a volume of dimensions 6.4x6.4x3.0 km containing 128x128x75 grid-boxes, using time-step of 2 seconds. 5 simu-

lations of 8 hours were performed, of which the last 5 hours were used to sample all clouds in the volume at every 5 minutes. This is considered to be a sampling rate low enough for two subsequent sampled cloud-fields to be independent of each other. This resulted in about 60.000 sampled clouds. For the SCMS case a volume of $6.4 \times 6.4 \times 5.0$ km was simulated with $128 \times 128 \times 125$ grid-boxes. A smaller time-step of 1 second, had to be used in order to prevent numerical instability due to the large vertical velocities in the SCMS case. The same sampling rate of 5 minutes was used. For the validation of the stochastic parcel model in section 5.6, randomly chosen instantaneous 3D LES fields of one of these simulations are used.

Appendix 5.B Numerics

To handle the set of coupled equations (5.12)-(5.14) numerically, we used an explicit finite-difference scheme on a staggered grid with w_p on the half levels and the conserved variables q_l and θ_l on the full levels. Equation (5.12) then becomes

$$\phi_{p,k+1} = \phi_{p,k} - \Delta z \left(\frac{\eta}{\tau_c} \frac{1}{w_{p,k}} \right) (\phi_{p,k} - \bar{\phi}_k) \quad (5.20)$$

where $w_{p,k}$ is obtained by linear interpolation between the half levels $k + \frac{1}{2}$ and $k - \frac{1}{2}$. It is obvious that in order to integrate $\phi_{p,k}$, we have to know w_p at these two half levels. So w_p is integrated first to half level $k + \frac{1}{2}$, being a function of buoyancy and vertical velocity at half level $k - \frac{1}{2}$ only,

$$(w_{p,k+\frac{1}{2}})^2 = (w_{p,k-\frac{1}{2}})^2 - 2\Delta z \left(\frac{\eta}{\tau_c} w_{p,k-\frac{1}{2}} - B_{p,k-\frac{1}{2}} \right). \quad (5.21)$$

Then the entrainment ϵ can be calculated on the full level k , by which we finally can integrate q_l and θ_l upward to $k + 1$. Liquid water q_l is calculated as a function of q_t , θ_l and pressure with an all-or-nothing condensation scheme, which means that the air within a parcel can only be entirely over-saturated or entirely under-saturated. We used an equidistant grid with a small vertical spacing of $5m$ to minimize numerical errors.

Chapter 6

Mass flux closures in diurnal cycles of shallow cumulus

Neggers, R. A. J., A. P. Siebesma, G. Lenderink and A. A. M. Holtslag. *Submitted to the Monthly Weather Review*, July 2002.

6.1 Summary

Three closure methods for the mass flux at cloud base in shallow cumulus are critically examined for the difficult case of a diurnal cycle over land. The various closures are diagnostically evaluated in a large-eddy simulation (LES) by sampling their parameters during the diurnal cycle. With these results in hand the impact of these closures on the development of the cloudy boundary layer is studied using an offline single column version of a regional atmospheric climate model.

Significant moistening occurs in the subcloud mixed layer in the first hours after cloud onset. Consequently, the subcloud layer equilibrium (SLE) closure (Tiedtke, 1989) substantially overestimates the mass flux at cloud base. As a result the boundary layer deepens unrealistically rapid at that stage in the single column model. The adjustment closure on the convective available potential energy (CAPE) based on the method of Fritsch and Chappell (1980) can not deal with the very shallow cloud layer with small values of CAPE in the early hours. At the end of the convective day the coupling of CAPE adjustment to the mass flux no longer holds, as cumulus convection is then limited by the decreasing surface fluxes. The w^* closure of Grant (2001) is promising, as it reproduces the timing of both the maximum and the final decrease of the cloud base mass flux in LES. Apparently this closure catches the coupling between the two layers at cloud base. As a consequence the development of the thermodynamic structure of the boundary layer in the 1D model strongly resembles that in LES.

6.2 Introduction

Mass flux models are widely used in convection schemes in operational general circulation models (GCM), such as climate models and numerical weather prediction (NWP) models. The large-eddy simulation (LES) results of Siebesma and Cuijpers (1995) on the steady state marine shallow cumulus case based on BOMEX (Barbados Oceanographic and Meteorological Experiment, see Holland and Rasmusson, 1973; Nitta and Esbensen, 1974) show that the mass flux concept is capable of reproducing 80% of the vertical turbulent flux by the

cumulus population. Although these results are encouraging, it is important to realize that many situations exist in which the boundary layer is far from steady state. A good example is a diurnal cycle associated with a cumulus topped boundary layer over land, for example as described by Brown et al. (2002). The strong variation of the surface heat fluxes during the daytime hours causes the boundary layer initially to grow in height by the heating of the mixed layer and by top-entrainment in the inversion. The moisture content of the mixed layer influences the onset of the clouds, as well as the height of the cloud base. Strong fluctuations of the temperature and the moisture content of the mixed layer are recorded in numerous observations.

The non-steady state nature of developing boundary layers may cause serious problems for mass flux schemes in single column (1D) models. As shallow cumulus clouds are actually the visible part of (over)saturated thermals which root deeply in the subcloud mixed layer (LeMone and Pennell, 1976), the subcloud and cloud layers strongly interact (Ogura and Cho, 1974). Therefore it is necessary that in a 1D model some coupling exists between the cumulus mass flux scheme and the subcloud mixed layer. This coupling is represented by the *closure* of the mass flux model at cloud base (Betts, 1973, 1976), in which typically boundary layer parameters are used to estimate the cloud base mass flux. Many different models for the mass flux closure have been formulated, often based on observations of marine steady state cumulus fields. The question remains how the closures based on steady state cases perform in the difficult non-equilibrium case of a diurnal cycle over land. Possibly related to this issue are the reported problems of GCMs in dealing with the timing of precipitation and the triggering of deep convection over continental regions (e.g. Mace et al., 1998).

A range of mass flux closure methods exists, for both shallow and deep convection. Three well-known and often applied closures will be studied in more detail. Based on budget studies of several field-experiments (e.g. Augstein et al., 1973; Holland and Rasmusson, 1973; Esbensen, 1975), the mass flux model of Tiedtke (1989) explicitly assumes the subcloud mixed layer to be in steady state, which implies a constant moisture flux throughout the subcloud layer. Grant (2001) uses turbulent kinetic energy arguments to link the cloud base mass flux to the convective vertical velocity scale of the mixed layer. In contrast to the previous methods, closures for deeper convection typically use characteristics of the cloud layer itself. Compared to shallow convection, deeper convection is driven by the relatively intense latent heat release in the convective clouds, which favours such an approach. One example is the Fritsch and Chappell (1980) closure, which associates the destruction of the convective available potential energy (CAPE) of the cloud layer with the compensating subsidence induced by the cumulus mass flux. Shallow cumulus often precedes deep cumulus on a convective day, and for parameterization purposes it is therefore important to know when the cloud layer is deep enough for this type of closure to work well.

This study follows the method of Siebesma and Holtslag (1996) of applying LES results in a 1D model and to study their impact on the development of the boundary layer. Firstly, the three mass flux closures mentioned above will be described in detail. Then the parameters which appear in the various closures will be sampled during LES simulations of diurnal cycles over land. This gives insight in the characteristics of each closure in such a situation. With these results in hand the closures are implemented in the convection scheme of Tiedtke (1989) as embedded in an offline single column version of the Regional Atmospheric Climate Model (RACMO, see e.g. Lenderink and Siebesma, 2000). In contrast to the LES runs, the

closures then affect the vertical transport and hence the (thermo)dynamics of the developing boundary layer. Their impact is studied in a sensitivity test.

The mass flux closures are described in Section 6.3. The cumulus cases and the LES results are described in Section 6.4. The RACMO 1D results are presented in Section 6.5. The final discussion and conclusive remarks can be found in Section 6.6.

6.3 Mass flux closures at cloud base

Applying the top-hat approach to the turbulent vertical flux of a conserved variable $\phi \in \{\theta_t, q_t\}$ results in the well-known mass flux equation (Ooyama, 1971; Betts, 1973),

$$\overline{w'\phi'} \approx M^c(\phi^c - \bar{\phi}), \quad (6.1)$$

where the mass flux M^c is defined as

$$M^c \equiv a^c w^c. \quad (6.2)$$

Here w is the vertical velocity, and the accent $'$ denotes a perturbation from the horizontal mean (denoted by the over-bar). The superscript c stands for the horizontal average over the cloud core, defined as the fractional area a^c which is both (over)saturated and positively buoyant. Equation (6.1) is the starting point of the mass flux model of Tiedtke (1989). In order to close the mass flux model, a closure at cloud base has to be formulated. Three basic methods will be described in the next paragraphs.

6.3.1 The subcloud layer equilibrium closure

The first mass flux closure evolved from the outcome of a series of cumulus field-experiments in the oceanic Trade-wind region in the past (BOMEX, ATEX). Budget studies based on such datasets (Augstein et al., 1973; Holland and Rasmusson, 1973; Ogura and Cho, 1974; Esbensen, 1975) have shown that the moisture-tendency in the subcloud layer (SL) is typically negligible. This implies that the moisture flux at cloud-base is equal to the moisture flux at the surface plus lateral advection at the sides of the domain, a situation referred to as *moisture convergence* (Kuo, 1965, 1974; Tiedtke, 1989). Applying (6.1) at cloud base and neglecting lateral advection at the sides for the moment then gives

$$M_b^c = \frac{(\overline{w'q_t})_s}{(q_t^c - \bar{q}_t)_b} \quad (6.3)$$

where q_t is the total specific humidity. The subscript b indicates cloud base and s the surface. Similarly, the moist static energy h can be used in this closure, which combines the heat and moisture fluxes,

$$M_b^c = \frac{(\overline{w'h'})_s}{(h^c - \bar{h})_b}, \quad (6.4)$$

where

$$h = c_p T + gz + Lq_t \quad (6.5)$$

and

$$(\overline{w'h'})_s = c_p (\overline{w'\theta'})_s + L (\overline{w'q'})_s. \quad (6.6)$$

Here T stands for the temperature, g for the gravitational acceleration and z for the height above the surface. The constant c_p is the specific heat of dry air at constant pressure and L is the specific latent heat of the phase change between water vapor and liquid water. Equation (6.4) is used for shallow convection in the current GCM of the European Centre of Medium-range Weather Forecasts (ECMWF, see Gregory et al., 2000), as well as the RACMO 1D offline model used in this study. For convenience (6.4) is referred to as the *subcloud layer equilibrium* (SLE) closure.

This closure assumes that M_b is totally controlled by the equilibrium budget of moisture or static energy in the subcloud layer. In this view the interaction between the two layers at cloud base is a result of forced convection, in which the overshooting thermals from the subcloud layer which become clouds control the mass flux at cloud base. The advantage of such an approach is that the mass flux at cloud base is directly linked to the surface fluxes, which are given parameters in a convection scheme. However, when a part of the surface input of moisture and heat is deposited in the SL, the flux profiles decrease with height. Consequently the mass flux at cloud base will be overestimated by the SLE closure. A critical test is therefore its application to the non-equilibrium case of a diurnal cycle over land, which is characterized by significant moisture and temperature tendencies in the boundary layer during the day.

6.3.2 CAPE adjustment

In contrast to the SLE closure, the adjustment closure is based on the assumption that the flux at cloud base is totally controlled by the conditions in the cloud layer. The quasi-equilibrium assumption states that any instability created by the slow changing large-scale forcings is quickly destroyed by fast process of cumulus convection (e.g. Arakawa and Schubert, 1974; Randall et al., 1997). Adjustment schemes associate a typical relaxation timescale with this process, relaxing the system towards a certain reference state (e.g. Manabe et al., 1965; Betts and Miller, 1986a,b). For a more elaborate review of closures based on this method see for instance Emanuel (1994).

The reference state can be formulated in terms of the virtual potential temperature, which is also used in the definition of the convective available potential energy (CAPE) of a cloud layer,

$$CAPE = \int_{z^b}^{z_i} \frac{g}{\Theta_v^0} (\theta_v^c - \overline{\theta}_v) dz. \quad (6.7)$$

Here z_i is the top of the cloud layer, θ_v is the virtual potential temperature, of which Θ_v^0 is a reference value. θ_v^c represents the profile of a moist adiabatically rising in-cloud element. $\overline{\theta}_v$ is the horizontal mean, which is chosen to be the reference state. The adjustment principle using CAPE is expressed in terms of the relaxation formula

$$\frac{\partial CAPE}{\partial t} = -\frac{CAPE}{\tau}, \quad (6.8)$$

where τ is the typical time scale associated with the adjustment process. It is the typical time-scale of the conversion of the available potential energy into kinetic energy by the cloud

ensemble. Arakawa and Schubert (1974) estimated the order of magnitude of τ at $10^3 - 10^4$ sec, based on the modeled scenario of the convective adjustment of a typical conditionally unstable cloud layer not maintained by large-scale forcings towards neutrality. When applied in GCMs the precise value of τ is chosen somewhat freely. Nordeng (1994) suggested a timescale of one hour, which is also used in this study. In the penetrative adjustment scheme of Betts and Miller (1986a,b) a relaxation timescale of two hours is used, for a discussion on this subject see Betts (1997).

The closure developed by Fritsch and Chappell (1980) links the adjustment of CAPE to the convective overturning invoked by the cloud ensemble. Based on this approach is the closure applied by Nordeng (1994) to deep convection in the ECMWF model (Gregory et al., 2000). The convective heating and drying is assumed to be dominated by compensating environmental subsidence, as the updraft and downdraft of the cloud ensemble is assumed to be in steady state (Tiedtke, 1989). Compensating subsidence acts to destroy CAPE by affecting the environmental profiles,

$$\left(\frac{\partial \bar{\theta}}{\partial t}\right)_{conv} \approx M^c \frac{\partial \bar{\theta}}{\partial z} \quad \text{and} \quad \left(\frac{\partial \bar{q}_l}{\partial t}\right)_{conv} \approx M^c \frac{\partial \bar{q}_l}{\partial z}. \quad (6.9)$$

Consequently the tendency of CAPE in (6.8) can be written as

$$\frac{\partial CAPE}{\partial t} \approx -M_b^c \int_{z_b}^{z_i} \frac{\eta g}{\Theta_v^0} \frac{\partial \bar{\theta}_v}{\partial z} dz, \quad (6.10)$$

where η is the normalized mass flux,

$$\eta(z) = \frac{M^c(z)}{M_b^c}. \quad (6.11)$$

In combination with (6.8) this gives

$$M_b^c = \frac{CAPE}{\tau} \left(\int_{z_b}^{z_i} \frac{\eta g}{\Theta_v^0} \frac{\partial \bar{\theta}_v}{\partial z} dz \right)^{-1}. \quad (6.12)$$

I
II

Term I in (6.12) represents the *required* breakdown-rate to fully destroy the existing CAPE in time τ , while term II is the inverse of the normalized *potential* breakdown-rate, being a function of the lapse rate of the environmental virtual potential temperature. Accordingly, the CAPE adjustment closure gives the mass flux at cloud base which is needed to break down the existing CAPE by compensating subsidence in a given adjustment time-scale τ .

6.3.3 Convective subcloud velocity scales

A third method for mass flux closure is to relate the mass flux activity at cloud base to the turbulent kinetic energy (TKE) in the SL. This idea is based on the fact that the clouds are actually the visible parts of thermals which root deeply into the dry SL (LeMone and Pennell, 1976). These rising thermals first have to pass through a shallow stable layer at the top

of the SL before they become positively buoyant at their level of free convection. Accordingly, the kinetic energy and distribution of these condensing thermals at that height bear the 'fingerprint' of the turbulence in the SL.

Following (6.2), the mass flux at cloud base is defined as the product of the core fraction and the vertical velocity at that height,

$$M_b^c \equiv a_b^c w_b^c. \quad (6.13)$$

The next step is to parameterize the two variables on the right hand side using SL characteristics. The most appropriate candidate for scaling w_b^c is the free convective vertical velocity scale of the SL w_{sub}^* (Deardorff, 1970a) defined as

$$w_{sub}^* = \left(\frac{gz_b}{\Theta_v^0} (\overline{w'\theta'_v})_s \right)^{\frac{1}{3}}, \quad (6.14)$$

where z_b is the depth of the SL, θ_v is the average virtual potential temperature of the SL, and $(\overline{w'\theta'_v})_s$ is the buoyancy flux at the surface.

w_{sub}^* only takes into account the vertical component of the TKE in the SL, while in high-shear situations the horizontal fluctuations may also contribute significantly. In those conditions some combination of w^* and u^* may be used in the definition of the subcloud turbulent velocity scale (e.g. Moeng and Sullivan, 1994). Also, in deeper convective situations the relatively massive latent heat release in the clouds and the occurrence of precipitation may seriously affect the turbulence in the SL, as is indicated by the occurrence of gusts in the vicinity of the deep cumulus clouds. For those situations one could include some deep convective velocity scale in the scaling of w_b^c , based on cloud layer properties such as CAPE. This combination in fact represents a superposition of the two different closure-CAPEs described before, the one controlled by the subcloud layer and the other by the cloud layer. Summarizing these options gives

$$w_b^c \sim \begin{cases} w_{sub}^* & \text{low shear} \\ f(w_{sub}^*, u_{sub}^*) & \text{high shear} \\ f(w_{sub}^*, u_{sub}^*, w_{cloud}^*) & \text{deeper convection} \end{cases} \quad (6.15)$$

The central question of this study is how the various closures perform in a typical diurnal cycle of shallow cumulus, characterized by relatively low shear values and the absence of deep convection. Accordingly here w_b^c will be scaled with w_{sub}^* only, and the other two options in (6.15) for deeper convection and more intense shear remain subjects for further study. The scaling of w_b^c with w_{sub}^* will be evaluated using LES results on the diurnal cycle, during which w_{sub}^* varies considerably due to the changing surface buoyancy flux and cloud base height.

Next the core fraction a_b^c in (6.13) needs consideration. The LES intercomparison study by working group 1 of GEWEX (Global Energy and Water-cycle Experiment) Cloud Systems Studies (GCSS) on the Atmospheric Radiation Measurement (ARM) case (Brown et al., 2002) showed that the maximum cloud fraction typically decreases during the existence of the cloud layer in such a diurnal cycle. The impact of this decreasing cloud fraction on

M_b^c can therefore be significant. When (6.13) is used in a 1D model one could therefore consider to use a parameterized cloud fraction for a_b^c , which in most 1D models is calculated in a cloud scheme. The RACMO 1D model in this study uses the statistical method of Cuijpers and Bechtold (1995). The cloud fraction N_{cb95} is formulated in terms of the normalized saturation deficit,

$$N_{cb95} \equiv f \left(\frac{\bar{s}}{\sigma_s} \right), \quad (6.16)$$

where the saturation deficit s is defined as

$$s \equiv q_r - q_{sat}, \quad (6.17)$$

and σ_s^2 is its variance. Chaboureau and Bechtold (2002) have extended (6.16) for all cloud types and evaluated its performance for deep cumulus. It has so far not been tested for diurnal cycles of shallow cumulus over land.

Equation (6.13) can now be written as

$$M_b^c = \kappa N_{cb95} \gamma w_{sub}^* \quad (6.18)$$

where γ is a factor of proportionality between w_{sub}^* and w_b^c , and κ a factor to account for the difference between cloud fraction and core fraction. When applied in a 1D model the inclusion of the parameterized cloud fraction in the mass flux closure introduces an interesting extra feedback between the shallow convection scheme and the cloud scheme. The core fraction is now needed to calculate the mass flux. The mass flux scheme produces detrainment rates which in turn are used in some cloud schemes. The statistical type cloud schemes based on (6.16) require some parameterization for σ_s . The variance equation for σ_s includes a production term which is a function of the moisture and heat flux, which in RACMO 1D are parameterized using the mass flux approach (Lenderink and Siebesma, 2000). Hence both classes of cloud schemes are linked to the mass flux scheme. This further intertwining of cloud- and convection-scheme may be realistic, but it is unknown how this affects the numerical stability of the 1D results.

The coupling of M_b^c to w_{sub}^* was first proposed by Grant (2001), using a simplified budget equation for the TKE in the SL to arrive at

$$M_b^c = \eta w_{sub}^*. \quad (6.19)$$

This equation actually states that the flux of TKE at cloud base is equal to the buoyant production minus viscous dissipation of TKE in the SL. The factor η is a function of the ratio of the surface to cloud base buoyancy flux and the viscous dissipation rate. Conditional sampling in LES in several different shallow cumulus cases gave $\eta = 0.03$. Loosely comparing this value to (6.18), one may interpret the factor 0.03 as a typical value for the core fraction at cloud base in shallow cumulus. This would suggest some relationship between core fraction and the TKE budget in the SL. However this is yet a simplistic view, as the factor η represents many assumptions and scaling factors. Nevertheless, as (6.18) and (6.19) have such a similar form they will be evaluated alongside each other during the discussion of the results.

6.4 Case descriptions and large-eddy simulation.

6.4.1 Cases

The cases representing the diurnal cycles are described here. The first case is based on the development of shallow cumulus over land as observed on June 21st, 1997 at the Southern Great Plains site in Oklahoma of the Atmospheric Radiative Measurement (ARM) program. This case has been designed for an intercomparison study by GCSS working-group I, and was later also used in the European Cloud Systems (EUROCS) project. It is described in great detail by Brown et al. (2002). A diurnal cycle was observed in a cumulus topped convective boundary layer over land. Radiosonde soundings, surface flux measurements and cloud radar observations were made on this day. The surface heat fluxes make a full cycle from very low values at dawn to peak values at mid-day and back again. It is expected that this causes problems for many closures, as the mass flux at cloud base may consequently change in time. The ARM case is therefore a suitable, critical testcase for the purpose of this paper. The structure of the cloud layer of the ARM case in LES is plotted in Fig.6.1a.

The second case also describes a diurnal cycle over land, as observed during the Small Cumulus and Micro-physics Study in August 1995 at Cocoa beach, Florida (SCMS). An LES case was constructed based on radiosonde soundings, measurements of the surface energy balance, temperature and moisture, and aircraft measurements inside the clouds (Neggers et al., 2003a). Generally speaking this case closely resembles the ARM case, but there are some subtle differences. It is somewhat moister than the ARM case, featuring a relatively high cloud cover with a peak value of 41% shortly after cloud onset. The cloud layer in SCMS

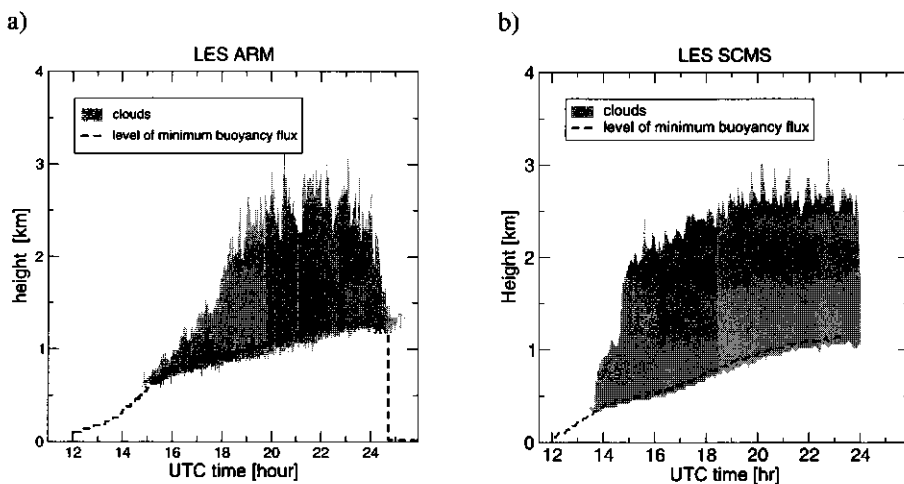


Figure 6.1 The time-series of the heights of cloud base and cloud top in LES for a) the ARM case and b) the SCMS case. The height of the minimum buoyancy flux is also shown to indicate the height of the mixed (subcloud) layer. Local time lags UTC time by 5 hours in the SCMS case (Florida) and by 6 hours in the ARM case (Oklahoma).

deepens relatively rapidly compared to the ARM case, due to the conditional instability already present at the heights where the clouds first develop (see Fig.6.1b). Finally, the mean horizontal wind was much weaker in SCMS, which makes it a low wind-shear case.

The basic characteristics and setup of these two cases are quite similar. Therefore, we focus the presentation of the results on the outcome of one particular case only. To this purpose we choose the ARM case, as it is at this moment the best known and most documented case of the two. In addition the SCMS case will primarily be used as a supplemental testground for the closures, to evaluate the universality of the results on the ARM case at some vital points where the two cases differ.

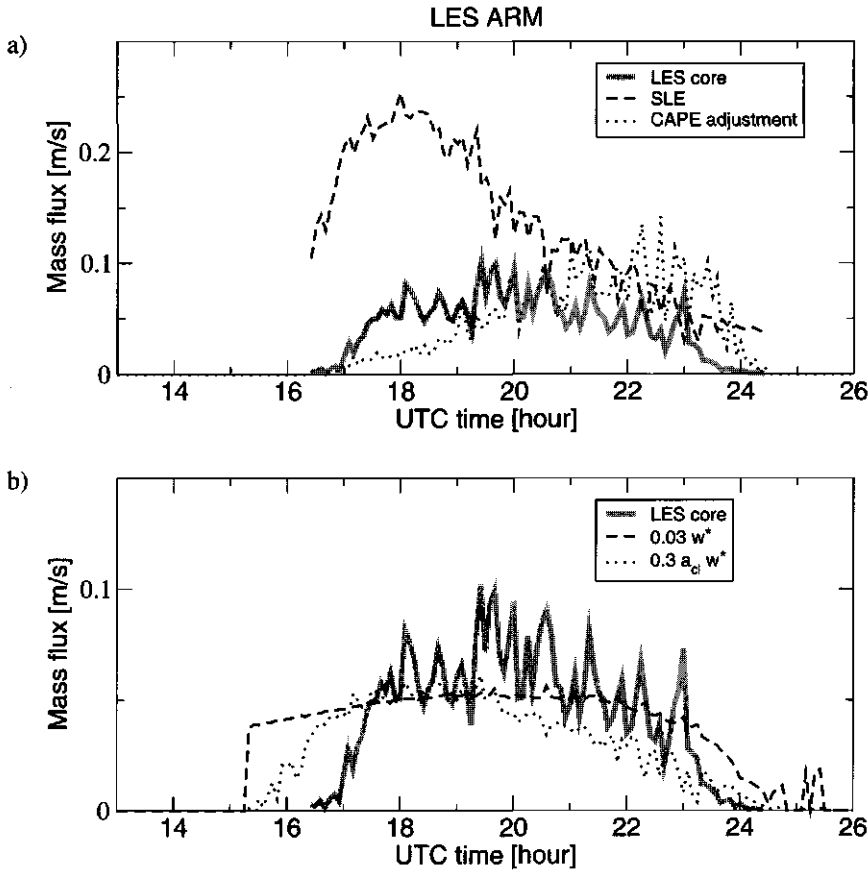


Figure 6.2 The cloud base mass flux in the ARM case as predicted by a) the SLE closure and the CAPE adjustment closure, and b) the two versions of the w^* closure, based on parameters sampled during the LES run. The cloud base value of the core mass flux in LES is plotted for reference.

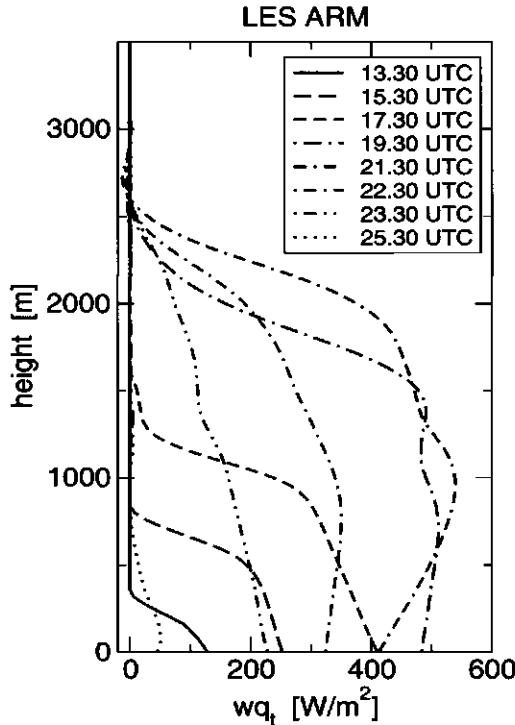


Figure 6.3 Vertical profiles of the hourly averaged total moisture flux during the diurnal cycle of the ARM case in LES.

6.4.2 LES results

LES is used to evaluate the performance of this range of closures in the two cases described above. The diurnal cycle is a critical test for these closures, as during the day the parameters on which the closures are based may change significantly. Time-series of these parameters are derived by sampling the simulated cloud fields during the whole simulation. The performance of the resulting mass flux closures is evaluated by comparing the parameterized mass flux at cloud base with the actual value sampled in LES. This should immediately reveal the possible conceptual shortcomings of the closures. As the closures are designed to predict the mass flux of the active transporting updrafts in the cloud layer, we choose to compare the closures to the mass flux of the *cloud core* in LES.

Figure 6.2a shows the timeseries of the mass flux at cloud base as resulting from the SLE closure and the CAPE closure. The SLE closure predicts too high values of the mass flux at cloud base during the first hours after cloud onset. Figure 6.3 offers a closer look into the moisture tendencies due to vertical transport in LES during the diurnal cycle. It is clear that in the period of over-prediction of M_b^c the SL experiences ongoing moistening. It is evident that assuming the SL to be a constant moisture-flux layer does not hold in this period. A significant part of the surface input of moisture is deposited in the SL, and consequently the

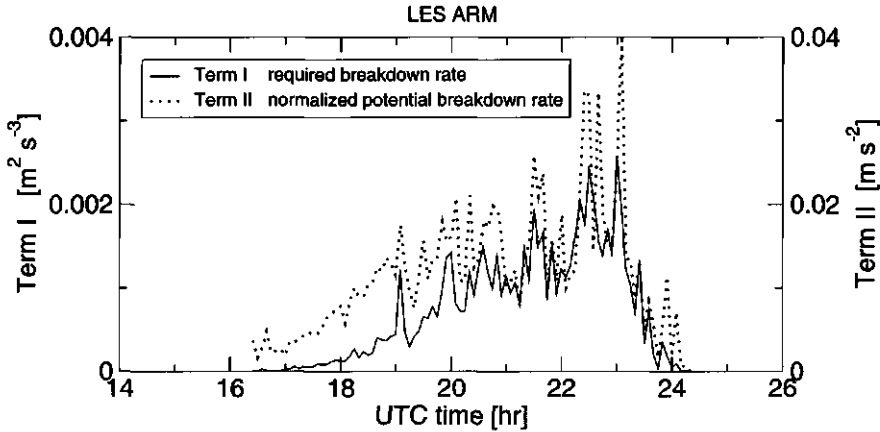


Figure 6.4 The evolution during the ARM case of the required breakdown-rate and the potential breakdown-rate of CAPE in LES. The terms correspond to term I and II of equation (6.12) respectively.

use of $(\overline{w'h'})_s$ in (6.4) is an overestimation for the actual total flux at cloud base $(\overline{w'h'})_b$. As a result the mass flux at cloud base is overestimated. Later on the day the flux-gradient in the SL in LES is much smaller, and consequently the SLE closure performs better. The significant overestimation of the cloud base mass flux by this closure in the early hours will cause too vigorous vertical transport into the cloud layer when applied in a 1D model.

The CAPE adjustment closure gives a very small mass flux at cloud base in the early hours after cloud onset. This results from the ratio of the required breakdown-rate to the potential breakdown-rate in (6.12) being relatively small at that stage, due to the small CAPE values of the shallow cloud layer, see Fig.6.4. Apparently, to break down all CAPE in time τ only a small mass flux is needed at this stage, but nevertheless the actual mass flux in LES is much larger. This indicates that the clouds are forced from below, being overshooting thermals driven by the subcloud layer turbulence. Later on the day (after 20:00 UTC) the cloud layer has deepened considerably (to about 1km) and contains much more CAPE. At this stage the situation is reversed, as the value predicted by the CAPE closure is now larger than the actual cloud base mass flux in LES. Although the cloud layer has enough CAPE to support moist convection, the mass flux at cloud base is now limited by the weakening convection in the subcloud layer, due to the decreasing surface fluxes. The rising thermals are simply less and less capable of reaching their level of free moist convection in the first place, and the connection between the cloud layer and the subcloud layer is lost.

In contrast to the previous two closures, the two versions of the w^* closure predict cloud base mass fluxes which are in phase with LES (see Fig. 6.2b). The maximum mass flux occurs at the right time, and the collapse of the cloud mass flux at the end of the day is also captured. The reason for this is illustrated by Fig.6.5, which shows that the cloud core average vertical velocity at cloud base w_b^c as sampled in LES scales rather well with w_{sub}^* , especially in the SCMS case. Apparently the turbulence in the SL really does control the vertical velocity at cloud base. Based on these results we assume $\gamma \approx 1$ in (6.18). Figure 6.6 illustrates that the decreasing cloud fraction with time in LES is captured by the parameterization N_{CB95} ,

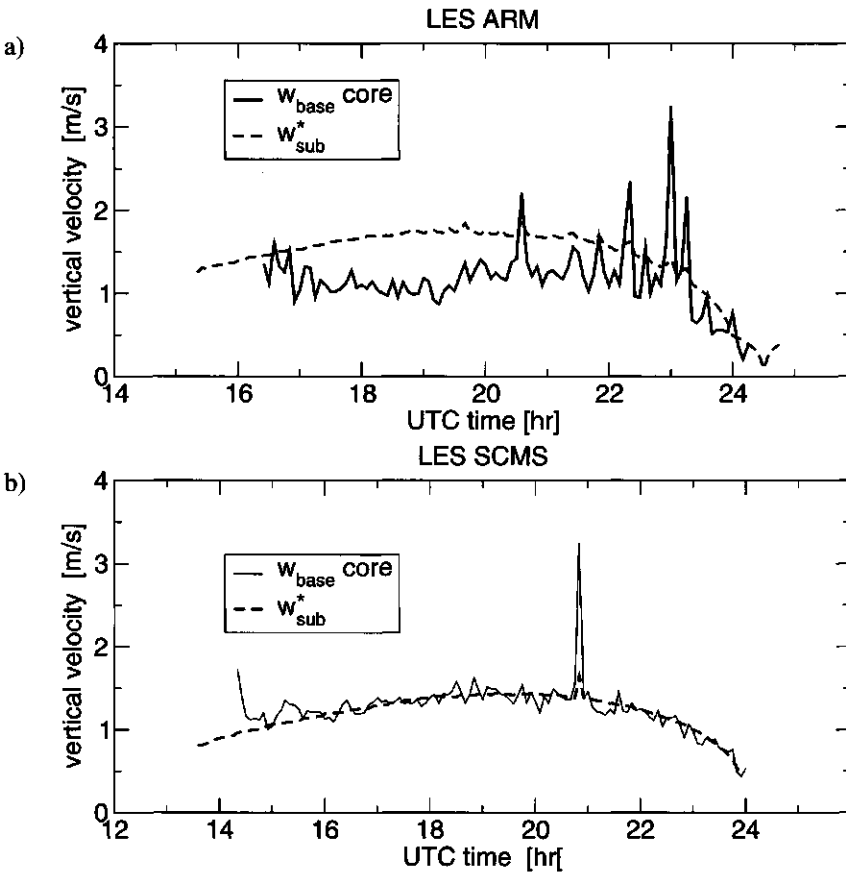


Figure 6.5 The conditionally sampled vertical velocity of the cloud core at cloud base, and the convective vertical velocity scale of the subcloud layer w^* . Panel a) shows the ARM case, panel b) the SCMS case.

although the early maximum is under-predicted by a factor 2. This is interesting enough, but nevertheless these values are still within the observed scatter in the results presented by Chaboureau and Bechtold (2002) using CRM results on a diurnal cycle of deep cumulus observed at the ARM SGP site. Based on Fig.6.6 we assume $\kappa = 0.3$.

Figure 6.2b shows that the differences between (6.18) and (6.19) are only small. A minor shortcoming of the $0.03w_{sub}^*$ version is that it misses the slow increase of the cloud base mass flux in LES in the early hours after onset. This is due to the fact that the turbulence in the subcloud layer is already well-developed while the cloud layer is still very shallow. The advantage of (6.18) is that it includes the cloud fraction, which suppresses M_b^c for some time after cloud onset. Ideally a parameterization for the core fraction should be used to avoid the use of the rather ad-hoc factor $\kappa = 0.3$, but such a parameterization has yet to be developed.

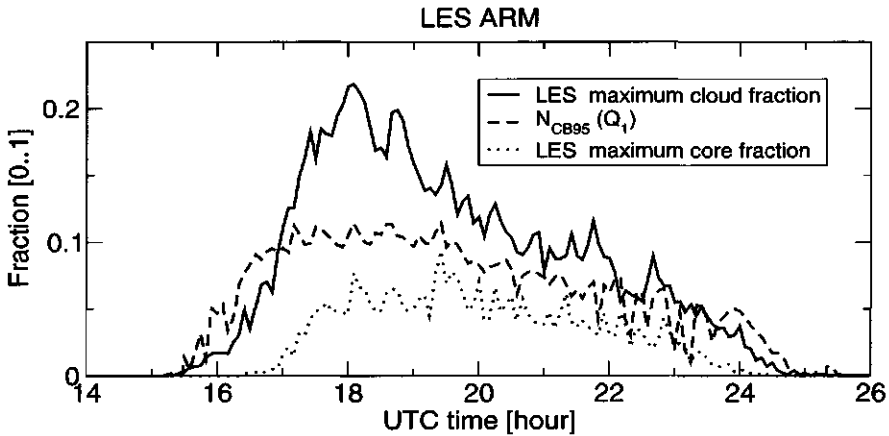


Figure 6.6 The cloud- and core-fraction at cloud base in LES, and the statistical parameterization of Cuijpers and Bechtold (1995).

6.5 Single column model results

6.5.1 Description of the model

The three closures are implemented in the convection scheme of the off-line RACMO 1D model. In the LES analysis described in the previous section the time-series of M_b predicted by the various closures are only diagnostic: they show what the closures predict given the parameters as they are in LES at that moment. In contrast, in the 1D runs the closures affect the development of the (thermo)dynamic state of the boundary layer. The underlying physical causes for the typical behaviour of the various closures are already analyzed and discussed in Section 6.4. This section focuses on how the development of the boundary layer in the 1D model is affected by the various closures.

A description of the RACMO 1D model is given by Lenderink and Siebesma (2000). The model consists of a dry turbulence scheme for mixed layer transport using a TKE mixing length (Lenderink and Holtslag, 2002), the mass flux convection scheme for cloud layer transport of Tiedtke (1989), and a statistical cloud scheme based on the parameterization of Cuijpers and Bechtold (1995). Firstly the turbulence scheme is executed, distributing moisture and heat fluxes at the surface over the mixed layer. The turbulence scheme overlaps the mass flux scheme at cloud base. Subsequently the closure for the cloud base mass flux is carried out, after which the mass flux profile is calculated in the convection scheme. The fixed entrainment and detrainment rates $\epsilon = 2 \times 10^{-3} \text{m}^{-1}$ and $\delta = 2.7 \times 10^{-3} \text{m}^{-1}$ are used as suggested by Siebesma and Cuijpers (1995), found to be appropriate in 1D context by Siebesma and Holtslag (1996). In the mixed layer, the mass flux is set to increase linearly with height towards its cloud base value. Above cloud top, any remaining mass flux is forced to zero in a massive detrainment layer following an exponentially decreasing profile with height. The mass flux is also used in a simplified diagnostic variance equation for σ_z , to calculate the cloud fraction using (6.16) (Lenderink and Siebesma, 2000)

For the SLE closure, the h-flux at cloud base is estimated by integrating with height all

tendencies in the SL,

$$M_b(\bar{h}^c - \bar{h})_b = \int_0^{z_b} \left(LS_{adv} + F_{rad} - \frac{\partial w' \bar{h}'_{turb}}{\partial z} \right) dz. \quad (6.20)$$

where the subscript *turb* indicates the flux by the dry turbulence scheme, LS_{adv} is the tendency due to large scale forcings, and F_{rad} is the tendency due to radiation. The result of (6.20) is the surface flux plus forcings minus the small flux of the still active turbulence scheme at cloud base. Note that the ARM case is known for its relatively small large-scale forcings, by which the surface fluxes dominate the total forcing of the system. In that limit (6.20) reduces to (6.4) (not accounting for the small dry turbulence flux at cloud base). w^* can easily be calculated from the surface buoyancy flux and the mixed layer height. If the cloud fraction is used in the w^* -closure its value at the previous time step is used. The CAPE adjustment closure also uses the values of the previous time step in order to calculate the terms in (6.12). If no shallow convection occurred at the previous time-step, a minimum value of 0.01m/s is assumed for M_b .

The simulations are performed on a vertical grid of 40 levels covering the lowest 4km of the atmosphere, which results in about 7 levels in the cloud layer. The time-integration step is 60s. The surface fluxes were prescribed, as were the other forcings and the initial conditions, using exactly the same settings as in the LES runs.

6.5.2 Results

Figure 6.7 shows the time-series of the cloud base mass flux during the ARM case in RACMO 1D. Comparing these to Fig.6.2 illustrates that in general the RACMO 1D results resemble the corresponding diagnostic tests in LES. For example, the SLE closure predicts a cloud base mass flux which is three times too large in the early hours. Figure 6.8 shows the corresponding flux profiles of heat and moisture at two moments in the diurnal cycle. At 17:30 UTC the SLE closure per definition predicts an almost constant moisture flux in the subcloud layer, while according to LES it should be moistening considerably. As a consequence most of the surface moisture flux is transported into the cloud layer and the inversion, where it causes a too rapidly deepening cloud layer, see Fig.6.9a. The resulting intense massive detrainment by the mass flux scheme in the inversion causes the SL to heat up too rapidly compared to LES which causes the cloud base to rise too fast, see Fig.6.9a. At 22:30 UTC when the cloud layer is fully developed the situation is reversed, as the heat and moisture fluxes at cloud base are now too small.

The application of the CAPE adjustment closure in RACMO 1D resembles its evaluation in LES, as the mass flux at cloud base shows the same, increasing trend. Figure 6.7a illustrates that first M_b is too small, but as the CAPE of the deepening cloud layer increases in time so does M_b , and is significantly over-predicted in the final hours. Figure 6.8d shows that the resulting too large moisture flux at cloud base causes too intense drying in the subcloud layer. The rise of cloud base with time in LES is reproduced by the closure, which results from the fact that the order of magnitude of the predicted mass flux at cloud base is comparable

to LES. Apparently the adjustment timescale τ of one hour works reasonably well for this situation.

Both versions of the w^* -closure predict the maximum cloud base mass flux at the right time, and also reproduce the collapse of mass flux transport at the end of the day, see Fig.6.7b. The flux profiles in Fig.6.8a and 6.8b show that this closure also reproduces the initial moistening and subsequent drying of the boundary layer. The only problem with the $0.03w^*$ version occurs in the first two hours, where the convection scheme is already active in RACMO 1D but the cloud scheme is not. The inclusion of the parameterized cloud fraction in the w^* closure instead of the constant factor 0.03 prevents mass flux activity without clouds. However, it then slightly overestimates M_b^c in the final hours of the cloud layer. This is caused by the parameterized cloud fraction, which does not show the typical decrease with time of LES (see Fig.6.10). The diagnostic test in LES discussed in the previous section showed that in

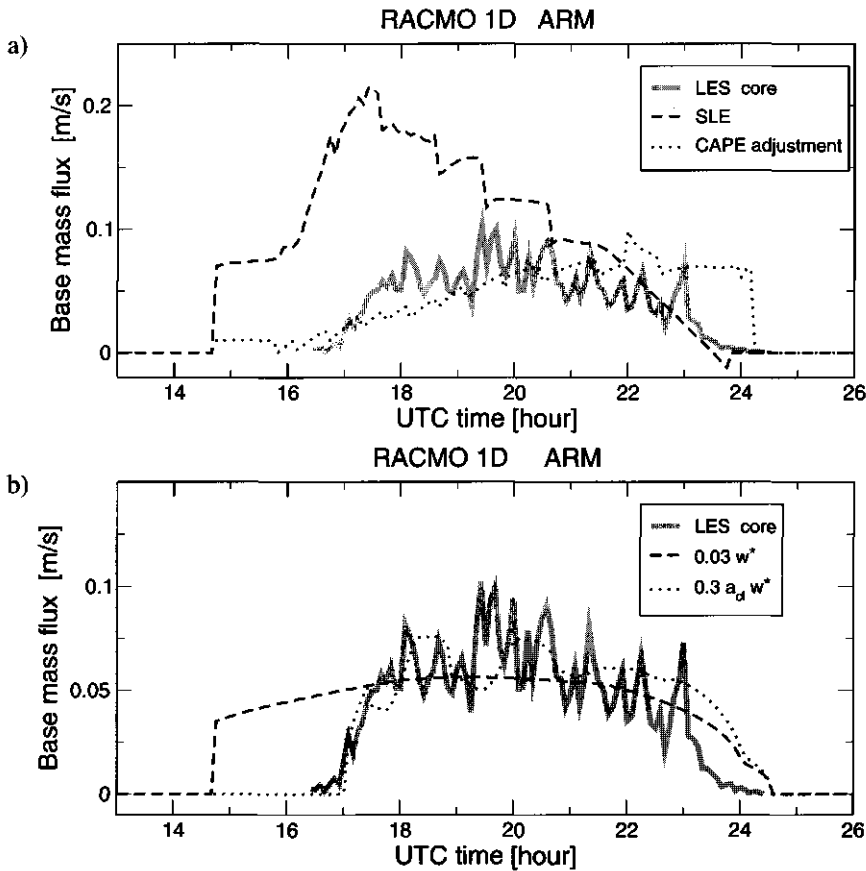


Figure 6.7 The cloud base mass flux in RACMO 1D as predicted by a) the SLE closure and the CAPE adjustment closure, and by b) the two versions of the w^* closure. The cloud base value of the core mass flux in LES is plotted for reference.

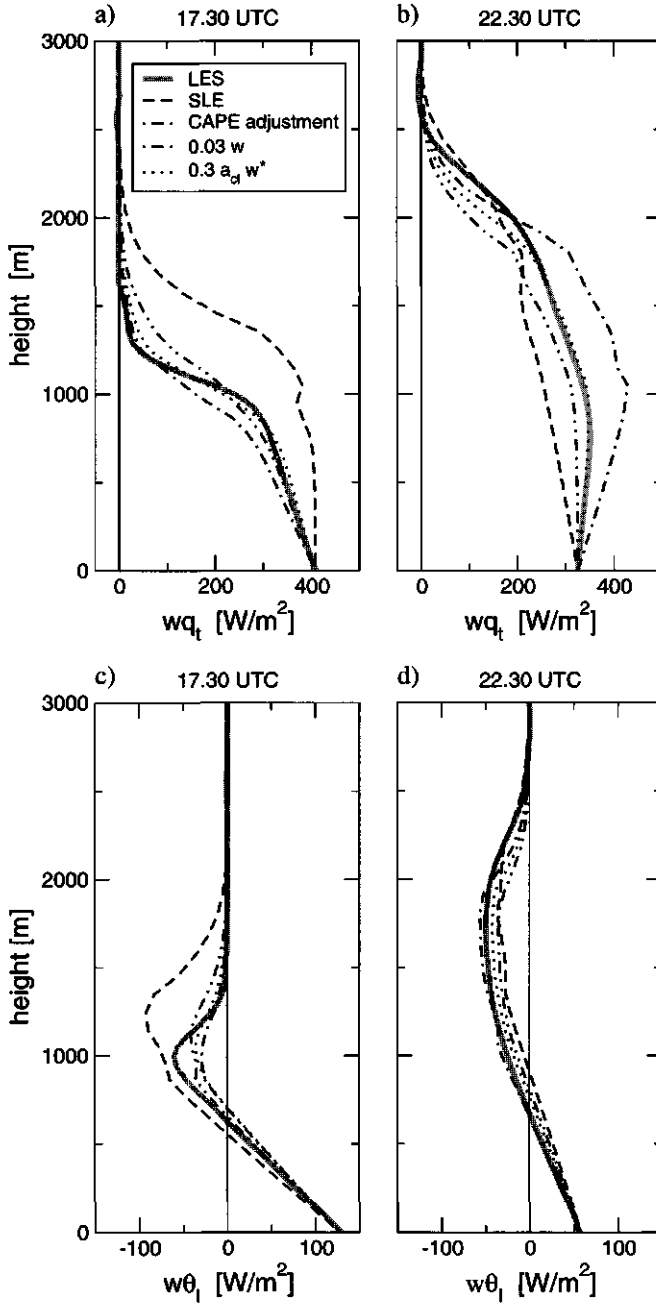


Figure 6.8 The total moisture and heat fluxes of the ARM case in RACMO 1D at 17.30 and 22.30 UTC. The LES profiles are also plotted for reference.

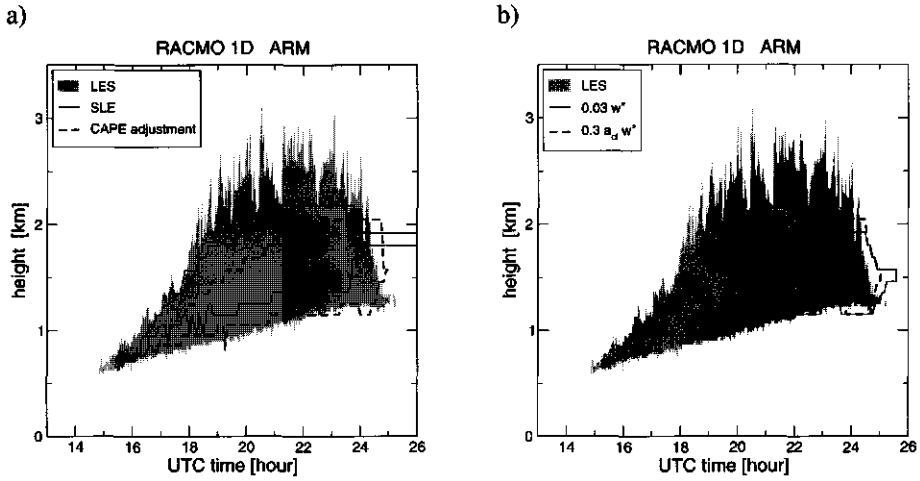


Figure 6.9 The heights of cloud base and cloud top during the RACMO 1D simulations of the ARM case. The LES cloud heights are also plotted for reference. Note that the top-hat massflux scheme in RACMO 1D is not designed to predict cumulus overshoots into the inversion, which appear as spikes in the cloud top height in LES.

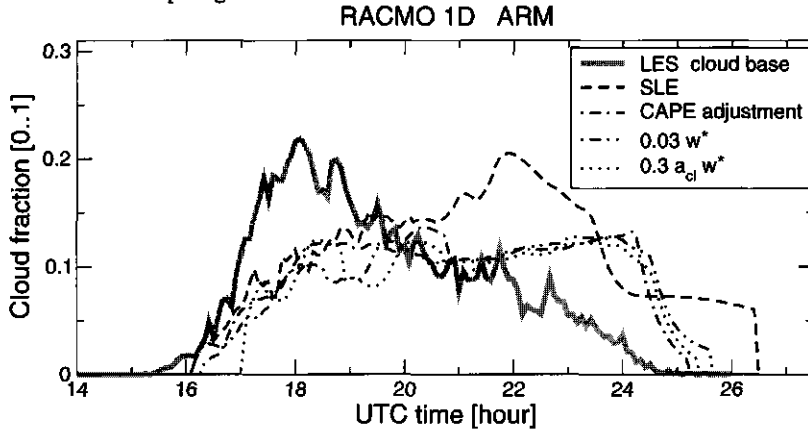


Figure 6.10 The cloud-fraction at cloud base during the RACMO 1D simulations. The LES time-series is also plotted for reference.

principle this method *does* predict a decreasing cloud fraction, given the right parameters (see Fig.6.6). Whether the estimate of the saturation deficit average or its variance does not develop correctly with time in RACMO. Thus, improving the parameterization of the saturation deficit remains a subject for further research.

6.6 Summary and conclusions

In this study three types of mass flux closure are critically examined for simulated diurnal cycles of shallow cumulus over land. It appears that each type of closure has specific advantages and disadvantages when applied in an operational convection scheme.

The SLE closure can not deal with significant moisture and temperature tendencies in the subcloud layer. Assuming the SL to be a constant flux layer leads to unrealistic intense vertical mixing, resulting in a too rapidly deepening cloudy boundary layer. This might have serious implications. For example, an outstanding issue in many GCMs is the timing of convection over land. For example, a comparison of ECMWF model results to the measured hydrometeor-occurrence at the ARM SGP site by Mace et al. (1998) showed that typically the model predicts the onset of deep cloud events too soon. As deep (precipitating) convection in diurnal cycles is often preceded by shallow convection earlier on the day, it is likely that the development of the shallow cumulus cloud layer in time at least partially determines the onset of deep convection. A too rapidly deepening cloud layer caused by the SLE closure might be one of the reasons for the early triggering. On time-scales much longer than a single diurnal cycle, a continuously overestimated intensity of the vertical mixing in and the deepening of the boundary layers over land may affect the thermodynamics and circulation in the overlying free troposphere in GCMs.

The CAPE adjustment closure fails to reproduce the development of the cloud base mass flux in time in LES. In the first hours the small CAPE makes the closure predict a smaller mass flux than observed in LES, which indicates that at that stage the cumulus convection is still forced by the subcloud turbulence. In contrast, in the later hours the large values of CAPE leads to an over-estimation of the mass flux at cloud base, indicating that the cloud-subcloud interaction gets limited by the weakening subcloud convection due to the decreasing surface energy fluxes. Summarizing these results we may conclude that the CAPE adjustment closure has serious problems in a diurnal cycle of shallow cumulus. To work well, this closure needs a cloud layer with considerable amounts of CAPE on top of a well-developed dry convective layer driven by surface energy fluxes. Its use lies therefore in the parameterization of deep convection.

The closure based on the convective velocity scale w^* (6.18) is most promising as it reproduces the evolution in time of the cloud base mass flux in LES. Apparently this closure catches the coupling which exists between the two layers at cloud base. As a consequence the development of the thermodynamic structure of the boundary layer in RACMO 1D strongly resembles that in LES. Including the parameterized cloud fraction in this closure prevents moist convection without clouds in the 1D model, but its success obviously depends on the skill of the cloud fraction parameterization.

The evaluation of the three closures shows that in general two basic approaches exist in modeling the cloud-subcloud interaction, namely domination by subcloud turbulence versus domination by the moist convective processes in the cloud layer. For a diurnal cycle of shallow cumulus, the coupling of the mass flux activity at cloud base to the subcloud turbulent velocity scale clearly gives the best 1D results. The question is if the strict relation between subcloud TKE and vertical velocity at cloud base still holds for high shear conditions or significantly deeper cloud layers, where the cloud dynamics is expected to play a more significant role in the cloud-subcloud interaction. To that purpose other relevant scales can be

included in the parameterization of the cloud base vertical velocity, such as u^* and w_{cloud}^* . The formulation and evaluation of this concept is a subject for further research.

The mass flux closures were evaluated for a controlled diurnal cycle with no large forcings other than the surface fluxes. The results show that the impact of the mass flux closure on the development of the boundary layer is significant. Therefore, the next step should be to implement these closures in a full three-dimensional GCM simulation. This gives insight in the impact of the closure on the horizontal circulation, cloud fraction and precipitation, the radiative budget and ultimately the climatology. Such a sensitivity test is in preparation as part of a planned European Cloud System (EUROCS) intercomparison on the Hadley cycle in the Northern Pacific.

Acknowledgements The LES results in this study were obtained using the supercomputer facilities of the European Centre for Medium-range Weather Forecasts (ECMWF) in Reading, UK. This study has been supported by the European Cloud Systems (EUROCS) project, and by the Netherlands Organization for Scientific Research (NWO) under Grant 750.198.06.

Chapter 7

Conclusions and Outlook

In this thesis the role of shallow cumulus cloud populations is examined in establishing and maintaining the turbulent transport of momentum, moisture and heat throughout the cloudy boundary layer. To this purpose, first the typical variability of shallow cumulus is assessed from different angles, in order to eventually capture its main characteristics in parametric formulations. Subsequently the results are put in a wider context by evaluating the nature of the coupling between clouds and the characteristics of the subcloud mixed layer. The method of research is primarily based on large-eddy simulation (LES), its representativeness in producing realistic shallow cumulus cloud fields being backed beforehand by an evaluation of LES results against cloud measurements obtained during an experimental field campaign. In this chapter the main results are summarized and their implications for boundary layer research are discussed.

7.1 Comprehensive summary

Large-eddy simulation results on shallow cumulus convection are directly evaluated against detailed cloud observations in Chapter 3, using aircraft-measurements of the Small Cumulus Microphysics Study (SCMS) as well as high-resolution Landsat images. The results show that given the correct initial and boundary conditions the LES concept is capable of realistically predicting the bulk thermodynamic properties of temperature, moisture and liquid water content of the cumulus cloud ensemble as observed in SCMS. Furthermore the vertical component of the in-cloud turbulent kinetic energy and the cloud size distribution in LES were in agreement with the observations. Several hypotheses which make use of conditionally sampled fields were tested on the SCMS data. The magnitudes and the decrease with height of the bulk entrainment rate following from the SCMS data confirm the typical values first suggested by Siebesma and Cuijpers (1995) using LES results on BOMEX. An alternative formulation of the lateral entrainment rate as a function of the liquid water content and the mean lapse rate agrees well with the original form based on the conserved variables. Applying the simplified equation for the cloud vertical velocity (Simpson and Wiggert, 1969) to the aircraft-measurements results in a reasonably closed budget. These results support the

credibility of cloud statistics as produced by LES in general, and encourage its use as a tool for testing hypotheses and developing parameterizations of shallow cumulus cloud processes.

The geometrical variability of shallow cumulus cloud populations is assessed in Chapter 4 by means of calculating cloud size densities. We find a power-law scaling at the small cloud sizes and the presence of a scale break. The corresponding functional parameters have values which are typical for observed populations. The scale-break size appears to be the relevant length-scale to non-dimensionalize the cloud size, as this causes a data-collapse of the cloud size densities over several different cumulus cases. These findings suggest that a universal functional form exists for the cloud size density of shallow cumulus. A better understanding of the scale-break size is essential for a complete definition of this function. The scale-break co-determines the cloud size density, and defines the intermediate dominating size in the mass flux and cloud fraction decompositions. Its intermediate position between the largest clouds and the grid-spacing in LES implies that the clouds which do matter are resolved well by LES.

In Chapter 5 the (thermo)dynamic variability of shallow cumulus is visualized by means of conserved variable diagrams, showing the joint pdfs of the conserved thermodynamic variables and (vertical) momentum. This approach inspired the formulation of a multi parcel model, meant to at least partially reproduce the joint pdfs. A new conceptual model for the lateral mixing of such an updraft-parcel is presented, based on an adjustment time-scale for the dilution of the excess of the conserved properties of this updraft parcel over its environment. A statistical analysis of many LES clouds showed that this adjustment time-scale is constant in all clouds, which implies a lateral mixing rate which is inversely proportional to the vertical velocity. This dynamical feedback between thermodynamics and vertical momentum is shown to be capable of reproducing the cloud population-average characteristics as well as the increase of the in-cloud variances with height.

Chapter 6 deals with the cloud-subcloud coupling, which manifests itself in many aspects of shallow cumulus topped boundary layers, not in the last place in the turbulent variability. The parameterization of the transport properties of the simplified top-hat pdf is expressed in the mass flux model, of which the closure at cloud base represents this cloud-subcloud interaction. Three closure methods for shallow cumulus are critically examined for the difficult case of a diurnal cycle of shallow cumulus over land. First the various closures are diagnostically evaluated in a large-eddy simulation of a diurnal cycle. Subsequently they are implemented in an offline 1D model to study their impact on the development of the modelled cloudy boundary layer. Significant moistening occurs in the subcloud mixed layer in the first hours after cloud onset in LES, which makes the boundary-layer equilibrium closure (Tiedtke, 1989) substantially overestimate the mass flux at cloud base. As a result the boundary layer deepens unrealistically rapidly at that stage in the single column model. The adjustment closure on the convective available potential energy (CAPE) of Fritsch and Chappell (1980) fails at the early and final stages of the diurnal cycle, when the cloud base transport is controlled by subcloud layer properties. The subcloud convective velocity scale closure of Grant (2001) is promising, as it reproduces the timing of both the maximum and the final decrease of the cloud base mass flux in LES. Apparently this closure catches the coupling between the two layers at cloud base. As a consequence the development of the thermodynamic structure of the boundary layer in the 1D model strongly resembles that in LES.

7.2 Perspectives

7.2.1 The current state of cumulus representations

The ongoing evaluation of the skills of present-day GCMs against global observations reveals major discrepancies between models and measurements in certain critical situations in which boundary layer clouds are involved. The results of the Atmospheric Model Intercom-

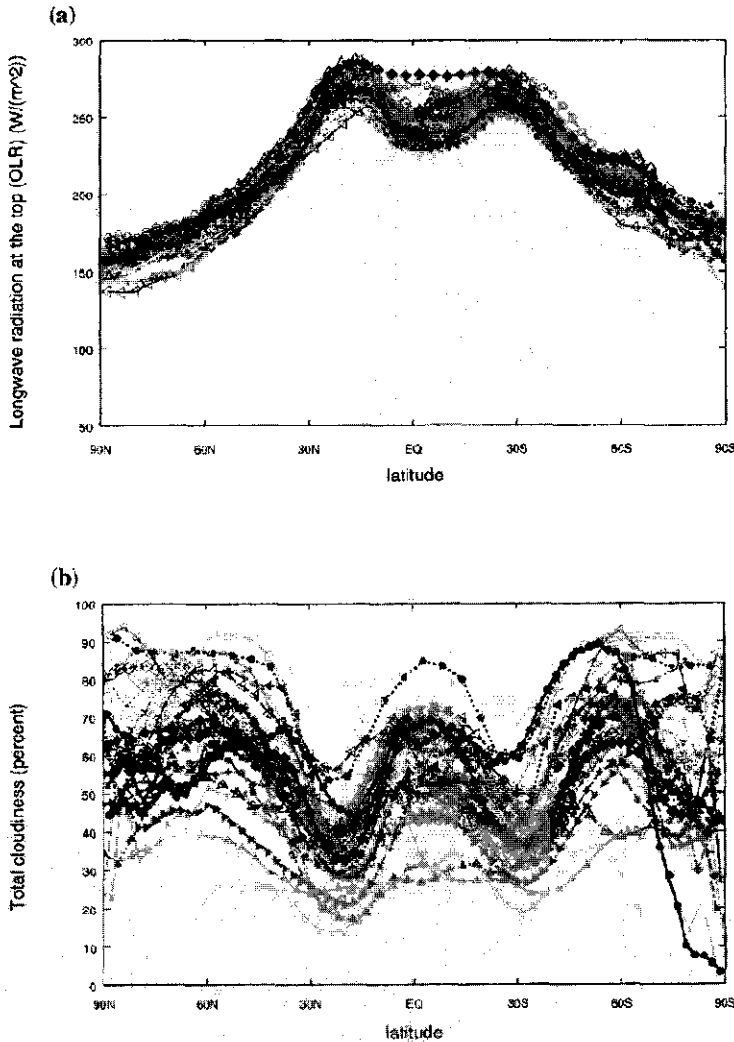


Figure 7.1 Zonally averaged variables simulated by the AMIP models compared to observations. a) The outgoing longwave radiation at the top of the atmosphere compared to NCEP data, and b) the total cloudiness compared with observations from ISCCP for 1983-1990. The observations are plotted as a black line, the participating models as grey lines. From Gates et al. (1999).

parison Project (AMIP I) show that although the average large-scale seasonal distributions of pressure, temperature, circulation and radiative transfer are reasonably close to the available observations, the total cloudiness is simulated rather poorly (Gates et al., 1999), as illustrated by Fig.7.1. This is remarkable, as the cloudiness plays such a vital role in the important global radiative transfer budget (Fouquart et al., 1990; Ramanathan et al., 1995).

Evaluation studies also take place for single GCMs or for only a few key-variables. For example, Duynkerke and Teixeira (2001) compared ECMWF Re-Analysis results (ERA, see Gibson et al., 1997) to observations of stratocumulus located off the coast of California during the FIRE I experiment. They conclude that typically the predicted optical cloud thickness is overestimated and the cloud cover and liquid water path are underestimated. Mace et al. (1998) also evaluated ERA results, this time against the hydrometeor occurrence at the ARM SGP site as measured by a continuously operating cloud radar. They conclude that the model shows good skill in predicting the vertical distribution of clouds and precipitation, but that the onset of deep cumulus is predicted too early and the cloud depth is overestimated. These evaluations can also be carried out for other boundary layer properties, for example as measured by fixed meteorological surface-stations (e.g. Mather et al., 1998).

These results show that many important boundary layer cloud characteristics are still poorly reproduced in GCMs. LES models are widely used to develop and test such parameterizations, and accordingly these results have inspired a series of intercomparison studies for both LES and SCM models. The LES intercomparison studies assessed the capability of LES

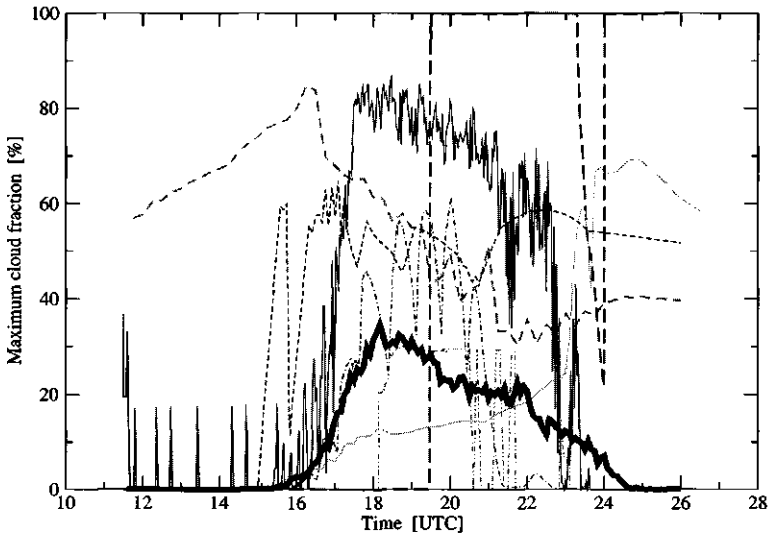


Figure 7.2 Timeseries of the maximum cloud fraction during the ARM case, as predicted by the models participating in the EUROCS SCM intercomparison on the diurnal cycle of the ARM case. The LES results are plotted as a black line, the participating models as grey lines.

in reproducing convective cloudy boundary layers, see Section 2.2.2. The resulting numerical simulated fields then supported the evaluation of the performance of (semi-)operational SCM models for the same cases. The SCM intercomparisons as described by Bechtold et al. (1996) and Duynkerke et al. (1999) were dedicated to stratocumulus. The intercomparisons on shallow cumulus (Siebesma et al., 2002; Stevens et al., 2001; Brown et al., 2002) were all combined LES / SCM studies. These evaluations further revealed the behaviour of current boundary layer 1D schemes for these difficult cases. For example, Figure 7.2 illustrates that the SCM models participating in the European Cloud Systems (EUROCS) intercomparison on the diurnal cycle of shallow cumulus over land (Lenderink et al., 2002) more or less fail collectively in reproducing the onset and area fraction of cumulus clouds. It is evident that significant improvements can still be made in boundary layer cloud parameterizations.

7.2.2 Contributions and implications

The various cumulus case studies referred to in this thesis have already led to a better understanding of this boundary layer cloud regime. Quantitative and qualitative descriptions now exist of convection and turbulence in a range of different observed situations (e.g. Schumann and Moeng, 1991a,b; Wyngaard and Moeng, 1992; Grant and Brown, 1999). The advective mass flux scheme has been shown to capture the bulk of the cumulus vertical transport, which has led to its application in operational 1D schemes alongside the older diffusive-type schemes (e.g. Tiedtke, 1989; Siebesma and Cuijpers, 1995; Siebesma and Holtslag, 1996; Gregory et al., 2000). The type of statistical cloud schemes is growing ever more popular in the 1D modelling community, after its potential has been shown to realistically predict the cloud fraction for most cloud regimes in the boundary layer (Sommeria and Deardorff, 1977; Cuijpers and Bechtold, 1995; Chaboureaud and Bechtold, 2002). The research presented and discussed in this thesis must be seen in the context of these recent developments. The emphasis lies on the dynamics of shallow cumulus convection, the description of its thermodynamic and geometric variability, and the interaction of cloud populations with the planetary boundary layer. In this section the meaning of the main results will be discussed, as well as the new questions raised by them.

The results of Chapter 3 and 4 indicate that the shallow cumulus cloud populations as resolved by LES at present-day resolutions are realistic, both in a geometrical and (thermo)dynamical sense. The typical bulk lateral entrainment rates as found by Siebesma and Cuijpers (1995) using LES are supported by the aircraft-measurements during SCMS. These findings justify the use of these mixing parameters in shallow cumulus mass flux schemes (e.g. Siebesma and Holtslag, 1996). Furthermore, the evaluation of the cloud size statistics in Chapter 4 shows that LES produces realistic cumulus populations. This analysis on population statistics supplements the results on individual cloud geometry in LES by Siebesma and Jonker (2000), who reported that the fractal dimension of cumulus clouds in LES resembles that of natural clouds as reported by Lovejoy (1982). To summarize, these results advocate the use of LES in studying problems in which the irregularity and distribution of cumulus populations play a role, such as the radiative transfer properties of these cloud fields.

One of the main themes of this thesis is the important role of the interaction between the cloud and subcloud layer in shallow cumulus convection. The interaction manifests itself in

the vertical fluxes of heat and moisture at cloud base (Nicholls and LeMone, 1980) and the cloud base mass flux (see Ogura and Cho, 1974; Betts, 1976). Accordingly, the closure of the mass flux model at cloud base should capture the typical development of this interaction in time. This is essential for reproducing the establishment (triggering) and maintenance of shallow cumulus in 1D models, and for the timing of transitions to and from other boundary layer cloud types. Nevertheless, the study on the diurnal cycle of shallow cumulus in Chapter 6 shows that especially during such changing conditions many existing mass flux closures are unreliable. The closure based on the subcloud convective velocity scale w_{sub}^* is an exception, as it captures the development of the cloud base transport in time. It is evident from these results that further development and refining on this type of closure is promising.

The study on the geometrical variability of shallow cumulus in Chapter 4 shows that the size statistics of cumulus cloud populations are also affected by the cloud-subcloud interaction. The size of the scale-break in the cloud size density and the related dominating size in the cloud fraction and mass flux decompositions varies over the range of shallow cumulus cases, but is shown to be the relevant parameter for reducing the cloud size pdf problem to the formulation of one scaled universal function. Therefore it is important to understand what actually controls this scale break size. Perhaps the two distinctly different regimes of the density above and below the scale-break represent two different physical processes, as was already suggested by Joseph and Cahalan (1990). The $l^{-1.70}$ powerlaw scaling for the small clouds (below the scale-break) might point at some turbulent decay process, for example the breakdown of large clouds into smaller ones. In turn, the large cloud sizes and the scale-break size might be controlled by the process which also determines the size of large coherent structures in the dry convective subcloud layer. Cahalan and Joseph (1989) suggested it was related to the size of the largest convective cell allowed to exist in the boundary layer, set by the BL height. A different view is suggested by the results of (Jonker et al., 1997, 1999a,b), who find that spectra of moisture in the boundary layer get dominated by meso-scales as time progresses. Nicholls and LeMone (1980) analyzed aircraft observations during GATE, and reported that the subcloud spectra of q and T in a shallow cumulus topped boundary layer are dominated by low-frequency meso-scale fluctuations. The domination of the spectra by these scales might well control the size of the scale-break. Further research on this subject is in progress.

The multi parcel model as formulated and tested in Chapter 5 deals with the parameterization of the (thermo)dynamic variability of shallow cumulus clouds by modeling a distribution of slightly different updraft parcels. It therefore belongs to the class of models known as the buoyancy sorting and episodic mixing models (e.g. Raymond and Blyth, 1986; Kain and Fritsch, 1990; Emanuel, 1991; Hu, 1997; Zhao and Austin, 2002). The most innovative aspect of the parcel model is the feedback between entrainment and dynamics, which in contrast to a fixed mixing rate reproduces the joint pdfs of humidity temperature and vertical velocity in the cloud layer. The model was shown to give reasonable results for two different cumulus cases, but for it to work in all situations the model should be equipped with a satisfying closure of the initial pdfs. Especially these pdfs are heavily controlled by the cloud-subcloud interaction, as indicated by numerous observations of subcloud convective plumes in the presence of fair weather cumuli (Lenschow, 1970; LeMone and Pennell, 1976; Nicholls and LeMone, 1980). Chapter 6 shows that the nature of the cloud-subcloud interaction is not in steady state but significantly changes in time. The closure of the cloudbase

joint-pdfs in these type of models is still an outstanding issue.

The combination of the parameterization of the (thermo)dynamic and geometrical variability forms the basis of so-called *spectral* models for cumulus convection. Typically in these models a decomposition is made of the total convective transport as a function of a certain wavelength, which can for instance be the cloud size (e.g. Arakawa and Schubert, 1974). A key problem in this class of models is the validation of the formulations against observations in natural clouds. There is yet little observational evidence for the important parameters in these models, like the cloud size dependence of the excess-values of conserved variables over the environment and the mixing rate. The recent high-resolutions of simulated cloud fields by LES models might provide an alternative dataset to evaluate these parameters, assuming that these numerical simulated fields are realistic. Any first or second order statistical moment of single clouds can easily be calculated from these fields when the spatial resolution is high enough to have a sufficient number of points inside each cloud. A first attempt in this direction was made in Chapter 5 by calculating the typical turn-over/adjustment time-scale of cumulus clouds as a function of cloud height. The next step is to calculate the cloud size densities of the (mass)fluxes and entrainment/detrainment rates. This approach is a subject for further research.

7.2.3 Future developments in convective cloud modeling

The feedback mechanisms between the large scale circulation and (cloudy) boundary layers in the coupled ocean-atmosphere system have been recognized as a key issue in numerical weather and climate prediction. It has been reported that different boundary layer schemes often lead to significant differences in the modeled general circulation and resolved variability of the atmosphere (e.g. Tiedtke et al., 1988; Slingo et al., 1994; Nordeng, 1994; Gregory, 1997). As 1D-models in GCMs are continuously subject to changes and improvements, evaluation of their impact on the resolved circulation remains necessary.

Although seemingly paradoxical, the ever increasing spatial and temporal resolutions of numerical GCMs might one day cause new problems, as certain convective processes will become resolved which are currently parameterized. Examples are meso-scale convective complexes and severe thunderstorms. This may require reformulation of the associated parameterization-schemes, because as a consequence the typical SGS length-scales will have to be adjusted. The representation of these systems will then become resolution-dependent. An alternative approach to SGS modeling is offered by the new concept of *super-parameterization*, which stands for the use of 2D cloud resolving models inside GCM-gridboxes in order to represent the SGS processes (Grabowski and Smolarkiewicz, 1999; Grabowski, 2001; Khairoutdinov and Randall, 2001). An advantage of this approach is that a large part of the unresolved range of subgrid scales is explicitly resolved.

The reported problems with current representations of convection stimulate the development of *unified* schemes. These SGS models may cover a range of unresolved scales and are capable of representing more than one convective cloud regime. This demands a realistic modeling of the occurrence of as well as transitions between the various scales and regimes. Nevertheless the current representation of these characteristics in GCMs has been reported to be rather unreliable. For example, Jacob and Siebesma (2002) show that improving the 'trigger'-function for convection has a profound impact on the distribution of different con-

vective cloud regimes and hence the model climate of the ECMWF GCM. The nature of many transitions is not fully understood, and efforts are made to increase our understanding on this subject (e.g. Bretherton and Wyant, 1997; Stevens, 2000). Also relevant in this respect are the evaluations of the limits of applicability of existing parameterizations, such as the study of mass flux closures in diurnal cycles in Chapter 6 or the evaluation of the mass flux approach for deep convection by Swann (2001).

Higher-order closure methods have received much attention recently, as they allow for a more sophisticated representation of small scale processes in bulk schemes. In turbulent boundary layers the transport, mixing and cloud processes are often dominated by the tails of the distributions of the (thermo)dynamic variables. Accordingly, a qualitative description and modeling of these processes therefore requires the knowledge of at least several higher statistical moments of these distributions. There are several recent examples of higher order schemes. The model of Lappen and Randall (2001a,b,c) combines a higher order closure scheme with a mass flux closure model for the parameterization of dry convection, stratocumulus and shallow cumulus convection. De Roode and Bretherton (2002) studied the second moment statistics of the vertical velocity inside clouds and calculated mass flux budgets. Statistical cloud schemes require the parameterization of the variance of the saturation deficit (Sommeria and Deardorff, 1977).

Finally a few words on the role of LES in boundary layer meteorology. In conjunction with the further evolution of supercomputers, the range of atmospheric scales as resolved by LES will expand at both ends of the spectrum. The next generation of cloud resolving models will explicitly resolve cloud dynamics and mixing processes at very small scales (Stevens et al., 2002). This would make LES increasingly suitable for simulating more stable situations. Also, the highly detailed simulated cloud populations can be used for studying the radiative transfer properties of shallow cumulus, for example by using Monte Carlo methods (Marchuk et al., 1980). On the other end, increasing the dimensions of simulated domain and including cloud micro-physics upgrades LES towards meso-scale models. The complete spectrum of motions from turbulent micro-scales up to convective meso-scales is then resolved. This range of scales covers the transition between shallow and deep convection as discussed before. As a consequence, an upgraded LES will be a useful platform to study the nature of this process.

Bibliography

- Ackerman, S. A., and S. K. Cox, 1981: Aircraft observations of the shortwave fractional absorptance of non-homogeneous clouds. *J. Appl. Meteor.*, **20**, 1510-1515.
- Albrecht, B. A., C. S. Bretherton, D. Johnson, W. H. Schubert, A. S. Frisch, 1995: The Atlantic Stratocumulus transition experiment-ASTEX. *Bull. Amer. Met. Soc.*, **76**, 889-904.
- Anthes, R. A., 1977: A cumulus parameterization scheme utilizing a one-dimensional cloud model. *Mon. Wea. Rev.*, **105**, 270-286.
- Arakawa, A., and W. H. Schubert, 1974: Interaction of a cumulus cloud ensemble with the large-scale environment, part I. *J. Atmos. Sci.*, **31**, 674-701.
- Asai, T., and A. Kasahara, 1967: A theoretical study of the compensating downward motions associated with cumulus clouds. *J. Atmos. Sci.*, **24**, 487-496.
- Augstein, E., H. Riehl, F. Ostapoff and V. Wagner, 1973: Mass and energy transports in an undisturbed Atlantic Trade-wind flow. *Mon. Wea. Rev.*, **101**, 101-111.
- , H. Schmidt and V. Wagner, 1974: The vertical structure of the atmospheric planetary boundary layer in undisturbed Trade winds over the Atlantic Ocean. *Bound.-Layer Meteor.*, **6**, 129-150.
- Austin, P.H., M. B. Baker, A. M. Blyth, and J. B. Jensen, 1985: Small-scale variability in warm continental cumulus clouds. *J. Atmos. Sci.*, **42**, 1123-1138.
- Balsey, B. B., and D. A. Carter, 1982: The spectrum of atmospheric velocity fluctuations at 8 km and 86 km. *Geophys. Res. Lett.*, **9**, 465-468.
- Barnes, G. M., J. C. Fankhauser and W. D. Browning, 1996: Evolution of the vertical mass flux and diagnosed net lateral mixing in isolated convective clouds. *Mon. Wea. Rev.*, **124**, 2764-2784.
- Bechtold, P., J. W. M. Cuijpers, P. Mascart and P. Trouilhet, 1995: Modeling of Trade wind cumuli with a low-order turbulence model: Towards a unified description of Cu and Sc clouds in meteorological models. *J. Atmos. Sci.*, **52**, 455-463.
- , S. K. Krueger, W. S. Lewellen, E. van Meijgaard, C.-H. Moeng, D. A. Randall, A. van Ulden and S. Wang, 1996: Modeling a stratocumulus-topped PBL: intercomparisons among different 1D codes and with LES. *Bull. Amer. Met. Soc.*, **77**, 2033-2042.

BIBLIOGRAPHY

- , and A. P. Siebesma, 1998: Organization and representation of boundary layer clouds. *J. Atmos. Sci.*, **55**, 888-895.
- Beniston, M. G., and Sommeria, G., 1981: Use of a detailed planetary boundary layer model for parameterization purposes. *J. Atmos. Sci.*, **38**, 780-797.
- Benner, T. C., and J. A. Curry, 1998: Characteristics of small tropical cumulus clouds and their impact on the environment. *J. Geoph. Res.*, **103**, 28753-28767.
- Betts, A. K., 1973: Non-precipitating cumulus convection and its parameterization. *Quart. J. Roy. Met. Soc.*, **99**, 178-196.
- , 1975: Parametric interpretation of Trade-wind cumulus budget studies. *J. Atmos. Sci.*, **32**, 1934-1945.
- , 1976: Modeling subcloud layer structure and interaction with a shallow cumulus layer. *J. Atmos. Sci.*, **33**, 2363-2382.
- , and M. J. Miller, 1986a: A new convective adjustment scheme. Part I: Observational and theoretical basis. *Quart. J. Roy. Met. Soc.*, **112**, 677-.
- , and ———, 1986b: A new convective adjustment scheme. Part II: Single column tests using GATE wave, BOMEX, ATEX and arctic air-mass data sets. *Quart. J. Roy. Met. Soc.*, **112**, -709.
- , and R. Boers, 1990: A cloudiness transition in a marine boundary layer. *J. Atmos. Sci.*, **47**, 1480-1497.
- , 1997: The parameterization of deep convection. *Buoyant Convection in Geophysical Flows*, E. J. Plate, E. E. Fedorovich, D. X. Viegas and J. C. Wyngaard, Eds., Kluwer Academic Publishers.
- Bjerknes, V., 1904: Das Problem von der Wettervorhersage, betrachtet vom Standpunkt der Mechanik und der Physik. *Meteor. Z.*, **21**, 1-7.
- Blyth, A. M., W. A. Cooper, and J. B. Jensen, 1988: A study of the source of entrained air in Montana cumuli. *J. Atmos. Sci.*, **45**, 3944-3964.
- , 1993: Entrainment in cumulus clouds. *J. App. Meteor.*, **32**, 626-641.
- Boatman, J. F., and A. H. Auer Jr., 1983: The role of cloud top entrainment in cumulus clouds. *J. Atmos. Sci.*, **40**, 1517-1534.
- Bretherton, C. S., and R. Pincus, 1995: Cloudiness and marine boundary layer dynamics in the ASTEX Lagrangian experiments. Part I: Synoptic setting and vertical structure. *J. Atmos. Sci.*, **52**, 2707-2723.
- , P. Austin and S. T. Siems, 1995: Cloudiness and marine boundary layer dynamics in the ASTEX Lagrangian experiments. Part II: Cloudiness, drizzle, surface fluxes and entrainment. *J. Atmos. Sci.*, **52**, 2724-2735.

- , and M. C. Wyant, 1997: Moisture transport, lower-tropospheric stability, and decoupling of cloud-topped boundary layers. *J. Atmos. Sci.*, **54**, 148-167.
- Brown, A. R., 1999a: Large-eddy simulation and parameterization of the effects of shear on shallow cumulus convection. *Bound.-Layer Met.*, **91**, 65-80.
- , 1999b: The sensitivity of large-eddy simulations of shallow cumulus convection to resolution and subgrid model. *Quart. J. R. Met. Soc.*, **125**, 469-482.
- , A. Chlond, C. Golaz, M. Khairoutdinov, D. C. Lewellen, A. P. Lock, M. K. MacVean, C-H. Moeng, R. A. J. Neggers, A. P. Siebesma and B. Stevens, 2002: Large-eddy simulation of the diurnal cycle of shallow cumulus convection over land. *Quart. J. Roy. Met. Soc.*, **128**, 1075-1094.
- Businger, J. A., and S. P. Oncley, 1990: Flux measurement and conditional sampling. *J. Atmos. Oceanic Tech.*, **7**, 349-352.
- Cahalan, R. F., and J. H. Joseph, 1989: Fractal statistics of cloud fields. *Mon. Wea. Rev.*, **117**, 261-272.
- Chaboureau, J.-P., and P. Bechtold, 2002: A simple cloud parameterization derived from cloud resolving model data: diagnostic and prognostic applications. *J. Atmos. Sci.*, **59**, 2362-2372.
- Charney, J. G., F. Fjørtoft, and J. von Neumann, 1950: Numerical integration of the barotropic vorticity equation. *Tellus*, **2**, 237-254., 1993: Large-eddy simulation of Trade-wind cumulus clouds. *J. Atmos. Sci.*, **50**, 3894-3908.
- Chen, T.-C., and A. Wiin-Nielsen, 1978: Non-linear cascades of atmospheric energy and enstrophy. *Tellus*, **30**, 313-322.
- Cotton, W. R., and R. A. Anthes, 1989: *Storm and cloud dynamics*. Geophysics Series No. 44, Academic Press, San Diego, Ca, 883pp.
- Cuijpers, J. W. M., and P. G. Duynkerke, 1993: Large-eddy simulation of Trade-wind cumulus clouds. *J. Atmos. Sci.*, **50**, 3894-3908.
- , 1994: *Large-eddy simulation of cumulus convection*. Proefschrift Technische Universiteit Delft, the Netherlands, 1994.
- , and P. Bechtold, 1995: A simple parameterization of cloud water related variables for use in boundary layer models. *J. Atmos. Sci.*, **52**, 2486-2490.
- De Roode, S. R. and P. G. Duynkerke, 1997: Observed lagrangian transition of stratocumulus into cumulus during ASTEX: mean state and turbulence structure. *J. Atmos. Sci.*, **54**, 2157-2173.
- , and C. S. Bretherton, 200: Mass flux budgets of shallow cumulus. *Accepted for publication in the J. Atmos. Sci.*

- Deardorff, J. W., 1970a: Convective velocity and temperature scales for the unstable planetary boundary layer and for rayleigh convection. *J. Atm. Sci.*, **27**, 1211-1212.
- , 1970b: A three-dimensional numerical investigation of the idealized planetary boundary layer. *Geophys. Fluid. Dyn.*, **1**, 377-410.
- , 1972: Numerical investigation of neutral and unstable planetary boundary layers. *J. Atm. Sci.*, **29**, 91-115.
- , 1980: Stratocumulus-capped mixed layers derived from a three-dimensional model. *Bound.-Layer Meteor.*, **18**, 495-527.
- Driedonks, A. G. M., and H. Tennekes, 1984: Entrainment effects in the well-mixed atmospheric boundary layer. *Bound.-Layer Meteor.*, **30**, 75-105.
- Duda, D. P., G. L. Stephens and S. K. Cox, 1991: Microphysical and radiative properties of marine stratocumulus from tethered balloon measurements. *J. Appl. Meteor.*, **30**, 170-186.
- Duynkerke, P. G., and J. Teixeira, 2001: Comparison of the ECMWF reanalysis with FIRE I observations: diurnal variation of marine stratocumulus. *J. of Climate*, **14**, 1466-1478.
- , P. J. Jonker, A. Chlond, M. C. van Zanten, J. Cuxart, P. Clark, E. Sanchez, G. Martin, G. Lenderink and J. Teixeira, 1999: Intercomparison of three- and one-dimensional model simulations and aircraft observations of stratocumulus. *Bound.-Layer Meteor.*, **92**, 453-487.
- Emanuel, K. A., 1991: A scheme for representing cumulus convection in large-scale models. *J. Atmos. Sci.*, **48**, 2313-2335.
- , 1994: *Atmospheric Convection*. Oxford University Press, New York, 580 pp.
- , 1997: Overview of atmospheric convection. *The Physics and Parameterization of Moist Atmospheric Convection*, edited by R. K. Smith. NATO ASI Series C, **505**. Kluwer Academic Publishers.
- Esbensen, S., 1975: An analysis of subcloud-layer heat and moisture budgets in the western Pacific Trades. *J. Atm. Sci.*, **32**, 1921-1923.
- Fiedler, F., and H. A. Panofsky, 1970: Atmospheric scales and spectral gaps. *Bull. Amer. Meteor. Soc.*, **51**, 1114-1119.
- Fiorino, M., cited 1998: The PCMDI observational data set. PCMDI Rep., Lawrence Livermore National Laboratory. [Available online at <http://www-pcmdi.llnl.gov/obs/pods>.]
- Fouquart, Y., J. C. Buriez, and M. Herman, 1990: The influence of clouds on radiation: A climate-modeling perspective. *Rev. Geophys.*, **28**, 145-166.
- Fraedrich, K., 1976: A mass budget of an ensemble of transient cumulus clouds determined from direct cloud observations. *J. Atmos. Sci.*, **33**, 262-268.

- French, J. R., G. Vali and R. D. Kelly, 1999: Evolution of small cumulus clouds in Florida: observations of pulsating growth. *Atmospheric Research*, **52**, 143-165.
- Fringsinger, H., 1977: *The History of Meteorology: to 1800*. American Meteorological Society, Boston.
- Frisch, U., 1995: *Turbulence: the legacy of A. N. Kolmogorov*. Cambridge University Press, Cambridge, UK, 296pp.
- Fritsch, J. M. and C. F. Chappell, 1980: Numerical prediction of convectively driven mesoscale pressure systems. Part I: convective parameterization. *J. Atmos. Sci.*, **37**, 1722-1733.
- Gates, W. L., J. S. Boyle, C. Covey, C. G. Dease, C. M. Doutriaux, R. S. Drach, M. Fiorino, P. J. Gleckler, J. J. Hnilo, S. M. Marlais, T. J. Phillips, G. L. Potter, B. D. Santer, K. R. Sperber, K. E. Taylor and D. N. Williams, 1999: An overview of the results of the atmospheric model intercomparison project (AMIP I). *Bull. Amer. Met. Soc.*, **80**, 29-55.
- Gerber, H., J. B. Jensen, A. B. Davis, A. Marshak, and W. J. Wiscombe, 2001: Spectral density of cloud liquid water content at high frequencies. *J. Atmos. Sci.*, **58**, 497-503.
- Gibson, J. K., P. Kallberg, S. Uppala, A. Hernandez, A. Nomura and E. Serrano, 1997: ECMWF re-analysis project report series. I. ERA description. *ECMWF, July 1997*.
- Grabowski, W. W., and P. K. Smolarkiewicz, 1999: CRCP: A cloud resolving convection parameterization for modeling the tropical convecting atmosphere. *Physica D*, **133**, 171-178.
- , 2001: Coupling cloud processes with the large-scale dynamics using the cloud-resolving convection parameterization (CRCP). *J. Atmos. Sci.*, **58**, 978-997.
- Grant, A. L. M., 2001: Cloud-base fluxes in the cumulus-capped boundary layer. *Quart. J. Roy. Met. Soc.*, **125**, 407-422.
- , and A. R. Brown, 1999: A similarity hypothesis for shallow-cumulus transports. *Quart. J. Roy. Met. Soc.*, **125**, 1913-1936.
- Greenhut, G. K., and S. J. S. Khalsa, 1982: Updraft and downdraft events in the atmospheric boundary layer over the equatorial Pacific Ocean. *J. Atmos. Sci.*, **39**, 1803-1818.
- , and ———, 1987: Convective elements in the marine atmospheric boundary layer. Part I: Conditional sampling statistics. *J. Climate Appl. Meteor.*, **26**, 813-822.
- Gregory, D., 1997: Sensitivity of general circulation model performance to convective parameterization. *The Physics and Parameterization of Moist Atmospheric Convection*, edited by R. K. Smith. NATO ASI Series C, **505**, Kluwer Academic Publishers.
- , J.-J. Morcrette, C. Jakob, A. C. M. Beljaars and T. Stockdale, 2000: Revision of convection, radiation and cloud schemes in the ECMWF Integrated Forecasting System. *Quart. J. Roy. Met. Soc.*, **126**, 1685-1710.

BIBLIOGRAPHY

- , 2001: Estimation of entrainment rate in simple models of convective clouds. *Quart. J. Roy. Met. Soc.*, **127**, 53-71.
- Hadley, G., 1735: Concerning the cause of the general Trade-winds. *Phil. Trans. Roy. Soc. London*, **39**, 58-62.
- Haltiner, G. J. and R. T. Williams, 1980: *Numerical prediction and dynamical meteorology*. John Wiley & Sons Inc, USA, 477pp.
- Heymsfield, A. J., P. N. Johnson, and J. E. Dye, 1978: Observations of moist adiabatic ascent in northeast Colorado cumulus clouds. *J. Atmos. Sci.*, **35**, 1689-1703.
- Hinze, J. O., 1959: *Turbulence*. McGraw-Hill, New York.
- Holland, J. Z., and E. M. Rasmusson, 1973: Measurement of atmospheric mass, energy and momentum budgets over a 500-kilometer square of tropical ocean. *Mon. Wea. Rev.*, **101**, 44-55.
- Holtslag, A. A. M., and C.-H. Moeng, 1991: Eddy diffusivity and countergradient transport in the convective atmospheric boundary layer. *J. Atmos. Sci.*, **48**, 1690-1698.
- , 2002: Atmospheric turbulence. *Encyclopedia of Physical Science and Technology*, Third Edition, edited by Robert A. Meyers. Academic Press.
- Horst, T.W., and S.P. Oncley, 1995: Flux-PAM measurement of scalar fluxes using cospectral similarity. Proceedings of the 9th Symposium on Meteorological Measurements and Instrumentation, March 27-31, Charlotte, NC, 495-500.
- Howard, L., 1802: Essay on Modifications of Clouds. *Rees' Cyclopaedia, Tilloch's Philosophical Magazine*. XVI, XVII.
- Hu, Q., 1997: A cumulus parameterization based on a cloud model of intermittently rising thermals. *J. Atmos. Sci.*, **54**, 2292-2307.
- Iribarne, J. V., and W. L. Godson, 1973: *Atmospheric Thermodynamics*. D. Reidel Publishing Company, Dordrecht, Holland. 222 pp.
- Jacob, C., and A. P. Siebesma: A new subcloud model for mass-flux convection schemes; Influence on triggering, updraft properties and model climate. *Submitted to the Mon. Wea. Rev.*, June 2002.
- Jensen, J. B., P. H. Austin, M. B. Baker, and A. M. Blyth, 1985: Turbulent mixing, spectral evolution and dynamics in a warm cumulus cloud. *J. Atmos. Sci.*, **42**, 173-192.
- Jonas, P. R., 1990: Observations of cumulus cloud entrainment. *Atmos. Res.*, **25**, 105-127.
- Jonker, H. J. J., P. G. Duynkerke, and J. W. M. Cuijpers, 1997: Energy spectra in the mesoscale range: An LES study. *Proc. 12th Symp. on Boundary Layers and Turbulence*, Vancouver, BC, Canada, Amer. Meteor. Soc., 225-226.

- , A. P. Siebesma and P. G. Duynkerke, 1999a: Development of mesoscale fluctuations in cloud-topped boundary layers. *Proceedings of the 13th symposium on boundary layers and turbulence*, Dallas, USA. American Meteorological Society, 45 Beacon Street, Boston Massachusetts, MA02108-3693, USA.
- , P. G. Duynkerke and J. W. M. Cuijpers, 1999b: Mesoscale Fluctuations in Scalars Generated by Boundary Layer Convection. *J. Atmos. Sci.*, **56**, 801-811.
- Joseph, J. H., and R. F. Cahalan, 1990: Nearest neighbor spacing of fair weather cumulus clouds. *J. Appl. Meteor.*, **29**, 793-805.
- Kain, J. S. and J. M. Fritsch, 1990: A one-dimensional entraining/detraining plume model and its application in convective parameterizations. *J. Atmos. Sci.*, **47**, 2784-2802.
- Khairoutdinov, M. F., and D. A. Randall, 2001: A cloud resolving model as a cloud parameterization in the NCAR community climate system model: preliminary results. *Geophys. Res. Lett.*, **28**, 3617-3620.
- Klaassen, G. P., and T. L. Clark, 1985: Dynamics of the cloud-environment interface and entrainment in small cumuli: Two-dimensional simulations in the absence of ambient shear. *J. Atmos. Sci.*, **42**, 2621-2642.
- Knight, C. A. and L. J. Miller, 1998: Early radar echoes from small, warm cumulus: Bragg and hydrometeor scattering. *J. Atmos. Sci.*, **55**, 2974-2992.
- Kollias, P., and B. A. Albrecht, 2000: The turbulence structure in a continental stratocumulus cloud from millimeter-wavelength radar observations. *J. Atmos. Sci.*, **57**, 2417-2434.
- , ——, R. Lhermitte, and A. Savtchenko, 2001: Radar observations of updrafts, downdrafts, and turbulence in fair-weather cumuli. *J. Atmos. Sci.*, **58**, 1750-1766.
- Kolmogorov, A. N., 1941: Energy dissipation in locally isotropic turbulence. *Doklady AN SSSR*, **32**, **1**, 19-21.
- Kuo, H. L., 1965: On formation and intensification of tropical cyclones through latent heat release by cumulus convection. *J. Atmos. Sci.*, **22**, 40-63.
- , 1974: Further studies of the parameterization of the influence of cumulus convection on large-scale flow. *J. Atmos. Sci.*, **31**, 1232-1240.
- Kuo, K. -S., R. M. Welch, R. C. Weger, M. A. Engelstad, and S. K. Sengupta, 1993: The three-dimensional structure of cumulus clouds over the ocean, I, Structural analysis. *J. Geoph. Res.*, **98**, 20685-20711.
- Lamontagne, R.G., and J. W. Telford, 1983: Cloud top mixing in small cumuli. *J. Atmos. Sci.*, **40**, 2148-2156.
- Lappen, C.-L., D. A. Randall, 2001a: Toward a unified parameterization of the boundary layer and moist convection. Part I: A new type of mass-flux model. *J. Atmos. Sci.*, **58**, 2021-2036.

BIBLIOGRAPHY

- , ——, 2001b: Toward a unified parameterization of the boundary layer and moist convection. Part II: Lateral mass exchanges and subplume-scale fluxes. *J. Atmos. Sci.*, **58**, 2037-2051.
- , ——, 2001c: Toward a unified parameterization of the boundary layer and moist convection. Part III: Simulations of clear and cloudy convection. *J. Atmos. Sci.*, **58**, 2052-2072.
- Lehrmitte, R., 1987: Small cumuli observed with a 3-mm wavelength Doppler radar. *Geoph. Res. Letters*, **14**, 707-710.
- LeMone, M. A., and Pennell, W. T., 1976: The relationship of Trade wind cumulus distribution to subcloud layer fluxes and structure. *Mon. Wea. Rev.*, **104**, 524-539.
- Lenderink, G., and A. P. Siebesma, 2000: Combining the massflux approach with a statistical cloud scheme. *Proceedings of the 14th Symposium on Boundary Layer and Turbulence of the American Meteorological Society*, 7-11 August 2000, Aspen, CO.
- , and A. A. M. Holtslag: An Integral Mixing Length Formulation for a TKE-1 Turbulence Closure in Atmospheric Models. *Submitted to the Mon. Wea. Rev.*, June 2002.
- , et al., 2002: The diurnal cycle of shallow cumulus over land: An intercomparison study for single column models. *In preparation*.
- Lenschow, D. H., 1970: Airplane measurements of planetary boundary layer structure. *J. Appl. Meteor.*, **9**, 874-884.
- , J. C. Wyngaard, W. T. Pennell, 1980: Mean field and second moment budgets in a baroclinic, convective boundary layer. *J. Atmos. Sci.*, **37**, 1313-1326.
- , and P. L. Stephens, 1980: The role of thermals in the convective boundary layer. *Bound.-Layer Meteor.*, **19**, 509-532.
- Lin, C., and A. Arakawa, 1997: The macroscopic entrainment processes of simulated cumulus ensemble. Part I: Entrainment sources. *J. Atmos. Sci.*, **54**, 1027-1043.
- Lin, J. W.-B., and J. D. Neelin, 2002: Considerations for stochastic convective parameterization. *J. Atmos. Sci.*, **59**, 959975.
- Lilly, D. K., 1967: The representation of small-scale turbulence in numerical simulation experiments. *Proc. IBM Sci. Comput. Symp. On Environmental Science*, Nov. 14-16, 1966, Thomas J. Watson Res. Center, Yorktown Heights, Ny, IBM Form 320-1951, 195-210.
- , and E. Petersen, 1983: Aircraft measurements of atmospheric kinetic energy spectra. *Tellus*, **35A**, 379-382.
- Lopez, R. E., 1977: The lognormal distribution and cumulus cloud populations. *Mon. Wea. Rev.*, **105**, 865-872.
- Lovejoy, S., 1982: Area-perimeter relation for rain and cloud areas. *Science*, **216**, 185-187.

- Mace, G. G., C. Jakob, and K. P. Moran, 1998: Validation of hydrometeor occurrence predicted by the ECMWF model using millimeter wave radar data. *Geoph. Res. Lett.*, **25**, 1645-1648.
- Manabe, S., J. Smagorinsky and R. F. Stricker, 1965: Simulated climatology of a general circulation model with a hydrologic cycle. *Mon. Wea. Rev.*, **93**, 769-798.
- , and R. T. Wetherald, 1967: Thermal equilibrium of the atmosphere with a given distribution of relative humidity. *J. Atmos. Sci.*, **24**, 241-259.
- Mapes, B. E., 1997: Equilibrium vs. activation control of large-scale variations of tropical deep convection. *The Physics and Parameterization of Moist Atmospheric Convection*, edited by R. K. Smith. NATO ASI Series C, **505**, Kluwer Academic Publishers.
- Marchuk, G., G. Mikhailov, M. Nazaratiev, R. Darbinjan, B. Kargin, and B. Elepov, 1980: *The Monte Carlo Methods in Atmospheric Optics*. Springer-Verlag, 208 pp.
- Marshak, A., A. Davis, and W. Wiscombe, 1995: Radiation smoothing in fractal clouds. *J. Geophys. Res.*, **100**, 26247-26261.
- , A. Davis, W. Wiscombe, W. Ridgway, and R. Cahalan, 1997: Biases in shortwave column absorption in the presence of fractal clouds. *J. Climate*, **11**, 431-446.
- Mason, P. J., 1989: Large-eddy simulation of the convective atmospheric boundary layer. *J. Atmos. Sci.*, **46**, 1492-1516.
- , and D. J. Thompson, 1992: Stochastic backscattering in large-eddy simulations of boundary layers. *J. Fluid Mech.*, **242**, 51-78.
- , 1994: Large-eddy simulation: a critical review of the technique. *Quart. J. Roy. Met. Soc.*, **120**, 1-26.
- Mather, J. H., T. P. Ackerman, W. E. Clements, F. J. Barnes, M. D. Ivey, L. D. Hatfield, and R. M. Reynolds, 1998: An atmospheric radiation and cloud station in the tropical Western Pacific. *Bull. Amer. Met. Soc.*, **79**, 627-642.
- Meneveau, C., and J. Katz, 2000: Scale-invariance and turbulence models in large-eddy simulation. *Ann. Rev. Fluid Mech.*, **32**, 1-32.
- Militzer, J.M., M.C. Michaelis, S.R. Semmer, K.S. Norris, T.W. Horst, S.P. Oncley, A.C. Delany, and F.V. Brock, 1995: Development of the prototype PAM III/Flux-PAM surface meteorological station. *Proceedings of the 9th Symposium on Meteorological Measurements and Instrumentation*, March 27-31, Charlotte, NC, pp 490-494.
- Moeng, C.-H., 1984: A large-eddy simulation model for the study of planetary boundary-layer turbulence. *J. Atmos. Sci.*, **41**, 2052-2062.
- , W. R. Cotton, B. Stevens, C. Bretherton, H. A. Rand, A. Chlond, M. Khairoutdinov, S. Krueger, W. S. Lewellen, M. K. MacVean, J. R. M. Pasquier, A. P. Siebesma, R. I. Sykes, 1996: Simulation of a stratocumulus-topped planetary boundary layer: intercomparison

BIBLIOGRAPHY

- among different numerical codes. *Bulletin of the American Meteorological Society*, **77**, 261-278.
- , and P. P. Sullivan, 1994: A comparison of shear- and buoyancy-driven planetary boundary layer flows. *J. Atmos. Sci.*, **51**, 999-1022.
- , 1998: Large eddy simulation of atmospheric boundary layers. *Clear and cloudy boundary layers*, A. A. M. Holtslag and P. G. Duynkerke Eds., Koninklijke Nederlandse Academie van Wetenschappen, Amsterdam 1998, 372 pp.
- Nastrom, G. D., and K. S. Gage, 1983: A first look at wavenumber spectra from GASP data. *Tellus*, **35A**, 383-388.
- Neelin, J. D., 1997: Implications of convective quasi-equilibrium for the large-scale flow. *The Physics and Parameterization of Moist Atmospheric Convection*, edited by R. K. Smith. NATO ASI Series C, **505**, Kluwer Academic Publishers.
- , and N. Zeng, 2000: A quasi-equilibrium tropical circulation model – formulation. *J. Atmos. Sci.*, **57**, 1741-1766.
- , and W. Weng, 1999: Analytical prototypes for oceanatmosphere interaction at mid-latitudes. Part I: Coupled feedbacks as a sea surface temperature dependent stochastic process. *J. Climate*, **12**, 6977-7001.
- Negers, R. A. J., A. P. Siebesma and H. J. J. Jonker, 2002a: A multi parcel model for shallow cumulus convection. *J. Atmos. Sci.*, **59**, 1655-1668.
- , H. J. J. Jonker and A. P. Siebesma, 2002b: Size statistics of cumulus cloud populations in large-eddy simulations. *Accepted for publication in the J. Atmos. Sci.*, August 2002.
- , P. G. Duynkerke and S. M. A. Rodts, 2003: Shallow cumulus convection: validation of large-eddy simulation against aircraft and Landsat observations. *Accepted for publication in the Quart. J. Roy. Met. Soc. pending minor revisions*, August 2002.
- , A. P. Siebesma, G. Lenderink and A. A. M. Holtslag, 2003: Mass flux closures in diurnal cycles of shallow cumulus over land. *Submitted to Mon. Wea. Rev.*, July 2002.
- Nicholls, S., and M. A. LeMone, 1980: Fair weather boundary layer in GATE: the relationship of subcloud fluxes and structure to the distribution and enhancement of cumulus clouds. *J. Atmos. Sci.*, **37**, 2051-2067.
- , M. A. LeMone and G. Sommeria, 1982: The simulation of a fair weather marine boundary layer in GATE using a three-dimensional model. *Quart. J. Roy. Met. Soc.*, **108**, 167-190.
- Nieuwstadt, F. T. M., P. J. Mason, C.-H. Moeng, and U. Schumann, 1991: Large-eddy simulation of the convective boundary layer: a comparison of four computer codes. *Proc. 8th Symposium on Turbulent Shear Flows*, München, Germany, 9-11 September 1991.

- Nitta, T., 1972: Energy budget of wave disturbances over the Marshall Islands during the years of 1956 and 1958. *J. Met. Soc. Japan*, **50**, 71-84.
- , and S. Esbensen, 1974: Heat and moisture budget analyses using BOMEX data. *Mon. Wea. Rev.*, **102**, 17-28.
- , 1975: Observational Determination of Cloud Mass Flux Distributions. *J. Atmos. Sci.*, **32**, 73-91.
- Nordeng, T. E., 1994: Extended versions of the convective parametrization scheme at ecmwf and their impact on the mean and transient activity of the model in tropics. *Tech. Memo. No. 206*, ECMWF, Shinfield Park, Reading, RG2 9AX, United Kingdom.
- Nucciarone, J. F., and G. S. Young, 1991: Aircraft measurements of turbulence spectra in the marine stratocumulus-topped boundary layer. *J. Atmos. Sci.*, **48**, 2382-2392
- Obukhov, A. M., 1941: Energy distribution in the spectrum of a turbulent flow. *Izvestiya AN SSSR, Ser. Geogr. Geofiz.*, **4-5**, 453-466.
- Ogura, Y., and H.-R. Cho, 1974: On the interaction between the subcloud and cloud layers in tropical regions. *J. Atmos. Sci.*, **31**, 1850-1859.
- Ooyama, K., 1971: A theory on parameterization of cumulus convection. *J. Meteor. Soc. Japan*, **49**, 744-756.
- Orlanski, I., 1975: A rational subdivision of scales for atmospheric processes. *Bull. Amer. Meteor. Soc.*, **56**, 529-530.
- Paluch, I. R., 1979: The entrainment of air in Colorado cumuli. *J. Atmos. Sci.*, **36**, 2467-2478.
- Papathakos, L. C., and D. Briehl, 1981: NASA Global Atmospheric Sampling Program (GASP) data report for tapes VL0015, VL0016, VL0017, VL0018, VL0019 and VL0030. NASA-TM-81661, 94pp
- Penc, R. S., and B. A. Albrecht, 1987: Parametric representation of heat and moisture fluxes in cloud-topped mixed layers. *Bound.-Layer Meteor.*, **38**, 225-248.
- Plank, V. G., 1969: The size distributions of cumulus clouds in representative Florida populations. *J. App. Met.*, **8**, 46-67.
- Pontikis, C., A. Rigaud, and E. Hicks, 1987: Entrainment and mixing as related to the microphysical properties of shallow warm cumulus clouds. *J. Atmos. Sci.*, **44**, 2150-2165.
- Raga, G. B., J. B. Jensen, and M. B. Baker, 1990: Characteristics of cumulus band clouds off the coast of Hawaii. *J. Atmos. Sci.*, **47**, 338-355.
- Ramanathan, V., B. Sivasilar, G. J. Zhang, W. Conant, R. D. Cess, J. T. Kiehl, G. Grassl, and L. Shi, 1995: Warm pool heat budget and short-wave cloud forcing: A missing physics?. *Science*, **267**, 499-503.

BIBLIOGRAPHY

- Randall, D. A., 1987: Turbulent fluxes of liquid water and buoyancy in partly cloudy layers. *J. Atmos. Sci.*, **44**, 850-858.
- , D.-M. Pan, P. Ding, and D. G. Cripe, 1997: Quasi-equilibrium. *The Physics and Parameterization of Moist Atmospheric Convection*, edited by R. K. Smith. NATO ASI Series C, **505**, Kluwer Academic Publishers.
- Raymond, D. J., and M. H. Wilkening, 1982: Flow and mixing in New Mexico mountain cumuli. *J. Atmos. Sci.*, **39**, 2211-2228.
- , and A. M. Blyth, 1986: A stochastic model for nonprecipitating cumulus clouds. *J. Atmos. Sci.*, **43**, 2708-2718.
- , 1995: Regulation of moist convection over the west Pacific warm pool. *J. Atmos. Sci.*, **52**, 3945-3959.
- Reed, R. J., and E. E. Recker, 1971: Structure and properties of synoptic-scale wave disturbances in the equatorial western Pacific. *J. Atmos. Sci.*, **28**, 1117-1133.
- Richardson, L. F., 1922: *Weather prediction by numerical process*. Cambridge University Press, reprinted Dover, 1965, 236pp.
- Rodts, S. M. A., P. G. Duynkerke and H. J. J. Jonker: Size distributions and dynamical properties of shallow cumulus clouds from aircraft observations and satellite data. *Submitted to J. Atmos. Sci.*, March 2002.
- Rosby, C. G., 1938: On the mutual adjustment of pressure and velocity distribution in certain simple current systems, II. *J. Marine Res.* (Sears Foundation), 239-263.
- , 1939: Relation between variations in the intensity of the zonal circulation of the atmosphere and the displacements of the semi-permanent centers of action. *J. Marine Res.*, **2**, 38-55.
- , 1940: Planetary flow patterns in the atmosphere. *Quart. J. Roy. Met. Soc.*, **66**, 68-87.
- Rosow, W. B., L. C. Garder, P. J. Lu and A. W. Walker, 1991: International satellite cloud climatology project (ISCCP): documentation of cloud data. WMO/TD-No.266, World Meteorological Organization, 76 pp.
- Schmidt, H. and U. Schumann, 1989: Coherent structure of the convective boundary layer derived from large-eddy simulations. *J. Fluid Mech.*, **200**, 511-562.
- Schumann, U., 1975: Subgrid scale model for finite difference simulations of turbulent flows in plane channels and annuli. *J. Comp. Physics*, **18**, 376-404.
- , and C.-H. Moeng, 1991a: Plume fluxes in clear and cloudy convective boundary layers. *J. Atmos. Sci.*, **48**, 1746-1757.
- , and C.-H. Moeng, 1991b: Plume budgets in clear and cloudy convective boundary layers. *J. Atmos. Sci.*, **48**, 1758-1770.

- Scorer, R. S., and F. H. Ludlam, 1953: Bubble theory of penetrative convection. *Quart. J. Roy. Met. Soc.*, **79**, 94-103.
- Siebesma, A. P., and Cuijpers, 1995: Evaluation of parametric assumptions for shallow cumulus convection. *J. Atmos. Sci.*, **52**, 650-666.
- , 1996: On the massflux approach for atmospheric convection. *ECMWF seminar proceedings on "New insights and approaches to convective parametrization"*, 4-7 Nov 1996, ECMWF, Shinfield Park, Reading, RG2 9AX, United Kingdom.
- , and A. A. M. Holtslag, 1996: Model impacts of entrainment and detrainment in shallow cumulus convection. *J. Atmos. Sci.*, **53**, 2354-2364.
- , 1998: Shallow cumulus convection. *Buoyant Convection in Geophysical Flows*, E. J. Plate, E. E. Fedorovich, D. X. Viegas and J. C. Wyngaard, Eds., Kluwer Academic Publishers, 441-486.
- , and H. J. J. Jonker, 2000: Anomalous scaling of cumulus cloud boundaries. *Phys. Rev. Letters*, **85**, 214-217.
- , C. S. Bretherton, A. Brown, A. Chlond, J. Cuxart, P. G. Duynkerke, H. Jiang, M. Khairoutdinov, D. Lewellen, C.-H. Moeng, B. Stevens and D. E. Stevens, 2002: An inter-comparison study for cloud resolving models of shallow cumulus convection. *Submitted to J. Atmos. Sci.*
- , and J. Teixeira, 2002: An advection-diffusion scheme for the convective boundary layer: description and 1D-results. *Proceedings of the 15th Symposium on Boundary Layers and turbulence of the American Meteorological Society*, 15-19 July 2002, Wageningen, The Netherlands.
- Simpson, J., R. H. D. Simpson, A. Andrews, and M. A. Eaton, 1965: Experimental cumulus dynamics. *Rev. Geophys.*, **3**, 387-431.
- , and V. Wiggert, 1969: Models of precipitating cumulus towers. *Mon. Wea. Rev.*, **97**, 471-489.
- , 1971: On cumulus entrainment and one-dimensional models. *J. Atmos. Sci.*, **28**, 449-455.
- Slingo, J. M., M. Blackburn, A. Betts, R. Brugge, B. J. Hoskins, M. J. Miller, L. Steenman-Clark and J. Thurnburn, 1994: Mean climate and transience in the tropics of the UGAMP GCM: Sensitivity to convective parameterization. *Quart. J. Roy. Met. Soc.*, **120**, 881-922.
- Smagorinsky, J., 1963: General circulation experiments with the primitive equations. I. The basic experiment. *Mon. Wea. Rev.*, 91-99.
- Sommeria, G., 1976: Three-dimensional simulation of turbulent processes in an undisturbed Trade-wind boundary layer. *J. Atmos. Sci.*, **33**, 216-241.

BIBLIOGRAPHY

- , and J. W. Deardorff, 1977: Subgrid-scale condensation in models of non-precipitating clouds. *J. Atmos. Sci.*, **34**, 344-355.
- , and M. A. LeMone, 1978: Direct testing of a three-dimensional model of the planetary boundary layer against experimental data. *J. Atmos. Sci.*, **35**, 25-39.
- Squires, P., 1958a: The microstructure and colloidal stability of warm clouds. Part I. The relation between structure and stability. *Tellus*, **10**, 256-261.
- , 1958b: The microstructure and colloidal stability of warm clouds. Part II. The causes of the variations in microstructure. *Tellus*, **10**, 262-271.
- , 1958c: The spatial variation of liquid water and droplet concentration in cumuli. *Tellus*, **10**, 372-380.
- , and J. S. Turner, 1962: An entraining jet model for cumulonimbus updraughts. *Tellus*, **14**, 422-434.
- Stephens, G. L., 1988: Radiative transfer through arbitrarily shaped media. Part II: Group theory and closures. *J. Atmos. Sci.*, **45**, 1837-1848.
- Stevens, B., C.-H. Moeng, and P. P. Sullivan, 1999: Large-eddy simulation of radiatively driven convection: sensitivities to the representation of small scales. *J. Atmos. Sci.*, **56**, 3963-3984.
- , 2000: Cloud-transitions and decoupling in shear-free stratocumulus topped boundary layers. *Geoph. Res. Letters*, **27**, 2557-2560.
- , A. S. Ackerman, B. A. Albrecht, A. R. Brown, A. Chlond, J. Cuxart, P. G. Duynkerke, D. C. Lewellen, M. K. MacVean, R. A. J. Neggers, E. Sanchez, A. P. Siebsema, D. E. Stevens, 2001: Simulations of Trade-wind cumuli under a strong inversion. *J. Atmos. Sci.*, **58**, 1870-1891.
- Stevens, D. E., A. S. Ackerman, and C. S. Bretherton: Effects of domain size and numerical resolution on the simulation of shallow cumulus convection. *Submitted October 2001*.
- Stommel, H., 1947: Entrainment of air into a cumulus cloud. *J. Meteorol.*, **4**, 91-94.
- Stull, R. B., 1976: The energetics of entrainment across a density difference. *J. Atmos. Sci.*, **33**, 1260-1267.
- , 1988: *An introduction to boundary layer meteorology*. Kluwer Academic Publishers, 1988, 666 pp.
- Sullivan, P. P., J. C. McWilliams and C.-H. Moeng, 1994: A subgrid-scale model for large-eddy simulation of planetary boundary-layer flows. *Bound.-layer Meteorol.*, **71**, 247-276.
- H. Swann, 2001: Evaluation of the mass-flux approach to parameterizing deep convection. *Quart. J. Roy. Met. Soc.*, **127**, 1239-1260.

- Taconet, O., and A. Weill, 1983: Convective plumes in the atmospheric boundary layer as observed with an acoustic Doppler sodar. *Bound.-Layer Meteor.*, **25**, 143-158.
- Taylor, B. R., and M. B. Baker, 1991: Entrainment and detrainment in cumulus clouds. *J. Atmos. Sci.*, **48**, 112-121.
- Telford, J. W., 1975: Turbulence, entrainment and mixing in cloud dynamics. *Pure Appl. Geophys.*, **113**, 1067-1084.
- Tennekes, H., 1973: A model for the dynamics of the inversion above a convective boundary layer. *J. Atmos. Sci.*, **30**, 558-567.
- Tiedtke, M., W. A. Heckley and J. Slingo, 1988: Tropical forecasting at ECMWF: The influence of physical parameterizations on the mean structure of forecasts and analyses. *Quart. J. Roy. Met. Soc.*, **114**, 639-665.
- , 1989: A comprehensive mass flux scheme for cumulus parameterization in large-scale models. *Mon. Wea. Rev.*, **117**, 1779-1800.
- , 1996: An extension of cloud-radiation parameterization in the ECMWF model: The representation of subgrid-scale variations in optical depth. *Mon. Wea. Rev.*, **124**, 745-750.
- Turner, J. S., 1962: The starting plume in neutral surroundings. *J. Fluid Mech.*, **13**, 356-368.
- , 1973: *Buoyancy effects in fluids*. Cambridge University Press, 367 pp.
- Vinnichenko, N. K., 1970: The kinetic energy spectrum in the free atmosphere - one second to five years. *Tellus*, **22**, 158-166.
- Van Dorland, R., 1999: *Radiation and climate: from radiative transfer modelling to global temperature response*. Ph.D. thesis, University of Utrecht, The Netherlands.
- Van der Hoven, I., 1957: Power spectrum of horizontal wind speed in the frequency range from 0.0007 to 900 cycles per hour. *J. Meteor.*, **14**, 160.
- Vogelezang, D., and A. A. M. Holtslag, 1996: Evaluation and model impacts of alternative boundary-layer height formulations. *Bound. Layer Met.*, **81**, 245-269
- Wang, S. and B. Stevens, 2000: Top-hat representation of turbulence statistics in cloud-topped boundary layers: a large-eddy simulation study. *J. Atmos. Sci.*, **57**, 423-441.
- Warner, J., 1955: The water content of cumuliform clouds. *Tellus*, **7**, 449-457.
- , 1969a: The microstructure of cumulus cloud. Part I. General features of the droplet spectrum. *J. Atmos. Sci.*, **26**, 1049-1059.
- , 1969b: The microstructure of cumulus cloud. Part II. The effect on droplet size distribution of the cloud nucleus spectrum and updraft velocity. *J. Atmos. Sci.*, **26**, 1272-1282.

BIBLIOGRAPHY

- , 1970a: The microstructure of cumulus cloud. Part III. The nature of the updraft. *J. Atmos. Sci.*, **27**, 682-688.
- , 1970b: On steady-state one-dimensional models of cumulus convection. *J. Atmos. Sci.*, **27**, 1035-1040.
- , 1977: Time variation of updraft and water content in small cumulus clouds. *J. Atmos. Sci.*, **34**, 1306-1312.
- Wielicki, B. A., and R. M. Welch, 1986: Cumulus cloud properties derived using landsat satellite data. *J. Clim. and Appl. Meteorol.*, **25**, 261-276.
- World Meteorological Organization, 1972: Parameterization of subgrid scale processes. GARP Publ. Ser. No. 8, WMO. (Available from Secretariat of WMO, Case Postale No. 1, CH-1211 Geneva 20, Switzerland.)
- Wyngaard, J. C., and C.-H. Moeng, 1992: Parameterizing turbulent diffusion through the joint probability density. *Bound.-Layer Meteor.*, **60**, 1-13.
- Xu, K.-M., and D. A. Randall, 2001: Updraft and downdraft statistics of simulated tropical and midlatitude cumulus convection. *J. Atmos. Sci.*, **58**, 1630-1649.
- Yanai, M., S. Esbensen and J. H. Cho, 1973: Determination of bulk properties of tropical cloud clusters from large-scale heat and moisture budgets. *J. Atmos. Sci.*, **30**, 611-627.
- Young, G. S., 1988a: Turbulence structure of the convective boundary layer. Part I: Variability of normalized turbulence statistics. *J. Atmos. Sci.*, **45**, 719-726.
- , 1988b: Turbulence structure of the convective boundary layer. Part II: Phoenix 78 aircraft observations of thermals and their environment. *J. Atmos. Sci.*, **45**, 727-735.
- , 1988c: Turbulence structure of the convective boundary layer. Part III: The vertical velocity budgets of thermals and their environment. *J. Atmos. Sci.*, **45**, 719-726.
- Zhao, M., and P. H. Austin: Episodic mixing and buoyancy sorting representations of shallow convection: a diagnostic study. *Submitted to the J. Atmos. Sci.*, May 2002.

Symbols and Acronyms

Acronyms

1D model	Single column model
AMIP	Atmospheric Model Intercomparison Project
ARM	Atmospheric Radiation Measurement program
ASTEX	Atlantic Stratocumulus Experiment
ATEX	Atlantic Trade-wind Experiment
BOMEX	Barbados Oceanographic and Meteorological Experiment
Ci	Cirrus
CRM	Cloud resolving model
Cu	Cumulus
CuNi	Cumulonimbus
ECMWF	European Centre for Medium Range Weather Forecasts
ERA	ECMWF reanalysis
EUROCS	European Cloud System studies
GASP	Global Atmospheric Sampling Program
GCM	General circulation model
GCSS	GEWEX Cloud System Studies
GEWEX	Global Energy and Water-cycle Experiment
IPCC	Intergovernmental Panel on Climate Change
IR	Infra red
ISCCP	International Satellite Cloud Climatology Project
ITCZ	Intra-tropical convergence zone
KNMI	Royal Netherlands Meteorological Institute
LCL	Lifting condensation level
LES	Large-eddy simulation
LFC	Level of free convection
LMC	Level of maximum core cover
LNB	Level of neutral buoyancy
LS	Large scale
LZB	Level of zero buoyancy
NASA	National Aeronautics & Space Administration
NCAR	National Center for Atmospheric Research
NWP	Numerical weather prediction

SYMBOLS AND ACRONYMS

PBL	Planetary boundary layer
PVM	Particle volume monitor
RICO	Rain In Cumulus over the Ocean (experiment)
SCM	Single column model
SCMS	Small Cumulus Microphysics Study
SGS	Subgrid-scale
ShCu	Shallow cumulus
SCu	Stratocumulus
SST	Sea surface temperature
TKE	Turbulent kinetic energy
UTC	Coordinated universal time (also known as Greenwich mean time)
UV	Ultra violet

Symbols

α^p	cloud size decomposition of the projected cloud fraction	
A	area	[m ²]
A^c	cloud area	[m ²]
A_p^c	projected cloud area	[m ²]
a^c	cloud fraction	[%]
a_p^c	vertically projected cloud fraction (shaded cloud fraction)	[%]
B_p	parcel buoyancy	[m s ⁻²]
C	ratio of the specific gas constants of dry and moist air	0.61
$CAPE$	convective available potential energy	[m ² s ⁻²]
$(c - e)$	net condensation rate minus net evaporation rate	[kg kg ⁻¹ s ⁻¹]
c_p	specific heat capacity for dry air at constant pressure	1004 J kg ⁻¹ K ⁻¹
$\Delta_x, \Delta_y, \Delta_z$	discretization sizes	[m]
δ_{ij}	Kronecker delta	
δ^c	fractional bulk lateral detrainment rate	[m ⁻¹]
δq	heat per unit mass added to a thermodynamic system	[J kg ⁻¹]
D	bulk lateral detrainment rate	[s ⁻¹]
ϵ_{ijk}	alternating unit tensor	
ϵ	turbulent dissipation rate	[m ² s ⁻³]
ϵ	fractional lateral entrainment rate	[m ⁻¹]
ϵ^c	bulk (population average)	
ϵ_R	laboratory plume	
ϵ_w	updraft-parcel model	
E	bulk lateral entrainment rate	[s ⁻¹]
e	turbulent kinetic energy	[m ² s ⁻²]

F_ϕ	tendency of ϕ due to remaining forcings (radiation, precipitation)	
f	Coriolis parameter as a function of latitude ϕ	$(1.46 \cdot 10^{-4})\sin(\phi)$ [s^{-1}]
Γ	lapse rate of θ_v	[$K m^{-1}$]
Γ_d	dry adiabatic	$\equiv 0$
Γ_m	moist adiabatic	
Γ_i	capping inversion	
g	gravitational acceleration	$9.81 m s^{-2}$
h	depth	[m]
I	indicator function in conditional sampling	
k	wave number	
k_e	energy producing scale	
k_d	dissipating, molecular scale	
ℓ	cloud size	[m]
L	specific latent heat of the phase change between water vapour and liquid water	$2.5 \times 10^6 J kg^{-1}$
L_x, L_y, L_z	domain sizes	[m]
L_b	parcel perimeter length	[m]
LH	surface latent heat flux	[$W m^{-2}$]
LS_ϕ	tendency of ϕ due to advection by the large-scale winds	
l	length	[m]
μ	cloud size decomposition of the vertical mass flux	
M	mass flux	[$m s^{-1}$]
m_v	mass of water vapour in a unit volume of air	[kg]
m_t	total mass of a unit volume of air	[kg]
N	cloud size density	
ν	kinematic viscosity	[$m^2 s^{-1}$]
N	number of clouds	
\hat{n}_h	horizontal unit vector	[m]
Π	Exner function	
p	atmospheric pressure	[Pa]
p_0	reference atmospheric pressure	$10^5 Pa$
Q_ϕ	apparent source in the conservation law for a conserved variable ϕ	
q	specific humidity	[$kg kg^{-1}$]
q_s	saturation specific humidity	
q_t	total specific humidity	
q_l	liquid water content	
q_v	water vapour content	
ρ	atmospheric density	[$kg m^{-3}$]

SYMBOLS AND ACRONYMS

R_d	specific gas constant for dry air	287.05 J kg ⁻¹ K ⁻¹
R_v	specific gas constant for moist air	461.51 J kg ⁻¹ K ⁻¹
RH	relative humidity	[%]
r_B	Bowen ratio	
σ^2	variance (second statistical moment)	
SH	surface sensible heat flux	[W m ⁻²]
τ	time scale	[s]
θ	potential temperature	[K]
θ_l	liquid water potential temperature	
θ_v	virtual potential temperature	
Θ_v^0	reference virtual potential temperature	
θ_e	equivalent potential temperature	
T	temperature	[K]
T_v	virtual temperature	[K]
t	time	[s]
v	specific volume	[m ³ kg ⁻¹]
$\vec{u} = (u, v, w)$	wind vector	[m s ⁻¹]
$\vec{U} = (U, V, W)$	mean wind vector	[m s ⁻¹]
$\vec{U}_g = (U_g, V_g)$	horizontal geostrophic wind vector	[m s ⁻¹]
w^*	convective vertical velocity scale	[m s ⁻¹]
x, y, z	spatial coordinates	[m]
z_b	height of cloud base	[m]

Nederlandse samenvatting

Wolken vervullen een belangrijke functie in het klimaat op aarde. Ten eerste spelen ze bijvoorbeeld een niet te verwaarlozen rol in de globale energiehuishouding van de atmosfeer, vanwege hun effect op het spectrum van de straling die de atmosfeer binnenkomt en weer verlaat. Enerzijds reflecteren en absorberen ze ultraviolette (zonne)straling, anderzijds zenden ze infrarode straling uit afhankelijk van hun temperatuur. Ten tweede wordt een belangrijk deel van het verticaal transport van vocht, warmte en momentum in de atmosfeer geassocieerd met de sterke verticale winden binnen in bepaalde typen wolken, ook wel convectieve wolken genoemd. Deze wolken gaan vaak gepaard met hevige neerslag, en spelen een belangrijke rol in de watercyclus op aarde evenals in tropische grootschalige luchtcirculaties.

De atmosferische grenslaag is gedefinieerd als de onderste paar kilometer van de atmosfeer die direct worden beïnvloed door het oppervlak van de aarde. In die laag vindt de directe uitwisseling plaats van vocht en thermische energie tussen atmosfeer en het aardoppervlak. Tevens worden in die laag de winden afgeremd door de ruwheid van het aardoppervlak, gevormd door bergen, bomen, en andere obstakels. De luchtwervelingen die hiervan het gevolg zijn worden ook wel turbulentie genoemd. Een tweede bron van turbulentie is het opwarmen overdag van de lucht door het aardoppervlak. Deze relatief warme lucht is lichter dan zijn omgeving, en zal als gevolg daarvan gaan stijgen. De turbulente lucht mengt vocht en warmte naar grotere hoogtes, en remt de luchtstromingen op die hoogtes af. Op het moment dat deze turbulente wervels zo zijn afgekoeld dat ze condenseren, worden het cumuliforme wolken. Deze wolken vormen het belangrijkste onderwerp van dit proefschrift.

Vanwege hun belangrijke rol in stralingstransport en verticale menging is het essentieel voor weers- en klimaatvoorspellingen om te weten waar, wanneer en in welke mate cumulus wolken voorkomen. Sinds enkele tientallen jaren worden numerieke modellen voor de globale circulatie gebruikt voor weers- en klimaatvoorspellingen. Ondanks de stormachtige ontwikkeling van de supercomputers die gebruikt worden voor de tijdsintegratie van deze modellen, zijn de spatiale en temporale resoluties nog steeds te laag om deze cumuluswolken op te lossen, voornamelijk vanwege hun typisch kleine afmetingen. Hun kracht ligt dus voornamelijk in hun aantal, aangezien ze typisch voorkomen als hele ensembles in grote aaneengesloten gebieden. Om hun effect en uitwerking op de globale circulatie en energiehuishouding toch in de modellen te representeren is de techniek van *parameterizatie* ontwikkeld. Dit houdt in dat het effect van hele cumulus ensembles wordt samengevat in sterk versimpelde formuleringen, afhankelijk van een paar relevante meteorologische parameters. Vanwege de complexiteit van dit probleem is al veel wetenschappelijk onderzoek aan dit onderwerp gewijd.

In cumulus parameterizaties in weer- en klimaatmodellen is het gebruikelijk om turbulent transport door cumulus wolken en de droge grenslaag daaronder apart te modelleren. Dit leidt vaak tot ongewenste interacties van deze transportmechanismen in de lagere atmosfeer. De doelstelling van dit project was tweeledig: ten eerste het begrijpen en modelleren van de uitwisseling van lucht tussen de droge grenslaag en cumulus wolken, ten tweede het kwantificeren en modelleren van de menging van die geventileerde lucht over de wolkenlaag. De data voor het bestuderen van dit soort eigenschappen van turbulente atmosferische grenslagen zijn gegenereerd door gebruik te maken van een numeriek model met een zeer hoge resolutie, ook wel bekend als een large-eddy simulation (LES) model. Hiermee de dynamica van wolken expliciet kan worden uitgerekend. Verder is er ook gebruik gemaakt van in-situ waarnemingen door vliegtuigen alsmede van remote sensing technieken zowel vanuit de ruimte (satelliet) als vanaf de grond (radar).

In Hoofdstuk 3 zijn wolkenvelden zoals geproduceerd door het KNMI LES model kritisch geëvalueerd tegen waarnemingen gemaakt tijdens de Small Cumulus Microphysics Study (SCMS). Dit meetexperiment vond plaats in augustus 1995 aan de oostkust van Florida, net ten noorden van Cape Canaveral. Naast een serie van grond-instrumenten heeft het C-130 meetvliegtuig van the National Center of Atmospheric Research (NCAR) in vele wolken metingen vericht van turbulentie en thermodynamica, en waren er tevens hoge-resolutie Landsat satelliet foto's van het gebied beschikbaar. De resultaten van de vergelijking tonen aan dat LES goed in staat is de gemiddelde profielen van vocht, temperatuur en vloeibaar water in de wolken te reproduceren. Verder zijn de verticale component van de turbulente kinetische energie (TKE) binnen de wolken alsmede de kansdichtheden van aantal wolken en bedekkingsgraad als functie van hun grootte in overeenstemming met de waarnemingen. Verscheidene parameterizaties die gebruik maken van wolkenvariabelen zijn getest op de SCMS dataset. De laterale entrainment snelheden afgeleid uit de metingen bevestigen de waarden als voorgesteld door Siebesma and Cuijpers (1995) op basis van LES resultaten. De gesimplificeerde verticale snelheidsvergelijking van Simpson and Wiggert (1969) blijkt een redelijk gesloten budget te geven.

Distributies van shallow cumulus wolken als functie van hun grootte zijn berekend in Hoofdstuk 4 met behulp van LES. Verscheidene onderling verschillende situaties zijn gesimuleerd, en de resulterende karakteristieken worden vergeleken met waarden afgeleid uit observaties van echte cumulus velden. Om een eerlijke vergelijking mogelijk te maken is exact dezelfde methode van berekenen gebruikt in LES als in de observationele studies die meestal gebruik maken van fotografie van grote hoogtes. Het blijkt dat de groottekansdichtheid van cumulus wolken afvalt met een universele machtswet van -1.70 tot een bepaalde kritische grootte waarna hij sneller dan een machtswet afvalt. De wolkengrootte horende bij deze breuk in schaling heeft een orde van grootte van 1 km, maar is zeker niet-universeel en verschilt significant per situatie. De bovengrens van deze schaling is echter een relevante parameter in een dimensieloze universele functionele vorm voor deze kansdichtheid. De dominerende wolkengrootte in de bedekkingsgraad wordt rechtstreeks bepaald door deze schaalbreuk. Het blijkt tevens dat veel kleinere wolken erg weinig bijdragen aan de totale verticale massafux in de wolkenlaag.

De typische variabiliteit van cumulus wolken populaties in de thermodynamische grootheden zoals vocht en temperatuur is onderzocht in Hoofdstuk 5. Een nieuwe parameterizatie voor cumulus convectie is ontwikkeld, die bestaat uit een distributie van kleine, opstijgende

luchtvolumes. LES resultaten zijn indirect gebruikt om de laterale menging van zo'n volume te parameterizeren. Een typische relaxatie-tijdschaal is gebruikt voor het mengproces, en zijn waarde is bepaald uit een evaluatie van de karakteristieke omlooptijd van een cumulus wolk. Het blijkt dat die tijdschaal redelijk constant is voor alle wolken, wat inhoudt dat de intensiteit van menging omgekeerd evenredig is met de verticale snelheid van het volume. Dit brengt een dynamische feedback tot stand: de dynamica beïnvloedt de intensiteit van menging, dat op zijn beurt weer de thermodynamische staat van het volume beïnvloedt, die op zijn beurt weer terugkoppelt op de dynamica. De vergelijking van het model met LES geeft aan dat het in staat is om de afnemende bedekkingsgraad met de hoogte, de ensemble-gemiddelde (thermo)dynamica en massaflux, de bijna-neutrale buoyancy en de typische variabiliteit van ondiepe cumulus velden te reproduceren.

Tenslotte is de interactie tussen de cumulus wolkenlaag en de droge grenslaag daaronder onderzocht in Hoofdstuk 6. Drie methoden voor de sluiting van het massa flux model op wolkenbasis worden kritisch geëvalueerd voor de moeilijke situatie van een dagelijkse gang van cumulus boven land. De betrokken parameters worden eerst diagnostisch gesampled tijdens een simuleerde dagelijkse gang met behulp van LES. Dit laat zien waar welke methode in principe geen goede sluiting geeft. Vervolgens wordt de impact bestudeerd van deze methodes op de ontwikkeling van de grenslaag in een eenkoloms-versie van het Regionaal Atmosferisch Klimaat Model (RACMO). Het blijkt dat de methode gebaseerd op vochtconvergentie geen rekening houdt met sterke vocht tendenzen in de grenslaag, waardoor de massaflux sterk wordt overschat. De methode gebaseerd op de relaxatie van convectieve potentiële energie (CAPE) kan niet overweg met situaties waarin de cumulus convectie sterk wordt gedomineerd door de turbulentie in de droge grenslaag. De methode gebaseerd op de turbulente kinetische energie in de droge grenslaag tenslotte reproduceert wel de waargenomen evolutie van de massa flux op wolkenbasis met de tijd. Als gevolg hiervan geeft deze sluiting de beste resultaten in het eenkoloms model.

De doorgaande validatie van globale weer- en klimaatmodellen met waarnemingen toont aan dat in veel situaties de eigenschappen van de atmosferische grenslaag niet goed zijn gerepresenteerd. Vooral wat betreft lage convectieve bewolking is het duidelijk dat de bestaande parameterizaties voor belangrijke meteorologische variabelen zoals de bedekkingsgraad en de verdeling van verschillende typen lage bewolking niet altijd even goed overeenkomen met de beschikbare observaties. Fouten in de representatie van deze eigenschappen kunnen enorme gevolgen hebben voor de gemodelleerde circulatie en klimatologie. Het is duidelijk dat verder onderzoek en ontwikkeling noodzakelijk is op dit gebied. De resultaten in dit proefschrift hebben daar in die zin aan bijgedragen dat a) de thermodynamische variabiliteit en de populatie statistiek van cumulus wolken velden verder in kaart is gebracht en gequantificeerd in nieuwe parametrische formuleringen, b) de interactie tussen wolken en de droge grenslaag in een typische dagelijkse gang boven land is geanalyseerd en gekarakteriseerd aan de hand van de massa flux op wolkenbasis, en c) is aangetoond dat LES modellen representatieve cumulus wolken populaties simuleren.

Publications

B. Stevens, A. S. Ackerman, B. A. Albrecht, A. R. Brown, A. Chlond, J. Cuxart, P. G. Duynkerke, D. C. Lewellen, M. K. MacVean, R. A. J. Neggers, E. Sanchez, A. P. Siebesma, D. E. Stevens, 2001: Simulations of Trade-wind cumuli under a strong inversion. *J. Atmos. Sci.*, **58**, 1870-1891.

Neggers, R. A. J., A. P. Siebesma and H. J. J. Jonker, 2002: A multi parcel model for shallow cumulus convection. *J. Atmos. Sci.*, **59**, 1655-1668.

A. R. Brown, A. Chlond, C. Golaz, M. Khairoutdinov, D. C. Lewellen, A. P. Lock, M. K. MacVean, C-H. Moeng, R. A. J. Neggers, A. P. Siebesma and B. Stevens, 2002: Large-eddy simulation of the diurnal cycle of shallow cumulus convection over land. *Quart. J. Roy. Met. Soc.*, **128**, 1075-1094.

Neggers, R. A. J., H. J. J. Jonker and A. P. Siebesma, 2002: Size statistics of cumulus cloud populations in large-eddy simulations. *Accepted for publication in the J. Atmos. Sci.*, August 2002.

Neggers, R. A. J., P. G. Duynkerke and S. M. A. Rodts, 2003: Shallow cumulus convection: validation of large-eddy simulation against aircraft and Landsat observations. *Accepted for publication in the Quart. J. Roy. Met. Soc. pending minor revisions*, August 2002.

Neggers, R. A. J., A. P. Siebesma, G. Lenderink and A. A. M. Holtslag, 2003: Mass flux closures in diurnal cycles of shallow cumulus over land. *Submitted to Mon. Wea. Rev.*, July 2002.

Curriculum Vitae

Ik ben geboren op 12 april 1974 in de Van der Duyn van Maasdamstraat te Veghel, en in die plaats ben ik ook opgegroeid. Na de lagere school heb ik de middelbare schoolopleiding genoten op het Zwijsen College, waar ik in 1992 het Gymnasium B diploma heb gehaald. Vervolgens ben ik in hetzelfde jaar Geofysica gaan studeren aan het Instituut voor Aardwetenschappen van de Universiteit Utrecht. In het tweede en derde jaar van die studie heb ik gekozen voor de specialisatie-richtingen theoretische geofysica en tectonofysica. In 1996 heb ik een half jaar in Bergen in Noorwegen gewoond, waar ik met een Europese ERASMUS beurs colleges heb gevolgd in de dynamische meteorologie en oceanografie op het Geofysische Instituut van de Universiteit van Bergen. Deels als voorbereiding hierop en deels als gevolg hiervan heb ik enkele jaren Scandinavische taal- en letterkunde gestudeerd aan de Universiteit van Amsterdam. Vanwege mijn inmiddels gegroeide enthousiasme voor de meteorologie heb ik het afstudeerproject van mijn studie als externe stage gedaan onder begeleiding van Dr. A. van Delden op het Instituut voor Marien en Atmosferisch Onderzoek Utrecht, met als onderwerp de frontogenese processen in afgesneden lagedrukgebieden op tropopauze hoogte. Op 27 mei 1998 kreeg ik mijn bul uitgereikt.

Mijn interesse voor het weer werd eigenlijk voor het eerst gewekt tijdens een vakantie naar Spanje toen ik vier jaar oud was, waar ik er maar niet over uit kon dat het elke dag 'alweer mooi weer!' was. Ik ben dus eigenlijk die eerste verbazing redelijk trouw gebleven door na het behalen van mijn bul in 1998 onderzoek te gaan doen naar 'fair-weather cumulus' (mooi weer cumulus), op het Koninklijk Nederlands Meteorologisch Instituut onder begeleiding van Dr. A. P. Siebesma, Prof. Dr. A. A. M. Holtslag en Dr. H. J. J. Jonker. Het onderwerp van dit project was de fysica en dynamica van ondiepe cumulus convectie en de interactie van deze wolken met de atmosferische grenslaag. Ik heb gebruik gemaakt van hoge-resolutie numerieke stromingsmodellen (large-eddy simulation), alsmede van waarnemingen in echte cumulus wolken tijdens de Small Cumulus Microphysics Study in Florida in 1995, in samenwerking met wijlen Dr. Ir. P. G. Duynkerke. Dit proefschrift is het resultaat van deze vier jaar onderzoek. In januari 2003 ga ik aan een postdoctoraal project beginnen aan de Universiteit van California te Los Angeles in samenwerking met Prof. Dr. B. Stevens en Prof. Dr. J. D. Neelin, met als onderwerp de interactie tussen atmosferische grenslagen en de grootschalige (tropische) circulatie.

The scientific research from which this thesis resulted was supported by the Earth and Life Sciences Foundation (ALW) of the Netherlands Organization for Scientific Research (NWO), Grant 750.198.06. The research was performed at the Royal Netherlands Meteorological Institute (KNMI), as part of the Atmospheric Research group of the Climate and Seismology Department. The LES results in this thesis were obtained using the supercomputer facilities of the European Centre for Medium-range Weather Forecasts (ECMWF) in Reading, UK.

Druk: Ponsen & Looijen, Wageningen, 2002.

Figures 2.9, 2.11 and 7.1 are used by courtesy of the American Meteorological Society. Figure 2.17 is used by courtesy of the Tellus journal.

Cover illustration: 'Bleachin Abbey' by John Constable.